Element and isotope geochemistry from iron formations and carbonates : new insights into the Fe cycle and paleoenvironmental reconstructions during the Neoarchean in Carajás, Brazil

Eric Siciliano Rego

THÈSE POUR OBTENIR LE GRADE DE DOCTEUR DE L'UNIVERSITÉ DE MONTPELLIER

En Géosciences

École doctorale GAIA

Unité de recherche Géosciences Montpellier

En partenariat international avec [Universidade de São Paulo, Instituto de Geociências, Brasil]

Element and isotope geochemistry from iron formations and carbonates: new insights into the Fe cycle and paleoenvironmental reconstructions during the Neoarchean in Carajás, Brazil

Présentée par Eric SICILIANO REGO

Le 28 Juin 2022

Sous la direction de Pascal PHILIPPOT (UM) et Marly Babinski (USP)

Devant le jury composé de

Delphine BOSCH, Président du jury, Directeur de recherche
Vincent BUSIGNY, Membre du jury, Professeur des universités
Ricardo TRINDADE, Membre du jury, Professeur
Marly BABINSKI, Co-Directeur de Thèse, Professeur
Pascal PHILIPPOT, Directeur de Thèse, Directeur de recherche
Franck POITRASSON, Rapporteur, Directeur de recherche
Roberto VENTURA SANTOS, Rapporteur, Professeur

UNIVERSITÉ DE MONTPELLIER

UNIVERSIDADE DE SÃO PAULO
INSTITUTO DE GEOCIÊNCIAS

Element and isotope geochemistry from iron formations and carbonates: new insights into the Fe cycle and paleoenvironmental reconstructions during the Neoarchean in Carajás, Brazil

ERIC SICILIANO REGO

Tese apresentada ao Programa de Geoquímica e Geotectônica para obtenção do título de Doutor em Ciências

Área de concentração: Geotectônica

Orientadores: Marly Babinski (USP) e Pascal Philippot (UM)
Coorientador: Vincent Busigny

SÃO PAULO
2022

Table of Contents

Acknowledgements

First and foremost, I would like to thank my two supervisors, Marly Babinski and Pascal Philippot, without whom none of this work would have been possible. Your encouragement and promptitude throughout this four-year period has made all the difference. I was also incredibly fortunate to have Vincent Busigny as co-supervisor, who dedicated countless hours for discussions and for showing me everything I know regarding clean room chemistry and mass spectrometry. Thank you for always being there. I am grateful to Stefan Lalonde for opening the doors of his lab and for innumerous exchange of ideas that contributed significantly to this thesis. I would like to express a huge gratitude to all colleagues and friends that I encountered during this journey. I feel like I'm highly indebted with so many of you. Camille, Francesco and Livia were there since the early days and early struggles, and I cannot thank you enough. There are so many of you in varying places spread throughout Brazil and France, from colleagues and friends in USP (IGc and IAG), to all the stable isotope crew at IPG, colleagues and friends in Géosciences Montpellier, at IUEM in Brest, colleagues and friends in Dijon; I feel blessed to have met each one of you. Thank you for your kindness and willingness to share ideas, moments and more often than not a shelter. There are others who contributed immensely, from engineers and technicians, to cleaning crews in all those institutions, whom cannot go by unnoticed. Finally, I would like to thank my family and friends for their endless support which always provided strength and motivation, not only during this period, but in life. This work was funded by Fundação de Amaparo à Pesquisa do Estado de São Paulo (FAPESP Projects 2018/05892-0, 2019/16271-0). We acknowledge and are thankful for all their support which made this work possible.

Abstract

Iron formations (IFs) are well-studied chemical archives of Precambrian seawater, thus offering evidence of past oceanic redox conditions, and providing insights on how the iron (Fe) cycle was operating throughout key periods of Earth's history. This work focuses on applying elemental and isotopic geochemical measurements in IFs and carbonates deposited in Neoarchean Carajás (~2.74 Ga), before the Great Oxidation Event (GOE). There is still a large debate regarding possible oxygenation events prior to the GOE, the role of microbial activity in reducing environments, nutrient availability in paleoseawater, and post-depositional effects imprinted in the sedimentary record. These topics will be addressed after a general introduction (Chapter 1), an overview of geological setting from which our samples came from (Chapter 2), and a description of the specific methods utilized to reach our main conclusions (Chapter 3).

In an attempt to reconstruct paleoenvironmental conditions in Neoarchean Carajás, petrographic work combined with major and trace element geochemistry, Fe isotope composition of bulk-rock, and C isotope measurements in organic matter have provided support for anoxic conditions (*i.e.* lack of negative Ce anomalies, positive and homogeneous $\delta^{56}Fe$ values). Organic carbon isotopes also favored the role of bacteria in oxidizing dissolved Fe(II) through anoxygenic photosynthesis (*i.e.* $\delta^{13}C_{org}$ similar to autotrophic organisms). We have also demonstrated that Fe had a prominent hydrothermal source shown by significantly positive Eu anomalies (Chapter 4). Additionally, by measuring phosphorus (P) and Fe content in IFs we have shown that these chemical sediments are indeed suitable archives of ancient seawater as shown by their analogous behavior with modern seawater. Hence, we estimated dissolved

phosphorous contents in paleoseawater locally and globally, based on measured, experimental, and literature data. Our data suggests P-limited conditions prevailed throughout most the Archean Eon (Chapter 5). Finally, after measuring Fe isotopes in carbonate leachates and magnetite (see Methods section, Chapter 3), C isotopes in carbonates, and applying Raman spectroscopy in organic-rich carbonate samples, we demonstrated that microbial dissimilatory iron reduction (DIR) was likely responsible for depleted ^{13}C isotopic signature measured in carbonates. However, the large Fe isotope fractionation expected for DIR as recorded by experimental studies was not observed. In fact, a constant fractionation was recorded in a basinal scale between carbonates and oxides, possibly arguing for a re-equilibration of the Fe-isotopic system at relatively low-temperature conditions (Chapter 6). These results hopefully contributed to the effort of reconstructing the key aspects of the Fe cycle in Neoarchean Carajás, and importantly showed the potential of these samples as significant paleoenvironmental archives.

Resumo

As formações ferríferas (iron formations, IFs) são consideradas arquivos químicos da água do mar Pré-cambriana, oferecendo evidências passadas de condições redox oceânicas e fornecendo informações sobre como o ciclo do ferro (Fe) estava operando ao longo dos principais períodos da história da Terra. Este trabalho tem como foca a aplicação de análises geoquímicas elementares e isotópicas em formações ferríferas e carbonatos depositados no Neoarqueano, Carajás (~2,74 Ga), antes do Grande Evento de Oxidação (GOE). Ainda há um grande debate sobre possíveis eventos de oxigenação anteriores ao GOE, o papel da atividade microbiana em ambientes redutores, disponibilidade de nutrientes na água do mar e efeitos pós-deposicionais impressos no registro sedimentar. Esses tópicos serão abordados após uma introdução geral (Capítulo 1), uma visão geral do cenário geológico de onde as amostras foram coletadas (Capítulo 2) e uma descrição dos métodos específicos utilizados para chegar às principais conclusões (Capítulo 3).

Descrições petrográficas em conjunto com a geoquímica de elementos maiores e traços, composição isotópica de Fe em rocha total e medições de isótopos de C em matéria orgânica, foram chave na tentativa de reconstruir as condições paleoambientais em Carajás durante o Neoarqueano. Tudo indica que condições anóxicas prevaleceram (i.e. falta de anomalias negativas de Ce, valores de $\delta^{56}Fe$ positivos e homogêneos). Os isótopos de carbono na matéria orgânica também favoreceram o papel das bactérias na oxidação do Fe(II) dissolvido através da fotossíntese anoxigênica (i.e. $\delta^{13}C_{org}$ semelhante a organismos autotróficos). Também demonstramos que o Fe teve uma fonte hidrotermal proeminente mostrada por anomalias de Eu significativamente positivas (Capítulo 4).

Além disso, medindo as concentrações de fósforo (P) e Fe em formações ferríferas, mostramos que esses sedimentos químicos são de fato arquivos representativos da água do mar no passado da Terra, como mostrado por seu comportamento análogo com a água do mar moderna. Assim, estimamos os teores de fósforo dissolvido no mar Neoarqueano em Carajás e globalmente, com base em dados analisados, experimentais e da literatura. Nossos dados sugerem que condições pobre em P prevaleceram durante a maior parte do Arqueano (Capítulo 5). Finalmente, após medir isótopos de Fe em frações lixiviadas de carbonato e em magnetita separadas magneticamente (consulte a seção Métodos, Capítulo 3), isótopos de C em carbonatos e aplicar espectroscopia Raman em amostras de carbonato ricas em matéria orgânica, demonstramos que a redução de ferro por dissimilação (dissimilatory iron reduction, DIR) foi provavelmente responsável pelas assinaturas isotópicas de carbonatos empobrecidos em ^{13}C. No entanto, o grande fracionamento isotópico de Fe esperado para DIR conforme registrado por estudos experimentais não foi observado. Ao invés, um fracionamento constante foi registrado em escala basinal entre carbonatos e óxidos, possivelmente sugerindo um reequilíbrio do sistema isotópico de Fe em condições de temperatura relativamente baixas (Capítulo 6). Espera-se que esses resultados tenham contribuído para o esforço de reconstrução dos principais aspectos do ciclo do Fe no Neoarqueano Carajás e, de forma importante, mostraram o potencial dessas amostras como importantes arquivos paleoambientais

Résumé

La co-évolution entre les différentes enveloppes de la Terre et les processus de maintien de la vie ont représenté un sujet de recherche majeur au cours des dernières décennies. Les questions relatives à l'habitabilité de la planète, notamment le moment où les océans et l'atmosphère sont devenus riches en oxygène, ne sont pas complètement élucidées. Ces questions concernent notamment l'origine du dioxygène (O_2) ainsi que le moment où celui-ci a commencé à s'accumuler dans l'atmosphère. La première moitié des 4,5 milliards d'années de l'histoire de la Terre est connue pour ses concentrations extrêmement faibles d'oxygène libre dans l'atmosphère (inférieures à 10^{-5} fois le niveau atmosphérique actuel – *Present-day Atmospheric Level* ; PAL). Les indices d'une oxygénation montrent que l'augmentation permanente de l'O_2 s'est réalisée au cours de deux transitions principales : la Grande Oxydation (*Great Oxidation Event* ; GOE) il y a environ 2,4 à 2,1 milliards d'années (Ga), puis l'événement d'oxygénation Néoprotérozoïque (*Neoproterozoic Oxydation Event* ; NOE), il y a environ 0,80 à 0,54 Ga (Holland et al, 1986 ; Och et Shields-Zhou, 2012 ; Lyons et al., 2014 ; Philippot et al., 2018). Avant ces événements d'oxygénation, seules des « bouffées » d'oxygène ont été déduites des archives géologiques (par exemple, Anbar et al., 2007 ; Eickmann et al., 2018 ; Johnson et al., 2021). Ces périodes fondamentales de changements globaux ont transformé une Terre primitive plus chaude, tectoniquement plus active et anoxique en une Terre plus jeune plus froide, plus stable et oxygénée.

L'augmentation du dioxygène atmosphérique au fil du temps est intrinsèquement liée à la disponibilité des nutriments dans les océans primitifs de la Terre (par exemple le phosphore, P). L'augmentation du dioxygène atmosphérique a également modulé une

tendance évolutive qui a pu favoriser et/ou retarder l'évolution du vivant (Bjerrum et Canfield, 2002 ; Reinhard et al., 2020 ; Reinhard et Planavsky, 2021). Les archives géologiques du Brésil qui couvrent le Néoarchéen, en particulier les grands dépôts de formations ferrifères, constituent des archives bien adaptées pour documenter les conditions paléoenvironnementales, notamment avant l'apparition de l'oxygène atmosphérique. La plupart des études précédentes se sont concentrées sur les archives sédimentaires archéennes de séries australiennes et sud-africaines, provenant respectivement des supergroupes Hamersley et Transvaal. Cependant, ces sites appartenaient probablement à un unique bassin sédimentaire (par exemple Beukes et Gutzmer, 2008). Notre vision globale des modifications de la surface de la Terre avant le GOE peut donc être fortement biaisée par les échantillons étudiés jusqu'à présent. Par conséquent, une comparaison avec d'autres endroits dans le monde est nécessaire.

Les formations de fer (*iron formations* ; IFs) sont des archives chimiques de l'eau de mer précambrienne et offrent la possibilité de documenter les conditions redox océaniques passées, ouvrant une fenêtre sur la compréhension du fonctionnement du cycle du fer (Fe) au cours de périodes clés de l'histoire de la Terre. Ce travail se concentre sur l'application de mesures géochimiques élémentaires et isotopiques dans les IFs et les carbonates déposés à Carajás durant le Néoarchéen (~2,74 Ga), avant la Grande Oxydation (GOE). Il existe encore un large débat concernant des événements d'oxygénation locals et partiels avant le GOE, le rôle de l'activité microbienne dans les environnements réducteurs, la disponibilité des nutriments dans les océans archéens et les effets post-dépôt imprimés dans les archives sédimentaires. Ces sujets seront abordés après une introduction générale (chapitre 1), qui passe en revue la littérature sur les formations ferrifères et les débats concernant les mécanismes de leur formation. L'utilisation des éléments traces, en particulier des terres rares (*Rare Earth Elements* ; REE

et de l'yttrium (Y) est également expliquée. L'utilisation des isotopes stables du fer dans les roches sédimentaires (basse température) y est également détaillée. Le chapitre 2 donne une vue d'ensemble du cadre géologique d'où proviennent nos échantillons, en mettant l'accent sur les unités sédimentaires du Bassin de Carajás, qui représente un dès plus gros gisements de fer au monde situé dans l'état de Pará, Brésil.

Le chapitre 3 est consacré à la description des méthodes spécifiques utilisées dans ce travail. L'approche analytique utilisée pour séparer les minéraux carbonatés des matrices rocheuses complexes (par exemple des IFs) consiste en des lixiviations par des acides faibles. Ce protocole permet de documenter les effets de la dissolution partielle et totale sur le fractionnement isotopique du Fe (Rego et al, soumis). La composition isotopique du fer des carbonates ferrugineux est couramment utilisée pour obtenir des informations sur les conditions environnementales anciennes. Cependant, il est souvent difficile de cibler uniquement les carbonates de fer (par exemple, la sidérite et l'ankérite) à partir d'échantillons contenant une variété d'autres minéraux contenant du fer (par ex. silicates de fer), comme cela est fréquemment observé dans les formations ferrifères précambriennes. Les méthodes d'extraction chimique (c'est-à-dire la lixiviation) des Fe-carbonates pourraient être une alternative aux mesures *in situ* et/ou aux techniques de micro-forage utilisées pour les études isotopiques. Pourtant, seules quelques études ont examiné les effets de la lixiviation des carbonates (par exemple, la dissolution partielle et/ou totale) sur leur composition isotopique en Fe. Une partie du chapitre 3 est consacrée aux tests de plusieurs protocoles de lixiviation. Ceux-ci ont été réalisés en utilisant de l'acide acétique (HAc) à des concentrations comprises entre 5 et 20% et de l'acide chlorhydrique HCl à une concentration de 0,4 $mol.L^{-1}$ (M) sur un standard de sidérite et trois échantillons naturels, incluant une formation ferrifère, des carbonates riches en Fe et des carbonates pauvres en Fe. Nous avons montré que la minéralogie des carbonates

exerce un fort contrôle sur la quantité de chaque phase minérale qui est dissoute, et que les variations de la concentration en HAc de 5% à 20% affectent peu la quantité de sidérite dissoute (par exemple ~30% de dissolution) sur une période de 12h à température ambiante. Il est important de noter que la composition isotopique du Fe de la sidérite partiellement dissoute a, dans la marge d'erreur, des valeurs identiques à celle de la roche totale (c'est-à-dire une dissolution complète), et ceci que ce soit avec les attaques acides par HAc et HCl. Les carbonates des trois échantillons naturels ont été presque complètement dissous avec le même protocole à 5 et 20% de HAc, tandis que les attaques de HCl à 0,4M ont dissous des phases minéralogiques supplémentaires, qui pourraient contribuer au lixiviat de Fe. De plus, la composition isotopique du fer des lixiviats de carbonate a été préservée sans engendrer de résultats anormaux. Par conséquent, les lixiviations chimiques réalisées avec des acides faibles représentent un outil fiable pour étudier la composition isotopique du Fe des carbonates afin de comprendre le fonctionnement du cycle du Fe au cours de l'histoire de la Terre.

Le chapitre 4 est divisé en deux parties : la première concerne la source de Fe dans le Bassin de Carajás suivi d'une discussion des principaux mécanismes d'oxydation ayant permis le dépôt des formations ferrifères au Néoarchéen dans ce bassin. Dans la première partie du chapitre, nous explorons le mécanisme d'oxydation qui transforme le Fe(II) d'origine hydrothermale en Fe(III), conduisant ainsi aux dépôts de formation de fer. Un débat actuel concerne le rôle de la photosynthèse anoxygénique dans le dépôt des IFs avant l'augmentation de l'oxygène atmosphérique. Nous fournissons des preuves géochimiques que les conditions du bassin étaient exclusivement anoxiques, avec une influence hydrothermale forte et continue pendant le dépôt des formations rubanées de Carajás. L'absence d'anomalies de cérium (Ce) révèle que les conditions étaient exclusivement anoxiques pendant le dépôt des IFs, tandis que des anomalies d'europium

(Eu) extrêmement élevées impliquent une activité hydrothermale intense comme source principale du fer. La composition isotopique du carbone de la matière organique, appauvrie en ^{13}C, indique la présence d'organismes autotrophes. Combinée avec les données isotopiques du Fe, qui indiquent seulement de faibles degrés d'oxydation du réservoir de Fe(II), nos résultats suggèrent que les bactéries oxydant le Fe étaient le principal agent d'oxydation du fer via une photosynthèse anoxygénique (ferrophototrophie). Ceci suggère un rôle important des photoferrotrophes pour le dépôt de IFs et renforce leur importance dans le paysage métabolique avant le GOE. Collectivement, nos résultats plaident en faveur de conditions réductrices pendant le dépôt des IFs et suggèrent la photosynthèse anoxygénique comme le mécanisme le plus plausible responsable de l'oxydation du Fe dans le Bassin de Carajás (Rego et al., 2020). Cette étude nous a donc permis, par l'examen détaillé des IFs Néoarchéens de la province minérale de Carajás et des carbonates qui y sont associés, de reconstituer les conditions redox et de déduire le mécanisme d'oxydation ayant conduit à la formation de l'un des plus grands gisements de fer du monde.

La seconde partie de ce chapitre 4 concerne la composition isotopique du Fe de siltites et d'argilites qui se situent stratigraphiquement au-dessus des dépôts riches en fer des principales formations ferrifères du Bassin de Carajás. Les siltites appartiennent au Groupe Igarapé Bahia (âge maximal de dépôt de 2684 $\pm$ 10 Ma ; Rossignol et al., 2020) et la Formation Azul (âge maximal de dépôt de 2273 $\pm$ 35 Ma ; Araujó et al., 2021). Les roches sédimentaires et les minéraux déposés entre ~2,7 et 2,5 Ga sont considérablement appauvris en ^{56}Fe par rapport à d'autres périodes de l'histoire de la Terre (Rouxel et al., 2005 ; Johnson et al., 2008 ; Planavsky et al., 2010 ; Ostrander et al., 2021). Actuellement, ces signatures isotopiques du Fe sont expliquées comme étant soit des produits d'une précipitation importante d'oxyhydroxydes de Fe(III) isotopiquement lourds (c'est-à-dire

dans des conditions réductrices) laissant un réservoir résiduel de Fe(II) isotopiquement léger à partir duquel les minéraux comme les pyrites pourraient précipiter soit directement par réduction dissimilatrice du fer (*Dissimilatory Iron Reduction* ; DIR) et/ou impliquant des effets isotopiques cinétiques. La distinction entre ces processus s'est avérée difficile (Heard et al., 2020 ; Ostrander et al., 2021), et des études supplémentaires sur d'autres secteurs que ceux déjà abondamment étudiés d'Australie occidentale, (formations de Mt. McRae Shale et Jeerinah) et d'Afrique du Sud (Formation de Klein Note) pourraient fournir des indices sur la façon dont le cycle du fer fonctionnait à cette époque. Nos résultats ont montré que les siltites et argilites néoarchéenne et paléoprotérozoïque sont considérablement enrichis en ^{56}Fe. Nous proposons que si le Fe provenait principalement des carbonates, il est possible que la réduction dissimilatrice du fer (DIR) ait joué un rôle dans la réduction des oxydes de fer, ce qui se serait traduit par la formation d'un réservoir de Fe(II) dissous enrichi en ^{56}Fe. Ce mécanisme pourrait expliquer les valeurs élevées en δ^{56}Fe mesurées dans les échantillons étudiés qui sont très différentes des valeurs faibles en δ^{56}Fe mesurées dans des sédiments similaires plus jeunes que 2,7 Ga ailleurs dans le monde. Une implication importante serait que les formation en fer de Carajás enregistre un processus unique localisé à ce bassin ; des investigations supplémentaires sont encore nécessaires cependant pour comprendre les réactions d'oxydation et de réduction impliquées dans la formation de telles signatures isotopiques du Fe dans ces roches siliciclastiques.

Dans le chapitre 5, nous discutons du rôle du phosphore (P) dissous dans les océans archéens. Le phosphore (P) est un nutriment essentiel pour tous les organismes vivants sur Terre et sa disponibilité a été cruciale pour le développement et la prolifération de la vie aux échelles de temps géologiques (Westheimer, 1987 ; Tyrrll T., 1999). Dans les océans, la disponibilité du P exerce un contrôle important sur la

productivité biologique, et sa concentration tout au long de l'histoire de la Terre a probablement modulé l'état redox de l'océan et de l'atmosphère (Bjerrum et Canfield, 2002 ; Hao et al., 2020 ; Alcott et al., 2022). L'évaluation quantitative des niveaux de P dans les océans primitifs sur la base des archives géologiques représente un défi majeur d'une importance capitale pour comprendre l'évolution du vivant et les couplages biogéochimiques au cours du temps (Planavsky et al., 2010b ; Reinhard et al., 2017b). Les reconstructions des concentrations en P dissous dans les océans précambriens sont très débattues et reposent en grande partie sur les teneurs en fer (Fe) et en P mesurées dans les IFs, en tant que reflet de la composition de l'eau de mer au moment de leur formation (Bjerrum et Canfield, 2002 ; Planavsky et al., 2010b ; Jones et al., 2015). Les travaux antérieurs ont conduits à des conclusions contrastées impliquant soit des concentrations en P dissous < 1 M, qui sont nettement inférieures aux valeurs moyennes des océans actuels (~2,3 M ; Bjerrum et Canfield, 2002 ; Jones et al., 2015), soit des teneurs en P de 5 à 50 fois supérieures aux valeurs modernes (~10 M à 100 M ; Rasmussen et al., 2021 ; Ingalls et al., 2022). Dans ce chapitre, nous montrons que le piégeage du P dissous par les oxydes de fer était un mécanisme actif tout au long de l'Archéen. Le concept d'un mécanisme de piégeage conjoint Fe-P au Précambrien a été initialement suggéré sur la base d'observations faites dans les océans actuels (Berner, 1973 ; Wheat et al., 1996 ; Feely et al., 1998 ; Bjerrum et Canfield, 2002), pour être ensuite validé par des simulations numériques (Derry, 2015 ; Reinhard et al., 2017). Cependant, aucune contrainte empirique claire issues des archives sédimentaires archéennes n'a été proposée. A partir de l'étude des formations ferrifères de Carajás et d'une revue détaillée des données disponibles dans la littérature, nous proposons ici que les teneurs en P dans l'océan archéen était faible. Par ailleurs, nous montrons à partir des IFs de Carajás, qu'il est possible de reconstituer les conditions environnementales passées de manière globale en raison du caractère

prévisible des réactions d'adsorption d'éléments mineurs et traces tels que le P par les oxydes de fer. Par analogie avec les environnements modernes, et en se basant sur des études expérimentales de la partition du P et du Fe dans les IFs, nous avons estimé qu'entre 3,8 et 2,6 Ga environ, les teneurs en P des océans archéens étaient très faibles de l'ordre de 0,063 $\pm$ 0,05 M. En supposant une profondeur de 1000 m et un faible flux de P, le temps de résidence du P dans le bassin de Carajás a été estimé à 146 ans, ce qui est significativement inférieur au temps de résidence du P dans l'océan moderne (20000 à 80000 ans ; Benitez-Nelson, 2000). La différence avec les valeurs modernes est encore plus marquée si l'on considère un flux de P élevé (par exemple 1,85 x 108 $mol.an^{-1}$), qui se traduit par un temps de résidence de 3 ans. Par conséquent, ces résultats impliquent que les IFs ont été un important puits de P et ont probablement limité la disponibilité du P dans les océans archéens.

La disponibilité à long terme du phosphore dans l'océan terrestre contrôle la capacité de l'oxygène à s'accumuler dans l'atmosphère en augmentant la production de biomasse primaire, qui lors de son enfouissement dans les sédiments, favorise l'accumulation nette d'O_2 (Reinhard et Planavsky, 2020). Récemment, il a été avancé que les changements dans le recyclage du P au fil du temps, suite à l'augmentation de la concentration en accepteurs d'électrons (c'est-à-dire lors de changements des conditions redox du milieu), auraient modulé la production biologique (Kipp et Stücken, 2017), et auraient été à l'origine du principal point de basculement redox de la Terre que représente l'évènement de grande oxydation (GOE) (Alcott et al., 2022). Par conséquent, avant que ne se mettent en place des taux élevés d'altération continentale du fait de l'émergence des continents se traduisant par une augmentation de l'afflux de P et de sulfate sur les marges continentales et donc la précipitation en masse de sulfures beaucoup moins efficaces pour absorber le P que les oxydes de fer (Krom et Berner, 1981

; Kraal et al., 2022)), il est fort probable que les concentrations en phosphore dans les océans ont prévalu pendant au moins la première moitié de l'histoire de la Terre. Ces faibles concentrations en P ont probablement fortement contribué à l'anoxie générale de l'atmosphère et de l'océan pendant une grande partie de l'Archéen.

Dans le chapitre 6, la composition isotopique du Fe des carbonates et de la magnétite est analysée en mettant en œuvre le protocole détaillé dans le chapitre 3 (lixiviation). Les compositions isotopiques du C des carbonates dans les IFs de Carajás sont également mesurées afin de comprendre s'ils reflètent des caractéristiques primaires (c'est-à-dire en équilibre avec l'eau de mer) et/ou secondaires du fait d'un ré-équilbrage diagénique précoce (par exemple la respiration microbienne) et/ou tardif (par exemple la diagénèse d'enfouissement ou le métamorphisme). La question de l'utilisation potentielle des carbonates de fer comme marqueurs fiables des conditions océaniques et atmosphériques fait l'objet d'un débat ancien (Rosing et al., 2010 ; Johnson et al., 2013). Pour certains auteurs, les carbonates précipitent en équilibre avec l'eau de mer, reflétant ainsi les conditions environnementales passées (Ohmoto et al., 2004 ; Rosing et al., 2010). Pour d'autres, ils sont liés à la réduction microbienne du fer durant la diagénèse précoce (Johnson et al., 2013 ; Craddock et Dauphas, 2011) ou formés directement de manière abiotique durant la diagénèse tardive (Jiang et al., 2022 ; Tsikos et al., 2022). Ces interprétations distinctes sont largement fondées sur des signatures isotopiques Fe et C particulières. En supposant une faible variabilité du réservoir isotopique de carbone inorganique dissous (DIC ; $\delta^{13}C \cong 0‰$) dans l'eau de mer tout au long de l'enregistrement géologique (par exemple, Fischer et al, 2009), les carbonates (Ca-Mg) pauvres en Fe avec des valeurs de $\delta^{13}C$ de $0 \pm 2‰$ sont généralement interprétés comme ayant précipité en quasi-équilibre avec l'eau de mer (Heimann et al., 2010 ; Craddock et Dauphas, 2011 ; Johnson et al., 2013). Au contraire, les carbonates avec de faibles valeurs en $\delta^{13}C$ (< -8‰)

sont interprétés comme des produits de la respiration microbienne, ce qui se traduit soit par un DIC appauvri en ^{13}C en raison de l'oxydation de la matière organique (Jonhson et al., 2013), soit du fait d'effets cinétiques associés à la précipitation minérale (Jiang et al., 2022). Dans le cas de la formation de carbonates riches en Fe, des expériences de précipitation de la sidérite de manière abiotique ont montré des fractionnements isotopiques du fer à l'équilibre de l'ordre de -0,48 $\pm$ 0,22‰ (Wiesli et al., 2014). De plus, des expériences impliquant la réduction dissimilatrice microbienne du fer (DIR) ont montré que le $Fe(II)_{aq}$ produit par la respiration anaérobie est toujours appauvri en ^{56}Fe par rapport au substrat ferrique précurseur ~-1 à -2,6‰ (Beard et al, 1999, 2003 ; Icopini et al., 2004 ; Johnson et al., 2005 ; Crosby et al., 2005 ; 2007 ; Wu et al., 2009 ; Tangalos et al., 2010 ; Percak-Dennett et al., 2011 ; Fortney et al., 2016, 2020). Par conséquent, en combinant les mesures des isotopes du C des carbonates, et des isotopes de Fe dans les carbonates et les oxydes, nous pensons pouvoir distinguer une composante d'eau de mer et/ou des caractéristiques diagénétiques.

Dans ce chapitre, nous avons mesuré la composition isotopique du C des IFs et des carbonates riches et pauvres en Fe ainsi que la composition isotopique du Fe des lixiviats carbonatés (voir chapitre 3, Rego et al., soumis) et de la magnétite provenant du même ensemble d'échantillons de Carajás. Les valeurs du $\delta^{56}Fe$ des échantillons de magnétite montrent une large gamme allant de +0,34 à +2,23‰ avec une moyenne à +1,01‰ (n=31). Des valeurs du $\delta^{56}Fe$ plus élevées sont enregistrées par la magnétite (+1,03 à +2,23‰), tandis que les carbonates riches et pauvres en fer présentent des valeurs de magnétite variant de +0,34 à +0,88‰ et de +0,52 à +0,93‰, respectivement. Les lixiviats carbonatés ont une composition isotopique en fer comprise entre -0,54 et +1,60‰ avec une valeur moyenne de +0,04‰ (n=31). Les lixiviats carbonatés des IFs présentent des valeurs de $\delta^{56}Fe$ allant de -0,01 à +0,66‰, à l'exception d'un échantillon anormal qui est

significativement enrichi en isotope de Fe (+1,60‰). Les lixiviats carbonatés riches et pauvres en Fe présentent des valeurs $\delta^{56}Fe$ similaires, de -0,53 à -0,06‰ et de -0,54 à +0,01‰, respectivement. Les magnétites et carbonates séparés présentent un fractionnement presque constant de ~1‰ entre les deux phases minéralogiques ($\Delta^{56}Fe_{mag}$ - $Fe_{carb.}$) = +0,98 $\pm$ 0,11‰, n = 31 paires de magnétite et de sidérite/ankérite). Le $\delta^{13}C$ du du carbonate suggère le rôle prépondérant de le respiration microbienne durant le dépôt des IFs et carbonates à Carajás, comme cela a été proposé dans d'autres formations sédimentaires en Australie, Afrique du Sud et Chine. En revanche, les isotopes du Fe dans les minéraux séparés semblent avoir été rééquilibrées durant une phase de métamorphisme de bas grade (T ≤ 250°C) oblitérant ainsi le signal primaire associé à la respiration microbienne (DIR). Nous suggérons donc que la composition isotopique du fer dans les carbonates peut difficilement être utilisée comme un indicateur de la composition de l'eau de mer ou de l'influence du DIR dans les roches sédimentaires archéennes. Une combinaison de travaux *in situ* et de mesures de haute précision sur roche totale (y compris, dans un avenir proche, des quatre isotopes stables du fer) pourrait être un outil prometteur pour reconstituer de manière plus fiable l'évolution conjointes des changements redox et de l'activité microbienne dans les océans et l'atmosphère anciens.

CHAPTER 1

1. General Introduction

The co-evolution of the Earth and its processes to sustain life have been a major research topic during the past decades. Questions regarding the planet's habitability, including when the ocean and the atmosphere became oxygen-rich, still imposes challenges to our understanding of how and when these resources evolved. The first half of Earth's 4.5-billion-year history is known for extremely low concentrations of free oxygen in the atmosphere (below 10^{-5} PAL, present atmospheric level) and evidence for a permanent rise in O_2 occurred across two main transitions: the Great Oxidation Event (GOE) ~2.4 to 2.1 billion years (Gyr) ago and later followed by the Neoproterozoic Oxygenation Event (NOE) ~0.80 to 0.54 Ga (Holland et al., 1986; Och and Shields-Zhou, 2012; Lyons et al., 2014; Philippot et al., 2018). Prior to these oxygenation events only "whiffs" of oxygen were deduced from the geological record (*e.g.* Anbar et al., 2007; Eickmann et al., 2018; Johnson et al., 2021). These fundamental periods of global changes transformed a hotter, tectonically more active and anoxic early Earth to a cooler, more stable and oxygenated younger Earth.

This increase in atmospheric oxygen through time was intrinsically related to nutrient availability (*e.g.* phosphorus) in Earth's early oceans and modulated an evolutionary trend that may have enhanced and/or delayed the evolution of life (Bjerrum and Canfield, 2002; Reinhard et al., 2020; Reinhard and Planavsky, 2021) (Fig. 1.1). The

geological record in Brazil spanning the Neoarchean provides well-suited archives to further explore paleoenvironmental conditions particularly before the rise of atmospheric oxygen. Most previous studies focused on the Archean sedimentary records of Australian and South African rocks, from the Hamersley and Transvaal Supergroups respectively, but these sites were likely combined into a unique sedimentary basin (e.g. Beukes and Gutzmer, 2008). Our global view of the Earth's surface modifications prior to the GOE may thus be strongly biased by the samples studied so far. Therefore, a comparison with other locations in the world is required.

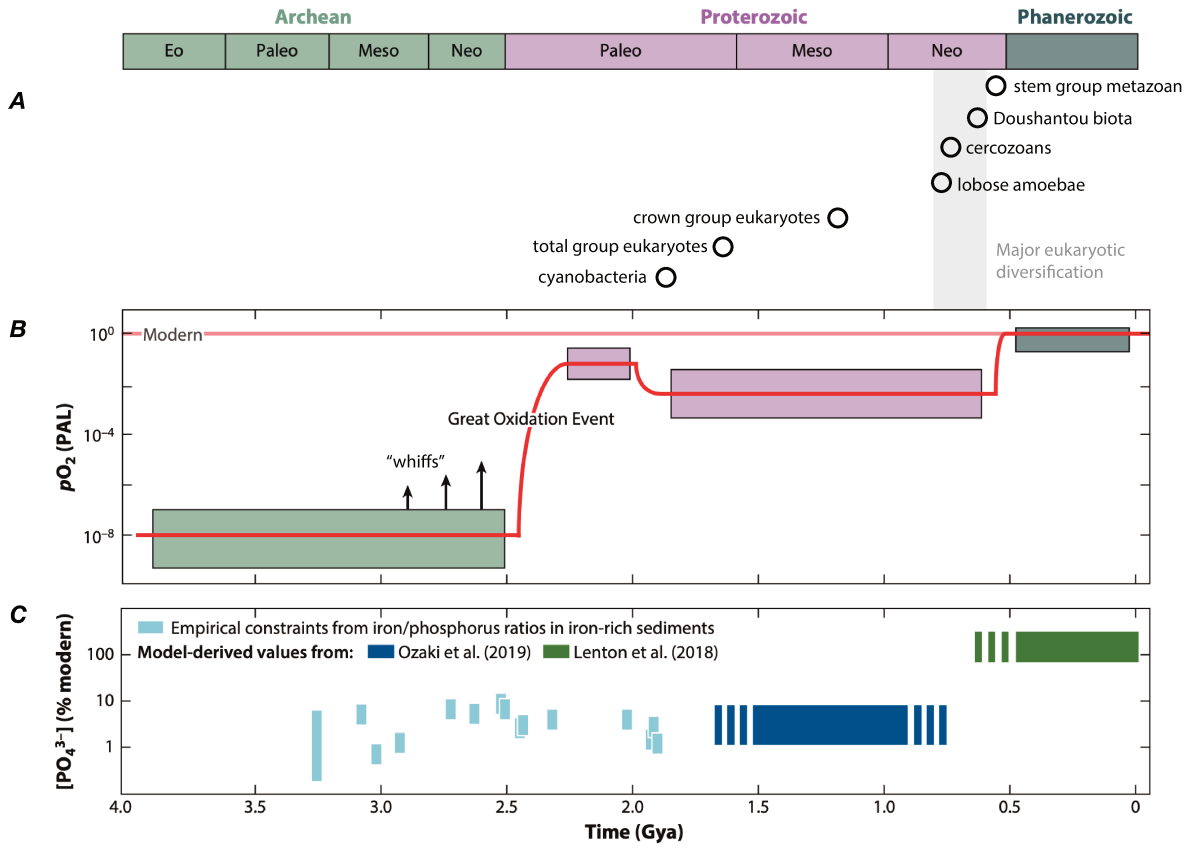

Figure 1. 1: The appearance of microfossils (A) and the varying atmospheric pO_2 (B) and oceanic phosphate (PO_4^{3-}) (C) through Earth's history (modified after Reinhard et al., 2020; Reinhard and Planavsky, 2021). Boxes in panel B show estimated ranges of pO_2 from geologic proxy constrains, while red line marks its trajectory through time. Arrows indicate whiffs of oxygen before the GOE (B). Light blue bars in panel (C) are estimates from Fe/P ratios in iron-rich chemical sediments,

and blue and green bars were determined by computer-based estimations (Lenton et al., 2018; Ozaki et al., 2019a).

The main goal of this thesis is to apply geochemical tools, such as iron (Fe) and carbon (C) isotopic variations, major and trace element concentrations, in iron formations and carbonates spanning the Neoarchean (~2.74 Ga) in Northern Brazil, Carajás, Pará (PA), to understand under which conditions these rocks formed (*i.e.* paleoenvironmental reconstruction) and its later diagenetic history. This was done mainly by studying in detail two well-preserved drill-cores composed of iron formation and carbonates. These data will be interpreted in a local context, and only afterwards placed within a global perspective. General questions concerning this distinct period in Earth's history include: (1) If these rocks are indeed archives of past oceanic conditions, what are the main paleoenvironment characteristics of Neoarchean in Carajás (*e.g.* Whiffs of O_2 in Carajás before the GOE?). (2) Is there any evidence for active microbial communities favoring these rocks to form ~2.74 Gy ago? And if so, (3) what are their relationship between oxidizing and reducing mineralogical phases that we encountered? (4) Are iron formations good indicators of nutrient availability in Archean seawater? Finally, (5) how does the Neoarchean in the South American platform contributes to our understanding of Fe, C and nutrient cycling in the past ocean and is there any similarities and/or discrepancies compared to other sites throughout the globe?

In order to address these questions, (1) major and trace element geochemistry including rare earth elements and yttrium (REY) systematics were applied to the full sample set in combination with petrographic and mineralogical observations. Additionally, (2) the iron isotope composition of iron formations (IFs) and carbonates were determined in whole-rock and (3) in separate mineral phases (*e.g.* carbonate leachates, Fe-oxides) to distinguish between primary, early and late diagenetic effects and

to ultimately identify fractionation associated to microbial processes and to obtain insights into the local (*i.e.* basin scale) iron cycle. Lastly, (4) these results will be compared and discussed taking into consideration all the previous literature with a global perspective aiming to hopefully shed new light into the mechanisms that favored these rocks to form and the subsequent processes they were exposed to.

All of these questions will be explored in detail in the following chapters after a general introduction of the main topics related to this thesis (**Chapter 1**). **Chapter 2** is dedicated to provide the geological context of the Carajás Basin, which includes a recently defined stratigraphic framework spanning the Neoarchean and Paleoproterozoic (Rossignol et al., 2020; 2021). **Chapter 3** focuses on the main methods utilized throughout this thesis. This chapter also describes the analytical approach used to separate carbonate minerals from complex rock matrixes (*e.g.* whole-rock IFs) by applying weak acid leaches and demonstrates the effects of partial and total dissolution on Fe isotope fractionation (Rego et al, submitted). **Chapter 4** aims to understand the oxidizing mechanisms that allowed iron formations to be deposited in the Carajás Fm., its relation to microbial activity, and suggests how reduced and/or oxidized Carajás paleoseawater was before the GOE (Rego et al, 2022). **Chapter 5** attempts to quantify nutrient availably (*e.g.* dissolved phosphorus concentration) locally in Carajás paleoseawater, but also throughout the globe during most of the Archean Eon (Rego et al, submitted). In **Chapter 6**, the Fe isotope composition of magnetite and carbonates reveals potential processes (*e.g.* primary vs. diagenetic signatures) that were once masked by measuring only whole-rock samples (Rego et al, in prep.). Finally, a 'conclusion and future perspectives' section highlights the main results obtained throughout the Ph.D. and provides additional views to be explored in the field of stable isotopes as tracers of past environmental conditions.

1.1 Iron formations as archives of Earth's ancient oceans

Iron formations (IFs) are chemical sedimentary rocks characterized by Fe bearing minerals (20-40 wt.% bulk Fe) normally interbedded with silica-rich layers, and whose occurrence is common in the Precambrian (James, 1954; Cloud, 1973; Garrels et al., 1973). Their mineralogy consists mainly of oxides (hematite, magnetite), carbonates (siderite, ankerite, Fe-dolomite and less commonly, calcite), chert and silicate (stilpnomelane, riebeckite, greenalite, minnesotaite), and rarely sulfides (locally pyrites), and phosphate (apatite) (Bekker et al., 2010; Konhauser et al., 2017). The varying mineralogical assemblages among IFs is dependent on the extent of the sample's preservation, which relates to early (*e.g.* microbial respiration) and/or late diagenetic effects and metamorphism. The majority of IFs deposits occurred in the Archean and Paleoproterozoic (~3.8 to 1.8 Ga), however, IFs reappeared in the geological record in lesser extent during the Mesoproterozoic (~1.4 to 1.3 Ga), Neoproterozoic (~700 to 600 Ma) and early Cambrian (Klein, 2005; Bekker et al., 2010; Canfield et al., 2018; Li et al., 2018; Yang et al., 2018, 2022). The origins for these younger IFs are still debated, but studies suggest a relation to volcanism and extensive periods of glacial conditions (*e.g.* during the Neoproterozoic).

Since the 1950s, a vast literature was produced concerning the origins of IFs, from experimental studies precipitating minerals in a myriad of conditions with and without the influence of a biological component, to geochemical investigations of the geological record and from observations of modern hydrothermal systems (James, 1954; Trendall and Blockley, 1970; Cairns-Smith, 1978; Anbar and Holland, 1992; Isley, 1995; Konhauser

et al., 2002; Posth et al., 2008; Planavsky et al., 2010a; Köhler et al., 2013; Rasmussen et al., 2014; Tosca et al., 2016; Halevy et al., 2017; Nie et al., 2017a; Rouxel et al., 2018; Thompson et al., 2019; Han et al., 2021; Dodd et al., 2022). However, until today, the origin of IFs remains debated. In general, there is a common view that ferrous iron (Fe^{2+}), which is highly soluble in anoxic conditions, is oxidized to form insoluble ferric iron (Fe^{3+}) minerals that are common in IFs.

One interpretation is that mobile dissolved Fe^{2+} was abundant in reducing oceans, therefore transported over great distances until it reached surface marine environments, where Fe^{2+} was ultimately oxidized forming insoluble mixed valance iron (oxyhydrox)oxides. These precipitates would settle in the ocean floor along with amorphous silica gels forming deposits consisting of alternate bands of Fe and Si, which is a typical feature of banded iron formations (Fig. 1.2). Recent studies have suggested that temperature fluctuations was likely responsible for such alternation between Fe and Si-rich bands (Schad et al., 2019a). The oxidizing mechanism, however, a key process to allow these chemical sediments to form, could have been driven either by oxygen produced by cyanobacteria, anoxygenic photosynthesis, and oxidation via UV radiation (Dauphas et al., 2004; Konhauser et al., 2017 and references therein). Alternatively, other studies have suggested that an Fe^{2+}-silicate mineral, known as greenalite, was the actual precursor of IFs (see Rasmussen et al., 2021 for a review). This model, which implies reconsidering in depth the interpretation of Precambrian seawater chemistry by advocating a lack of an Fe^{2+} oxidant and a marine photic zone biosphere, was recently shown to be highly unlikely (Robbins et al., 2019a).

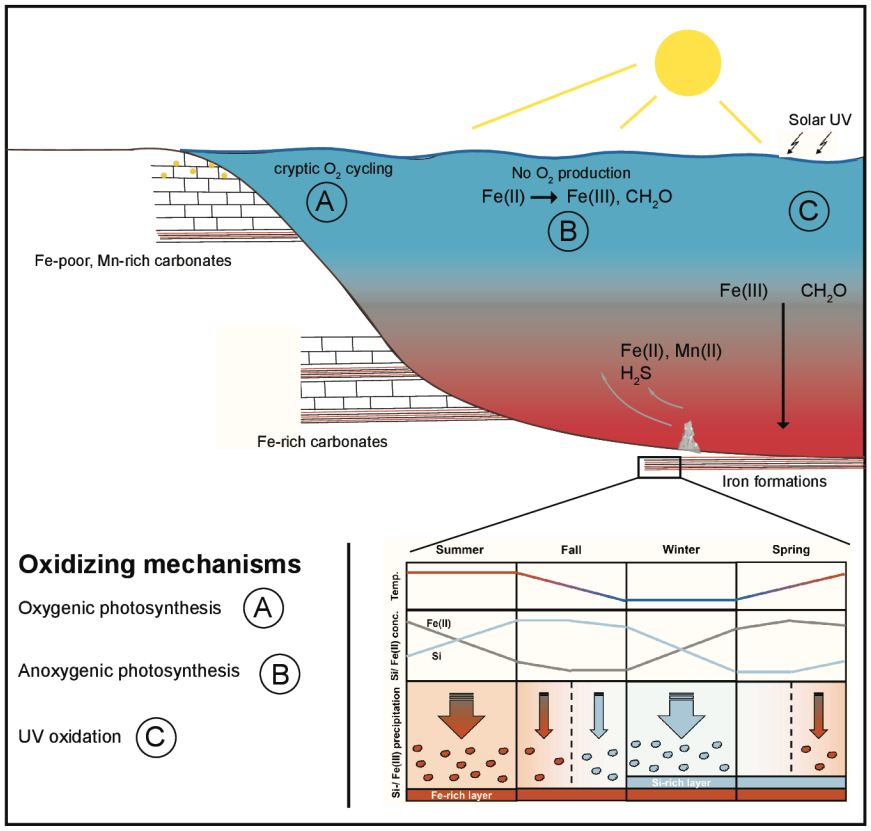

Figure 1. 2: Main oxidizing mechanisms responsible for iron formation deposition in the Archean and Proterozoic. These include (a) oxygenic photosynthesis, (b) anoxygenic photosynthesis, and (c) UV oxidation. Schematic diagram showing Fe-rich and Si-rich layer deposition as a function of changing seasons (modified after Schad et al., 2019).

Most studies concerning IFs as an archive for the early chemistry of the oceans and atmosphere agree with mixed valance iron (oxyhydrox)oxides as precursors of IFs (*e.g.* Planavsky et al., 2010). This is due to the predictable nature of trace element adsorption to mineral precursors that would have precipitated from, and equilibrated with, contemporaneous seawater (Oonk et al., 2018). Rare earth elements and yttrium (REY) patterns in IFs, for example, may have similar characteristics to seawater, suggesting that some IFs preserved a primary seawater signature (Derry and Jacobsen, 1990; Bau, 1993; Bau and Dulski, 1996; Bolhar et al., 2004; Lawrence and Kamber, 2006). The search for a modern seawater-like signature in these ancient chemical sediments is a common practice

among studies involving IFs, and more importantly, they have proven to be consistent and displaying indeed seawater characteristics in rocks throughout the entire Precambrian.

1.2 Rare Earth Elements and Yttrium systematics

Shale-normalized rare earth element and yttrium (REY) abundances in IFs is a common tool used in understanding the origins of IFs, which can be attributed to their less susceptibility of alteration by diagenesis and metamorphism, and their capability to track redox conditions (*e.g*. Banner et al., 1988; Bau, 1991, 1993). Yttrium (Y) is not part of the lanthanides, however, it is chemically similar to holmium (Ho) (Bau, 1996). Despite chemical similarities, Y behaves differently from Ho due to surface complexation effects, and given different chemical bonding, Y attaches not as strongly to surface complexes as Rare Earth elements. Thus, Y stays in seawater and generates superchondritic Y/Ho ratios in the modern ocean (Bau, 1996). In these modern environments, the lanthanide elements are controlled by terrestrial versus hydrothermal inputs and by particle-solution interactions that change with water depth, salinity and local redox conditions (Elderfield and Sholkovitz, 1987; Elderfield et al., 1988; Bolhar et al., 2004; Lawrence and Kamber, 2006). The most preserved IFs, normally devoid of any detrital contamination ($\leq$ 0.2 wt.% Al), show patterns similar to modern seawater: a depletion of light REY (LREY) as opposed to heavy REY (HREY), positive Y anomalies, and in some cases a negative cerium (Ce) anomaly (Planavsky et al., 2010).

The trend in REY abundances when normalized to the post Archean Australian Shale (PAAS, Pourmand et al., 2012) tends to be smooth and predictable due to a gradual

decrease in ionic radii from lanthanum (La, 1.18 Å) to lutecium (Lu, 0.97 Å) linked to the progressive filling of the 4f electron orbital (Tostevin et al., 2016; Oonk et al., 2017). In some cases, the REY elements may show an anomalous behavior, which is normally quantified by standardizing the measured abundance with the neighboring element (*e.g*. Bau and Dulski, 1996; Bolhar et al., 2004; Lawrence et al., 2006). In the case of an element that has no neighbor REY, such as La, its anomaly can be demonstrated by comparing a Ce anomaly, expressed as $[Ce/Ce^*] = Ce/(0.5La + 0.5Pr)$, against a Pr anomaly, expressed as $[Pr/Pr^*] = Pr/0.5Ce + 0.5Nd)$ (Bau and Dulski, 1996).

Rare earth elements are usually found in a trivalent (+3) oxidation state but cerium (Ce) and europium (Eu) can show variable redox state and are considered as redox-sensitive elements, when compared with/to neighbor elements. Specifically, divalent (+2) Eu occurs in strongly reducing environments, and under high temperature (> 250 ºC), is more efficiently extracted by hydrothermal fluids than other REYs in the +3 state. As a consequence, positive Eu anomalies, calculated as $[Eu/Eu^*] = Eu/(0.67Sm + 0.33Tb)$, are interpreted to reflect the mixing of seawater with hydrothermal fluids and are particularly common in IFs from the Archean and Paleoproterozoic (*e.g*. Viehmann et al., 2015).

Cerium can be found in either soluble +3 or insoluble +4 oxidation states. In modern oxygenated marine environments, Ce has a strong negative anomaly when normalized to PAAS mainly due to changes in its solubility, which allows a preferential removal of Ce onto Mn(IV)-Fe(III)-oxyhydroxides, organic matter, and clay particles (German and Elderfield, 1990; Bau and Koschinsky, 2009). The search for Ce anomalies in the geological record is a common practice throughout the Archean, Paleoproterozoic and Neoproterozoic to look for changes in paleoseawater redox state. For instance, to identify "oxygen oasis" prior to the GOE (*e.g*. Riding et al., 2014), to evaluate local redox-

stratified water column and estimate atmospheric oxygen levels in the Paleoproterozoic (*e.g*. Bellefroid et al., 2018; dos Santos et al., 2022), and to characterize redox conditions during and after the Neoproterozoic (*e.g*. Wallace et al., 2017). A compilation of Ce anomalies from the geological record through time, including IFs and carbonates, shows clear negative anomalies during the Neoproterozoic, which becomes more pronounced after ~0.5 Ga (Fig. 1.3). This suggests that Neoproterozoic oceans were more oxidized compared to the Archean, Paleo and Mesoproterozoic oceans. Additionally, pronounced negative Ce anomalies after ~0.5 Ga are in agreement with an increase in dissolved oxygen concentrations in deep-oceans as estimated from $Fe^{3+}/\sum Fe$ in submarine basalts (Stolper and Keller, 2018).

The utilization of Ce anomalies as indicator of redox changes has also limitations, including inhibition of Ce^{3+} oxidation in the presence of abundant Mn^{2+} and under strong alkaline conditions, and post-depositional alteration imprinted by fluid circulations (Moffett, 1994; Pourret et al., 2008; Bonnand et al., 2020). Moreover, cerium has a high reduction potential, which requires elevated oxygen concentrations to oxidize Ce^{3+} to Ce^{4+}, as opposed to smaller oxygen concentrations necessary to oxidize Fe^{2+} to Fe^{3+} (Tostevin et al., 2016). This is the main limiting factor for the identification of environments with low-oxygen content, which was likely dominant throughout the first half of Earth's history. As an alternative to Ce concentrations, the measurement of its stable isotopes seems to be a promising tool to further constrain redox changes (Nakada et al., 2013, 2016; Bonnand et al., 2019). Stable isotope fractionation, particularly from some heavy elements (*e.g*. Mo, Cr, Fe) are key for tracing oxidizing processes through time. In the present PhD thesis, we will focus on iron (Fe) stable isotopes as tracers of past redox changes.

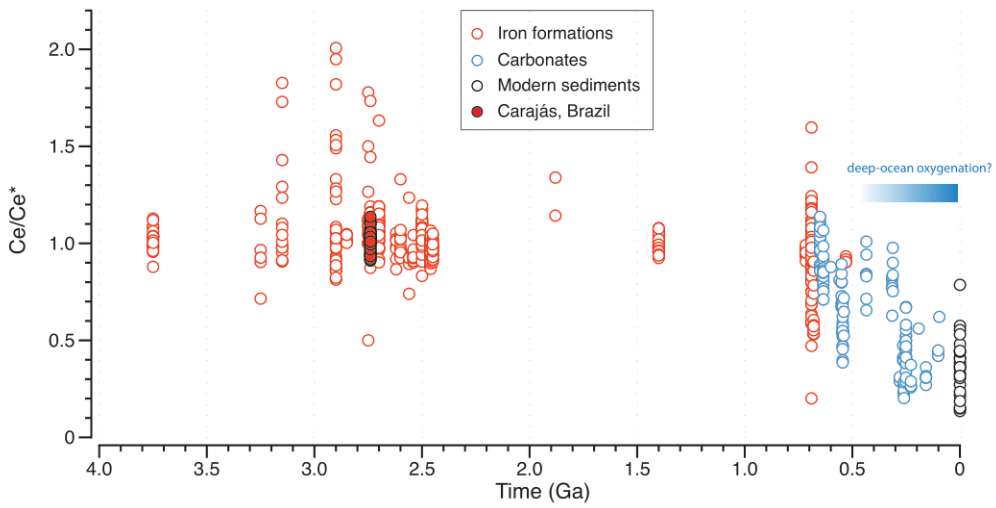

Figure 1. 3: Compilation of Ce anomalies through time. Literature data are from iron formations, carbonates and modern sediments (Derry and Jacobsen, 1990; Danielson et al., 1992; Bau and Dulski, 1996; Lottermoser and Ashley, 2000; Hofmann, 2005; Bhattacharya et al., 2007; Frei and Polat, 2007; Frei et al., 2008; Bau and Alexander, 2009; Fabre et al., 2011; Halverson et al., 2011; Mloszewska et al., 2012; Haugaard et al., 2013; Viehmann et al., 2015b; Garcia et al., 2016; Haugaard et al., 2016a; Viehmann et al., 2016; Haugaard et al., 2017; Wallace et al., 2017; Teixeira et al., 2017; Busigny et al., 2018; Canfield et al., 2018; Lantink et al., 2018a; Li et al., 2018; Warchola et al., 2018; Lechte et al., 2019a).

1.3 Stable Iron Isotopes

Iron is the fourth most abundant transition metal in the Earth's crust, and has three oxidation states: metallic iron (Fe^0), ferrous iron (Fe^{2+}) and ferric iron (Fe^{3+}). In Earth's core, metallic iron is dominant and occurs as alloys with nickel (Ni) and a few light elements (*e.g.* S and O). In the silicate Earth, Fe^{2+} is present in greater abundance in the mantle, while Fe^{3+} is characteristic of more oxidized surface environments. In some cases, however, metallic iron and ferric iron can be found in lower portions of the mantle due to Fe^{2+} disproportionation, and it can also exists in surface environments from rare occurrences of meteorite falls, reduction of lavas in contact with coal sediments and as

josephinite (awaruite) due to serpentinization reactions in peridotites (Dauphas et al., 2017; Frost et al., 2004). Even though all the redox states can be found as solids in oxygenated environments, only Fe^{3+} is thermodynamically stable (Raiswell and Canfield, 2012). The solubility of iron has a major role on its availability and distribution throughout Earth's main reservoirs. In oxygenated surface environments, Fe^{3+} is insoluble at neutral pH (but is soluble under highly acidic conditions), thus inhibiting solid-liquid reactions and limiting bioavailability (Johnson and Beard, 2006). Iron has an essential role as a co-factor in cellular enzymes linked to photosynthesis, respiration and nitrogen fixation, which in turn influences primary productivity and the biogeochemistry of the global oceans (Tagliabue et al., 2017; Kappler et al., 2021).

Isotopes are atoms that have the same number of protons but distinct number of neutrons in its nuclei, and therefore have different atomic masses. Iron has four naturally occurring stable isotopes: ^{54}Fe, ^{56}Fe, ^{57}Fe, and ^{58}Fe, with relative abundancies of 5.85, 91.75, 2.12, and 0.28 atom%, respectively of the total (Berglund and Wieser, 2011; Meija et al., 2016). Distinguishing these mass differences among chemical elements in natural samples have been one of the most fundamental tools to uncover the history of our Solar System and its planets. The partitioning of isotopes between the two phases (*e.g.* aqueous Fe^{2+} and Fe^{3+}), normally referred to as fractionation, is driven by chemical reactions, either resulting from equilibrium distribution of isotopic species among coexisting phases and/or kinetic effects of a specific reaction (Hoefs, 2009; Ibañez-Mejia and Tissot, 2021). When the degree of fractionation scales proportionally with isotopic mass differences, this is called a mass-dependent fractionation (MDF). Any statistically-significant deviation from a mass-dependent fractionation is known as mass-independent fractionation (MIF; Amor et al., 2016; Dauphas and Schauble, 2016).

The isotopic composition of an element can be expressed as the abundance ratio of two isotopes i and j:

$$R^{i/j} = \frac{E^i}{E^j}, \qquad (1.0)$$

where the heavy and light isotopes are the numerator and denominator, respectively. Given the small scale of variations between isotopic ratios, particularly for heavier elements, the δ-notation is often used, which represents a sample's departure from a well-known standard and is reported in per mil (‰) as:

$$\delta^{i/j}(‰) = \left(\frac{R^{i/j}_{sample}}{R^{i/j}_{standard}} - 1\right) \times 10^3. \quad (1.1)$$

For simplicity, the δ-notation is often expressed including only the heavy isotope in its upper script (*e.g.* δ^{56}Fe, δ^{13}C). In order to express the difference in isotopic composition between two phases A and B, it is common to refer to the fractionation factor α:

$$\alpha_{A-B} = \frac{R_A}{R_B}. \quad (1.2)$$

The isotopic difference Δ between the two phases A and B is called isotope fractionation and is calculated as:

$$\Delta_{A-B} = \delta_A - \delta_B. \qquad (1.3)$$

The relationship between $\alpha_{A\text{-}B}$ and Δ_{A-B} can be determined by including δ_A and δ_B in the equation 1.2:

$$\alpha_{A-B} = \frac{(\delta_A/1000 + 1)}{(\delta_B/1000 + 1)} = \frac{\delta_A + 1000}{\delta_B + 1000} \quad (1.4)$$

Now subtracting one from each side:

$$\alpha_{A-B} - 1 = \frac{\delta_A - \delta_B}{\delta_B + 1000} \approx \frac{\delta_A - \delta_B}{1000} \quad (1.5)$$

If the numerator on the right-hand side (RHS) of the equation is replaced by the Δ_{A-B},

$$\Delta_{A-B} \approx (\alpha_{A-B} - 1) \times 10^3 \quad (1.6)$$

and considering that $\alpha_{A\text{-}B}$ is close to unity for small isotopic fractionations, then $\ln \alpha_{A\text{-}B} \approx \alpha_{A\text{-}B} - 1$. This means that,

$$\Delta_{A-B} \approx 10^3 \ln \alpha_{A-B} \quad (1.7)$$

In this work, the delta notation (Equation 1.1) will be used extensively to report mainly, but not exclusively, fractionation among the different Fe isotopes.

In the case of Fe, the standard δ-notation is used to report isotopic data in units of per mil (‰) using the $^{56}Fe/^{54}Fe$ ratio (Beard et al., 2003). Isotope values are usually reported as $\delta^{56}Fe$ relative to the reference standard IRMM-014:

$$\delta^{56}Fe\ (‰) = [\ (^{56}Fe/^{54}Fe)_{Sample}\ /\ (^{56}Fe/^{54}Fe)_{IRMM\text{-}014}\ \text{-}1] \times 10^3 \quad (1.8)$$

Alternatively, there are also works that report Fe isotopic data as $\delta^{57}Fe$ (*i.e.* utilizing the $^{57}Fe/^{54}Fe$ ratio instead of $^{56}Fe/^{54}Fe$; Poitrasson et al., 2004; Sossi et al., 2016; Williams et al., 2021). Given the low relative isotopic abundance of ^{58}Fe, it is still challenging to measure precisely $^{58}Fe/^{54}Fe$ ratios. Since most Fe isotope fractionation processes are mass-dependent, changes in $\delta^{56}Fe$ can be predicted to be ~2/3 times the change in $\delta^{57}Fe$ for the same process, thus yielding a linear array (*e.g.* plotting $\delta^{56}Fe$ vs. $\delta^{57}Fe$) known as a mass fractionation line (MFL). In order to explore processes that are likely not detectable by measuring only two isotope ratios, some studies rely on the "triple Fe isotope" technique along with high precision Fe isotopic measurements to go one step further: identifying subtle changes in predicted MFL. This relies on mass-dependence processes being not strictly linear, and classifying fractionation process in relation to small changes in slopes for their different MFL (Dauphas and Schauble, 2016; Nie et al., 2017a; Heard et al., 2020).

In regard of mass-independent processes, studies have identified isotopic anomalies of nucleosynthetic origins in iron meteorites (Hopp et al., 2022) as well as in pre-solar silicon carbide grains (Marhas et al., 2008; Trappitsch et al., 2018), and possibly in calcium-aluminum-rich inclusions (Völkening and Papanastassiou, 1989). Moreover, magnetite biomineralized by cultures of magnetotactic bacteria have also shown mass-independent Fe isotope fractionation (Amor et al., 2016; 2018), thus certainly providing motivation for future studies to possibly unravel mass-independent process in low-temperature environments.

In natural low-temperature systems, large mass-dependent Fe isotope fractionations are observed in relation to distinct oxidation and reduction (*i.e.* redox) reactions (Anbar and Rouxel, 2007; Johnson et al., 2008). This is in strong contrast with terrestrial and extraterrestrial high temperature samples, which yield δ^{56}Fe values of ~0‰ (Shahar and Young, 2020). For instance, the equilibrium fractionation between dissolved Fe^{2+} and Fe^{3+} as determined from theoretical and experimental studies is ~3‰ at 22°C (Welch et al., 2003; Anbar et al., 2005). Other studies have tried to determine the extent of Fe isotope fractionations related to distinct Fe oxidation and/or reduction processes, such as dissimilatory Fe(III) reduction (Johnson et al., 2005; Crosby et al., 2007), anaerobic photosynthesis (*e.g.* photoferrotrophy) oxidizing Fe(II) (Croal et al., 2004; Wu et al., 2017), abiotic Fe(II) oxidation and precipitation (Bullen et al., 2001; Balci et al., 2006), and sorption of aqueous Fe(II) onto ferric hydroxides (Icopini et al., 2004). These processes that yield fractionations > 1‰ have been shown to be transferred into modern marine and non-marine environments (Severmann et al., 2008; Busigny et al., 2014). If similar redox reactions occurred on ancient Earth, it is thought that similar Fe isotope fractionation processes would be recorded in the geological record.

Throughout the archives of ancient Earth, iron formations and shales are commonly used as evidence of past redox changes and also display significantly large Fe isotope fractionation. The (Fe) isotope compositions of Archean and Proterozoic marine sedimentary rocks have been a subject of major debates in the past decades, which are mainly due to distinct lines of interpretations of the isotopic record (*e.g.* Rouxel et al., 2005; Johnson et al., 2008). There are well-established trends in the global sedimentary iron isotope record (Fig. 1.4), which are most prevalent in the pyrite record but also observed in bulk-rock analyses. This is mainly due to the hypothesis that Fe isotope variations in sedimentary pyrite are sensitive to the concentrations of dissolved Fe(II) and can be used to place important constraints on the sources and sinks of the Fe(II) reservoirs (Rouxel et al., 2005).

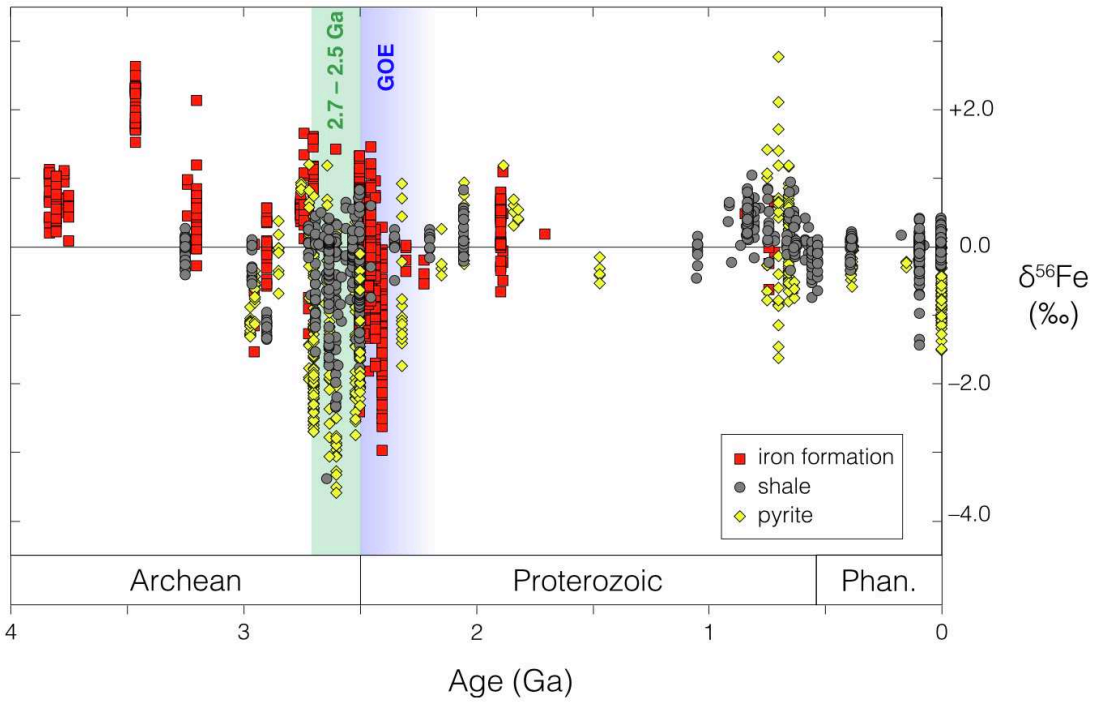

Figure 1. 4: Compilation of δ^{56}Fe values throughout the entire geological record measured on iron formations, shales, and pyrite (modified after Ostrander et al., 2021).

One of the most remarkable temporal trend in the sedimentary iron isotope record is the shift from variable and highly negative δ^{56}Fe values between ~2.7 and 2.5 Ga to near-crustal values. Clearly the iron cycle went through significant change during this time. However, the processes that caused such negative δ^{56}Fe values are still extensively debated (Rouxel et al., 2005; Yamaguchi et al., 2005; Johnson et al., 2008a). One model links the isotope variability to a shift in the marine redox conditions, in which partial oxidation (*i.e*. reducing conditions) created isotopically heavy ferric iron (Fe(III)) and left an isotopically-depleted dissolved ferrous iron (Fe(II)) reservoir to be captured and transferred to the sedimentary record (Rouxel et al., 2005; Planavsky et al., 2012; Busigny et al., 2014). In this case, the decline in iron isotope variability observed at ~2.4 Ga is linked to the oxygenation of the upper ocean as a consequence of the GOE. A second model suggests this iron isotope trend to reflect changes in the extent of microbial dissimilatory iron reduction (DIR), which facilitates the release of isotopically light ferrous iron (Yamaguchi et al., 2005; Johnson et al., 2008a; Severmann et al., 2008). Consequently, the rise of DIR, an iron respiration process operated by microorganisms, would have caused the Fe isotopic shift. In a third model, very negative Fe isotope values were also linked to a large kinetic isotope fractionation related to pyrite precipitation in the laboratory and in natural settings (Guilbaud et al., 2011; Rolison et al., 2018).

Recent studies have tried to tackle this issue by compiling δ^{34}S and δ^{56}Fe values measured in pyrites and iron formations. This has led to the notion that sulfur availability during pyritization likely drove trends in δ^{56}Fe fractionation before the GOE (Heard and Dauphas, 2020). Moreover, a new dataset from Western Australia (Mt. McRae Shales and Jeerinah Formation) and South Africa (Klein Naute Formation) spanning ~2.65 to 2.5 Ga also showed depleted ^{56}Fe in bulk shales and pyrites, which suggested a negative δ^{56}Fe composition for global seawater at the end of the Archean as a consequence of extensive

Fe oxidation in mostly reducing conditions (Ostrander et al., 2022). Future studies aiming to investigate ^{56}Fe depleted pyrites and to distinguish between local and global contexts, and finally identify early or late diagenetic effects, could look for (i) alternative samples (*i.e.* from other locations in the globe) spanning the same time period, (ii) perform extensive petrographic work to track the diagenetic histories of the samples, and (iii) compare mineral based measurements (*e.g.* in-situ, chemical extractions) with bulk data across multiple locations during key periods of Earth history. An example of such "re-examination" of the rock record, specifically samples from Mt McRae Shales (*i.e.* where very light $\delta^{56}Fe$ were measured on pyrites), has been made and previous interpretations concerning the increase of O_2 in the atmosphere have been questioned. The authors have suggested a post depositional effect as the main cause responsible for signals of more oxidative conditions (Slotznick et al., 2022). It is always a major challenge to identify primary and secondary features in the geological rock record, but the combination of in-situ techniques, petrographic work and bulk measurements might be the next step to further constrain the ancient Fe cycle.

1.4 References

Amor, M., Busigny, V., Louvat, P., Gélabert, A., Cartigny, P., Durand-Dubief, M., Ona-Nguema, G., Alphandéry, E., Chebbi, I., and Guyot, F., 2016, Mass-dependent and -independent signature of Fe isotopes in magnetotactic bacteria: Science, v. 352, p. 705–708, doi:10.1126/science.aad7632.

Amor, M. et al., 2018, Iron uptake and magnetite biomineralization in the magnetotactic bacterium Magnetospirillum magneticum strain AMB-1: An iron isotope study: Geochimica et Cosmochimica Acta, v. 232, p. 225–243, doi:10.1016/j.gca.2018.04.020

Anbar, A.D. et al., 2007, A whiff of oxygen before the great oxidation event? Science, v. 317, p. 1903–1906, doi:10.1126/science.1140325.

Anbar, A.D., and Holland, H.D., 1992, The photochemistry of manganese and the origin of banded iron formations: Geochimica et Cosmochimica Acta, v. 56, p. 2595–2603, doi:10.1016/0016-7037(92)90346-K.

Anbar, A.D., Jarzecki, A.A., and Spiro, T.G., 2005, Theoretical investigation of iron isotope fractionation between Fe(H2O)63+ and Fe(H2O) 62+: Implications for iron stable isotope geochemistry: Geochimica et Cosmochimica Acta, v. 69, p. 825–837, doi:10.1016/j.gca.2004.06.012.

Anbar, A.D., and Rouxel, O., 2007, Metal Stable Isotopes in Paleoceanography: Annual Review of Earth and Planetary Sciences, v. 35, p. 717–746, doi:10.1146/annurev.earth.34.031405.125029.

Balci, N., Bullen, T.D., Witte-Lien, K., Shanks, W.C., Motelica, M., and Mandernack, K.W., 2006, Iron isotope fractionation during microbially stimulated Fe(II) oxidation and Fe(III) precipitation: Geochimica et Cosmochimica Acta, v. 70, p. 622–639, doi:10.1016/j.gca.2005.09.025.

Banner, J.L., Hanson, G.N., and Meyers, W.J., 1988, Rare earth element and Nd isotopic variations in regionally extensive dolomites from the Burlington-Keokuk Formation (Mississippian): implications for REE mobility during carbonate diagenesis: Journal of Sedimentary Petrology, v. 58, p. 415–432, doi:10.1306/212F8DAA-2B24-11D7-8648000102C1865D.

Bau, M., 1996, Controls on the fractionation of isovalent trace elements in magmatic and aqueous systems: Evidence from Y/Ho, Zr/Hf, and lanthanide tetrad effect: Contributions to Mineralogy and Petrology, v. 123, p. 323–333, doi:10.1007/s004100050159.

Bau, M., 1993, Effects of syn- and post-depositional processes on the rare-earth element distribution in Precambrian iron-formations: European Journal of Mineralogy, v. 5, p. 257–268, doi:10.1127/ejm/5/2/0257.

Bau, M., 1991, Rare-earth element mobility during hydrothermal and metamorphic fluid-rock interaction and the significance of the oxidation state of europium: Chemical Geology, v. 93, p. 219–230, doi:10.1016/0009-2541(91)90115-8.

Bau, M., and Alexander, B.W., 2009, Distribution of high field strength elements (Y, Zr, REE, Hf, Ta, Th, U) in adjacent magnetite and chert bands and in reference standards FeR-3 and FeR-4 from the Temagami iron-formation, Canada, and the redox level of the Neoarchean ocean: Precambrian Research, v. 174, p. 337–346, doi:10.1016/j.precamres.2009.08.007.

Bau, M., and Dulski, P., 1996, Distribution of yttrium and rare-earth elements in the Penge and Kuruman iron-formations, Transvaal Supergroup, South Africa: Precambrian Research, v. 79, p. 37–55.

Bau, M., and Koschinsky, A., 2009, Oxidative scavenging of cerium on hydrous Fe oxide: Evidence from the distribution of rare earth elements and yttrium between Fe oxides and Mn oxides in hydrogenetic ferromanganese crusts: Geochemical Journal, v. 43, p. 37–47, doi:10.2343/geochemj.1.0005.

Beard, B.L., Johnson, C.M., Skulan, J.L., Nealson, K.H., Cox, L., and Sun, H., 2003, Application of Fe isotopes to tracing the geochemical and biological cycling of Fe: Chemical Geology, v. 195, p. 87–117, doi:10.1016/S0009-2541(02)00390-X.

Bekker, A., Slack, J.F., Planavsky, N., Krapez, B., Hofmann, A., Konhauser, K.O., and Rouxel, O.J., 2010, Iron Formation: The Sedimentary Product of a Complex Interplay among Mantle, Tectonic, Oceanic, and Biospheric Processes: Economic Geology, v. 105, p. 467–508, doi:10.2113/gsecongeo.105.3.467.

Bellefroid, E.J., Hood, A.V.S., Hoffman, P.F., Thomas, M.D., Reinhard, C.T., and Planavsky, N.J., 2018, Constraints on paleoproterozoic atmospheric oxygen levels: Proceedings of the National Academy of Sciences of the United States of America, v. 115, p. 8104–8109, doi:10.1073/pnas.1806216115.

Berglund, M., and Wieser, M.E., 2011, Isotopic compositions of the elements 2009 (IUPAC technical report): Pure and Applied Chemistry, v. 83, p. 397–410, doi:10.1351/PAC-REP-10-06-02.

Bhattacharya, H.N., Chakraborty, I., and Ghosh, K.K., 2007, Geochemistry of some banded iron-formations of the archean supracrustals, Jharkhand-Orissa region, India: Journal of Earth System Science, v. 116, p. 245–259, doi:10.1007/s12040-007-0024-4.

Bjerrum, C.J., and Canfield, D.E., 2002, Ocean productivity before about 1.9 Gyr ago limited by phosphorus adsorption onto iron oxides: Nature, v. 417, p. 159–162, doi:10.1038/417159a.

Bolhar, R., Kamber, B.S., Moorbath, S., Fedo, C.M., and Whitehouse, M.J., 2004, Characterisation of early Archaean chemical sediments by trace element signatures: Earth and Planetary Science Letters, v. 222, p. 43–60, doi:10.1016/j.epsl.2004.02.016.

Bonnand, P., Israel, C., Boyet, M., Doucelance, R., and Auclair, D., 2019, Radiogenic and stable Ce isotope measurements by thermal ionisation mass spectrometry: Journal of Analytical Atomic Spectrometry, v. 34, p. 504–516, doi:10.1039/c8ja00362a.

Bonnand, P., Lalonde, S.V., Boyet, M., Heubeck, C., Homann, M., Nonnotte, P., Foster, I., Konhauser, K.O., and Köhler, I., 2020, Post-depositional REE mobility in a Paleoarchean banded iron formation revealed by La-Ce geochronology: A cautionary tale for signals of ancient oxygenation: Earth and Planetary Science Letters, v. 547, p. 116452, doi:10.1016/j.epsl.2020.116452.

Bullen, T.D., White, A.F., Childs, C.W., Vivit, D. V., and Schultz, M.S., 2001, Demonstration of significant abiotic iron isotope fractionation in nature: Geology, v. 29, p. 699–702, doi:10.1130/0091-7613(2001)029<0699:DOSAII>2.0.CO;2.

Busigny, V., Planavsky, N.J., Goldbaum, E., Lechte, M.A., Feng, L., and Lyons, T.W., 2018, Origin of the Neoproterozoic Fulu iron formation, South China: Insights from iron isotopes and rare earth element patterns: Geochimica et Cosmochimica Acta, v. 242, p. 123–142, doi:10.1016/j.gca.2018.09.006.

Busigny, V., Planavsky, N.J., Jézéquel, D., Crowe, S., Louvat, P., Moureau, J., Viollier, E., and Lyons, T.W., 2014, Iron isotopes in an Archean ocean analogue: Geochimica et Cosmochimica Acta, v. 133, p. 443–462, doi:10.1016/j.gca.2014.03.004.

Cairns-Smith, A.G., 1978, Precambrian solution photochemistry, inverse segregation, and banded Iron Formations: Nature, v. 276, p. 807–808, doi:10.1038/276807a0.

Canfield, D.E., Zhang, S., Wang, H., Wang, X., Zhao, W., Su, J., Bjerrum, C.J., Haxen, E.R., and Hammarlund, E.U., 2018, A Mesoproterozoic iron formation: Proceedings of the National Academy of Sciences of the United States of America, v. 115, p. E3895–E3904, doi:10.1073/pnas.1720529115.

Cloud, P., 1973, Paleoecological Significance of the Banded Iron Formation: Economic Geology, v. 68, p. 1135–1143.

Croal, L.R., Johnson, C.M., Beard, B.L., and Newman, D.K., 2004, Iron isotope fractionation by Fe(II)-oxidizing photoautotrophic bacteria: Geochimica et Cosmochimica Acta, v. 68, p. 1227–1242, doi:10.1016/j.gca.2003.09.011.

Crosby, H.A., Roden, E.E., Johnson, C.M., and Beard, B.L., 2007, The mechanisms of iron isotope fractionation produced during dissimilatory Fe(III) reduction by Shewanella putrefaciens and Geobacter sulfurreducens: Geobiology, v. 5, p. 169–189, doi:10.1111/j.1472-4669.2007.00103.x.

Danielson, A., Möller, P., and Dulski, P., 1992, The europium anomalies in banded iron formations and the thermal history of the oceanic crust: Chemical Geology, v. 97, p. 89–100.

Dauphas, N., Van Zuilen, M., Wadhwa, M., Davis, A.M., Marty, B., and Janney, P.E., 2004, Clues from Fe isotope variations on the origin of early Archean BIFs from Greenland: Science, v. 306, p. 2077–2080, doi:10.1126/science.1104639

Dauphas, N., and Schauble, E.A., 2016, Mass Fractionation Laws, Mass-Independent Effects, and Isotopic Anomalies: Annual Review of Earth and Planetary Sciences, v. 44, p. 709–783, doi:10.1146/annurev-earth-060115-012157.

Derry, L.A., and Jacobsen, S.B., 1990, The chemical evolution of Precambrian seawater: Evidence from REEs in banded iron formations: Geochimica et Cosmochimica Acta, v. 54, p. 2965–2977, doi:10.1016/0016-7037(91)90174-4.

Dodd, M.S. et al., 2022, Abiotic anoxic iron oxidation, formation of Archean banded iron formations, and the oxidation of early Earth: Earth and Planetary Science Letters, v. 584, p. 117469, doi:10.1016/j.epsl.2022.117469.

Eickmann, B., Hofmann, A., Wille, M., Bui, T.H., Wing, B.A., and Schoenberg, R., 2018, Isotopic evidence for oxygenated Mesoarchaean shallow oceans: Nature Geoscience, v. 11, p. 133–138, doi:10.1038/s41561-017-0036-x.

Elderfield, H., and Sholkovitz, E.R., 1987, Rare earth elements in the pore waters of reducing nearshore sediments: Earth and Planetary Science Letters, v. 82, p. 280–288, doi:10.1016/0012-821X(87)90202-0.

Elderfield, H., Whitfield, M., Burton, J.D., Bacon, M.P., and Liss, P.S., 1988, The oceanic chemistry of the rare-earth elements: Philosophical Transactions of the Royal Society of London, v. 325, p. 105–126, doi:10.1098/rsta.1988.0046.

Fabre, S., Nédélec, A., Poitrasson, F., Strauss, H., Thomazo, C., and Nogueira, A., 2011,

Iron and sulphur isotopes from the Carajás mining province (Pará , Brazil): Implications for the oxidation of the ocean and the atmosphere across the Archaean – Proterozoic transition: Chemical Geology, v. 289, p. 124–139, doi:10.1016/j.chemgeo.2011.07.019.

Frei, R., Dahl, P.S., Duke, E.F., Frei, K.M., Hansen, T.R., Frandsson, M.M., and Jensen, L.A., 2008, Trace element and isotopic characterization of Neoarchean and Paleoproterozoic iron formations in the Black Hills (South Dakota, USA): Assessment of chemical change during 2.9-1.9 Ga deposition bracketing the 2.4-2.2 Ga first rise of atmospheric oxygen: Precambrian Research, v. 162, p. 441–474, doi:10.1016/j.precamres.2007.10.005.

Frei, R., and Polat, A., 2007, Source heterogeneity for the major components of ~ 3.7 Ga Banded Iron Formations (Isua Greenstone Belt, Western Greenland): Tracing the nature of interacting water masses in BIF formation: Earth and Planetary Science Letters, v. 253, p. 266–281, doi:10.1016/j.epsl.2006.10.033.

Frost, D.J., Liebske, C., Langenhorst, F., McCammon, C.A., Trønnes, R.G., and Rubie, D.C., 2004, Experimental evidence for the existence of iron-rich metal in the Earth's lower mantle: Nature, v. 428, p. 409–412, doi:10.1038/nature02413.

Garcia, T.I., Gorton, M.P., Li, H., Wortmann, U.G., and Spooner, E.T.C., 2016, The geochemistry of the 2.75 Ga-old Helen Iron Formation, Wawa, Ontario - Insights into iron formation deposition from carbon isotopes and rare earth elements: Precambrian Research, v. 275, p. 357–368, doi:10.1016/j.precamres.2016.01.013.

Garrels, R.M., Perry, E.A., and Mackenzie, F.T., 1973, Genesis of Precambrian iron-formations and development of atmospheric oxygen: Economic Geology, v. 68, p. 1173–1179.

German, C.R., and Elderfield, H., 1990, Application of the Ce anomaly as a paleoredox indicator: The ground rules: Paleoceanography, v. 5, p. 823–833, doi:10.1029/PA005i005p00823.

Guilbaud, R., Butler, I.B., Ellam, R.M., Rickard, D., and Oldroyd, A., 2011, Experimental determination of the equilibrium Fe isotope fractionation between Feaq2+ and FeSm (mackinawite) at 25 and 2°C: Geochimica et Cosmochimica Acta, v. 75, p. 2721–2734, doi:10.1016/j.gca.2011.02.023.

Halevy, I., Alesker, M., Schuster, E.M., Popovitz-Biro, R., and Feldman, Y., 2017, A key role for green rust in the Precambrian oceans and the genesis of iron formations: Nature Geoscience, v. 10, p. 135–139, doi:10.1038/ngeo2878.

Halverson, G.P., Poitrasson, F., Hoffman, P.F., Nédélec, A., Montel, J.M., and Kirby, J., 2011, Fe isotope and trace element geochemistry of the Neoproterozoic syn-glacial Rapitan iron formation: Earth and Planetary Science Letters, v. 309, p. 100–112, doi:10.1016/j.epsl.2011.06.021.

Han, X., Tomaszewski, E.J., Schoenberg, R., Konhauser, K.O., Amor, M., Pan, Y., Warter, V., Kappler, A., and Byrne, J.M., 2021, Using Zn and Ni behavior during magnetite precipitation in banded iron formations to determine its biological or abiotic origin: Earth and Planetary Science Letters, v. 568, p. 117052, doi:10.1016/j.epsl.2021.117052.

Haugaard, R., Frei, R., Stendald, H., and Konhauser, K., 2013, Petrology and geochemistry of the ~2.9 Ga Itilliarsuk banded iron formation and associated supracrustal rocks, West Greenland: Source characteristics and depositional environment: Precambrian Research, v. 229, p. 150–176, doi:10.1016/j.precamres.2012.04.013.

Haugaard, R., Ootes, L., Creaser, R.A., and Konhauser, K.O., 2016, The nature of Mesoarchaean seawater and continental weathering in 2.85 Ga banded iron

formation, Slave craton, NW Canada: Geochimica et Cosmochimica Acta, v. 194, p. 34–56, doi:10.1016/j.gca.2016.08.020.

Haugaard, R., Ootes, L., and Konhauser, K., 2017, Neoarchaean banded iron formation within a ~2620 Ma turbidite-dominated deep-water basin, Slave craton, NW Canada: Precambrian Research, v. 292, p. 130–151, doi:10.1016/j.precamres.2017.01.025.

Heard, A.W., and Dauphas, N., 2020, Constraints on the coevolution of oxic and sulfidic ocean iron sinks from archean-paleoproterozoic iron isotope records: Geology, v. 48, p. 358–362, doi:10.1130/G46951.1.

Heard, A.W., Dauphas, N., Guilbaud, R., Rouxel, O.J., Butler, I.B., Nie, N.X., and Bekker, A., 2020, Triple iron isotope constraints on the role of ocean iron sinks in early atmospheric oxygenation: Science, v. 370, p. 446–449, https://www.sciencemag.org/lookup/doi/10.1126/science.aaz8821.

Hoefs, J., 2009, Stable isotope geochemistry: v. 6, 1–285 p

Hofmann, A., 2005, The geochemistry of sedimentary rocks from the Fig Tree Group, Barberton greenstone belt: Implications for tectonic, hydrothermal and surface processes during mid-Archaean times: Precambrian Research, v. 143, p. 23–49, doi:10.1016/j.precamres.2005.09.005.

Holland, H.D., Lazar, B., and McCaffrey, M., 1986, Evolution of the atmosphere and oceans: Nature, v. 320, p. 27–33, doi:10.1038/320027a0.

Hopp, T., Dauphas, N., Spitzer, F., Burkhardt, C., and Kleine, T., 2022, Earth's accretion inferred from iron isotopic anomalies of supernova nuclear statistical equilibrium origin: Earth and Planetary Science Letters, v. 577, p. 117245, doi:10.1016/j.epsl.2021.117245.

Ibañez-Mejia, M., and Tissot, F.L.H., 2021, Reading the Isotopic Code of Heavy Elements:

Elements, v. 17, p. 379–382, doi:10.2138/gselements.17.6.379

Icopini, G.A., Anbar, A.D., Ruebush, S.S., Tien, M., and Brantley, S.L., 2004, Iron isotope fractionation during microbial reduction of iron: The importance of adsorption: Geology, v. 32, p. 205–208, doi:10.1130/G20184.1.

Isley, A.E., 1995, Hydrothermal plumes and the delivery of iron to banded iron formation: Journal of Geology, v. 103, p. 169–185, doi:10.1086/629734.

James, H.L., 1954, Sedimentary facies of iron-formation: Economic Geology, v. 49, p. 235–293.

Johnson, C.M., and Beard, B.L., 2006, Fe isotopes: An emerging technique for understanding modern and ancient biogeochemical cycles: GSA Today, v. 16, p. 4–10, doi:10.1130/GSAT01611A.1.

Johnson, C.M., Beard, B.L., Klein, C., Beukes, N.J., and Roden, E.E., 2008, Iron isotopes constrain biologic and abiologic processes in banded iron formation genesis: Geochimica et Cosmochimica Acta, v. 72, p. 151–169, doi:10.1016/j.gca.2007.10.013.

Johnson, A.C., Ostrander, C.M., Romaniello, S.J., Reinhard, C.T., Greaney, A.T., Lyons, T.W., and Anbar, A.D., 2021, Reconciling evidence of oxidative weathering and atmospheric anoxia on Archean Earth: , p. 1–10.

Johnson, C.M., Roden, E.E., Welch, S.A., and Beard, B.L., 2005, Experimental constraints on Fe isotope fractionation during magnetite and Fe carbonate formation coupled to dissimilatory hydrous ferric oxide reduction: Geochimica et Cosmochimica Acta, v. 69, p. 963–993, doi:10.1016/j.gca.2004.06.043.

Kappler, A., Bryce, C., Mansor, M., Lueder, U., Byrne, J.M., and Swanner, E.D., 2021, An evolving view on biogeochemical cycling of iron: Nature Reviews Microbiology, doi:10.1038/s41579-020-00502-7.

Klein, C., 2005, Some Precambrian banded iron-formations (BIFs) from around the world:

Their age, geologic setting, mineralogy, metamorphism, geochemistry, and origin: American Mineralogist, v. 90, p. 1473–1499, doi:10.2138/am.2005.1871.

Köhler, I., Konhauser, K.O., Papineau, D., Bekker, A., and Kappler, A., 2013, Biological carbon precursor to diagenetic siderite with spherical structures in iron formations: Nature Communications, v. 4, p. 1–7, doi:10.1038/ncomms2770.

Konhauser, K.O., Hamade, T., Raiswell, R., Morris, R.C., Ferris, F.G., Southam, G., and Canfield, D.E., 2002, Could bacteria have formed the Precambrian banded iron formations? Geology, v. 30, p. 1079–1082, doi:10.1130/0091-7613(2002)030<1079:CBHFTP>2.0.CO;2.

Lantink, M.L., Oonk, P.B.H., Floor, G.H., Tsikos, H., and Mason, P.R.D., 2018, Fe isotopes of a 2.4 Ga hematite-rich IF constrain marine redox conditions around the GOE: Precambrian Research, v. 305, p. 218–235, doi:10.1016/j.precamres.2017.12.025.

Lawrence, M.G., and Kamber, B.S., 2006, The behaviour of the rare earth elements during estuarine mixing-revisited: Marine Chemistry, v. 100, p. 147–161, doi:10.1016/j.marchem.2005.11.007.

Lechte, M.A., Wallace, M.W., van Smeerdijk Hood, A., Li, W., Jiang, G., Halverson, G.P., Asael, D., McColl, S.L., and Planavsky, N.J., 2019, Subglacial meltwater supported aerobic marine habitats during Snowball Earth: Proceedings of the National Academy of Sciences of the United States of America, v. 116, p. 25478–25483, doi:10.1073/pnas.1909165116.

Lenton, T.M., Daines, S.J., and Mills, B.J.W., 2018, COPSE reloaded: An improved model of biogeochemical cycling over Phanerozoic time: Earth-Science Reviews, v. 178, p. 1–28, doi:10.1016/j.earscirev.2017.12.004.

Li, Z.Q., Zhang, L.C., Xue, C.J., Zheng, M.T., Zhu, M.T., Robbins, L.J., Slack, J.F.,

Planavsky, N.J., and Konhauser, K.O., 2018, Earth's youngest banded iron formation implies ferruginous conditions in the Early Cambrian ocean: Scientific Reports, v. 8, p. 1–10, doi:10.1038/s41598-018-28187-2.

Lottermoser, B.G., and Ashley, P.M., 2000, Geochemistry, petrology and origin of Neoproterozoic ironstones in the eastern part of the Adelaide Geosyncline, South Australia: Precambrian Research, v. 101, p. 49–67, doi:10.1016/S0301-9268(99)00098-4.

Lyons, T.W., Reinhard, C.T., and Planavsky, N.J., 2014, The rise of oxygen in Earth ' s early ocean and atmosphere: Nature, v. 506, p. 307–315, doi:10.1038/nature13068.

Marhas, K.K., Amari, S., Gyngard, F., Zinner, E., and Gallino, R., 2008, Iron and Nickel Isotopic Ratios in Presolar SiC Grains: The Astrophysical Journal, v. 689, p. 622–645, doi:10.1086/592599.

Meija, J. et al., 2016, Isotopic compositions of the elements 2013 (IUPAC Technical Report): Pure and Applied Chemistry, v. 88, p. 293–306, doi:10.1515/pac-2015-0503.

Mloszewska, A.M., Pecoits, E., Cates, N.L., Mojzsis, S.J., O'Neil, J., Robbins, L.J., and Konhauser, K.O., 2012, The composition of Earth's oldest iron formations: The Nuvvuagittuq Supracrustal Belt (Québec, Canada): Earth and Planetary Science Letters, v. 317–318, p. 331–342, doi:10.1016/j.epsl.2011.11.020.

Moffett, J.W., 1994, The relationship between cerium and manganese oxidation in the marine environment: Limnology and Oceanography, v. 39, p. 1309–1318, doi:10.4319/lo.1994.39.6.1309.

Nakada, R., Takahashi, Y., and Tanimizu, M., 2016, Cerium stable isotope ratios in ferromanganese deposits and their potential as a paleo-redox proxy: Geochimica et Cosmochimica Acta, v. 181, p. 89–100, doi:10.1016/j.gca.2016.02.025.

Nakada, R., Takahashi, Y., and Tanimizu, M., 2013, Isotopic and speciation study on

cerium during its solid-water distribution with implication for Ce stable isotope as a paleo-redox proxy: Geochimica et Cosmochimica Acta, v. 103, p. 49–62, doi:10.1016/j.gca.2012.10.045.

Nie, N.X., Dauphas, N., and Greenwood, R.C., 2017, Iron and oxygen isotope fractionation during iron UV photo-oxidation: Implications for early Earth and Mars: Earth and Planetary Science Letters, v. 458, p. 179–191, doi:10.1016/j.epsl.2016.10.035.

Och, L.M., and Shields-Zhou, G.A., 2012, The Neoproterozoic oxygenation event: Environmental perturbations and biogeochemical cycling: Earth-Science Reviews, v. 110, p. 26–57, doi:10.1016/j.earscirev.2011.09.004.

Oonk, P.B.H., Mason, P.R.D., Tsikos, H., and Bau, M., 2018, Fraction-specific rare earth elements enable the reconstruction of primary seawater signatures from iron formations: Geochimica et Cosmochimica Acta, v. 238, p. 102–122, doi:10.1016/j.gca.2018.07.005.

Oonk, P.B.H., Tsikos, H., Mason, P.R.D., Henkel, S., Staubwasser, M., Fryer, L., Poulton, S.W., and Williams, H.M., 2017, Fraction-specific controls on the trace element distribution in iron formations: Implications for trace metal stable isotope proxies: Chemical Geology, v. 474, p. 17–32, doi:10.1016/j.chemgeo.2017.10.018.

Ostrander, C.M., Severmann, S., Gordon, G.W., Kendall, B., Lyons, T.W., Zheng, W., Roy, M., and Anbar, A.D., 2022, Significance of 56Fe depletions in late-Archean shales and pyrite: Geochimica et Cosmochimica Acta, v. 316, p. 87–104, doi:10.1016/j.gca.2021.10.013.

Ozaki, K., Reinhard, C.T., and Tajika, E., 2019, A sluggish mid-Proterozoic biosphere and its effect on Earth's redox balance: Geobiology, v. 17, p. 3–11, doi:10.1111/gbi.12317.

Philippot, P. et al., 2018, Globally asynchronous sulphur isotope signals require re-

definition of the Great Oxidation Event: Nature Communications, v. 9, doi:10.1038/s41467-018-04621-x.

Planavsky, N., Bekker, A., Rouxel, O.J., Kamber, B., Hofmann, A., Knudsen, A., and Lyons, T.W., 2010, Rare Earth Element and yttrium compositions of Archean and Paleoproterozoic Fe formations revisited: New perspectives on the significance and mechanisms of deposition: Geochimica et Cosmochimica Acta, v. 74, p. 6387–6405, doi:10.1016/j.gca.2010.07.021.

Planavsky, N., Rouxel, O.J., Bekker, A., Hofmann, A., Little, C.T.S., and Lyons, T.W., 2012, Iron isotope composition of some Archean and Proterozoic iron formations: Geochimica et Cosmochimica Acta, v. 80, p. 158–169, doi:10.1016/j.gca.2011.12.001.

Poitrasson, F., Halliday, A.N., Lee, D.C., Levasseur, S., and Teutsch, N., 2004, Iron isotope differences between Earth, Moon, Mars and Vesta as possible records of contrasted accretion mechanisms: Earth and Planetary Science Letters, v. 223, p. 253–266, doi:10.1016/j.epsl.2004.04.032.

Posth, N.R., Hegler, F., Konhauser, K.O., and Kappler, A., 2008, Alternating Si and Fe deposition caused by temperature fluctuations in Precambrian oceans: Nature Geoscience, v. 1, p. 703–708, doi:10.1038/ngeo306.

Pourmand, A., Dauphas, N., and Ireland, T.J., 2012, A novel extraction chromatography and MC-ICP-MS technique for rapid analysis of REE, Sc and Y: Revising CI-chondrite and Post-Archean Australian Shale (PAAS) abundances: Chemical Geology, v. 291, p. 38–54, doi:10.1016/j.chemgeo.2011.08.011.

Pourret, O., Davranche, M., Gruau, G., and Dia, A., 2008, New insights into cerium anomalies in organic-rich alkaline waters: Chemical Geology, v. 251, p. 120–127, doi:10.1016/j.chemgeo.2008.03.002.

Rasmussen, B., Krapež, B., and Meier, D.B., 2014, Replacement origin for hematite in 2.5

Ga banded iron formation: Evidence for postdepositional oxidation of iron-bearing minerals: Bulletin of the Geological Society of America, v. 126, p. 438–446, doi:10.1130/B30944.1.

Rasmussen, B., Muhling, J.R., and Krapež, B., 2021, Greenalite and its role in the genesis of early Precambrian iron formations – A review: Earth-Science Reviews, v. 217, doi:10.1016/j.earscirev.2021.103613.

Reinhard, C.T., and Planavsky, N.J., 2021, The History of Ocean Oxygenation: Annual Review of Marine Science, v. 14, p. 331–353, doi:10.1146/annurev-marine-031721-104005.

Reinhard, C.T., Planavsky, N.J., Ward, B.A., Love, G.D., Le Hir, G., and Ridgwell, A., 2020, The impact of marine nutrient abundance on early eukaryotic ecosystems: Geobiology, v. 18, p. 139–151, doi:10.1111/gbi.12384.

Riding, R., Fralick, P., and Liang, L., 2014, Identification of an Archean marine oxygen oasis: Precambrian Research, v. 251, p. 232–237, doi:10.1016/j.precamres.2014.06.017.

Robbins, L.J. et al., 2019, Hydrogeological constraints on the formation of Palaeoproterozoic banded iron formations: Nature Geoscience, v. 12, p. 558–563, doi:10.1038/s41561-019-0372-0.

Rolison, J.M., Stirling, C.H., Middag, R., Gault-Ringold, M., George, E., and Rijkenberg, M.J.A., 2018, Iron isotope fractionation during pyrite formation in a sulfidic Precambrian ocean analogue: Earth and Planetary Science Letters, v. 488, p. 1–13, doi:10.1016/j.epsl.2018.02.006.

Rouxel, O.J., Bekker, A., and Edwards, K.J., 2005, Iron Isotope Constraints on the Archean and Paleoproterozoic Ocean Redox State: Science, v. 307, p. 1088–1091, doi:10.1126/science.1105692.

Rouxel, O., Toner, B., Germain, Y., and Glazer, B., 2018, Geochemical and iron isotopic

insights into hydrothermal iron oxyhydroxide deposit formation at Loihi Seamount: Geochimica et Cosmochimica Acta, v. 220, p. 449–482, doi:10.1016/j.gca.2017.09.050.

dos Santos, F.H., da Silva Amaral, W., Chi-Fru, E., de Souza, A.C.B., and Bosco-Santos, A., 2022, Paleoproterozoic manganese oxide precipitation in oxic seawater surface and reductive enrichment in anoxic seafloor: Chemical Geology, v. 588, p. 120655, doi:10.1016/j.chemgeo.2021.120655.

Schad, M., Halama, M., Bishop, B., Konhauser, K.O., and Kappler, A., 2019, Temperature fluctuations in the Archean ocean as trigger for varve-like deposition of iron and silica minerals in banded iron formations: Geochimica et Cosmochimica Acta, v. 265, p. 386–412, doi:10.1016/j.gca.2019.08.031.

Severmann, S., Lyons, T.W., Anbar, A., McManus, J., and Gordon, G., 2008, Modern iron isotope perspective on the benthic iron shuttle and the redox evolution of ancient oceans: Geology, v. 36, p. 487, doi:10.1130/G24670A.1.

Shahar, A., and Young, E.D., 2020, An assessment of iron isotope fractionation during core formation: Chemical Geology, v. 554, p. 119800, doi:10.1016/j.chemgeo.2020.119800.

Slotznick, S.P., Johnson, J.E., Rasmussen, B., Raub, T.D., Webb, S.M., Zi, J.W., Kirschvink, J.L., and Fischer, W.W., 2022, Reexamination of 2.5-Ga "whiff" of oxygen interval points to anoxic ocean before GOE: Science Advances, v. 8, doi:10.1126/sciadv.abj7190.

Sossi, P.A., Nebel, O., and Foden, J., 2016, Iron isotope systematics in planetary reservoirs: Earth and Planetary Science Letters, v. 452, p. 295–308, doi:10.1016/j.epsl.2016.07.032.

Stolper, D.A., and Keller, C.B., 2018, A record of deep-ocean dissolved O2 from the oxidation state of iron in submarine basalts: Nature, v. 553, p. 323–327,

doi:10.1038/nature25009.

Tagliabue, A., Bowie, A.R., Boyd, P.W., Buck, K.N., Johnson, K.S., and Saito, M.A., 2017, The integral role of iron in ocean biogeochemistry: Nature, v. 543, p. 51–59, doi:10.1038/nature21058.

Teixeira, N.L., Caxito, F.A., Rosière, C.A., Pecoits, E., Vieira, L., Frei, R., Sial, A.N., and Poitrasson, F., 2017, Trace elements and isotope geochemistry (C, O, Fe, Cr) of the Cauê iron formation, Quadrilátero Ferrífero, Brazil: Evidence for widespread microbial dissimilatory iron reduction at the Archean/Paleoproterozoic transition: Precambrian Research, v. 298, p. 39–55, doi:10.1016/j.precamres.2017.05.009.

Thompson, K.J. et al., 2019, Photoferrotrophy, deposition of banded iron formations, and methane production in Archean oceans: Science Advances, v. 5, p. 1–10, doi:10.1126/sciadv.aav2869.

Tosca, N.J., Guggenheim, S., and Pufahl, P.K., 2016, An authigenic origin for Precambrian greenalite: Implications for iron formation and the chemistry of ancient seawater: Bulletin of the Geological Society of America, v. 128, p. 511–530, doi:10.1130/B31339.1.

Tostevin, R., Shields, G.A., Tarbuck, G.M., He, T., Clarkson, M.O., and Wood, R.A., 2016, Effective use of cerium anomalies as a redox proxy in carbonate-dominated marine settings: Chemical Geology, v. 438, p. 146–162, doi:10.1016/j.chemgeo.2016.06.027.

Trappitsch, R. et al., 2018, Simultaneous iron and nickel isotopic analyses of presolar silicon carbide grains: Geochimica et Cosmochimica Acta, v. 221, p. 87–108, doi:10.1016/j.gca.2017.05.031.

Trendall, A.F., and Blockley, J.G., 1970, The iron formations of the Precambrian Hamersley Group Western Australia: Geological Survey of Western Australia Bulletin, v. 119, p. 391.

Viehmann, S., Bau, M., Bühn, B., Dantas, E.L., Andrade, F.R.D., and Walde, D.H.G., 2016, Geochemical characterisation of Neoproterozoic marine habitats: Evidence from trace elements and Nd isotopes in the Urucum iron and manganese formations, Brazil: Precambrian Research, v. 282, p. 74–96, doi:10.1016/j.precamres.2016.07.006.

Viehmann, S., Bau, M., Hoffmann, J.E., and Münker, C., 2015a, Geochemistry of the Krivoy Rog Banded Iron Formation, Ukraine, and the impact of peak episodes of increased global magmatic activity on the trace element composition of Precambrian seawater: Precambrian Research, v. 270, p. 165–180, doi:10.1016/j.precamres.2015.09.015.

Viehmann, S., Bau, M., Smith, A.J.B., Beukes, N.J., Dantas, E.L., and Bühn, B., 2015b, The reliability of ~2.9 Ga old Witwatersrand banded iron formations (South Africa) as archives for Mesoarchean seawater: Evidence from REE and Nd isotope systematics: Journal of African Earth Sciences, v. 111, p. 322–334, doi:10.1016/j.jafrearsci.2015.08.013.

Völkening, J., and Papanastassiou, D.A., 1989, Iron isotope anomalies: The Astrophysical Journal, v. 347, p. 43–46.

Wallace, M.W., Hood, A., Shuster, A., Greig, A., Planavsky, N.J., and Reed, C.P., 2017, Oxygenation history of the Neoproterozoic to early Phanerozoic and the rise of land plants: Earth and Planetary Science Letters, v. 466, p. 12–19, doi:10.1016/j.epsl.2017.02.046.

Warchola, T., Lalonde, S. V., Pecoits, E., von Gunten, K., Robbins, L.J., Alessi, D.S., Philippot, P., and Konhauser, K.O., 2018, Petrology and geochemistry of the Boolgeeda Iron Formation, Hamersley Basin, Western Australia: Precambrian Research, v. 316, p. 155–173, doi:10.1016/j.precamres.2018.07.015.

Welch, S.A., Beard, B.L., Johnson, C.M., and Braterman, P.S., 2003, Kinetic and equilibrium Fe isotope fractionation between aqueous Fe(II) and Fe(III): Geochimica et Cosmochimica Acta, v. 67, p. 4231–4250, doi:10.1016/S0016-7037(03)00266-7.

Williams, H.M., Matthews, S., Rizo, H., and Shorttle, O., 2021, Iron isotopes trace primordial magma ocean cumulates melting in Earth's upper mantle: Science Advances, v. 7, doi:10.1126/SCIADV.ABC7394.

Wu, W., Swanner, E.D., Kleinhanns, I.C., Schoenberg, R., Pan, Y., and Kappler, A., 2017, Fe isotope fractionation during Fe(II) oxidation by the marine photoferrotroph Rhodovulum iodosum in the presence of Si – Implications for Precambrian iron formation deposition: Geochimica et Cosmochimica Acta, v. 211, p. 307–321, doi:10.1016/j.gca.2017.05.033.

Yamaguchi, K.E., Johnson, C.M., Beard, B.L., and Ohmoto, H., 2005, Biogeochemical cycling of iron in the Archean–Paleoproterozoic Earth: Constraints from iron isotope variations in sedimentary rocks from the Kaapvaal and Pilbara Cratons: Chemical Geology, v. 218, p. 135–169, doi:10.1016/j.chemgeo.2005.01.020.

Yang, X., Mao, J., Santosh, M., Li, R., Wu, C., Gao, J., Zhang, X., and Wang, Z., 2022, Ediacaran iron formations from the North Qilian Orogenic Belt, China: Age, geochemistry, Sm–Nd isotopes and link with submarine volcanism: Precambrian Research, v. 368, p. 106498, doi:10.1016/j.precamres.2021.106498.

Yang, X., Zhang, Z., Santosh, M., Duan, S., and Liang, T., 2018, Anoxic to suboxic Mesoproterozoic ocean: Evidence from iron isotope and geochemistry of siderite in the Banded Iron Formations from North Qilian, NW China: Precambrian Research, v. 307, p. 115–124, doi:10.1016/j.precamres.2018.01.007.

CHAPTER 2

2. Geological context of the Carajás Basin, Pará, Brazil

2.1 Regional context

The Amazonian Craton (AC) (Fig. 2.1A) occupies the northern part of the present day South American continent and it is one of the largest cratons on Earth (Almeida et al., 2000; Cordani and Teixeira, 2007). The AC is subdivided into the Guyana Shield to the north and the Central Brazilian Shield to the south (Fig. 2.1B). It comprises several tectonic provinces defined by coherent structural and geochronological patterns, which correspond to different blocks that accreted together during the Proterozoic (Tassinari and Macambira, 1999; Santos et al., 2000; Cordani and Teixeira, 2007; Cordani et al., 2009). The tectonic provinces that form the AC are mostly composed of Proterozoic continental crust (Santos et al., 2000; Cordani and Teixeira, 2007; Cordani et al., 2009), but locally preserve remnants of Paleoarchean and Eoarchean crust (Milhomem Neto and Lafon, 2019). Recent paleomagnetic work suggests that towards the end of the Archean Eon, the AC was likely located in a low latitude, close to the paleoequator (Martins et al., 2021).

The Carajás Mineral Province (CMP) is located in the southeastern portion of the Amazonia Craton. It consists of a remarkable metallogenic diversity including world-class deposits of iron oxide-copper-gold (IOCG), large IFs, and Mn ores (Klein and Ladeira, 2002; Moreto et al., 2015). The Carajás Basin, within the CMP, is an elongated, E-W trending sedimentary basin (Fig. 2.2A; B) that was deposited over an Archean

basement made up of granulites, migmatites and metavolcanic rocks emplaced from ca. 3080 Ma to ca. 3000 Ma (Machado et al., 1991; Pidgeon et al., 2000; Moreto et al., 2015b).

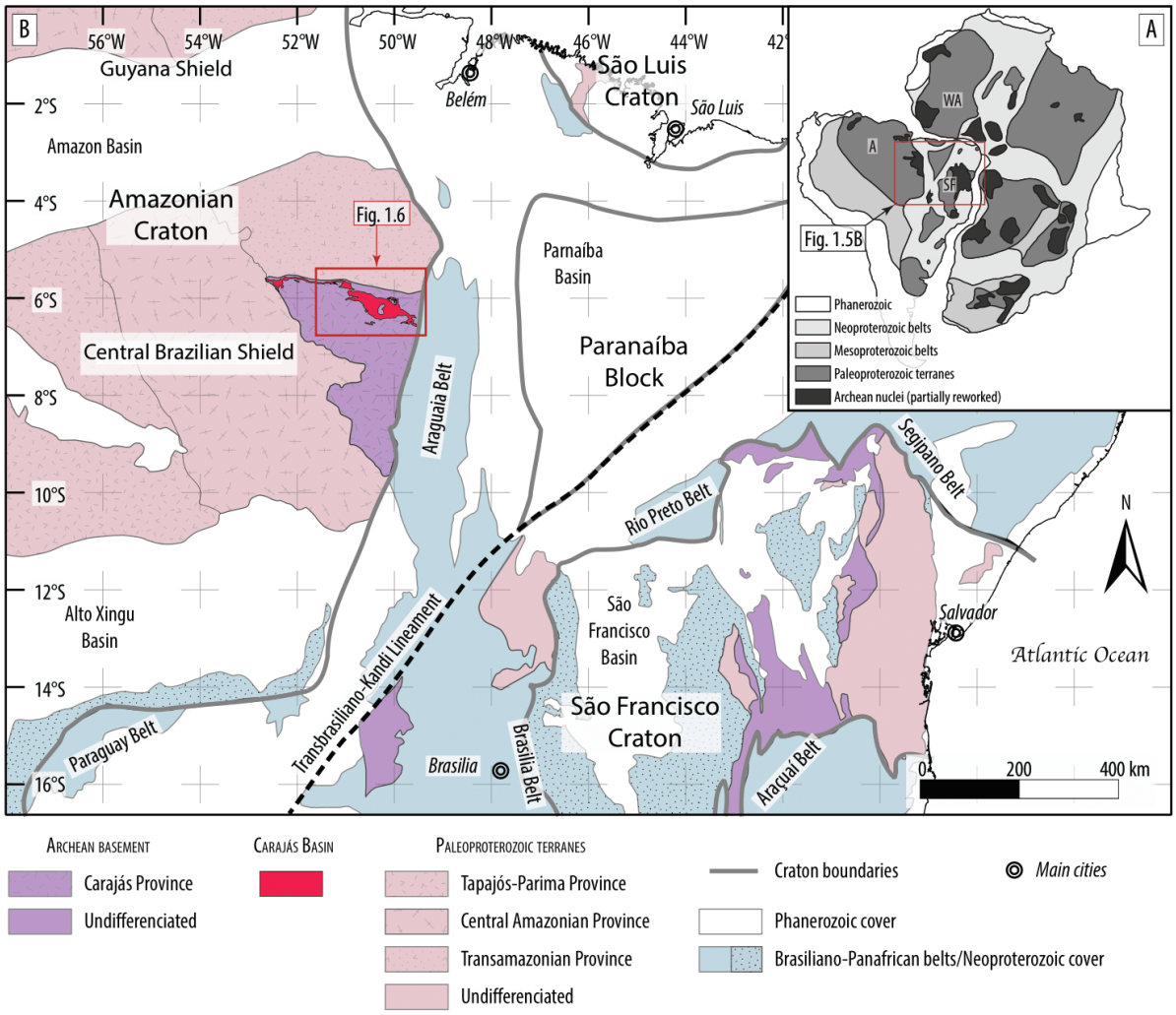

Figure 2. 1: Geological framework of the Amazonia Craton and the Carajás Basin (after Rossignol et al., 2021). (A) Reconstruction of the main tectonic elements of South America and Africa (after Cordani et al., 2016), (B) Location of the Carajás Basin within the Amazonia Craton.

The basement has been later intruded by tonalites, trondhjemites and granodiorites (TTG) between ca. 2960 Ma and ca. 2930 Ma (Feio et al., 2013) and between ca. 2870 Ma to 2830 Ma (Machado et al., 1991; Pidgeon et al., 2000; Feio et al., 2013; Moreto et al., 2015b). Between ca. 2760 Ma and ca. 2730 Ma, various ultramafic, mafic and felsic magmatic rocks have been emplaced in the SE Amazonian Craton (Machado et al., 1991;

Sardinha et al., 2006; de Mesquita Barros et al., 2009; Feio et al., 2012, 2013). This magmatic episode was followed by the development of a rift (Olszewski et al., 1989; Martins et al., 2017a; Toledo et al., 2019), that allowed chemical and detrital sediments to accumulate, initiating the development of the Carajás Basin.

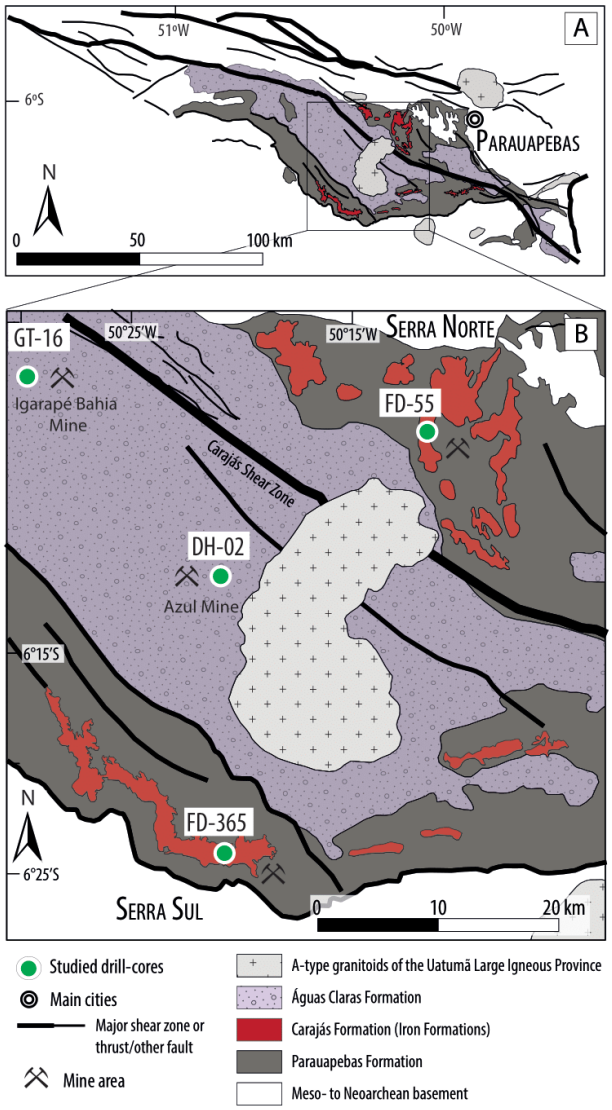

Figure 2. 2: Geological map of the Carajás Basin (a) highlighting the main lithological components and (b) showing the distinct position of the studied drill cores (after Rego et al., 2021).

A minor magmatic event later occurred at 2701 ± 30 Ma (Melo et al., 2017), and a long-lasting but poorly characterized tectono-thermal event occurred between ca. 2600 and

2450 Ma (Machado et al., 1991; Requia et al., 2003; Tallarico et al., 2005; Grainger et al., 2008; Melo et al., 2017; Toledo et al., 2019). To the west, the Carajás Basin is underneath by volcanic and volcaniclastic rocks of the Uatumã Supergroup of the ca. 1.88 Ga Uatumã Silicic Large Igneous Province (Antonio et al., 2017) and to the east, the Carajás Basin is bounded by the Neoproterozoic Araguaia Belt.

During the end of the Neoarchean and the Paleoproterozoic, different tectonic events affected the basement and overlying sediments, forming a WNW trending strike-slip system (Pinheiro and Holdsworth, 1997; Tavares et al., 2018; Toledo et al., 2019). Major shear zones are sealed by the ca. 1.88 Ga granitoids (Fig. 2.2A, B), and the Carajás Basin has only been subjected to minor tectonic activity afterward (Pinheiro and Holdsworth, 1997). However, two magmatic events dated at ca. 535 Ma and ca. 200 Ma occurred in this region (Teixeira et al., 2019) and are attributed to a post-collisional event following the collision along the Araguaia Belt and to the Central Atlantic Magmatic Province, respectively (Teixeira et al., 2019).

2.2 Stratigraphic framework

Neoarchean sediments of the Carajás Basin consist of the Itacaiúnas Supergroup, divided into the Grão Pará and Igarapé Bahia groups (Fig. 2.3). At the base of the Grão Pará Group, the Parauapebas Formation (Fig. 2.3) unconformably overlies the previously described Archean basement. This formation consists mainly of basalts and basaltic andesite with minor pyroclastic rocks and rhyolites (Machado et al., 1991; Martins et al., 2017a) that underwent submarine hydrothermal alteration (Martins et al., 2017a; Figueiredo e Silva et al., 2020; Lacasse et al., 2020). The volcanic activity spanned from ca. 2770 to ca. 2750 Ma, as indicated by numerous U-Pb analyses on zircon (Wirth et al., 1986;

Olszewski et al., 1989; Machado et al., 1991; Trendall et al., 1998; Martins et al., 2017a). The Parauapebas Formation and associated magmatic rocks of similar age were emplaced in an intraplate tectonic setting, and are characteristic of a large igneous province (LIP) (Rossignol et al., 2021).

The Parauapebas Formation is conformably overlain by the Carajás Formation (Fig. 2.3), which consists mainly of oxide-facies banded iron formations (BIFs) alternating between iron-rich and chert layers, but, minor black shales and conglomeratic layers have also been reported (Cabral et al., 2013, 2017). These were interpreted to have been deposited in a range of environments from shallow water, low energy environments, to deep and quiet water settings (Tolbert et al., 1971; Lindenmayer et al., 2001; Macambira and Schrank, 2002a; Ribeiro da Luz and Crowley, 2012). Geochemical analyses of BIFs show very low content in lithophile elements, suggesting that the Carajás Formation has been deposited on a wide and shallow platform localized far away from emerged lands (Macambira & Schrank, 2002; Justo *et al.*, 2020; Rego et al., 2021). The Carajás Formation was deposited, at least in part, coevally with the Parauapebas Formation, as shown by the interlayering of volcanic rocks and BIFs (Gibbs et al., 1986; Martins et al., 2017a). These stratigraphic relationships provide a lower bound for the age of the Carajás Formation, which must be younger than the 2759 ± 2 Ma emplacement age of underlying volcanic rocks (Machado et al., 1991). A poorly characterized rock, tentatively interpreted as a tuff or an intrusive sill, yielded a zircon U-Pb date of 2743 ± 11 Ma (Trendall et al., 1998). Dolerite sills intruded some BIFs at 2751 ± 4 Ma (Krymsky et al., 2007a) and 2740 ± 8 Ma (Table 1.0; Trendall et al., 1998). Re-Os dates in black shales of 2661 ± 110 Ma and 2682 ± 150 Ma intercalated with BIFs are roughly consistent with the above-mentioned U-Pb dating results (Cabral et al., 2013).

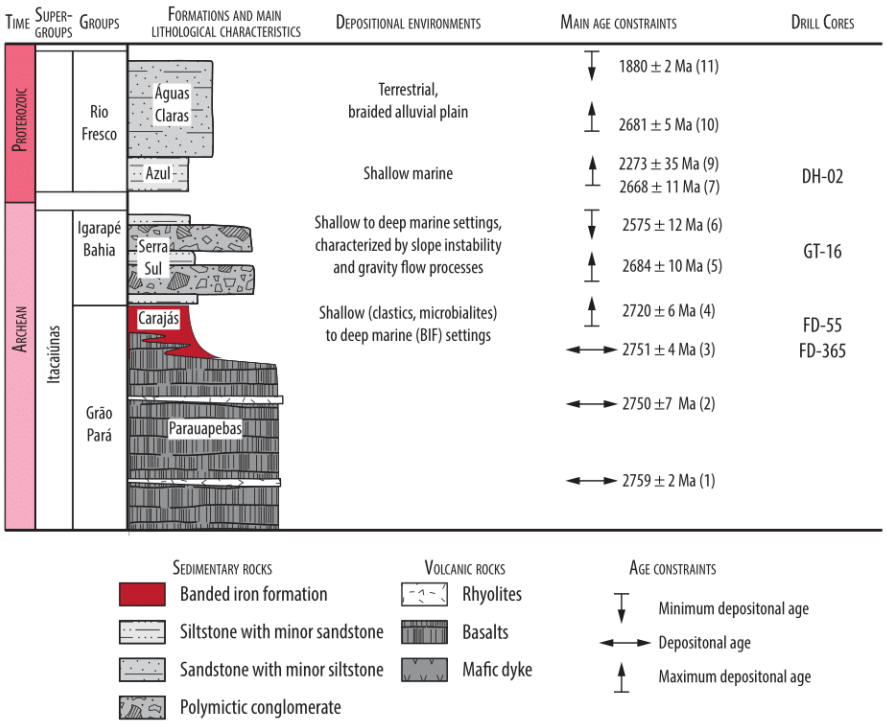

Figure 2. 3: Stratigraphic framework proposed for the Carajás Basin showing its main sedimentary units and age constrains based on previous literature (after Rossignol et al., 2021).

Above the Carajás Formation, the Igarapé Bahia Group forms the uppermost unit of the Itacaiúnas Supergroup (Fig. 2.3). The contact between the Carajás Formation and the Igarapé Bahia Group has not been observed but is generally assumed to be concordant (Araújo et al., 2021a). However, at least in some localities, the Igarapé Bahia Group directly overlies the basalts of the Parauapebas Formation (Dreher et al., 2005; Melo et al., 2019), suggesting that the Igarapé Bahia Group could overlie discordantly the Carajás Formation. At its base, the Igarapé Bahia Group comprises BIF layers up to 10 m thick, grading upward to sandstone and siltstone interbedded with polymictic conglomerate containing angular clasts of BIF, chert, and volcanic rocks (Dreher et al., 2008, 2005; Galarza et al., 2008; Melo et al., 2019). Volcanism coeval to the sedimentation has been suggested based on the occurrence of volcanic pebbles in the conglomerate. A

maximum depositional age (MDA) of 2784 ± 27 Ma, relying on only one detrital zircon grain, has been proposed for this unit (Melo et al., 2019), while zircon from sandstones and conglomerates from the new Serra Sul Formation, here placed within the Igarapé Bahia group, gave a U-Pb date of 2684 ± 10 Ma (Rossignol et al., 2020). Hydrothermal monazite gave a U-Pb date of 2575 ± 12 Ma interpreted as the age of fluid circulation (Tallarico et al., 2005), which suggests that the Igarapé Bahia Group would be older than ca. 2.6 Ga (Table 2.1). At a regional scale, the age of hydrothermal circulations is further corroborated by Re-Os dates on sulfide minerals at 2576 ± 8 Ma and 2568 ± 8 Ma (Requia et al., 2003), and by the emplacement of small bodies of granitic rocks and pegmatites at 2557 ± 26 Ma and 2562 ± 39 Ma, respectively (U-Pb zircon age; Toledo et al., 2019).

Table 2. 1: Summary of the age constrains for the main sedimentary units of the Carajás Basin.

Number in Fig. 1.7	Method	Object	Interpretation	Age (Ma)	Reference
Parauapebas Formation					
1	Zircon U-Pb	Metarhyolite	Depositional age	2759 ± 2	Machado et al., 1991
2	Zircon U-Pb	Metabasalt	Depositional age	2750 ± 7	Martins et al., 2017
Carajás Formation					
3	Zircon U-Pb	Dolerite sill intruding the Carajás Formation	Minimum depositional age	2751 ± 4	Krymsky et al., 2007
4	Zircon U-Pb	Volcaniclastic layer	Depositional age	2720 ± 6	Rossignol et al., submitted
Igarapé Bahia Group					
5	Zircon U-Pb	Sandstones to conglomerates	Maximum depositional age	2684 ± 10	Rossignol et al., 2020
6	Monazite U-Pb	Hydrothermal vein	Minimum depositional age	2575 ± 12	Tallarico et al., 2005
Azul Formation					
7	Zircon U-Pb	Sandstone	Maximum depositional age	2668 ± 11	Rossignol et al., 2021
8*	Zircon U-Pb	Rhythmite	Maximum depositional age	2373± 4	Justo et al., 2018
9	Zircon Pb-Pb	Rhythmite	Maximum depositional age	2273 ± 35	Araujó et al., 2021
Águas Claras Formation					
10	Zircon U-Pb	Sandstone	Depositional age	2681 ± 5	Trendall et al., 1998
11	Zircon U-Pb	Granite intruding the Águas Claras Formation	Minimum depositional age	1880 ± 2	Machado et al., 1991

11*	Pb-Pb	Pyrite	Diagenetic – hydrot. age	2060 ± ?	Mougeot et al., 1996

Uncertainties are given at the 2σ level.

*Unpublished ages, taken from works (*e.g.* Abstracts) presented at the annual Brazilian Congress of Geology. These were not included in Figure 2.3.

Overlaying the Igarapé Bahia Group lies unconformably the Rio Fresco Group, which is composed of siliciclastic successions known as Azul and Aguás Claras Formation. The Azul Formation was recently dated with a maximum depositional age of 2273 $\pm$ 25 (Araújo et al., 2021), while the Aguas Claras Formation has its age still undefined between 2681 ± 5 Ma (maximum depositional age; Trendall et al., 1998) and 1880 ± 2 Ma (granite intruding the Águas Claras Formation; Machado et al., 1991). The Azul and Aguás Claras Formation consists of Rhythmite sandstones and mudstones, locally enriched in manganese (Mn) and are interpreted to have been deposited in marine and fluvial settings, respectively, representing the stratigraphic record of a transgressive-regressive sequence (Araújo Filho et al., 2020; Araújo et al., 2021).

All the studied drill cores (FD 55, FD 365, GT 16 and DH 02) intercepting the above-mentioned formations, spanning the Neoarchean and potentially early Paleoproterozoic sedimentary rocks are shown in Figure 2.2 with their respective location in the Carajás Basin and in Figure 2.3 next to their respective ages. It is important to mention that a major effort has been placed to constrain the stratigraphic framework of the Carajás Basin, which included extensive field work, description and sampling of various drill-cores to obtain ages for the Carajás Formation, Serra Sul Formation, Igarapé Bahia Group and Rio Fresco Group, sedimentological descriptions of drill cores throughout the basin intercepting the main formations (Carajás, Igarapé Bahia/Serra Sul, and Azul/ Águas Claras), and finally sample preparation for geochemistry. Publish-related contributions are shown in the references bellow and can be found attached in the Annex section of the thesis:

Rossignol, C., **Siciliano Rego, E**., Narduzzi, F., Teixeira, L., Ávila, J.N., Silva, M.A.L., Lana, C., and Philippot, P., 2020, Stratigraphy and geochronological constraints of the Serra Sul Formation (Carajás Basin, Amazonian Craton, Brazil): Precambrian Research, v. 351, p. 105981, doi:10.1016/j.precamres.2020.105981.

Rossignol, C., Antonio, P. Y. J., Narduzzi, F., **Siciliano Rego, E**., Teixeira, L., Ávila, J.N., Silva, M.A.L., Lana, C., Trindade, R., and Philippot, P., 2021, Geoscience Frontiers Unraveling one billion years of geological evolution of the southeastern Amazonia Craton from detrital zircon analyses: Geoscience Frontiers, p. 101202, doi:10.1016/j.gsf.2021.101202

Rossignol, C., **Siciliano Rego, E**., Narduzzi, F., Teixeira, L., Ávila, J.N., Silva, M.A.L., Lana, C., and Philippot, P., 2020, Neoarchean environments associated to a Large Igneous Province: insights from the Carajás Basin, Amazonia Craton, *submitted to* Precambrian Research.

2.3 References

Almeida, F.F.M. De, Brito Neves, B.B. De, and Dal Ré Carneiro, C., 2000, The origin and evolution of the South American platform: Earth Science Reviews, v. 50, p. 77–111, doi:10.1016/S0012-8252(99)00072-0.

Antonio, P.Y.J., D'Agrella-Filho, M.S., Trindade, R.I.F., Nédélec, A., de Oliveira, D.C., da Silva, F.F., Roverato, M., and Lana, C., 2017, Turmoil before the boring billion: Paleomagnetism of the 1880–1860 Ma Uatumã event in the Amazonian craton:

Gondwana Research, v. 49, p. 106–129, doi:10.1016/j.gr.2017.05.006.

Araújo, R., Araújo Filho, R.C., and Costa, L., 2021a, Tectono-sedimentary evolution of the Paleoproterozoic succession of the Carajás Basin, southeastern Amazonian Craton, Brazil: Insights from sedimentology, stratigraphy, and U–Pb detrital zircon geochronology: Precambrian Research, v. 362, p. 106290, doi:10.1016/j.precamres.2021.106290.

Araújo, R., Filho, R.A., and Costa, L., 2021b, Tectono-sedimentary evolution of the Paleoproterozoic succession of the Carajás Basin, southeastern Amazonian Craton, Brazil: Insights from sedimentology, stratigraphy, and U–Pb detrital zircon geochronology: Precambrian Research, v. 362, p. 106290, doi:10.1016/j.precamres.2021.106290.

Araújo Filho, R.C., Nogueira, A.C.R., and Araújo, R.N., 2020, New stratigraphic proposal of a Paleoproterozoic siliciclastic succession: Implications for the evolution of the Carajás Basin, Amazonian craton, Brazil: Journal of South American Earth Sciences, v. 102, p. 102665, doi:10.1016/j.jsames.2020.102665.

Cabral, A.R. et al., 2013, Trace-element and multi-isotope geochemistry of Late-Archean black shales in the Carajás iron-ore district, Brazil: Chemical Geology, v. 362, p. 91–104, doi:10.1016/j.chemgeo.2013.08.041.

Cabral, A.R., Bühn, B., Seabra Gomes, A.A., Galbiatti, H.F., Lehmann, B., and Halder, S., 2017, Multiple sulfur isotopes from the Neoarchaean Serra Sul black shale, Carajás mineral province, northern Brazil: Journal of South American Earth Sciences, v. 79, p. 377–383, doi:10.1016/j.jsames.2017.08.002.

Cordani, U.G., and Teixeira, W., 2007a, Proterozoic accretionary belts in the Amazonian Craton: Memoir of the Geological Society of America, v. 200, p. 297–320, doi:10.1130/2007.1200(14).

Cordani, U.G., and Teixeira, W., 2007b, Proterozoic accretionary belts in the Amazonian Craton: Memoir of the Geological Society of America, v. 200, p. 297–320, doi:10.1130/2007.1200(14).

Cordani, U.G., Teixeira, W., D'Agrella-Filho, M.S., and Trindade, R.I., 2009, The position of the Amazonian Craton in supercontinents: Gondwana Research, v. 15, p. 396–407, doi:10.1016/j.gr.2008.12.005.

Dreher, A.M., Xavier, R.P., and Martini, S.L., 2005, Fragmental rocks if the Igarape Bahia Cu-Au deposits, Carajas minaral Province, Brazil: Revista Brasileira de Geociências, v. 35, p. 359–368.

Dreher, A.M., Xavier, R.P., Taylor, B.E., and Martini, S.L., 2008, New geologic, fluid inclusion and stable isotope studies on the controversial Igarapé Bahia Cu-Au deposit, Carajás Province, Brazil: Mineralium Deposita, v. 43, p. 161–184, doi:10.1007/s00126-007-0150-6.

Feio, G.R.L., Dall'Agnol, R., Dantas, E.L., Macambira, M.J.B., Gomes, A.C.B., Sardinha, A.S., Oliveira, D.C., Santos, R.D., and Santos, P.A., 2012, Geochemistry, geochronology, and origin of the Neoarchean Planalto Granite suite, Carajás, Amazonian craton: A-type or hydrated charnockitic granites? Lithos, v. 151, p. 57–73, doi:10.1016/j.lithos.2012.02.020.

Feio, G.R.L., Dall'Agnol, R., Dantas, E.L., Macambira, M.J.B., Santos, J.O.S., Althoff, F.J., and Soares, J.E.B., 2013, Archean granitoid magmatism in the Canaã dos Carajás area: Implications for crustal evolution of the Carajás province, Amazonian craton, Brazil: Precambrian Research, v. 227, p. 157–185, doi:10.1016/j.precamres.2012.04.007.

Figueiredo e Silva, R.C., Lobato, L.M., Zucchetti, M., Hagemann, S., and Vennemann, T., 2020, Geotectonic signature and hydrothermal alteration of metabasalts under- and overlying the giant Serra Norte iron deposits, Carajás mineral Province: Ore Geology

Reviews, v. 120, doi:10.1016/j.oregeorev.2020.103407.

Galarza, M.A., Macambira, M.J.B., and Villas, R.N., 2008, Dating and isotopic characteristics (Pb and S) of the Fe oxide-Cu-Au-U-REE Igarapé Bahia ore deposit, Carajás mineral province, Pará state, Brazil: Journal of South American Earth Sciences, v. 25, p. 377–397, doi:10.1016/j.jsames.2007.07.006.

Gibbs, A.K., Wirth, K.R., Hirata, W.K., and Olszewski, W.J., 1986, Age and composition of the Grão Pará Group volcanics, Serra dos Carajás: Revista Brasileira de Geociências, v. 16, p. 201–211.

Grainger, C.J., Groves, D.I., Tallarico, F.H.B., and Fletcher, I.R., 2008, Metallogenesis of the Carajás Mineral Province, Southern Amazon Craton, Brazil: Varying styles of Archean through Paleoproterozoic to Neoproterozoic base- and precious-metal mineralisation: Ore Geology Reviews, v. 33, p. 451–489, doi:10.1016/j.oregeorev.2006.10.010.

Justo, A.P., Dantas, E.L., Bau, M., Freitas-Silva, F.H., Santos, R.V., and Schorscher, J.H.D., 2020, Paleobasinal to band-scale REE+Y distribution in Iron Formations from Carajás Amazon Craton, Brazil: Ore Geology Reviews, p. 103750, doi:10.1016/j.oregeorev.2020.103750.

Klein, C., and Ladeira, E.A., 2002, Petrography and geochemistry of the least altered banded iron-formation of the Archean Carajás formation, northern Brazil: Economic Geology, v. 97, p. 643–651, doi:10.2113/gsecongeo.97.3.643.

Krymsky, R.S., Macambira, M.J.B., Lafon, J.-M., and Estumano, G.S., 2007, Uranium-lead dating method at the Pará-Iso isotope geology laboratory, UFPA, Belém - Brazil: Anais da Academia Brasileira de Ciencias, v. 79, p. 115–128, doi:10.1590/S0001-37652007000100014.

Lacasse, C.M., Ganade, C.E., Mathieu, L., Teixeira, N.A., Lopes, L.B.L., and Monteiro,

C.F., 2020, Restoring original composition of hydrothermally altered Archean metavolcanic rocks of the Carajás Mineral Province (Brazil): Geodynamic implications for the transition from lid to mobile tectonics: Lithos, v. 372–373, p. 105647, doi:10.1016/j.lithos.2020.105647.

Lindenmayer, Z., Laux, J., and Teixeira, J., 2001, Consideração sobre a origem das formações ferríferas da Formação Carajás, Serra dos Carajás: Revista Brasileira de Geociências, v. 31, p. 21–28.

Macambira, J.B., and Schrank, A., 2002a, Químio-estratigrafia e evolução dos jaspilitos da Formação Carajás (PA): Revista Brasileira de Geociências, v. 32, p. 567–578.

Macambira, M.J.B., and Schrank, A., 2002b, Químio-estratigrafia e evolução dos jaspilitos da Formação Carajás (PA): Revista Brasileira de Geociências, v. 32, p. 567–578, doi:10.25249/0375-7536.2002324567578.

Machado, N., Lindenmayer, Z., Krogh, T.E., and Lindenmayer, D., 1991, U-Pb geochronology of Archean magmatism and basement reactivation in the Carajás area, Amazon shield, Brazil: Precambrian Research, v. 49, p. 329–354, doi:10.1016/0301-9268(91)90040-H.

Martins, P.L.G., Toledo, C.L.B., Silva, A.M., Antonio, P.Y.J., Chemale, F., Assis, L.M., and Trindade, R.I.F., 2021, Low paleolatitude of the Carajás Basin at ~2.75 Ga: Paleomagnetic evidence from basaltic flows in Amazonia: Precambrian Research, v. 365, p. 106411, doi:10.1016/j.precamres.2021.106411.

Martins, P.L.G., Toledo, C.L.B., Silva, A.M., Chemale, F., Santos, J.O.S., and Assis, L.M., 2017, Neoarchean magmatism in the southeastern Amazonian Craton, Brazil: Petrography, geochemistry and tectonic significance of basalts from the Carajás Basin: Precambrian Research, v. 302, p. 340–357,

doi:10.1016/j.precamres.2017.10.013.

Melo, G.H.C., Monteiro, L.V.S., Xavier, R.P., Moreto, C.P.N., Arquaz, R.M., and Silva, M.A.D., 2019, Evolution of the Igarapé Bahia Cu-Au deposit, Carajás Province (Brazil): Early syngenetic chalcopyrite overprinted by IOCG mineralization: Ore Geology Reviews, v. 111, p. 102993, doi:10.1016/j.oregeorev.2019.102993.

Melo, G.H.C., Monteiro, L.V.S., Xavier, R.P., Moreto, C.P.N., Santiago, E.S.B., Dufrane, S.A., Aires, B., and Santos, A.F.F., 2017, Temporal evolution of the giant Salobo IOCG deposit, Carajás Province (Brazil): constraints from paragenesis of hydrothermal alteration and U-Pb geochronology: Mineralium Deposita, v. 52, p. 709–732, doi:10.1007/s00126-016-0693-5.

de Mesquita Barros, C.E., Sardinha, A.S., de Oliveira Barbosa, J. d. P., Macambira, M.J.B., Barbey, P., and Boullier, A.-M., 2009, STRUCTURE, PETROLOGY, GEOCHEMISTRY AND ZIRCON U/Pb AND Pb/Pb GEOCHRONOLOGY OF THE SYNKINEMATIC ARCHEAN (2.7 Ga) A-TYPE GRANITES FROM THE CARAJAS METALLOGENIC PROVINCE, NORTHERN BRAZIL: The Canadian Mineralogist, v. 47, p. 1423–1440, doi:10.3749/canmin.47.6.1423.

Milhomem Neto, J.M., and Lafon, J.M., 2019, Zircon U-Pb and Lu-Hf isotope constraints on Archean crustal evolution in Southeastern Guyana Shield: Geoscience Frontiers, v. 10, p. 1477–1506, doi:10.1016/j.gsf.2018.09.012.

Moreto, C.P.N., Monteiro, L.V.S., Xavier, R.P., Creaser, R.A., DuFrane, S.A., Melo, G.H.C., Delinardo da Silva, M.A., Tassinari, C.C.G., and Sato, K., 2015a, Timing of multiple hydrothermal events in the iron oxide–copper–gold deposits of the Southern Copper Belt, Carajás Province, Brazil: Mineralium Deposita, v. 50, p. 517–546, doi:10.1007/s00126-014-0549-9.

Moreto, C.P.N., Monteiro, L.V.S., Xavier, R.P., Creaser, R.A., DuFrane, S.A., Tassinari,

C.C.G., Sato, K., Kemp, A.I.S., and Amaral, W.S., 2015b, Neoarchean and paleoproterozoic iron oxide-copper-gold events at the sossego deposit, Carajás Province, Brazil: Re-Os and U-Pb geochronological evidence: Economic Geology, v. 110, p. 809–835, doi:10.2113/econgeo.110.3.809.

Olszewski, W.J., Wirth, K.R., Gibbs, A.K., and Gaudette, H.E., 1989, The age, origin, and tectonics of the Grão Pará Group and associated rocks, Serra dos Carajás, Brazil: Archean continental volcanism and rifting: Precambrian Research, v. 42, p. 229–254, doi:10.1016/0301-9268(89)90013-2.

Pidgeon, R.T., MacAmbira, M.J.B., and Lafon, J.M., 2000, Th-U-Pb isotopic systems and internal structures of complex zircons from an enderbite from the Pium Complex, Carajas Province, Brazil: Evidence for the ages of granulite facies metamorphism and the protolith of the enderbite: Chemical Geology, v. 166, p. 159–171, doi:10.1016/S0009-2541(99)00190-4.

Pinheiro, R.V.L., and Holdsworth, R.E., 1997, Reactivation of Archaean strike-slip fault systems, Amazon region, Brazil: Journal of the Geological Society, v. 154, p. 99–103, doi:10.1144/gsjgs.154.1.0099.

Requia, K., Stein, H., Fontboté, L., and Chiaradia, M., 2003, Re-Os and Pb-Pb geochronology of the Archean Salobo iron oxide copper-gold deposit, Carajás mineral province, northern Brazil: Mineralium Deposita, v. 38, p. 727–738, doi:10.1007/s00126-003-0364-1.

Ribeiro da Luz, B., and Crowley, J.K., 2012, Morphological and chemical evidence of stromatolitic deposits in the 2.75Ga Carajás banded iron formation, Brazil: Earth and Planetary Science Letters, v. 355–356, p. 60–72, doi:10.1016/j.epsl.2012.08.028.

Ronze, P.C., Soares, A.D.V., Santos, M.G.S., and Barreira, C.F., 2000, Alemao copper-gold (U-REE) deposits, Carajas, Brazil, *in* Porter, T.M. ed., Hydrothermal iron oxide

copper-gold and related deposits: a global perspective, PCG Publishing, p. 191–202.

Rossignol, C. et al., 2021, Geoscience Frontiers Unraveling one billion years of geological evolution of the southeastern Amazonia Craton from detrital zircon analyses: Geoscience Frontiers, p. 101202, doi:10.1016/j.gsf.2021.101202.

Rossignol, C., Siciliano Rego, E., Narduzzi, F., Teixeira, L., Ávila, J.N., Silva, M.A.L., Lana, C., and Philippot, P., 2020, Stratigraphy and geochronological constraints of the Serra Sul Formation (Carajás Basin, Amazonian Craton, Brazil): Precambrian Research, v. 351, p. 105981, doi:10.1016/j.precamres.2020.105981.

Santos, J.O.S., Hartmann, L.A., Gaudette, H.E., Groves, D.I., Mcnaughton, N.J., and Fletcher, I.R., 2000, A New Understanding of the Provinces of the Amazon Craton Based on Integration of Field Mapping and U-Pb and Sm-Nd Geochronology: Gondwana Research, v. 3, p. 453–488, doi:10.1016/S1342-937X(05)70755-3.

Sardinha, A.S., Barros, C.E.M., and Krymsky, R., 2006, Geology, geochemistry, and U-Pb geochronology of the Archean (2.74 Ga) Serra do Rabo granite stocks, Carajás Metallogenetic Province, northern Brazil: Journal of South American Earth Sciences, v. 20, p. 327–339, doi:10.1016/j.jsames.2005.11.001.

Tallarico, F.H.B., Figueiredo, B.R., Groves, D.I., Kositcin, N., McNaughton, N.J., Fletcher, I.R., and Rego, J.L., 2005, Geology and SHRIMP U-Pb geochronology of the Igarapé Bahia deposit, Carajás copper-gold belt, Brazil: An Archean (2.57 Ga) example of Iron-Oxide Cu-Au-(U-REE) mineralization: Economic Geology, v. 100, p. 7–28, doi:10.2113/100.1.0007.

Tassinari, C.C.G., and Macambira, M.J.B., 1999, Geochronological provinces of the Amazonian Craton: Episodes, v. 22, p. 174–182, doi:10.18814/epiiugs/1999/v22i3/004.

Tavares, F.M., Trouw, R.A.J., da Silva, C.M.G., Justo, A.P., and Oliveira, J.K.M., 2018, The

multistage tectonic evolution of the northeastern Carajás Province, Amazonian Craton, Brazil: Revealing complex structural patterns: Journal of South American Earth Sciences, v. 88, p. 238–252, doi:10.1016/j.jsames.2018.08.024.

Teixeira, W., Hamilton, M.A., Girardi, V.A.V., Faleiros, F.M., and Ernst, R.E., 2019, U-Pb baddeleyite ages of key dyke swarms in the Amazonian Craton (Carajás/Rio Maria and Rio Apa areas): Tectonic implications for events at 1880, 1110 Ma, 535 Ma and 200 Ma: Precambrian Research, v. 329, p. 138–155, doi:10.1016/j.precamres.2018.02.008.

Tolbert, G.E., Tremaine, J.W., Melcher, G.C., and Gomes, C.B., 1971, The Recently Discovered Serra dos Carajas Iron Deposits, Northern Brazil: Economic Geology, v. 66, p. 985–994, doi:10.2113/gsecongeo.66.7.985.

Toledo, P.I.F., Moreto, C.P.N., Xavier, R.P., Gao, J.F., de Matos, J.H.S.N., and de Melo, G.H.C., 2019, Multistage evolution of the Neoarchean (ca. 2.7 Ga) Igarapé cinzento (GT-46) iron oxide copper-gold deposit, Cinzento shear zone, Carajás Province, Brazil: Economic Geology, v. 114, p. 1–34, doi:10.5382/econgeo.2019.4617.

Trendall, A.F., Basei, M.A.S., De Laeter, J.R., and Nelson, D.R., 1998, SHRIMP zircon U-Pb constraints on the age of the Carajas formation, Grao Para Group, Amazon Craton: Journal of South American Earth Sciences, v. 11, p. 265–277, doi:10.1016/S0895-9811(98)00015-7.

Wirth, K.R., Gibbs, A.K., and Olszewski, W.J., 1986, U-Pb ages of zircons from the Grão-Pará Group and Serra dos Carajás Granites, Pará, Brazil: Revista Brasileira de Geociências, v. 16, p. 195–200.

CHAPTER 3

3. Material and Methods

This chapter will go over the material and methods, including an overview of sampling strategy, sample preparation, Fe chemistry, and main instruments utilized throughout the thesis. Finally, the effects of carbonate leaching on Fe isotopes is also included, demonstrating that Fe-carbonates can be targeted utilizing weak acid treatments. All rock samples studied in this thesis came from fresh drill-cores, which were sampled during field trips (total of approximately 5 weeks) in Carajás, Pará, Brazil. Several drill-cores were initially selected at Vale drill-core repository. Afterwards, a sample strategy was developed based on the material available, which involved the selection of key stratigraphic intervals throughout the Carajás Basin. This included sampling and logging drill-cores with lithologies composed of iron formations and carbonates, conglomerates, sandstones, siltstones, and shales. The most preserved cores (*i.e.* not altered by secondary features such as post-depositional mineralization, weathering, and etc.) were selected for geochemical measurements. Samples were brought to the University of São Paulo (USP), and stored at the Instituto the Astronomia e Geofísica (IAG-USP), where they were later prepared for geochemical analysis. Approximately 300 samples were cut (*i.e.* to facilitate the crushing procedure and/or for thin-section preparation), later crushed, and finally pulverized.

3.1 Sample preparation for geochemical analysis

In order to avoid contamination from trace elements, samples were cut with diamond blades, and afterwards crushed and pulverized in an agate mortar at the IAG-USP. The mortar was always precleaned by pulverizing fine silica sand grains prior to any sample and subsequently washed with Milli-Q water, at least twice. Compressed-air was utilized to speed-up the drying processes of the mortar after each cleaning round. After pulverization, samples were transferred to precleaned plastic vials to be stored and/or to Teflon beakers for digestion.

All clean room laboratory work was done in class-100 clean room with class-10 laminar flow hoods. In order to proceed with geochemical measurements, samples were digested with distilled AR grade acids (69% HNO_3, 37% HCl). A general digestion protocol was used (*e.g.* for ~ 20 mg of rock powder), which included a first step of concentrated HF:HNO_3 (1:2) attack followed by overnight heating with closed beakers at 110ºC. Samples were evaporated the following day and a second attack consisting concentrated HNO_3:HCl (1:2) followed. Samples were heated overnight (110ºC) and evaporated in the morning. The HNO_3:HCl step was repeated to ensure that all Fe was in its ferric state. In the case of samples rich in organic matter, 0.750 mL of $HClO_4$ was added to the dry sample, heated during the day at 110ºC, and evaporated during the night utilizing an Evapoclean device. The final digestion step was to bring all samples back in 6M HCl.

3.2 Iron extraction by chromatography

The procedure to separate iron from other elements have been described in detail before (Dauphas et al., 2004a, 2009; Busigny et al., 2014) and it is routinely used at the Institut de Physique du Globe de Paris (IPGP), where all the Fe isotopic work for this thesis has been done. Given the partitioning behavior of elements in anion exchange resins (*e.g.* Strelow, 1980), matrix elements can be eluded while Fe is retained in more concentrated HCl. After matrix elution, Fe is subsequently extracted using diluted HCl. Chromatography columns are prepared by loading 1 mL of AG1-X8 resin (200-400 mesh, 0.038-0.075 mm bead diameter) into a Bio-Rad Poly-Prep empty column (10 mL total reservoir of 8 mm diameter and 90 mm length). The samples are purified in the columns following the procedure described in Table 3.1. The entire purification procedure was repeated twice.

Table 3. 1: Elution scheme for Fe purification

Step	Acid	Volume	Comment
Column cleaning	Milli-Q H_2O	10 mL	Waste
	1M HNO_3	5 mL	Waste
	Milli-Q H_2O	10 mL	Waste
	1M HNO_3	5 mL	Waste
	Milli-Q H_2O	10 mL	Waste
	0.4M HCl	10 mL	Waste
	Milli-Q H_2O	5 mL	Waste
Conditioning	6M HCl	2 mL	Waste
Sample loading	6M HCl	0.2 mL	Waste

Matrix elution	6M HCl	8 mL	Waste
Iron elution	0.4M HCl	10 mL	Collect iron

3.3 MC-ICP-MS measurements

Multi-collector inductively-coupled-plasma mass-spectrometry (MC-ICP-MS) allows distinct isotopes to be separated based on the mass to charge ratio (m/z) of charged particles, and therefore, it is possible to discriminate between isotopes of the same element and measure different isotopic ratios. Samples are commonly introduced in the liquid form (other ways are solid forms by laser ablation), such as in 2% HNO_3, by aspiration through a nebulizer which yields an aerosol. The samples are efficiently ionized with an argon plasma at ~ 8000 K, and positively charged particles are accelerated and focused prior going into a magnetic sector with a constant magnetic field. Differential magnetic deflection will occur for ions with distinct m/z ratios. At a fixed charge, accelerating voltage, and magnetic field, the radius of the curvature is proportional to the square root of the ion's mass (*e.g.* heavier atoms, larger radius). Accelerating ions of a given mass are collected in Faraday cups (*e.g.* as an electric charge and converted to counts per second) which finally permits the identification of distinct isotopes.

Samples were introduced into the MC-ICP-MS utilizing a dual cyclonic-Scott type spray chamber, which despite having a lower sample introduction efficiency and higher argide interferences, proved to be more stable compared to a desolvating nebulizer system. Samples were always introduced in the MC-ICP-MS in 2% HNO_3 as 2-3 ppm solutions that corresponded to ~16 to 20V on ^{56}Fe. The isotopes $^{54}Fe^+$, $^{56}Fe^+$, $^{57}Fe^+$ and $^{58}Fe^+$ were measured simultaneously, while $^{53}Cr^+$ and $^{60}Ni^+$ were also measured to monitor and correct any contribution on $^{54}Fe^+$ and $^{58}Fe^+$, respectively. Faraday cups were collecting

masses 53, 54, 56, 57, 58, and 60 in Low 3, Low 2, C, High 1, High 2, and High 4, respectively. Iron isotopes were fully resolved from argide interferences ($^{40}Ar^{14}N^{+}$, $^{40}Ar^{16}O^{+}$, $^{40}Ar^{16}O^{1}H^{+}$) using the high-resolution mode of the Neptune (Weyer and Schwieters, 2003). Interreferences of Cr and Ni are shown in Figure 3.1A using a solution containing 0.1 ppm of Fe and 10 ppb of Cr and Ni. Iron isotope measurements were made on flat-topped peak shoulders to avoid specifically argide interferences (Figure 3.1B). Instrumental mass discrimination was corrected using the conventional sample-standard bracketing (SSB) approach (Rouxel et al., 2003). The $^{56}Fe/^{54}Fe$ and $^{57}Fe/^{54}Fe$ ratios were expressed in the usual δ notation in per mil (‰) as,

$$\delta^{56}Fe\ (‰) = [(^{56}Fe/^{54}Fe)_{sample}\ /(^{56}Fe/^{54}Fe)_{standard} - 1] \times 1000$$

$$\delta^{57}Fe\ (‰) = [(^{57}Fe/^{54}Fe)_{sample}\ /(^{57}Fe/^{54}Fe)_{standard} - 1] \times 1000$$

where the standard is IRMM-014, a pure synthetic Fe metal from the Institute for Reference Materials and Measurements (Taylor et al., 1992).

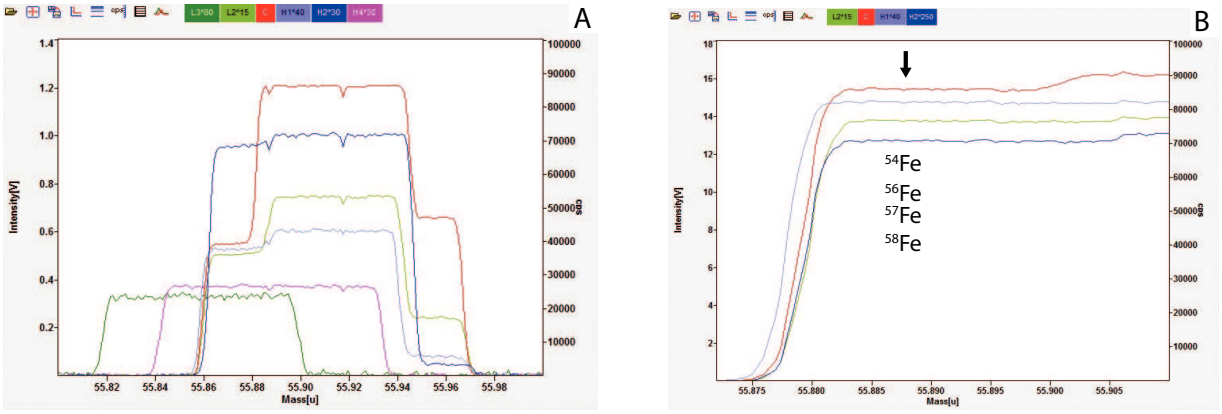

Figure 3. 1: Mass scans performed with the MC-ICP-MS highlighting potential interferences (*e.g.* Cr and Ni) on Fe isotopes (A), and flat shoulders where iron isotopes were measured (B).

3.4 Trace elements: chemistry and measurements

All trace element chemistry was done in bulk rock samples. Between 80 and 100 mg of powdered samples were dissolved using a mixture of concentrated HF-HNO_3, evaporated to dryness and re-dissolved in Aqua Regia solution, all in PFA beakers heated to 80 Cº in a class 1000 clean lab. The residues were then re-dissolved in 5 mL 6M HCl overnight at 80 Cº and archived. Splits of 100 μL from the archive solutions were taken up in 5 mL ~0.28M HNO_3 for ICP-MS measurements. The HNO_3 solutions were dopped with 2 ppb indium (In) to check and correct for any instrumental drift during analysis. Two geostandards (BHVO-2 and CAL-S) and a procedural blank were also prepared with the samples. Elemental concentrations were measured with a High-Resulution Inductively-Coupled-Plasma Mass-Spectrometer (HR-ICP-MS) Element XR (Thermo Fisher Scientific) at the PSO/IUEM (Pôle Spectrométrie Océan, Institut Universitaire Européen de la Mer, Brest, France). Concentrations were calibrated using serially-diluted mixtures of commercial NIST-traceable ICP-MS calibration standards (SPEX Certi-Prep) prepared gravimetrically for the analyses.

Trace element measurements were done with three different mass resolutions: low- (~ 400; LR), medium- (~ 4,000; MR), and high-resolution (~ 10,000; HR). The resolution depends on the mass of the ion to be analyzed and the difference in mass between the mass of the ion and the nearest neighbor (or the width of the peak at mid-height). In case of a lower the resolution, a larger entrance slit is chosen for the passage of the plasma, which yields a wider peak shape and consequently makes difficult the distinction between two peaks. A choice of resolution per element is made in order to control the possible interferences between the target element and its close neighbors.

3.5 Carbon isotopes in carbonates

The carbon isotope compositions of carbonates were carried out at the PSO/IUEM (Pôle Spectrométrie Océan, Institut Universitaire Européen de la Mer, Brest, France) and at the Institut de Physique du Globe de Paris (IPGP). At PSO/IUEM 52 samples were measured using a MAT-235 (Thermo Scientific) mass spectrometer, coupled with a Carbo-Kiel Device for automated CO_2 preparation from IFs, Fe-rich and Fe-poor carbonate samples. The measured CO_2 was produced by reacting bulk powdered samples (*e.g.* ~400 to 4000 μg, depending on the amount of carbonate in each sample) with 100% phosphoric acid (H_3PO_4) at 70ºC for 400 seconds. Isotopic data are reported in conventional delta (δ) notation, relative to the Vienna Pee Dee Belemnite (VPDB). Two calcite standards (NSB-18 and -19) and an internal standard were used. Analytical uncertainties based on replicates and standard analyses are ±0.05‰. At IPGP a similar procedure was done, however, samples (*i.e.* the same IFs, Fe-rich and Fe-poor carbonates) were treated with 100% phosphoric acid at 130°C for 2h (Rosenbaum and Sheppard, 1986; Busigny et al., 2013; Lebeau et al., 2014). This was done to check if there were any differences in carbonate dissolution compared to the previous method utilized at PSO/IUEM, which used lower temperature and a shorter reaction time. Additionally, samples in IPGP were measured using a continuous-flow mass-spectrometer (AP-2003) operated with helium as a carrier gas (Lebeau et al., 2014). Carbonate content in samples was estimated from the ion intensity of the CO_2 peak in the mass-spectrometer with a precision better than ±10% (2SD). Samples that reacted longer in higher temperature conditions showed a higher carbonate content of ~5 wt.% and slightly lighter $\delta^{13}C_{carb}$ composition (~ -0.5 ‰) for all three lithologies compared to samples treaded in lower

temperatures under a shorter reaction time (Fig. 3.2). This could be due to the presence of Fe-carbonates, which are not as easily dissolved as calcite. Therefore, for samples containing siderite and/or ankerite, longer reaction time under higher temperature exposure would likely be more suited for estimations of carbonate content and composition of $\delta^{13}C$ in carbonates. This will be relevant for studies dealing with Fe-carbonate dissolution as it is shown below.

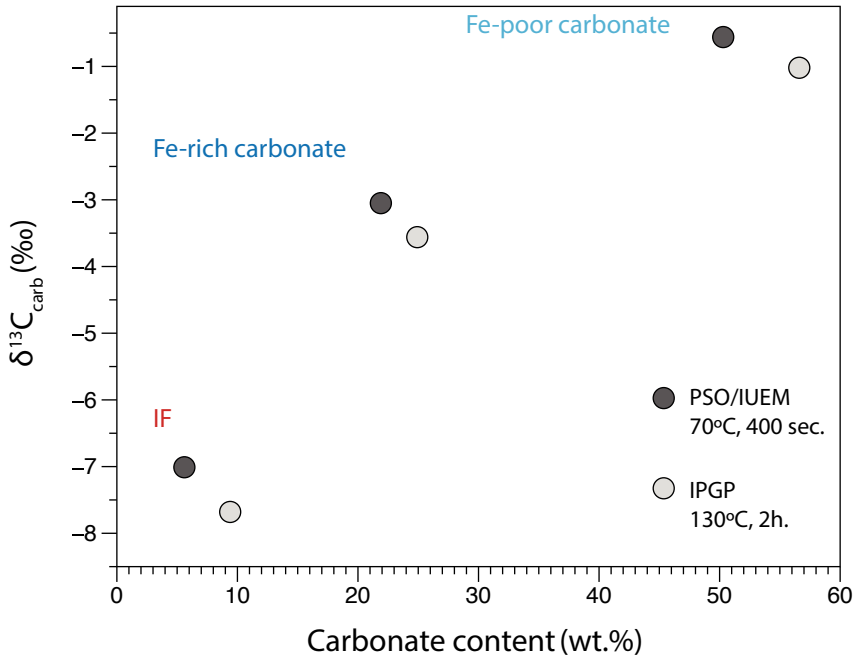

Figure 3. 2: Differences in reaction time (i.e. between bulk- rock and phosphoric acid to produce CO_2) and temperature in which reaction occurred utilized for carbon isotope and carbonate content measurements.

3.6 Chemical extraction of iron from carbonate in banded iron formations for isotope analysis

Abstract

The iron isotope composition of iron-bearing carbonates is commonly used to obtain insights into ancient environmental conditions. However, it is often challenging to target only Fe-carbonates (*e.g*. siderite and ankerite) from samples containing a variety of other Fe-bearing minerals, such as observed in Precambrian iron formations. Chemical extraction (*i.e*. leaching) methods of Fe-carbonates could be an alternative to *in-situ* measurements and/or micro-drilling techniques applied to isotopic studies. Yet, only few studies have looked at the effects of leaching carbonates (*e.g*. partial and/or total dissolution) on their Fe isotope composition. Here, we tested several leaching protocols, using 5 to 20% acetic acid (HAc) and 0.4M HCl, on a siderite standard and three natural samples, including an iron formation, Fe-rich and Fe-poor carbonates. We showed that carbonate mineralogy has a strong control on how much of each mineral phase is being dissolved, and that variations in HAc concentration from 5% to 20% are less likely to change how much siderite dissolves (*e.g*. ~30% dissolution) under a 12h period at room temperature. Importantly, the Fe isotope composition of partially dissolved siderite had undistinguishable values within error from the whole-rock composition (*i.e*. complete dissolution) as shown with HAc and HCl attacks. Carbonates from the three natural samples were almost completely dissolved under the same protocol with 5 to 20% HAc, while 0.4M HCl attacks dissolved additional mineralogical phases, which might contribute to the Fe leachate. Moreover, the iron isotope composition of carbonate leachates was preserved without generating anomalous results. Hence, weak chemical leaches represent a reliable tool to study Fe isotopic composition of carbonate to understand how the Fe cycle was operating throughout Earth's history.

3.6.1 Introduction

The chemical evolution of Earth's oceans through time is largely recorded by sedimentary iron-bearing minerals (Konhauser et al., 2017). There is a general view that iron-bearing carbonates (*e.g.* siderite and ankerite) and associated iron formations reflect environmental conditions in which they formed, specifically related to anoxic and ferruginous seawater chemistry prior to the Great Oxidation Event (Holland, 2002). Siderite [$FeCO_3$] and ankerite [$Ca(Fe^{2+}, Mg, Mn,)CO_3$] represent the dominant and best-preserved carbonate minerals in iron formations (Fe-dolomite and calcite being less common), and have provided key insights into the biogeochemical cycles of iron and carbon throughout Earth's history (James, 1954; Holland, 1984; Klein and Beukes, 1989; Beukes and Klein, 1990; Kaufman et al., 1990; Klein, 2005; Konhauser et al., 2005, 2017; Raiswell and Canfield, 2012). Significant contributions towards the origin of Fe-carbonates in Precambrian rocks have been made, which rely to some extent in measuring the carbon and iron isotope compositions of these rocks.

Carbon and iron (Fe) isotope signatures are widely used as tools for understanding the processes of Fe-carbonate formation, such as the remineralization of organic matter to produce a depleted ^{13}C inorganic carbon source (Beukes et al., 1990; Fischer et al., 2009; Heimann et al., 2010; Johnson et al., 2013), the identification of biological reduction of Fe(III) minerals leading to the enrichment of light Fe isotope (i.e. ^{54}Fe) in the reduced Fe phase (Johnson et al., 2008a; Craddock and Dauphas, 2011a; McCoy et al., 2017), and the distinction of kinetic effects associated to mineral precipitation (Jiang and Tosca, 2019; Jiang et al., 2022). Carbon isotope composition in carbonates is easily measured in iron formations through gas extraction via reaction of

whole-rock powders with orthophosphoric acid (Becker and N. Clayton, 1972; Kaufman et al., 1991; Fischer et al., 2009; Busigny et al., 2013; Lebeau et al., 2014; Garcia et al., 2021). In contrast, the analysis of Fe isotope composition of distinct Fe-mineral phases such as carbonates, as well as oxides (*e.g*. magnetite, hematite), sulfides (*e.g*. locally pyrites), and minor phyllosilicates (*e.g*. stilpnomelane, riebeckite), is often more challenging. Previous studies have tackled this issue using micro-drilling techniques (Heimann et al., 2010), in-situ analysis (Steinhoefel et al., 2010; Marin-Carbonne et al., 2020), and chemical leaching procedures to target distinct minerals (Frost et al., 2007; Hyslop et al., 2008; von Blanckenburg et al., 2008). In the case of carbonates, this might be difficult using only micro-drilling techniques, particularly in IFs, where siderite and/or ankerite can be disseminated in chert matrixes closely associated and surrounded by Fe-oxides with varying sizes (*e.g.* nm to cm) (*e.g*. Kaufman et al, 1990).

A simple method used for isotope analysis of carbonates is weak acetic acid extractions, as illustrated for Sr isotopes measurement (Bayon et al., 2002). However, only a few studies have reported the effect of leaching carbonates on their Fe isotope composition (Hyslop et al., 2008; von Blanckenburg et al., 2008). Therefore, it is not clear if acetic acid can be efficiently applied for Fe isotope analysis of Fe-bearing carbonates. Importantly, when targeting only carbonates, all of the other mineral phases should be avoided. The sequential extraction of Fe-carbonates with sodium acetate has shown to be an efficient technique dissolving completely the carbonates contained in sediments (PC method; Poulton and Canfield, 2005). However, the PC method has also proven to be challenging particularly in carbonates exposed to higher metamorphic grades (Slotznick et al., 2018), although no Fe isotopic work has been done examining specifically the Fe speciation proxy in Precambrian rocks (only modern sediments were studied; Henkel et al., 2016). The present contribution aims at filling this gap by testing the effect of a simple

weak acetic acid leaching protocol on iron isotope fractionation in a siderite standard and three natural rock samples. The selected natural samples contain various mixtures of Fe minerals with different shapes and sizes, and include one Precambrian iron formation (Fe-oxide facies), as well as one Fe-rich and one Fe-poor carbonate. The protocols are shown to be reproducible, reliable and accurate, and can therefore be used as a tool for targeting carbonates in the ancient rock record without significantly dissolving other minerals. More importantly, this method provides a mean to identify Fe isotope signatures that could be masked when utilizing other mineral separation and/or dissolution methods.

3.6.2 Samples and method

The three samples analyzed in this study comprise an iron formation, and Fe-rich and Fe-poor carbonates from the 2.7 Ga-old Carajás Formation, Brazil, and were recently described in Rego et al. (2021). Additionally, a siderite powder (SID) from the deposits of La Mûre, France (Lebeau et al., 2014), was selected for our experiments. International geostandards used uniquely for Fe isotopic measurements includes BCR-2 (basalt, Columbia River, Oregon, USA – USGS), BHVO-2 (basalt, Kilauea, Hawaii, USA – USGS), AC-E (granite, Ailsa Craig Island, Scotland – SARM), IF-G (iron formation, Isua, Greenland – SARM), and an internal Fe standard referred to as ISVB (Institut de Physique du Globe de Paris - IPGP, France). All of the following procedures and measurements were performed at IPGP.

Leaching protocol

Approximately 40 mg of whole rock powder of iron formation (FD-55 463), Fe-rich (FD-55 521) and Fe-poor carbonates (FD-55 478) were digested in a pre-cleaned 15 ml polypropylene tube by adding 3 ml of ultra-pure acetic acid (HAc) with different concentrations (5%, 10%, and 20% v/v). In parallel, the procedure was also performed using 0.4 M HCl (Fig. 3.3). All the samples were left overnight at room temperature (12h), and centrifuged (6 min/5000 rpm) the next day. The clear supernatant was then transferred into acid-cleaned Savillex Teflon beakers, while the residues were washed three times with MilliQ H_2O, dried, and weighted to record any mass loss after digestion. The supernatant was evaporated, and subsequently digested with concentrated HNO_3 and HCl (2:1 volume ratio) and heated overnight at 100°C. Samples were evaporated the next day and were brought back into solution in 6 M HCl. The same complete procedure was applied to the siderite standard (SID), but only 4 mg of SID powder was used and digested in 3 ml of 5%, 10%, and 20% HAc, and in 5 ml of HCl 0.4M. At least two replicates were made for each treated sample.

Iron isotope analysis

Iron isotopic compositions were measured on the leachate fraction (*see above*) and on whole rock samples, including the siderite SID and international geostandards. In the case of whole rock measurements, approximately 10 to 20 mg of rock powder were dissolved with concentrated mixtures of HF, HCl, HNO_3 to ensure complete digestion and that all iron was in its ferric state.

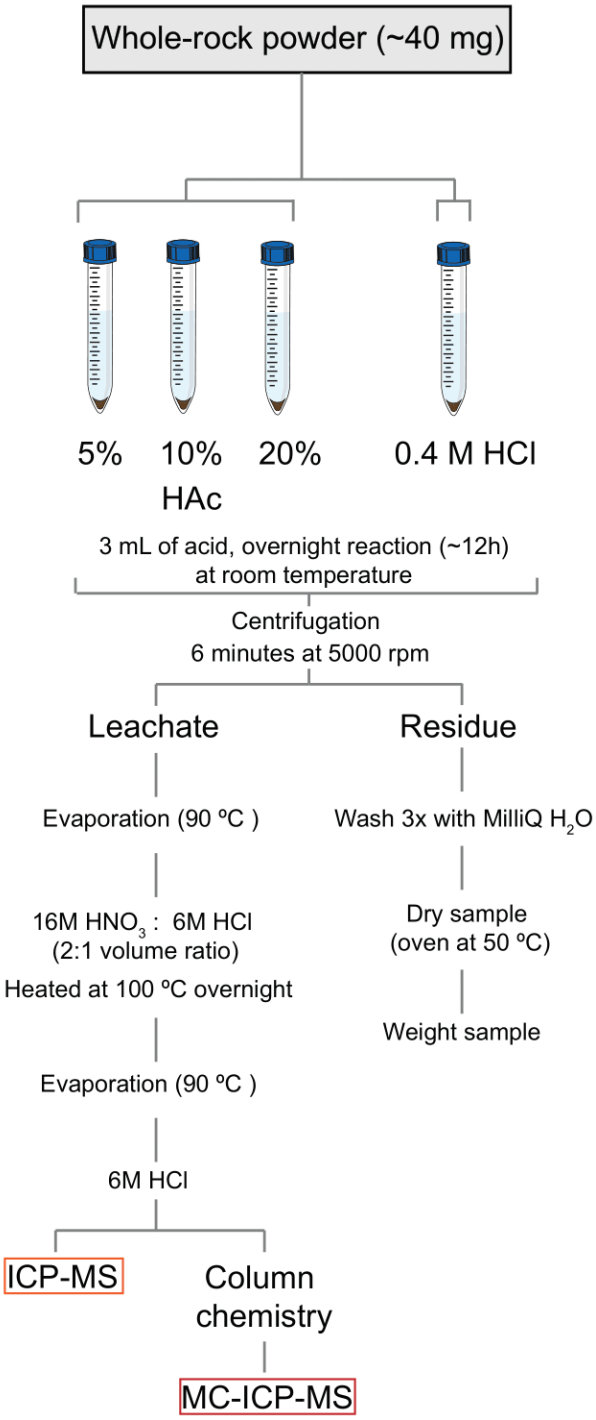

Figure 3. 3: Chemical leaching protocol utilized in this study

All samples were dissolved in 6M HCl prior to iron column chemistry. Iron was purified twice through anion exchange chromatography following an adaptation from Dauphas et al. (2004, 2009) which has been described in previous studies (*e.g.* Busigny et al., 2014, 2017, 2018). In brief, Bio-Rad Poly-Prep columns were filled with 1 ml anion exchange resin (AG1-X8 200-400 mesh chloride form). The resin was cleaned three times with 10 ml H_2O and 5 ml 1 M HNO_3. It was then preconditioned in HCl medium by running 10 ml H_2O, 10 ml 0.4 M HCl, 5 ml H_2O and 2 ml 6 M HCl. Matrix elements were eluted in 8 ml 6 M HCl, whereas Fe(III) was strongly adsorbed on the resin and quantitatively retained. Iron was subsequently eluted in 10 ml 0.4 M HCl.

Iron isotope compositions were measured using a ThermoFischer Neptune MC-ICP-MS (Multiple Collector Inductively Coupled Plasma Mass Spectrometer) at the Institut de Physique du Globe de Paris (IPGP). The samples were introduced into the mass spectrometer with a quartz cyclonic spray chamber and analyzed in 0.3 M HNO_3 at a concentration of ~2-3 ppm, which gave a signal of ~16 to 20 V on ^{56}Fe. The isotopes $^{54}Fe^+$, $^{56}Fe^+$, $^{57}Fe^+$ and $^{58}Fe^+$ were measured simultaneously, while $^{53}Cr^+$ and $^{60}Ni^+$ were also measured to monitor and correct any contribution on $^{54}Fe^+$ and $^{58}Fe^+$, respectively. Faraday cups were collecting masses 53, 54, 56, 57, 58, and 60 in Low 3, Low 2, C, High 1, High 2, and High 4, respectively. Iron isotopes were fully resolved from argide interferences ($^{40}Ar^{14}N^+$, $^{40}Ar^{16}O^+$, $^{40}Ar^{16}O^1H^+$) using the high-resolution mode of the Neptune (Weyer and Schwieters, 2003). Instrumental mass discrimination was corrected using the conventional sample-standard bracketing (SSB) approach (Rouxel et al., 2003). The $^{56}Fe/^{54}Fe$ and $^{57}Fe/^{54}Fe$ ratios were expressed in the usual δ notation in per mil (‰) as,

$$\delta^{56}Fe\ (‰) = [(^{56}Fe/^{54}Fe)_{sample} / (^{56}Fe/^{54}Fe)_{standard} - 1] \times 1000$$

$$\delta^{57}Fe\ (‰) = [(^{57}Fe/^{54}Fe)_{sample} / (^{57}Fe/^{54}Fe)_{standard} - 1] \times 1000$$

where the standard is IRMM-014, a pure synthetic Fe metal from the Institute for Reference Materials and Measurements (Taylor et al., 1992). The Fe blank level of the present procedure has been evaluated by systematic analyses of one blank in each sample series, prepared as described above but without any sample powder. The blank was always below 20 ng Fe, thus representing less than 0.3 % of the total Fe measured in sample solutions.

Table 3. 2: Measured iron isotopic composition of international geostandards

Standard	δ^{56}Fe (‰)[a]	±2SD[b]	δ^{57}Fe (‰)[a]	±2SD[b]
AC-E	0.324	0.006	0.505	0.052
	0.310	0.044	0.483	0.080
	0.323	0.016	0.497	0.052
BCR-2	0.071	0.028	0.116	0.056
BHVO-2	0.107	0.020	0.145	0.048
	0.103	0.042	0.178	0.052
IF-G (n=12)	0.613	0.021	0.895	0.076

Accuracy and analytical precision were determined by measuring international rock geostandards AC-E, BCR-2, BHVO-2, and IF-G as shown in Table 3.2, while long-term $\delta^{56/54}$Fe, $\delta^{57/54}$Fe, and $\delta^{57/56}$Fe measurements of IF-G and the internal standard ISVB are shown in Figure 3.4. The Fe isotopic compositions of the geostandards had external precision and accuracy always better than 0.046 ‰ for δ^{56}Fe and 0.08 ‰ for δ^{57}Fe (2SD) and were in good agreement with recommended values (Craddock and Dauphas, 2011b).

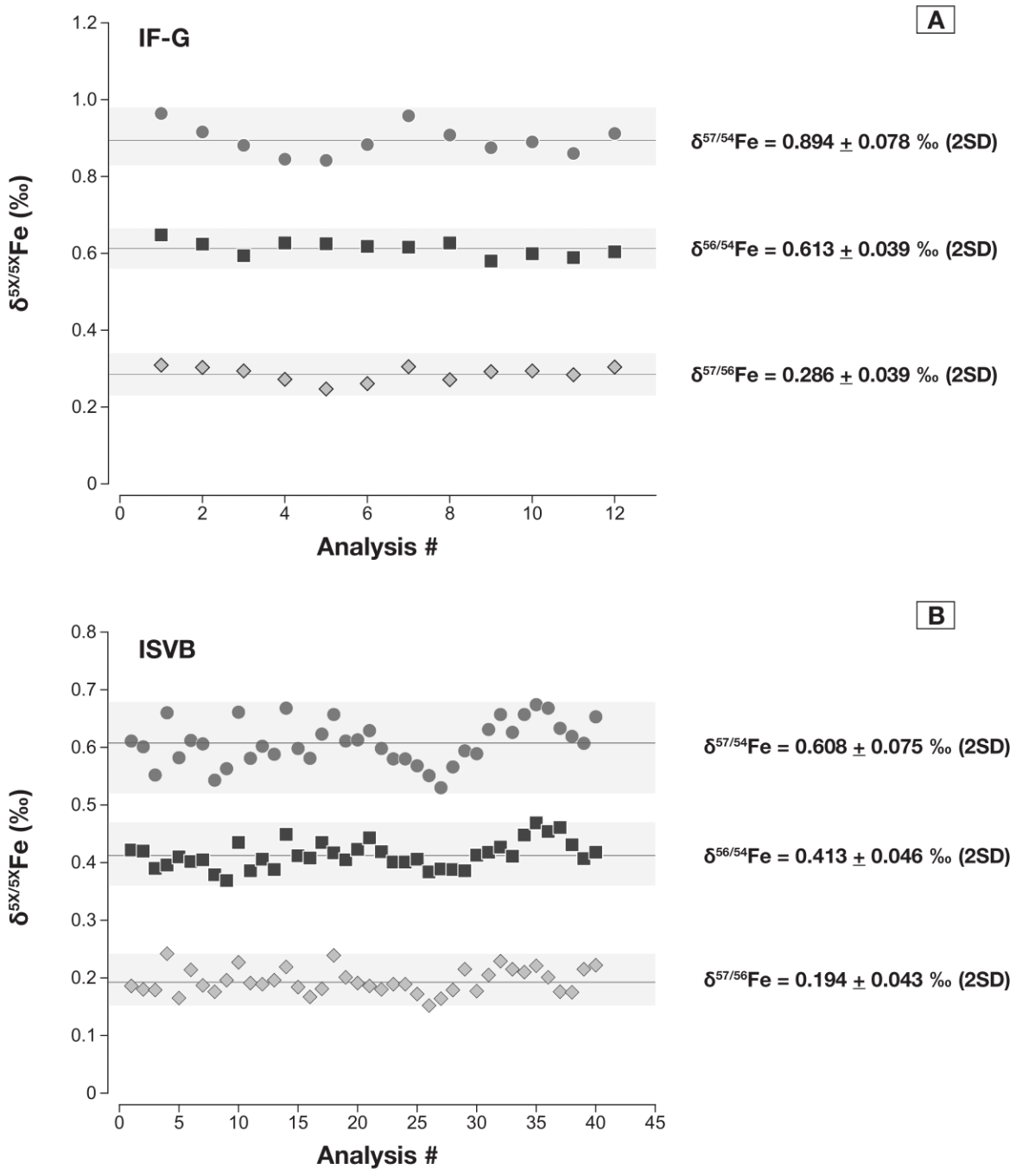

Figure 3. 4: Long-term measurements of the iron isotope compositions of IF-G geostandard and ISVB (internal Fe standard)

Iron concentration

Iron concentrations were obtained using an Agilent 7900 quadrupole ICP-MS at IPGP. Measurements were done using a collision-reaction cell with helium gas (5mL/min) to remove polyatomic interferences. A scandium internal-standard was injected after inline mixing with the samples to correct for signal drift and matrix effects. A set of iron calibration standards was analyzed to confirm and model (through simple linear regression) the linear relationship between signal and concentration. The model was then used to convert measured sample counts to concentrations. Reported uncertainties were calculated using error propagation equations and considering the combination of standard deviation on replicated consecutive signal acquisitions (n = 3), internal-standard ratio and blank subtraction. The non-linear term (internal-standard ratio) was linearized using a first-order Taylor series expansion to simplify error propagation.

Mineralogy

Mineralogical characterization was determined from thin sections observation by reflected and transmitted light microscopy at the Université de Montpellier. This was complemented by scanning electron microscopy (SEM) and energy-dispersive X-ray spectroscopy (EDS) on carbon-coated samples, utilizing a Zeiss EVO MA10 SEM for semi-quantitative *SEM-EDS* analysis at the Institut de Physique du Globe de Paris (IPGP). Standard operating conditions for SEM imaging and EDS analysis were 15 kV accelerating voltage, working distance of 12 mm, and 2 – 3 nA electron beam current (see detailed conditions in Rego et al., 2021).

Carbonate content

Approximately 40 mg, 10 mg, and 5 mg of sample powder was used for IF, Fe-rich, and Fe-poor carbonates, respectively. The powder was loaded in Labco Exetainer® sample vials, flushed with helium and treated with 100% phosphoric acid at 130°C for 2h to dissolve all carbonates, including siderite (Rosenbaum and Sheppard, 1986; Busigny et al., 2013; Lebeau et al., 2014). The produced CO_2 was measured using a continuous-flow mass-spectrometer (AP-2003) operated with helium as a carrier gas (Lebeau et al., 2014). Carbonate content in samples was estimated from the ion intensity of the CO_2 peak in the mass-spectrometer with a precision better than ±10% (2SD).

Magnetite separation

In order to test if acetic acid treatments dissolves, even partially, magnetite, a mineral commonly present with carbonates in Precambrian sediments, we separated ~10 mg of magnetite grains from two samples, including an iron formation and an Fe-carbonate (Fig. 3.5). Magnetite was separated from whole-rock powders by utilizing a neodymium-iron-boron magnet (disc magnet with a diameter of 5 mm and a height of 5 mm). Whole-rock samples were washed in a pre-cleaned 15 ml polypropylene tubes at least 10 times using MilliQ H_2O and magnetite was removed simultaneously with an aid from the magnet. The non-magnetic fraction was discarded and the sample was washed until all the magnetic fraction was separated. After washing, the magnetic fraction was dried in an oven at 50°C overnight. The following day, the same leaching protocol described previously (5%, 10%, 20% HAc; 12h reaction, room temperature; see section 2.1) was applied to the magnetite grains. The dissolution was monitored by measuring Fe concentration by ICP-MS in the supernatant solution after the leaching treatment.

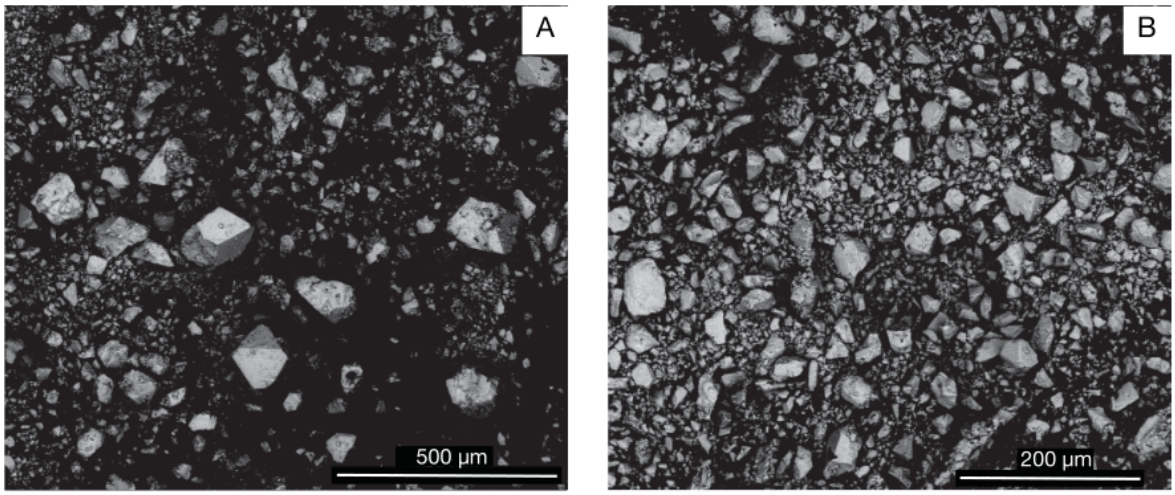

Figure 3. 5: Magnetite grains of varying sizes removed from (A) an iron formation sample and from (B) Fe-rich carbonate sample.

3.6.3 Results

As explained above, weak acid leaching protocols were tested on a siderite ($FeCO_3$) standard (Lebeau et al., 2014) and in Neoarchean (~2.74 Ga) iron formation and carbonate samples from Carajás, Brazil (Rego et al., 2021). The results of the leaching experiments and whole rock sample dissolution are reported in Tables 3.3 and 3.4. It includes sample's mass loss (wt.%) after each treatment, whole-rock carbonate content (%) determined from CO_2 extraction and measurement, the fraction of Fe-carbonate dissolved (%) calculated based on the Fe concentration in solution after leaching treatments (i.e. assuming that ankerite was the dissolved Fe-carbonate phase for all Neoarchean samples), and Fe isotope compositions of various leachates or bulk powder dissolutions. Additionally, acetic acid (HAc) leaching protocol was also performed on pure magnetite grains to identify any dissolution, which could bring a potential source of contamination to the carbonate fraction leached from natural samples (Table 3.5).

Siderite standard

The siderite standard was leached with three distinct HAc concentrations (*i.e.* 5 %, 10 %, and 20 % HAc) for 12 hours at room temperature. When treated with 5 % HAc, the mass loss ranged from 27.7 to 31.6 wt. % (average of 29.7 $\pm$ 2.69 %, n=2) while treatments with 10 and 20 % HAc induced a mass loss between 22.2 to 37.1 wt. % (average of 29.65 $\pm$ 10.54 %, n=2), and 33.3 to 59.3 wt. % (average of 46.3 $\pm$ 18.38 %, n=2), respectively (Table 3.3). Specifically, one sample treated with 20 % HAc had significantly larger mass loss (*i.e.* 59.3 wt. %) when compared to all other samples (Table 3.3). The average dissolved Fe-carbonate content for our siderite standard (Fe-carb$_{siderite}$) was calculated based on the amount of Fe measured in the leachate fraction after HAc treatments. The values were 23.95 $\pm$ 14.78 % Fe-carbonate$_{siderite}$ dissolved for 5 % HAc (n=2), 27.30 $\pm$ 9.48 % (n=2), and 31.30 $\pm$ 7.78 % Fe-carbonate$_{siderite}$ dissolved (n=2) for 10 % and 20 % HAc, respectively. A similar protocol was implemented utilizing 5 ml of 0.4 M HCl to leach the same siderite powder. All three replicates were almost completely digested with 80.6 to 101.81 % of dissolved siderite after a 96h treatment at room temperature (Table 3.3).

The average δ^{56}Fe value for the whole rock siderite standard was -0.33 $\pm$ 0.02 ‰ (n=2), indistinguishable from the leaching with 5 %, 10 %, and 20 % HAc, after 12h reaction time at room temperature (-0.30 $\pm$ 0.01 ‰ (n=2), -0.31 $\pm$ 0.02 ‰ (n=2), and -0.31 $\pm$ 0.02 ‰ (n=2), respectively). Moreover, siderite samples leached with 0.4M HCl after a 96h reaction time at room temperature, had an average δ^{56}Fe value of -0.32 $\pm$ 0.03 ‰ (n=3) (Fig. 3.6).

Table 3. 3: Results of various leaching protocols showing changes in mass loss, Fe dissolved in leachate, and iron isotopic compositions of the leachate fraction for specific carbonate phases. Literature data are added when available.

Acid treatments	Samples	Time (h)	Temp. (°C) [a]	Mass loss (wt. %) [b]	Fe-carbonate dissolved in leachate (%)[c]	δ^{56}Fe (‰)[d]	±2SD [e]	δ^{57}Fe (‰)[d]	±2SD [e]	References
5 % HAc	Siderite (SID)	12	20-21	31.6	13.5	-0.29	0.02	-0.44	0.03	This study
5 % HAc	Siderite (SID)	12	20-21	27.8	34.4	-0.30	0.02	-0.46	0.03	This study
10 % HAc	Siderite (SID)	12	20-21	22.2	34.0	-0.30	0.04	-0.48	0.06	This study
10 % HAc	Siderite (SID)	12	20-21	37.1	20.6	-0.33	0.02	-0.53	0.03	This study
10 % HAc	Dolomite	12	20-21		34.2					von Blanckenburg et al., 2008
10 % HAc	Stromatolitic calcite LN-01	12	20-21		54.7					von Blanckenburg et al., 2008
10 % HAc	Stromatolitic calcite BL-1	12	20-21		68.9					von Blanckenburg et al., 2008
10 % HAc	Ankerite	12	20-21		93.6					von Blanckenburg et al., 2008
20 % HAc	Siderite (SID)	12	20-21	33.3	25.8	-0.33	0.03	-0.50	0.04	This study
20 % HAc	Siderite (SID)	12	20-21	59.3	36.8	-0.30	0.01	-0.46	0.02	This study
20 % HAc	Siderite powder	24	40		61.5					Hyslop et al., 2008
0.4 M HCl	Siderite (SID)	96	20-21		101.81	-0.31	0.08	-0.49	0.18	This study
0.4 M HCl	Siderite (SID)	96	20-21		95.45	-0.35	0.05	-0.48	0.28	This study
0.4 M HCl	Siderite (SID)	96	20-21		80.06	-0.29	0.08	-0.42	0.09	This study
0.75 M HCl	Siderite powder	43	20-21		99.6					Hyslop et al., 2008
Whole rock/complete dissolution	Siderite (SID)					-0.31	0.08	-0.45	0.14	This study
Whole rock/complete dissolution	Siderite (SID)					-0.34	0.03	-0.53	0.10	This study

[a] Temperatures between 20 and 21°C are considered room temperature.
[b] Mass loss weight percent calculated by weighting the residue after leaching protocol.
[c] The amount of Fe-carbonate (i.e. siderite) dissolved calculated relative to the Fe content in the leachate solution. Fe concentrations were measured by ICP-MS.
[d] Iron isotopic (δ^{56}Fe and δ^{57}Fe) ratios are reported in per mil difference relative to iron metal standard IRMM-014.
[e] Analytical errors are reported as 2 standard-deviation (2SD).

Iron formation and carbonates

The studied samples consisting of IF, Fe-rich and Fe-poor carbonates from Carajás basin have been previously described in Rego et al. (2021) and the mineralogical assemblages were similar to those shown by Justo et al. (2020). Carbonates in IF facies in Carajás occur commonly as ankerite [$Ca(Fe^{2+},Mg,Mn)CO_3$] disseminated in a microcrystalline quartz (chert) matrix (Fig. 3.7A,B). Other Fe-mineral phases in IF include abundant euhedral magnetite crystals, microscopic spheroidal hematite, minor Fe-silicates, and very few pyrites (Rego et al., 2021). Iron-rich and iron-poor carbonate rock samples show higher carbonate content, but differ from each other particularly by the occurrence of calcite [$CaCO_3$] and framboidal pyrites [FeS_2] within Fe-poor facies (Figs 3.7C and 3.8).

Table 3. 4: Variations in mass loss, amount of Fe dissolved, and iron isotopic compositions for different acid leachates using rock matrix (IF, Fe-rich, and Fe-poor carbonates), including carbonate content measured on whole-rock.

Sample	Lithology	Acid treatment	Mass loss (wt. %)	Fe-carbonate dissolved in leachate (%)[a]	Carbonate (calcite %)[b]	Carbonate (ankerite %)[b]	Carbonate (siderite %)[b]	$\delta^{56}Fe$ (‰)[c]	±2SD[d]	$\delta^{57}Fe$ (‰)[c]	±2SD[d]
FD55 463.52	IFs	5 % HAc	18.4	9.72	9.34	9.41	10.83	0.14	0.04	0.23	0.06
		5 % HAc	13.6	8.48	9.44	9.52	10.96	0.15	0.08	0.22	0.09
		10 % HAc	13.0	6.56				0.14	0.04	0.16	0.06
		10 % HAc	18.0	6.80				0.17	0.06	0.23	0.07
		20 % HAc	12.9	5.60				0.12	0.06	0.18	0.09
		20 % HAc	13.8	6.83				0.14	0.06	0.20	0.12
		0.4 M HCl	38.2					0.20	0.05	0.31	0.08
FD55 521.63	Fe-rich carb.	5 % HAc	28.5	26.88	25.12	25.32	29.14	-0.74	0.06	-1.12	0.06
		5 % HAc	28.2	48.31	24.71	24.91	28.67	-0.73	0.07	-1.10	0.08
		10 % HAc	27.2	35.78				-0.70	0.03	-1.06	0.08
		10 % HAc	27.7	39.33				-0.70	0.04	-1.05	0.06
		20 % HAc	29.1	36.65				-0.73	0.04	-1.06	0.07
		20 % HAc	27.4	35.87				-0.71	0.05	-1.06	0.11
		0.4 M HCl	32.9					-0.67	0.06	-1.00	0.08

FD55 478.03	Fe-poor carb.	5 % HAc	55.3	35.69	61.81	62.30	71.70	-0.15	0.05	-0.22	0.07
		5 % HAc	56.7	41.80	51.54	51.82	59.63	-0.16	0.07	-0.20	0.10
		10 % HAc	58.0	39.34				-0.16	0.02	-0.29	0.03
		10 % HAc	59.0	46.82				-0.14	0.02	-0.20	0.05
		20 % HAc	60.1	43.97				-0.14	0.03	-0.23	0.07
		20 % HAc	58.6	45.22				-0.17	0.07	-0.26	0.11
		0.4 M HCl	54.8					-0.19	0.06	-0.27	0.10
		0.4 M HCl	64.3					-0.19	0.04	-0.27	0.07

[a] The amount of Fe-carbonate (i.e. ankerite) dissolved calculated relative to the Fe content in the leachate solution. Fe concentrations were measured by ICP-MS.
[b] Carbonate content measured on whole-rock in AP-2003 after reaction with 100% orthophosphoric (2h at 130°C). Relative error of ± 10 wt.% established after measuring siderite standard (average=103.3 ± 9.5 wt.% ,1sd, n=3).
[c] Iron isotopic ($\delta^{56}Fe$ and $\delta^{57}Fe$) ratios are reported in per mil difference relative to iron metal standard IRMM-014.
[d] Analytical errors are reported as 2 standard-deviation (2SD).

In order to target only carbonate phases, we applied the same leaching protocol (*i.e*. 5%, 10% and 20% HAc and 0.4M HCl) among three distinct samples, including an IF (FD 55 - 463.55), Fe-rich (FD 55 - 521.63) and Fe-poor (FD 55 - 478.03) carbonate sample. The average mass loss after HAc treatment (5%, 10%, and 20% HAc, 12h, room temperature) for the IF sample was 14.95 ± 2.5 wt.% (n=6), while Fe-rich and Fe-poor carbonate samples lost 28.02 ± 0.7 wt.% (n=6) and 57.95 ± 1.7 wt.% (n=6) of their masses, respectively (Table 3.4). The amount of Fe-carbonate dissolved after HAc treatment, here considering that carbonates were ankerite ($Fe\text{-}carbonate_{ankerite}$), was lower for the IF sample, ranging from 5.60 to 9.72% (average of 7.3 ± 1.5 % n=6), and higher for Fe-rich and Fe-poor carbonates, varying between 26.88 to 48.31% (average of 37.1 ± 6.9 %, n=6), and 35.69 to 46.82% (average of 42.1 ± 4.1 %, n=6), respectively. Additionally, samples treated with 0.4M HCl with the same experimental conditions (12h at room temperature) showed higher mass loss, particularly the IF sample. Iron formation and Fe-rich carbonate samples lost 38.2 wt.% and 32.9 wt.% of their masses, respectively, while Fe-poor carbonate sample lost up to 64.3 wt.% of its mass (Table 3.4). The carbonate content estimated from CO_2 measurements of IFs and Fe-rich carbonates was 9.5 ± 0.08 %

(average, n=2) and 25.12 + 0.29 % (average, n=2), respectively. These values were calculated by assuming that ankerite [$Ca(Fe^{2+},Mg,Mn)CO_3$] is the dominant carbonate phase in those samples. In Fe-poor carbonates, calcite content increases, and carbonate estimates based on CO_2 extraction averages 56.68 $\pm$ 7.26 % $CaCO_3$ (n=2).

The iron isotope composition of IF leachates treated with 5%, 10%, and 20% HAc varied between +0.12 ‰ to +0.17 ‰ with an average of +0.14 $\pm$ 0.02 ‰ (n=6), slightly lighter compared to 0.4 M HCl treatment that showed a $\delta^{56}Fe$ value of +0.20 $\pm$ 0.05 ‰ (Table 3.4, Fig. 3.9). Iron-rich carbonate leached with HAc displayed $\delta^{56}Fe$ values averaging -0.72 $\pm$ 0.02 ‰ (n=6), again slightly lighter compared to the HCl treatment (*i.e.* $\delta^{56}Fe$ value of -0.67 $\pm$ 0.06 ‰). In contrast, the iron-poor carbonate sample had moderately heavier iron isotopic composition for HAc leachates (*e.g.* average $\delta^{56}Fe$ value of -0.15 $\pm$ 0.01 ‰, n=6) compared to the HCl leachate (*e.g.* $\delta^{56}Fe$ = -0.19 $\pm$ 0.01 ‰, n=2, Table 3.4, Fig. 3.9).

Magnetite dissolution

Magnetite grains treated with 5% and 10% HAc at room temperature for 12 hours showed a negligible fraction of Fe in their leachate solution, ranging from 0.003% to 0.08% of Fe with an average of 0.04 $\pm$ 0.04 % Fe (n=3) after both treatments (Table 3.5).

Table 3. 5: Magnetite dissolution tests with 5% and 10% acetic acid (HAc).

Sample	Treatment	Weight (mg)[a]	Fe in leachate (%)[b]
Magnetite 1	5 % HAc, 25°C, 12h	11.2	0.04
Magnetite 2	5 % HAc, 25°C, 12h	7.1	0.003
Magnetite 3	10 % HAc, 25°C, 12h	9.1	0.08

[a] weight of sample loaded for magnetite dissolution experiment (acetic acid volume was 5 mL)

[b] Fe in leachate corresponds to the fraction of Fe expressed relative to total Fe (calculated from the magnetite mass and assuming a pure Fe_3O_4).

3.6.4 Discussion

Partial dissolution of Fe-carbonate standard but preservation of its Fe isotope composition

We tested the acetic acid leaching protocol on a siderite ($FeCO_3$) standard (Lebeau et al., 2014) with the aim of (i) estimating how much of the carbonate is being dissolved and (ii) determining if the Fe isotope composition of the dissolved fraction is representative of its whole rock composition. There was no significant mass loss variation (22.2 wt. % to 37.1 wt. %) for acid digestions with distinct HAc concentrations (Table 3.3). Although a single sample lost 59.3 wt. % of its mass when treated with 20 % HAc, this may be due to mass loss while washing, drying and weighting the sample (*i.e*. not related to siderite dissolution). Specifically, the amount of Fe-carbonate$_{siderite}$ dissolved, as calculated relative to the Fe concentration in the leachate fraction for this sample, was not significantly different from other samples. All HAc treatments (*e.g*. 5%, 10%, and 20 % HAc) yielded an average of 27.51 $\pm$ 9.2 % (n=6) of Fe-carbonate$_{siderite}$ dissolved in the leachate (Table 3.3), suggesting a partial digestion of siderite for all treatments. This is in agreement with previous estimates that performed similar tests (*e.g*. 10 % HAc digestion, 12h period, room temperature) in dolomitic carbonate (34.2 % Fe dissolved), however lower than expected when compared to Fe dissolved in stromatolitic calcite (57.4 %) and ankerite (93.6 %) (von Blanckenburg et al., 2008) (see literature data also compiled in Table 3.3). Interestingly, Hyslop et al. (2008) reported that siderite dissolution during longer time (24hr) and at higher temperature (40°C) was also partial (61.5%) (Table 3.3).

Altogether, the present and previous results indicate that carbonate mineralogy (composition, structure, grain size, porosity) has a strong control on how much of each mineral phase is being dissolved, and that variations in HAc concentration from 5% to 20% are less likely to change how much siderite is being dissolved under a 12h period at room temperature.

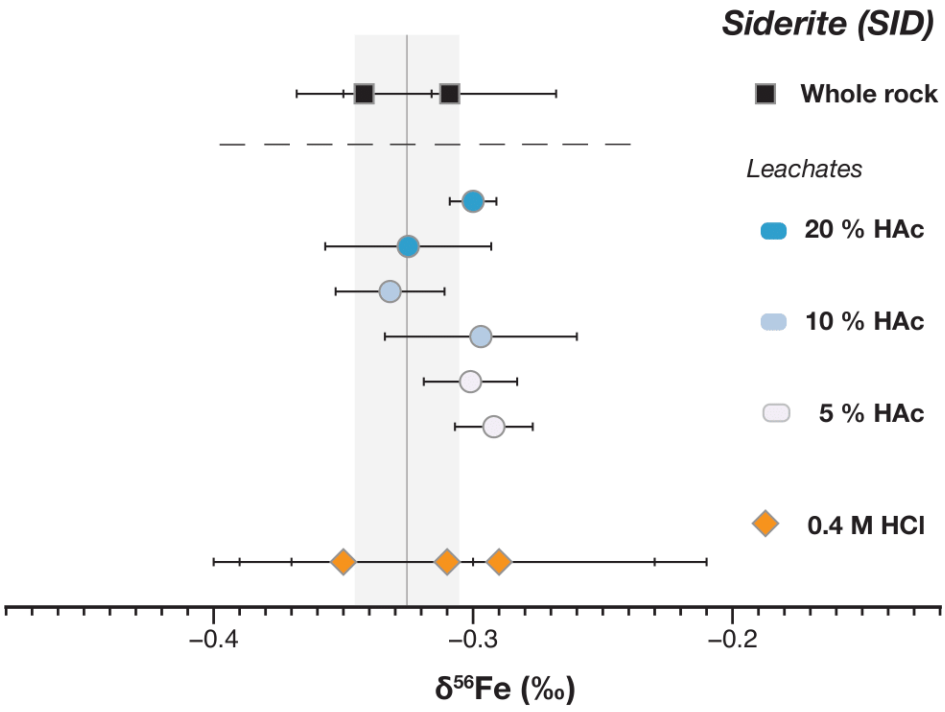

Figure 3. 6: Iron isotope ($\delta^{56}Fe$) composition of whole-rock siderite and leachates utilizing acetic acid (HAc) of different concentrations (5 to 20%) and 0.4M HCl. Error bars represent analytical errors reported as 2 standard-deviation.

Other dissolution techniques, such as the utilization of sodium (Na) acetate to target Fe-carbonates from modern and ancient sediments, have shown to dissolved ~100% of the Fe-carbonate phase in the sample (Poulton and Canfield, 2005). Only few studies have adapted this sequential extraction protocol with an aim to measure the Fe

isotope composition of different Fe-phases in modern and Phanerozoic sediments (Henkel et al., 2016; Havas et al., 2021). Despite showing a good extraction efficiency for Fe-carbonates, the Na-acetate method is significantly longer and cumbersome (*e.g.* adjusting pH, removing Na-acetate prior to Fe chromatography, etc.) compared with the proposed protocol. Therefore, identifying other efficient leaching techniques, such as weak HAc and HCl digestions, could be advantageous and suitable for Fe isotopic studies.

Even though our results support previous findings that diluted HAc does not achieve complete dissolution of siderite (*e.g.* Rongemaille et al., 2011), the remaining question is whether partial dissolution of siderite, as opposed to near complete dissolution (*see* Table 3.3), could still preserve the Fe isotopic composition of the bulk siderite. Given that a fraction of ~30% of Fe-carbonate was dissolved with different HAc concentrations, we show that the iron isotopic composition of the leachates (-0.30 $\pm$ 0.01 ‰ for 5% HAc; -0.31 $\pm$ 0.02 ‰ for 10% HAc; and -0.31 $\pm$ 0.02 ‰ for 20% HAc) had undistinguishable values within error from the whole-rock composition (-0.33 $\pm$ 0.02 ‰, n=2) (Fig. 3.6). Moreover, there is also no significant difference in Fe isotope composition between different acid treatments (Fig. 3.6). This shows that HAc (5 %, 10 % and 20 %) and 0.4 M HCl are capable of leaching siderite and still preserve its Fe isotopic composition despite partial or almost complete dissolution of the Fe-carbonate phase. Finally, this will have implications particularly when applying the leaching protocol to powders from complex rock matrixes, in which the presence of other mineralogical phases (*e.g.* Fe-oxides, phyllosilicates) might challenge the precise targeting of carbonates.

Reliable iron isotope measurements of carbonates in natural samples from acetic acid leaching

In order to evaluate complete and/or partial carbonate dissolution in typical Archean samples, such as IF, Fe-rich and Fe-poor carbonates, we examine the results of three independent methods, and compare (i) carbonate content measured on whole-rock powders from CO_2 extraction with (ii) changes in mass loss determined after HAc leaching, and with (iii) the amount of Fe-carbonate estimated from Fe concentrations obtained in the leachate fraction (Table 3.4). The IF sample had a carbonate content of 9.5 $\pm$ 0.08 % (n=2) calculated for ankerite based on its whole-rock composition, and had a similar amount of Fe-carbonate$_{ankerite}$ determined from Fe in the leachate (*e.g.* average of 7.33 $\pm$ 1.5 %, n=6). This implies that most of the Fe-carbonates, predominantly ankerite as shown by petrographic work (Figs 3.7 and 3.8) (Justo et al., 2020; Rego et al., 2021), were dissolved. The average mass loss of 14.95 $\pm$ 2.5 wt. % (n=6) after HAc treatments was slightly higher when compared to the carbonate content and Fe-carbonate$_{ankerite}$ dissolution estimates. This difference may reflect additional dissolution of another phase (containing no Fe) and/or a systematic error associated to the mass loss estimate (*e.g.* by weighing the sample before treatment, weighing empty tubes, weighing samples after treatment, washing and removing solution after centrifugation, etc.). The relative uncertainty on carbonate content determination from mass loss may be high particularly in this sample because of its low carbonate content compare to other samples.

Iron-rich carbonate sample has a higher carbonate content of 25.12 $\pm$ 0.29 % (n=2) as determined from CO_2 production, close to the value of 28.02 $\pm$ 0.7 wt.% (n=6) estimated from its mass loss after HAc treatment (Table 3.4). This suggests again that most carbonates were dissolved after HAc treatment. However, the average fraction of

dissolved Fe-carbonate$_{ankerite}$ calculated based on the Fe concentration in the leachate was significantly higher, with a value of 37.14 $\pm$ 6.9 % (n=6).

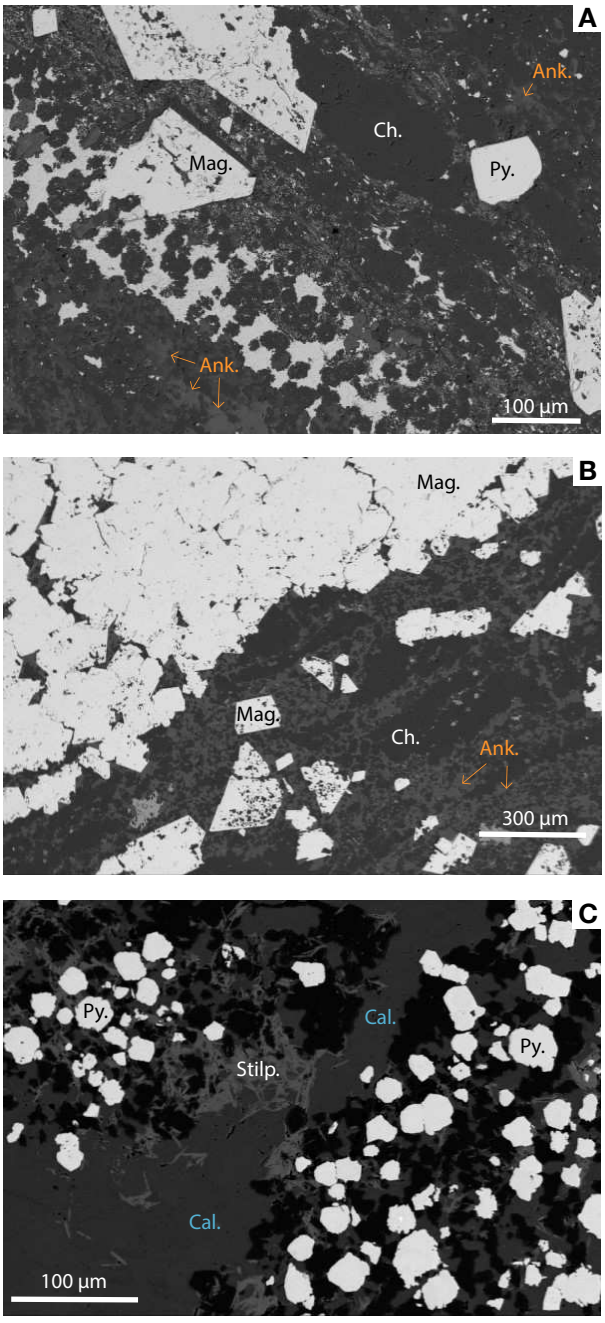

Figure 3. 7: Petrographic context of an (A) iron formation, (B) Fe-rich, and (C) Fe-poor carbonate samples showing ankerite (Ank.) disseminated in a chert matrix surrounded by magnetite (Mag.) grains (A and B), while calcite (Cal.) is more abundant in the Fe-poor sample also containing framboidal pyrites (Py.) and few stilpnomelane (Stilp.) (C).

This difference possibly results from the dissolution an additional Fe-bearing phase during acid treatments. Comparably, the HAc treatments dissolved all carbonates in the Fe-poor carbonate sample, as shown by indistinguishable values in measured carbonate content (*e.g.* 56.68 $\pm$ 7.26 %, n=2) and mass loss values (*e.g.* 57.95 $\pm$ 1.7 wt.%, n=6). Given that the Fe-poor carbonate sample contains a large amount of calcite in addition to ankerite (Figs 3.7 and 3.8; Rego et al., 2021), a lower fraction of dissolved Fe-carbonate$_{ankerite}$ determined from the HAc leachate is expected in this sample. This is supported by our data that show only an average of 42.14 $\pm$ 4.1 % (n=6) dissolved Fe-carbonate$_{ankerite}$ based on the Fe content in the leachate. Therefore, the present data suggest that HAc leachates dissolved most (if not all) carbonates, including calcite and Fe-carbonates among the IF, Fe-rich and Fe-poor studied samples.

Samples treated with 0.4 M HCl showed larger mass loss compared to HAc treatments, particularly for IF and Fe-rich carbonate samples. This implies that other mineralogical phases (distinct from carbonates) may have been dissolved. This inference is supported by the slightly heavier δ^{56}Fe values observed in the 0.4 M HCl leachates for IF (+0.20 $\pm$ 0.05 ‰) and Fe-rich carbonate (-0.67 $\pm$ 0.06 ‰) compared to average δ^{56}Fe values from HAc leachates (IF, +0.14 $\pm$ 0.02 ‰, n=6; Fe-rich carbonate, -0.72 $\pm$ 0.02 ‰, n=6; Fig. 3.9). In this case, partial dissolution of other phases, such as Fe-oxides which are often enriched in ^{56}Fe compared to Fe-carbonates (Wiesli et al., 2004; Johnson et al., 2008b; Frierdich et al., 2014a, 2019) may have contributed to a heavier isotopic composition in the HCl treatments. In contrast, iron-poor carbonates treated with 0.4 M HCl showed slightly lower δ^{56}Fe value compared to HAc treatments possibly reflecting partial dissolution of a depleted ^{56}Fe source. Pyrite is abundant in this Fe-poor carbonate sample

and represents a potential contributor to the dissolved iron pool (Fig. 3.7C; Rego et al., 2021). An important conclusion is that, despite a small difference in Fe isotope composition between HCl and HAc treatments, the values are relatively similar considering analytical error and isotopic variability between different samples (Table 3.4, Fig. 3.9).

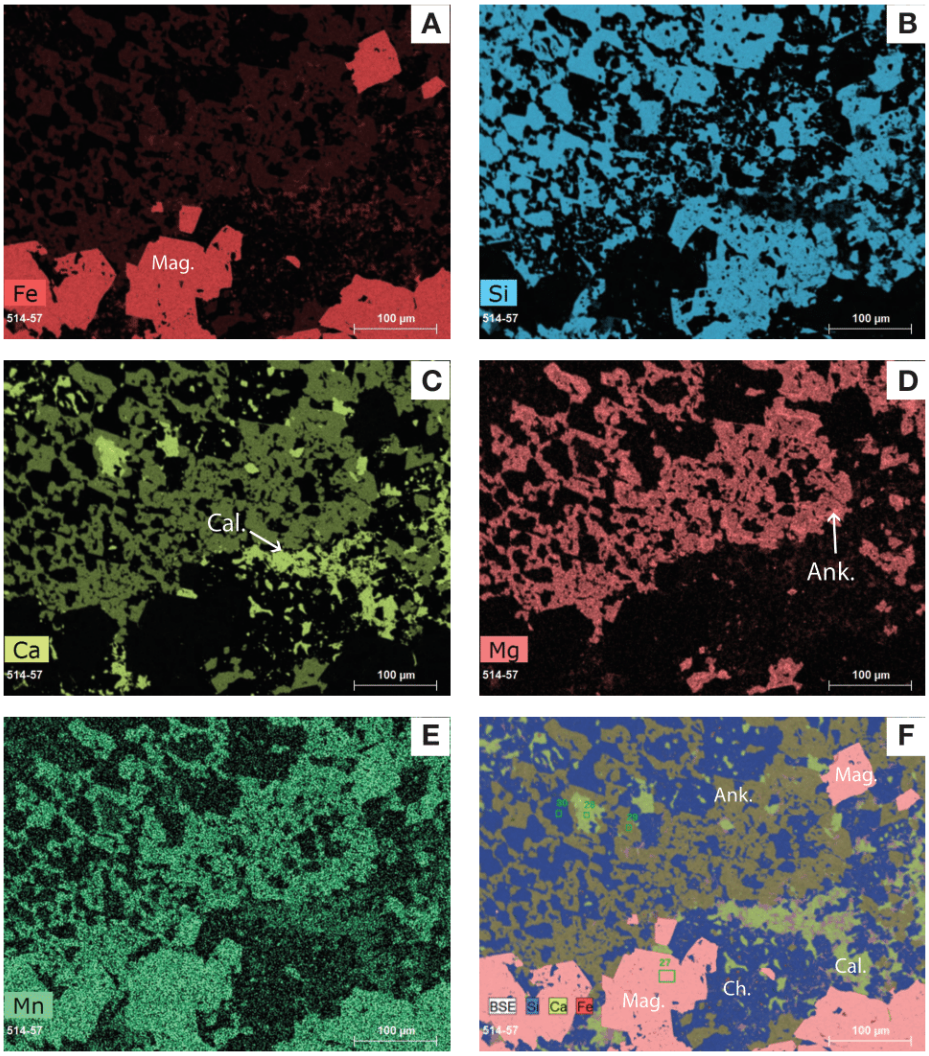

Figure 3. 8: Elemental map done by scanning electron microscopy (SEM) showing (A) Fe, (B) Si, (C) Ca, (D) Mg, (E) Mn, and (F) a composite showing the occurrence of ankerite and calcite together in the Fe-poor carbonate sample.

Importantly, no analytical artefact was observed related to carbonate dissolution utilizing 5, 10 or 20 % HAc treatments as illustrated with the lack correlation between the amount of Fe-carbonate dissolved and its δ^{56}Fe values (Fig. 3.10). A previous study observed anomalous Fe isotope fractionation related to dissolution of magnetite with 20 % HAc (Hyslop et al., 2008), however, von Blanckenburg et al. (2008) were not able to reproduce such anomalies. Additionally, we performed similar dissolution tests with HAc (5% and 10%) in pure magnetite grains of variable sizes (Fig. 3.4), and the results support previous findings in which only very low Fe content was measured in the leachate (*i.e.* < 1% Fe, Table 3.5) after treatment (von Blanckenburg et al. 2008).

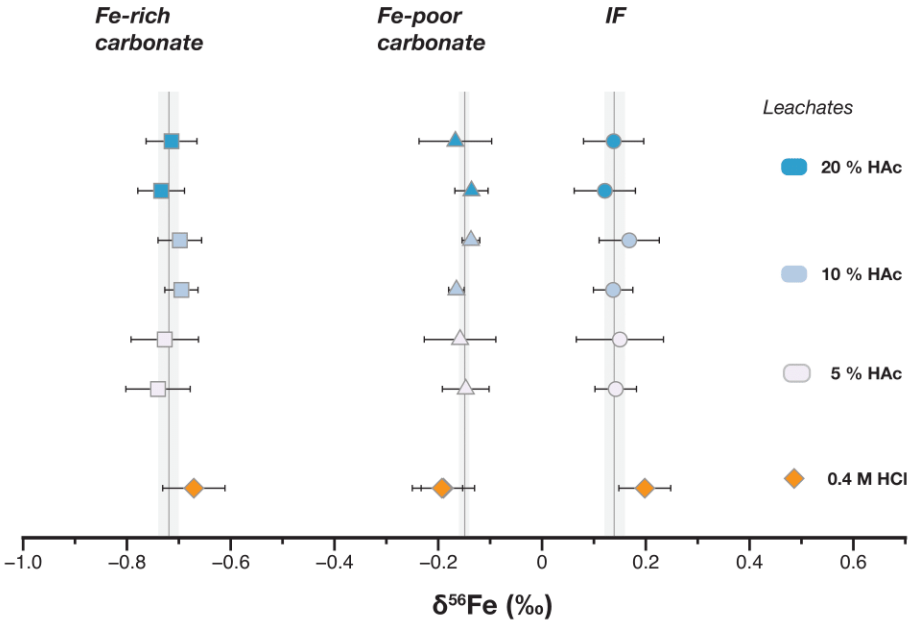

Figure 3. 9: Iron isotope (δ^{56}Fe) composition of leachates using acetic acid (HAc 5%, 10% and 20%) and 0.4M HCl from three natural samples, including an iron formation, Fe-rich and Fe-poor carbonate.

To summarize, the differences in HAc concentrations (5, 10, and 20%) do not change the amount of mass loss variation, the fraction of Fe-carbonate being dissolved,

and the iron isotope composition of IF, Fe-rich and Fe-poor carbonate leachates, at least when using the present protocol (*i.e.* room temperature, reaction time of 12 hours). Weak HAc dissolution is shown to achieve complete dissolution of carbonates in IF, Fe-rich and Fe-poor carbonate samples. Dissolution tests with 0.4 M HCl demonstrate higher mass loss compared to carbonate content, thus likely reflecting partial dissolution of other mineralogical phases (*e.g.* Fe-oxides, Fe-sulfides). Previous studies have shown that weak HAc attacks can dissolve most ankerite (93.6 % fraction of Fe in leachate) (von Blanckenburg et al., 2008), and even though only partial digestion of siderite is attained with 5 to 10 % HAc (*e.g.* Rongemaille et al., 2011; this study), we show here that its iron isotope composition is preserved without generating anomalous results. Accordingly, when targeting Fe isotope composition of Archean IF and Fe-carbonates samples, weak HAc should be preferentially used to avoid dissolution of other mineralogical phases. This method could represent an alternative to other mineral-specific extraction protocols (*e.g.* Poulton and Canfield, 2005; Henkel et al., 2016) and to *in-situ* measurements, and providing key insights into isotopic fractionation associated to Fe-carbonate formation processes and Fe biogeochemical cycle in the Precambrian ocean.

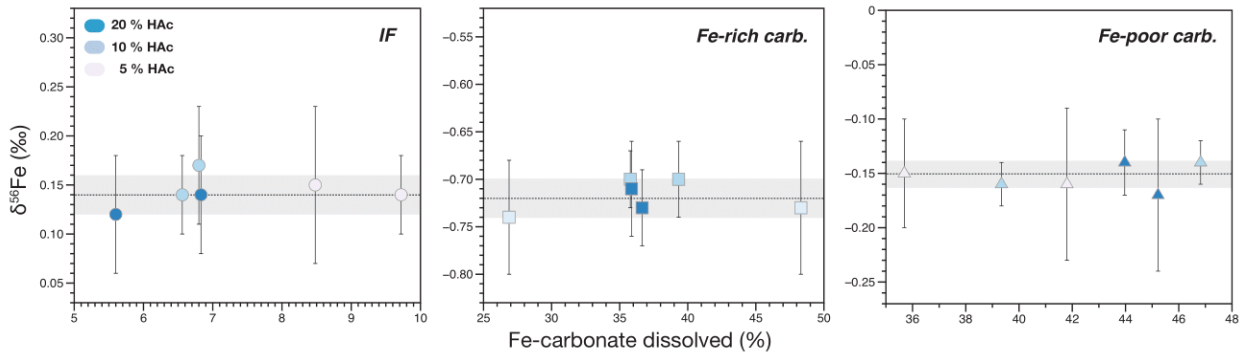

Figure 3. 10: Iron isotope ($\delta^{56}Fe$) composition of leachates using acetic acid (HAc 5%, 10% and 20%) from three natural samples (iron formation, Fe-rich and Fe-poor carbonate) and its relation to the amount of Fe-carbonate dissolved after each treatment. Analytical errors for each measurement is reported with error bars as 2 standard-deviation, while dashed line represents

the average $\delta^{56}Fe$ value among all HAc treatments and gray-shaded area represents the 1 standard-deviation.

Implications for paleo-environment reconstructions

By measuring the Fe isotope composition of carbonates, we can obtain insights into mineral formation processes, which could be related to either mineral precipitating from a primary seawater component or result from early to late diagenetic transformations (*e.g*. Johnson et al., 2013). The $\delta^{56}Fe$ values of Fe-carbonates extracted from IF, Fe-rich, and Fe-poor carbonates in Carajás Formation are +0.14 $\pm$ 0.02‰ (n=6), –0.74 $\pm$ 0.02‰ (n=6), and –0.15 $\pm$ 0.01‰ (n=6), respectively. Given that dissolved Fe(II) was hydrothermally sourced to the Carajás Basin (*e.g*. Rego et al., 2021) with similar isotopic composition of modern hydrothermal fluids ($-0.5 < \delta^{56}Fe_{hydrothermal\ fluid} < +0.1$; Sharma et al., 2001; Beard et al., 2003; Johnson et al., 2008; Bennett et al., 2009; Rouxel et al., 2016), Fe-carbonates (*i.e*. siderite) forming in equilibrium with Archean seawater are expected to have $\delta^{56}Fe$ values between ~–0.26 to –0.70‰ as determined experimentally (Wiesli et al., 2004). Therefore, iron-rich carbonate (ankerite dominated) with $\delta^{56}Fe$ values of –0.74 $\pm$ 0.02‰ (n=6) is consistent with a precipitation in equilibrium with Carajás' paleoseawater. Similarly, this could be the case for the Fe-poor carbonate with abundant calcite in its composition as shown by petrographic observations (Figs 3.7 and 3.8, Rego et al., 2021). In this sample, there is likely a higher contribution from Fe incorporated into calcite grains, thus reflecting a hydrothermal fluid-like composition as shown with heavier $\delta^{56}Fe$ values (*e.g*. –0.15 $\pm$ 0.01‰, n=6) compared to the Fe-rich carbonate sample. This suggests that carbonates from Fe-rich and Fe-poor samples could have formed in equilibrium with seawater, and hence be a proxy for past seawater conditions. Equivalent

light $\delta^{56}Fe$ values were observed in platform carbonates from the Hamersley Basin, Australia, (*e.g*. Wittenoon Dolomite; Craddock and Dauphas et al., 2011) and the Transvaal Basin, South Africa *(e.g*. Gamohaan Formation; Heimann et al., 2010).

In contrast, the positive $\delta^{56}Fe$ values measured in Fe-carbonates from IF ($+0.14 \pm 0.02‰$, n=6) are unlikely to be reflecting precipitation in isotopic equilibrium with Archean seawater, as demonstrated experimentally and theoretically (Schauble et al., 2001; Wiesli et al., 2004; Anbar et al., 2005; Blanchard et al., 2009). Iron-carbonates with a positive $\delta^{56}Fe$ value can be explained by ankerite and/or siderite precipitating from a pool of $Fe(II)_{aq}$ enriched in ^{56}Fe (Heimann et al., 2010; Craddock and Dauphas et al., 2011a). Different degrees of partial oxidation favored by photoferrotrophs likely induced the formation of Fe-oxides with positive $\delta^{56}Fe$ values in the Carajás Basin (Rego et al., 2021). An efficient reductive dissolution of Fe-oxides by microbial respiration (*i.e*. dissimilatory iron reduction, DIR) could explain an authigenic Fe(II) reservoir enriched in ^{56}Fe in sediment pore space where carbonates were likely precipitating from (Craddock and Dauphas, 2011a; Johnson et al., 2013). This DIR model supports the positive $\delta^{56}Fe$ values measured in carbonates from IFs and are in agreement with previous studies that also invoked microbial respiration as a mechanism favoring carbonate precipitation in pore water particularly within Fe-rich and IF samples (Johnson et al., 2008a, 2013; Heimann et al., 2010; Craddock and Dauphas, 2011a; Tong et al., 2021). Moreover, the lower content of total organic carbon (TOC) measured in IF samples compared to the Fe-rich and Fe-poor carbonate samples (*e.g*. Rego et al., 2021) supports oxidation of organic carbon coupled to the reduction of Fe(III) as a product of DIR. Collectively, Fe-carbonates from IF reflect microbial processes in sediment pore space (*i.e*. early diagenesis), whereas Fe-rich and Fe-poor carbonates record shallow seawater chemistry and surface-environmental conditions. Distinguishing between different Fe isotope signatures among

carbonates provides constrain on the Fe biogeochemical cycle during the Neoarchean, and shows that similar mechanism (*e.g*. microbial DIR) described from the geological record elsewhere (Australia and South Africa) was also operating in Carajás, Brazil ~2.74 Gyr ago.

3.6.5 Conclusions and Perspectives

We measured the Fe isotope composition of Fe-carbonate phases extracted by weak acetic acid leaching protocols. A series of test with distinct acids (*e.g*. HAc and HCl) at different concentrations performed on Fe-carbonate standard (*i.e.* siderite) and natural samples common in the Precambrian (*i.e.* iron formations and Fe-rich and –poor carbonates) have shown that partial and/or total dissolution may occur depending on the Fe-carbonate mineral being dissolved. Partial dissolution of siderite (~ 13 to 60 %) was observed using 5 to 20% acetic acid for 12h at room temperature. However, the Fe isotope composition of the partially dissolved leachate fraction was undistinguishable from the values measured for a total siderite dissolution (*i.e*. utilizing HCl for longer reaction times, or concentrated HCl-HNO_3 solution). Moreover, the same protocol achieved mostly complete dissolution of Fe-carbonates and carbonate (ankerite and calcite) from natural samples, while 0.4M HCl attacks was potentially dissolving other mineralogical phases.

We therefore recommend the utilization of 5 to 10% HAc digestions to target Fe-carbonates in natural samples, particularly those dominated by ankerite and calcite, to finally avoid substantial dissolution of other mineral phases. In the case of siderite-rich samples, we noticed that ~30 % dissolution of a pure siderite standard still preserves the

Fe isotope composition of its whole rock value. However, in the case of sequential extraction, one should have in mind that part of the siderite may remain in the residue and be cumulated to the next extraction stages. Despite other sequential extraction methods proven to be efficient (Poulton and Canfield, 2005), our acetic acid leaching protocol is less laborious/arduous and could be an alternative option to effectively target Fe-carbonates particularly for Fe isotopic studies trying to reconstruct ancient Fe cycling on Earth and elsewhere based on Fe-bearing minerals.

Chapter 3 is intended to be published in *Chemical Geology*

3.7 References

Anbar, A.D., Jarzecki, A.A., and Spiro, T.G., 2005, Theoretical investigation of iron isotope fractionation between Fe(H2O)63+ and Fe(H2O) 62+: Implications for iron stable isotope geochemistry: Geochimica et Cosmochimica Acta, v. 69, p. 825–837, doi:10.1016/j.gca.2004.06.012.

Bayon, G., German, C.R., Boella, R.M., Milton, J.A., Taylor, R.N., and Nesbitt, R.W., 2002, An improved method for extracting marine sediment fractions and its application to Sr and Nd isotopic analysis: Chemical Geology, v. 187, p. 179–199, doi:10.1016/S0009-2541(01)00416-8.

Beard, B.L., Johnson, C.M., Skulan, J.L., Nealson, K.H., Cox, L., and Sun, H., 2003, Application of Fe isotopes to tracing the geochemical and biological cycling of Fe: Chemical Geology, v. 195, p. 87–117, doi:10.1016/S0009-2541(02)00390-X.

Becker, R.H., and N. Clayton, R., 1972, Carbon isotopic evidence for the origin of a banded

iron-formation in Western Australia: Geochimica et Cosmochimica Acta, v. 36, p. 577–595, doi:10.1016/0016-7037(72)90077-4.

Bekker, A., Slack, J.F., Planavsky, N., Krapez, B., Hofmann, A., Konhauser, K.O., and Rouxel, O.J., 2010, Iron Formation: The Sedimentary Product of a Complex Interplay among Mantle, Tectonic, Oceanic, and Biospheric Processes: Economic Geology, v. 105, p. 467–508, doi:10.2113/gsecongeo.105.3.467.

Bennett, S.A., Rouxel, O., Schmidt, K., Garbe-Schönberg, D., Statham, P.J., and German, C.R., 2009, Iron isotope fractionation in a buoyant hydrothermal plume, 5°S Mid-Atlantic Ridge: Geochimica et Cosmochimica Acta, v. 73, p. 5619–5634, doi:10.1016/j.gca.2009.06.027.

Beukes, N.J., and Klein, C., 1990, Geochemistry and sedimentology of a facies transition - from microbanded to granular iron-formation - in the early Proterozoic Transvaal Supergroup, South Africa: Precambrian Research, v. 47, p. 99–139, doi:10.1016/0301-9268(90)90033-M.

Beukes, N.J., Klein, C., Kaufman, A.J., and Hayes, J.M., 1990, Carbonate Petrography, Kerogen Distribution, and Carbon and Oxygen Isotope Variations in an Early Proterozoic Transition from Limestone to Iron-Formation Deposition, Transvaal Supergroup, South Africa: Economic Geology, v. 85, p. 663–690.

Blanchard, M., Poitrasson, F., Méheut, M., Lazzeri, M., Mauri, F., and Balan, E., 2009, Iron isotope fractionation between pyrite (FeS2), hematite (Fe2O3) and siderite (FeCO3): A first-principles density functional theory study: Geochimica et Cosmochimica Acta, v. 73, p. 6565–6578, doi:10.1016/j.gca.2009.07.034.

von Blanckenburg, F., Mamberti, M., Schoenberg, R., Kamber, B.S., and Webb, G.E., 2008, The iron isotope composition of microbial carbonate: Chemical Geology, v. 249, p. 113–128, doi:10.1016/j.chemgeo.2007.12.001.

Busigny, V., Lebeau, O., Ader, M., Krapež, B., and Bekker, A., 2013, Nitrogen cycle in the Late Archean ferruginous ocean: Chemical Geology, v. 362, p. 115–130, doi:10.1016/j.chemgeo.2013.06.023.

Busigny, V., Marin-Carbonne, J., Muller, E., Cartigny, P., Rollion-Bard, C., Assayag, N., and Philippot, P., 2017, Iron and sulfur isotope constraints on redox conditions associated with the 3.2 Ga barite deposits of the Mapepe Formation (Barberton Greenstone Belt, South Africa): Geochimica et Cosmochimica Acta, v. 210, p. 247–266, doi:10.1016/j.gca.2017.05.002.

Busigny, V., Planavsky, N.J., Goldbaum, E., Lechte, M.A., Feng, L., and Lyons, T.W., 2018, Origin of the Neoproterozoic Fulu iron formation, South China: Insights from iron isotopes and rare earth element patterns: Geochimica et Cosmochimica Acta, v. 242, p. 123–142, doi:10.1016/j.gca.2018.09.006.

Busigny, V., Planavsky, N.J., Jézéquel, D., Crowe, S., Louvat, P., Moureau, J., Viollier, E., and Lyons, T.W., 2014, Iron isotopes in an Archean ocean analogue: Geochimica et Cosmochimica Acta, v. 133, p. 443–462, doi:10.1016/j.gca.2014.03.004.

Craddock, P.R., and Dauphas, N., 2011a, Iron and carbon isotope evidence for microbial iron respiration throughout the Archean: Earth and Planetary Science Letters, v. 303, p. 121–132, doi:10.1016/j.epsl.2010.12.045.

Craddock, P.R., and Dauphas, N., 2011b, Iron Isotopic Compositions of Geological Reference Materials and Chondrites: Geostandards and Geoanalytical Research, v. 35, p. 101–123, doi:10.1111/j.1751-908X.2010.00085.x.

Dauphas, N., Janney, P.E., Mendybaev, R.A., Wadhwa, M., Richter, F.M., Davis, A.M., Van Zuilen, M., Hines, R., and Foley, C.N., 2004, Hromatographic separation and multicollection-ICPMS analysis of iron. Investigating mass-dependent and -independent isotope effects: Analytical Chemistry, v. 76, p. 5855–5863,

doi:10.1021/ac0497095.

Dauphas, N., Pourmand, A., and Teng, F.Z., 2009, Routine isotopic analysis of iron by HR-MC-ICPMS: How precise and how accurate? Chemical Geology, v. 267, p. 175–184, doi:10.1016/j.chemgeo.2008.12.011.

Fischer, W.W., Schroeder, S., Lacassie, J.P., Beukes, N.J., Goldberg, T., Strauss, H., Horstmann, U.E., Schrag, D.P., and Knoll, A.H., 2009, Isotopic constraints on the Late Archean carbon cycle from the Transvaal Supergroup along the western margin of the Kaapvaal Craton, South Africa: Precambrian Research, v. 169, p. 15–27, doi:10.1016/j.precamres.2008.10.010.

Frierdich, A.J., Beard, B.L., Reddy, T.R., Scherer, M.M., and Johnson, C.M., 2014, Iron isotope fractionation between aqueous Fe(II) and goethite revisited: New insights based on a multi-direction approach to equilibrium and isotopic exchange rate modification: Geochimica et Cosmochimica Acta, v. 139, p. 383–398, doi:10.1016/j.gca.2014.05.001.

Frierdich, A.J., Nebel, O., Beard, B.L., and Johnson, C.M., 2019, Iron isotope exchange and fractionation between hematite (α-Fe2O3) and aqueous Fe(II): A combined three-isotope and reversal-approach to equilibrium study: Geochimica et Cosmochimica Acta, v. 245, p. 207–221, doi:10.1016/j.gca.2018.10.033.

Frost, C.D., von Blanckenburg, F., Schoenberg, R., Frost, B.R., and Swapp, S.M., 2007, Preservation of Fe isotope heterogeneities during diagenesis and metamorphism of banded iron formation: Contributions to Mineralogy and Petrology, v. 153, p. 211–235, doi:10.1007/s00410-006-0141-0.

Garcia, A.K., Cavanaugh, C.M., and Kacar, B., 2021, The curious consistency of carbon biosignatures over billions of years of Earth-life coevolution: ISME Journal, v. 15, p. 2183–2194, doi:10.1038/s41396-021-00971-5.

Havas, R., Savian, J.F., and Busigny, V., 2021, Iron isotope signature of magnetofossils and oceanic biogeochemical changes through the Middle Eocene Climatic Optimum: Geochimica et Cosmochimica Acta, v. 311, p. 332–352, doi:10.1016/j.gca.2021.07.007.

Heimann, A., Johnson, C.M., Beard, B.L., Valley, J.W., Roden, E.E., Spicuzza, M.J., and Beukes, N.J., 2010, Fe, C, and O isotope compositions of banded iron formation carbonates demonstrate a major role for dissimilatory iron reduction in ~2.5Ga marine environments: Earth and Planetary Science Letters, v. 294, p. 8–18, doi:10.1016/j.epsl.2010.02.015.

Henkel, S., Kasten, S., Poulton, S.W., and Staubwasser, M., 2016, Determination of the stable iron isotopic composition of sequentially leached iron phases in marine sediments: Chemical Geology, v. 421, p. 93–102, doi:10.1016/j.chemgeo.2015.12.003.

Holland, H.D., 1984, The Chemical Evolution of the Atmosphere and Oceans: Princeton, Princeton University Press, 598 p.

Holland, H.D., 2002, Volcanic gases , black smokers , and the Great Oxidation Event: Geochimica et Cosmochimica Acta, v. 66, p. 3811–3826, doi:0016-7037/02.

Hyslop, E.V., Valley, J.W., Johnson, C.M., and Beard, B.L., 2008, The effects of metamorphism on O and Fe isotope compositions in the Biwabik Iron Formation, northern Minnesota: Contributions to Mineralogy and Petrology, v. 155, p. 313–328, doi:10.1007/s00410-007-0244-2.

James, H.L., 1954, Sedimentary facies of iron-formation: Economic Geology, v. 49, p. 235–293.

Jiang, C.Z., Halevy, I., and Tosca, N.J., 2022, Kinetic isotope effect in siderite growth: Implications for the origin of banded iron formation siderite: Geochimica et Cosmochimica Acta, v. 322, p. 260–273, doi:10.1016/j.gca.2022.01.029.

Jiang, C.Z., and Tosca, N.J., 2019, Fe(II)-carbonate precipitation kinetics and the chemistry

of anoxic ferruginous seawater: Earth and Planetary Science Letters, v. 506, p. 231–242, doi:10.1016/j.epsl.2018.11.010.

Johnson, C.M., Beard, B.L., Klein, C., Beukes, N.J., and Roden, E.E., 2008a, Iron isotopes constrain biologic and abiologic processes in banded iron formation genesis: Geochimica et Cosmochimica Acta, v. 72, p. 151–169, doi:10.1016/j.gca.2007.10.013.

Johnson, C.M., Beard, B.L., and Roden, E.E., 2008b, The Iron Isotope Fingerprints of Redox and Biogeochemical Cycling in Modern and Ancient Earth: Annual Review of Earth and Planetary Sciences, v. 36, p. 457–493, doi:10.1146/annurev.earth.36.031207.124139.

Johnson, C.M., Ludois, J.M., Beard, B.L., Beukes, N.J., and Heimann, A., 2013, Iron formation carbonates: Paleoceanographic proxy or recorder of microbial diagenesis? Geology, v. 41, p. 1147–1150, doi:10.1130/G34698.1.

Justo, A.P., Dantas, E.L., Bau, M., Freitas-Silva, F.H., Santos, R.V., and Schorscher, J.H.D., 2020, Paleobasinal to band-scale REE + Y distribution in iron formations from Carajás, Amazon Craton, Brazil: Ore Geology Reviews, v. 127, p. 103750, doi:10.1016/j.oregeorev.2020.103750.

Kaufman, A.J., Hayes, J.M., and Klein, C., 1990, Primary and diagenetic controls of isotopic compositions of iron-formation carbonates: Geochimica et Cosmochimica Acta, v. 54, p. 3461–3473, doi:10.1016/0016-7037(90)90298-Y.

Kaufman, A.J., Hayes, J.M., Knoll, A.H., and Germs, G.J.B., 1991, Isotopic compositions of carbonates and organic carbon from upper Proterozoic successions in Namibia: stratigraphic variation and the effects of diagenesis and metamorphism: Precambrian Research, v. 49, p. 301–327, doi:10.1016/0301-9268(91)90039-D.

Klein, C., 2005, Some Precambrian banded iron-formations (BIFs) from around the world: Their age, geologic setting, mineralogy, metamorphism, geochemistry, and origin:

American Mineralogist, v. 90, p. 1473–1499, doi:10.2138/am.2005.1871.

Klein, C., and Beukes, N.J., 1989, Geochemistry and sedimentology of a facies transition — from limestone to iron-formation deposition in the early Proterozoic Transvaal Supergroup, South Africa: Economic Geology, v. 84, p. 1733–1774, doi:10.1016.

Konhauser, K.O. et al., 2017, Iron formations: A global record of Neoarchaean to Palaeoproterozoic environmental history: Earth-Science Reviews, v. 172, p. 140–177, doi:10.1016/j.earscirev.2017.06.012.

Konhauser, K.O., Newman, D.K., and Kappler, A., 2005, The potential significance of microbial Fe(III) reduction during deposition of Precambrian banded iron formations: Geobiology, v. 3, p. 167–177.

Lebeau, O., Busigny, V., Chaduteau, C., and Ader, M., 2014, Organic matter removal for the analysis of carbon and oxygen isotope compositions of siderite: Chemical Geology, v. 372, p. 54–61, doi:10.1016/j.chemgeo.2014.02.020.

Marin-Carbonne, J. et al., 2020, In Situ Fe and S isotope analyses in pyrite from the 3.2 Ga Mendon Formation (Barberton Greenstone Belt, South Africa): Evidence for early microbial iron reduction: Geobiology, p. 1–20, doi:10.1111/gbi.12385.

McCoy, V.E., Asael, D., and Planavsky, N., 2017, Benthic iron cycling in a high-oxygen environment: Implications for interpreting the Archean sedimentary iron isotope record: Geobiology, v. 15, p. 619–627, doi:10.1111/gbi.12247.

Poulton, S.W., and Canfield, D.E., 2005, Development of a sequential extraction procedure for iron: implications for iron partitioning in continentally derived particulates: Chemical Geology, v. 214, p. 209–221, doi:10.1016/j.chemgeo.2004.09.003.

Raiswell, R., and Canfield, D.E., 2012, The iron biogeochemical cycle past and present: Geochemical Perspectives, v. 1, p. 1–232, doi:10.7185/geochempersp.1.1.

Rego, E.S., Busigny, V., Lalonde, S. V., Philippot, P., Bouyon, A., Rossignol, C., Babinski, M., and Cássia Zapparoli, A., 2021, Anoxygenic photosynthesis linked to Neoarchean iron formations in Carajás (Brazil): Geobiology, v. 19, p. 326–341, doi:10.1111/gbi.12438.

Rongemaille, E., Bayon, G., Pierre, C., Bollinger, C., Chu, N.C., Fouquet, Y., Riboulot, V., and Voisset, M., 2011, Rare earth elements in cold seep carbonates from the Niger delta: Chemical Geology, v. 286, p. 196–206, doi:10.1016/j.chemgeo.2011.05.001.

Rosenbaum, J., and Sheppard, S.M.F., 1986, An isotopic study of siderites dolomites and ankerites at high temperatures: Geochimica et Cosmochimica Acta, v. 50, p. 1147–1150, http://file//localhost(null)%0Apapers3://publication/uuid/60B174D1-916D-4D53-888A-37C2045CE5CD.

Rouxel, O., Dobbek, N., Ludden, J., and Fouquet, Y., 2003, Iron isotope fractionation during oceanic crust alteration: Chemical Geology, v. 202, p. 155–182, doi:10.1016/j.chemgeo.2003.08.011.

Rouxel, O., Toner, B.M., Manganini, S.J., and German, C.R., 2016, Geochemistry and iron isotope systematics of hydrothermal plume fall-out at East Pacific Rise 9°50′N: Chemical Geology, v. 441, p. 212–234, doi:10.1016/j.chemgeo.2016.08.027.

Schauble, E.A., Rossman, G.R., and Taylor, H.P., 2001, Theoretical estimates of equilibrium Fe-isotope fractionations from vibrational spectroscopy: Geochimica et Cosmochimica Acta, v. 65, p. 2487–2497, doi:10.1016/S0016-7037(01)00600-7.

Sharma, M., Polizzotto, M., and Anbar, A.D., 2001, Iron isotopes in hot springs along the Juan de Fuca Ridge: Earth and Planetary Science Letters, v. 194, p. 39–51, doi:10.1016/S0012-821X(01)00538-6.

Slotznick, S.P., Eiler, J.M., and Fischer, W.W., 2018, The effects of metamorphism on iron mineralogy and the iron speciation redox proxy: Geochimica et Cosmochimica Acta,

v. 224, p. 96–115, doi:10.1016/j.gca.2017.12.003.

Steinhoefel, G., Blanckenburg, F. Von, Horn, I., Konhauser, K.O., Beukes, N.J., and Gutzmer, J., 2010, Deciphering formation processes of banded iron formations from the Transvaal and the Hamersley successions by combined Si and Fe isotope analysis using UV femtosecond laser ablation: Geochimica et Cosmochimica Acta, v. 74, p. 2677–2696, doi:10.1016/j.gca.2010.01.028.

Strelow, F.W.E., 1980, Improved separation of iron from copper and other elements by anion-exchange chromatography on a 4% cross-linked resin with high concentrations of hydrochloric acid: Talanta, v. 27, p. 727–732, doi:10.1016/0039-9140(80)80166-4.

Taylor, P.D.P., Maeck, R., and De Bièvre, P., 1992, Determination of the absolute isotopic composition and Atomic Weight of a reference sample of natural iron: International Journal of Mass Spectrometry and Ion Processes, v. 121, p. 111–125, doi:10.1016/0168-1176(92)80075-C.

Tong, X. et al., 2021, Iron and carbon isotope constraints on the formation pathway of iron-rich carbonates within the dagushan iron formation, North China Craton: Minerals, v. 11, p. 1–20, doi:10.3390/min11010094.

Weyer, S., and Schwieters, J.B., 2003, High precision Fe isotope measurements with high mass resolution MC-ICPMS: International Journal of Mass Spectrometry, v. 226, p. 355–368, doi:10.1016/S1387-3806(03)00078-2.

Wiesli, R.A., Beard, B.L., and Johnson, C.M., 2004, Experimental determination of Fe isotope fractionation between aqueous Fe(II), siderite and “green rust” in abiotic systems: Chemical Geology, v. 211, p. 343–362, doi:10.1016/j.chemgeo.2004.07.002.

CHAPTER 4

4. Iron cycling in the Carajás Basin: a perspective from Neoarchean sediments.

This chapter is divided into two sections, which concerns (i) the source of Fe to the Carajás basin and discusses the main oxidizing mechanisms that allowed Neoarchean iron formations to be deposited in the Carajás Basin, and a second shorter section (ii) providing a characterization of the iron isotope composition of potentially Paleoproterozoic siltstones and shales located stratigraphically above the Fe-rich sediments.

4.1 Anoxygenic photosynthesis linked to Neoarchean iron formations in Carajás (Brazil)

Abstract

Microbial activity is often invoked as a direct or indirect contributor to the precipitation of ancient chemical sedimentary rocks such as Precambrian iron formations (IFs). Determining a specific metabolic pathway from the geological record remains a challenge however, due to a lack of constraints on the initial conditions and microbially-induced redox reactions involved in the formation of iron oxides. Thus, there is ongoing debate concerning the role of photoferrotrophy, that is the process by which inorganic carbon is fixed into organic matter using light as an energy source and Fe(II) as an electron donor,

in the deposition of IFs. Here, we examine ~2.74 Ga old Neoarchean IFs and associated carbonates from the Carajás Mineral Province, Brazil, to reconstruct redox conditions and to infer the oxidizing mechanism that allowed one of the world's largest iron deposits to form. The absence of cerium (Ce) anomalies reveals that conditions were pervasively anoxic during IF deposition, while unprecedented europium (Eu) anomalies implies that Fe was supplied by intense hydrothermal activity. A positive and homogeneous Fe isotopic signal in space and time in these IFs indicates a low degree of partial oxidation of Fe(II), which, combined with the presence of ^{13}C-depleted organic matter, point to a photoautotrophic metabolic driver. Collectively, our results argue in favor of reducing conditions during IF deposition and suggest anoxygenic photosynthesis as the most plausible mechanism responsible for Fe oxidation in the Carajás Basin.

Summary Statement

Iron Formations (IFs) deposited throughout the globe require an oxidizing mechanism to transform hydrothermally-sourced Fe(II) into Fe(III). Debate is ongoing concerning the role of anoxygenic photosynthesis in the deposition of IFs prior to the rise of atmospheric oxygen. We provide geochemical evidence for pervasively anoxic conditions with continuous hydrothermal influence during the deposition of the Carajás Mineral Province, the largest Neoarchean IFs worldwide. The carbon isotope composition of organic matter indicates the presence of autotrophic organisms. Together with Fe isotope data indicating only small degrees of oxidation of the Fe(II) pool, our results suggest that Fe-oxidizing bacteria were the main agent for iron oxidation via anoxygenic photosynthesis. This supports a strong role for photoferrotrophs during IF deposition

and reinforces their significance in the metabolic landscape prior to the Great Oxidation Event.

Key words: anoxygenic photosynthesis, Fe isotopes, iron formations, Neoarchean, Carajás

4.2 Introduction

The geological record preserves extensive deposits of iron-rich chemical sediments, referred to as iron formations (IFs). These rocks are characterized by a high content (>15 - 20%) of iron bearing-minerals, typically layered or massive, interbedded with silica and/or carbonate-rich layers that were deposited throughout the Precambrian (James, 1983; Klein, 2005). Over the past few decades, studies have employed the chemical and isotopic composition of IFs to constrain past environmental conditions (*e.g.* Planavsky et al., 2014; Satkoski et al., 2015) and to understand how the microbial iron cycle evolved alongside redox conditions through time (Rouxel et al., 2005; Johnson et al., 2008a; Heard and Dauphas, 2020). Even though there is still ongoing debate as to how IFs are formed, most models rely on either oxygenic and/or anoxygenic photosynthesis, or abiotic photochemical oxidation by UV radiation, as the main process that allowed ferrous iron [Fe(II)] to be oxidized and removed from ferruginous waters and subsequently deposited as mixed valence iron (oxyhydr)oxides and carbonates (Thompson et al., 2019) [see (Tosca et al., 2016) for alternative model]. A combination of experiments and thermodynamic models have shown that UV photo-oxidation of Fe(II) could have made important contributions to IF precipitation, but was possibly not a major oxidizing mechanism for the deposition of large IFs (Konhauser et al., 2007a;

Pecoits et al., 2015). If correct, these results would point to microbial activity, either through oxygenic or anoxygenic photosynthesis, as the main oxidizing mechanism (Konhauser et al., 2002; Kappler and Newman, 2004).

Recent studies have argued that anoxygenic photosynthesis could be the evolutionary predecessor of oxygenic photosynthesis (*e.g.* Blankenship et al., 2007; Fischer et al., 2016; Martin et al., 2018; Hamilton, 2019) and that photoferrotrophic microorganisms likely played a significant role in nutrient cycling as primary producers prior to the rise of atmospheric oxygen ~2.4 billion years (Ga) ago, the so-called the Great Oxidation Event (GOE) (Canfield et al., 2006; Holland, 2006; Jones et al., 2015; Thompson et al., 2017). Accordingly, the hypothesis that IF deposition may have been driven by oxidation of Fe(II) via anoxygenic photosynthesis has received significant attention, particularly to explain IF deposition during periods of low oxygen concentrations such as the Archean Eon (Widdel et al., 1993; Canfield et al., 2000; Farquhar et al., 2000; Konhauser et al., 2002). Photoferrotrophs utilize Fe(II) as an electron donor and light energy to fix inorganic carbon into biomass and produce Fe(III) as a metabolic by-product as illustrated by the following reaction:

$$CO_2 + 4Fe^{2+} + 11H_2O \xrightarrow{hv} \langle CH_2O \rangle + 4Fe(OH)_3 + 8H^+ \quad (1)$$

Despite observations of these organisms performing iron oxidation in modern environments (*e.g.* Archean analogs; Crowe *et al.*, 2008; Llirós *et al.*, 2015), and a vast bibliography arguing in favor of photoferrotrophy as a potential mechanism that allowed IFs to form under oxygen-free conditions (*e.g.* Croal et al., 2009; Johnston et al., 2009; Czaja et al., 2013, 2018; Gauger et al., 2015, 2016; Thompson et al., 2019), there is still little evidence reported from the geological record supporting Fe oxidation by photoferrotrophs. Here we combined Fe and C stable isotopes with trace element

analyses of two pristine drill cores intercepting well-preserved Neoarchean IFs from the Carajás Mineral Province, Brazil, and show that photoferrotrophs played a key role in IF deposition, particularly under anoxic and ferruginous conditions. Considering that the two drill cores investigated are 50 km away from each other, we suggest that anoxygenic photosynthesis was the main oxidizing pathway that allowed these rocks to form at the scale of the Carajás Basin, which is one of the major iron-rich deposit in Brazil.

4.3 Geological Setting

The Carajás Mineral Province (CMP) is located in the southeastern part of the Amazonian Craton, Brazil (Fig. 4.1A), and contains remarkable metallogenic diversity including world-class deposits of iron oxide-copper-gold (IOCG), large IFs, and Mn ore (Klein and Ladeira, 2002; Moreto et al., 2015b). The Carajás Basin, within the CMP (Fig. 4.1B), has a Mesoarchean (ca. 3.0 – 2.86 Ga) basement composed of mafic granulites, migmatites and metavolcanic rocks (Machado et al., 1991). The crystalline basement is overlain unconformably by Neoarchean and Paleoproterozoic volcano-sedimentary sequences from the Grão Pará Group that have undergone subgreenschist to low-greenschist facies metamorphism (Machado et al., 1991; Rosière et al., 2006; Krymsky et al., 2007b). The volcano-sedimentary sequences are composed initially by basalts and basaltic andesites of the Parauapebas Formation, while IFs from the Carajás Formation conformably overlie or are occasionally interlayered with the basalts, a typical characteristic of Algoma-type IFs (Klein and Ladeira, 2002; Dalstra and Guedes, 2004; Martins et al., 2017b). The main lithology comprising the Carajás Formation are banded iron formations alternating between iron-rich and chert layers, but, minor black shales and conglomeratic layers have also been reported (Cabral et al., 2013, 2017). These were

interpreted to have been deposited in a range of environments from shallow water, low energy environments, to deep and quiet water settings (Tolbert et al., 1971; Lindenmayer et al., 2001; Macambira and Schrank, 2002a; Ribeiro da Luz and Crowley, 2012).

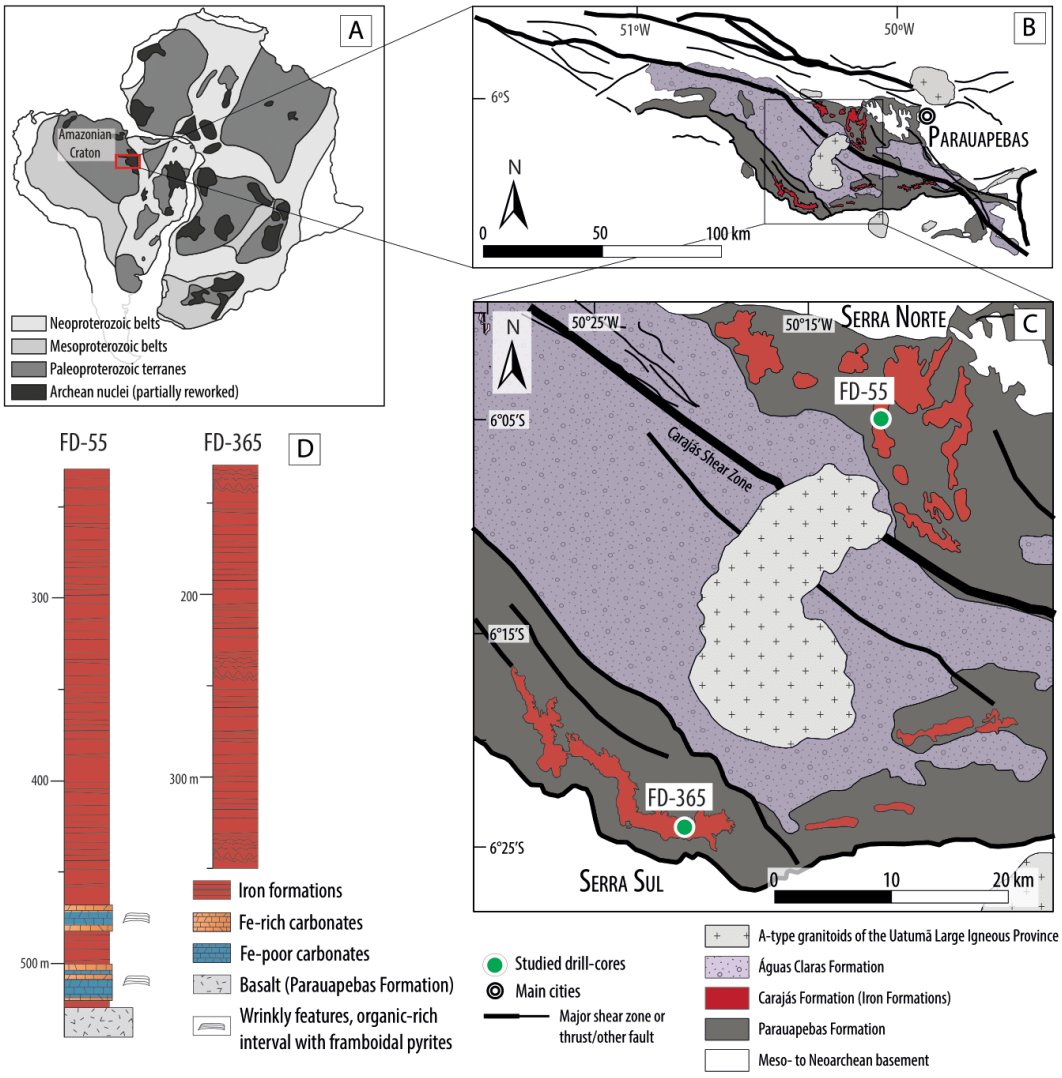

Figure 4. 1: Geological map of the Carajás Mineral Province within the Amazonian Craton (A) and its relation to the São Francisco and West-African Cratons, highlighting the main lithological components of the Carajás Basin (B,C) as well as the positions of the studied drill-cores FD-55 and FD-365 in Serra Norte and Serra Sul, respectively

A Late Archean to Early Paleoproterozoic sedimentary cover overlies the IFs, however its age is still debated (Rossignol et al., 2020). The depositional age of the Carajás IFs is well-constrained by U-Pb zircon ages of ca. 2.755-2.740 Ga in the basalts underlying and intercalating the IFs (Gibbs et al., 1986; Machado et al., 1991; Krymsky et al., 2007b) and U-Pb zircon ages from a possible tuff (2743 ± 11 Ma) and a dolerite dyke (2740 ± 8 Ma) cross-cutting the Carajás Formation (Trendall et al., 1998). Other age constraints include a Sm-Nd age of ca. 2593 ± 260 Ma in jaspilites from Serra Norte (Lindenmayer et al., 2001) and two Re-Os ages of 2661 ± 110 Ma and 2710 ± 38 Ma in black shales intercalated with IFs in Serra Sul (Cabral et al., 2013). The iron deposits have an average thickness of 200-250 m in the Serra Norte and 300 m in the Serra Sul regions (Beisiegel et al., 1973) and pristine drill cores intercepting the IFs were selected from each locality (FD-55 and FD-365, respectively), spanning a distance of 50 km, to examine spatial variations in the basin (Fig. 4.1C).

4.4 Material and Methods

4.4.1 Mineralogy

The mineralogy was determined using thin sections examined by reflected and transmitted light microscopy at the Université de Montpellier, complemented by scanning electron microscopy (SEM) and energy dispersive X-ray spectroscopy (EDS) using a Zeiss EVO MA10 SEM for semi-quantitative SEM-EDS analysis at the Institut de Physique du Globe de Paris (IPGP). Standard operating conditions for SEM imaging and EDS analyses were 15 kV accelerating voltage, working distance of 12 mm, and electron beam current of 2-3 nA. Samples were coated with C prior to analysis.

4.4.2 Major elements

Approximately 250 mg of rock powder were dissolved in closed teflon vessel (Savillex) at about 90°C for one day using 3 ml of concentrated HF (40%), 3 ml of concentrated HCl (32%), and 1 ml of concentrated HNO_3 (65%). Afterwards, 93 ml of H_3BO_3 aqueous solution (20 g/L H_3BO_3) were added to neutralize the excess HF. All reagents used were graded analytically. Elements were measured by Inductively Coupled Plasma-Atomic Emission Spectrometry (ICP-AES) using a Horiba Jobin Yvon® Ultima 2 spectrometer at the PSO/IUEM (Pôle Spectrométrie Océan, Institut Universitaire Européen de la Mer, Brest, France), following the analytical procedure of Cotten *et al.* (1995). The boron included in the solution was used as an internal standard. The precision and accuracy were evaluated using international standards IF-G, ACE, JB2 and WSE. The relative standard deviation was ≤1% for SiO_2 and ≤2% for the other major elements.

4.4.3 Trace elements

Between 80 and 100 mg of powdered samples were dissolved using a mixture of concentrated HF-HNO_3, evaporated to dryness and re-dissolved in Aqua Regia solution, all in PFA beakers heated to 80 ºC in a class 1000 clean lab. The residues were then re-dissolved in 5 mL 6M HCl overnight at 80 ºC and archived. Splits of 100 μL from the archive solutions were taken up in 5 mL ~0.28M HNO_3 for ICP-MS measurements. Two geostandards (BHVO-2 and CAL-S) and a procedural blank were also prepared with the samples. Elemental concentrations were measured with a HR-ICP-MS Element XR (Thermo Fisher Scientific) at the PSO/IUEM (Pôle Spectrométrie Océan, Institut Universitaire Européen de la Mer, Brest, France) using indium as an internal standard for

correcting drift of the signal during analysis. Concentrations were calibrated using serially-diluted mixtures of commercial NIST-traceable ICP-MS calibration standards (SPEX Certi-Prep) prepared gravimetrically for the analyses. Results on the geostandards were within the range published in the literature.

4.4.4 Fe isotopes

The method applied here for Fe isotope measurement was described in a previous contribution (Busigny et al., 2014). Approximately 10-30 mg of powdered samples were dissolved with mixtures of HF, HCl, HNO_3, and eventually additional $HClO_4$ depending on the sample composition, to ensure complete digestion and that all iron was in its ferric state. Iron was separated from other elements in the sample matrix by anion exchange chromatography (Strelow, 1980) to avoid mass bias in the mass spectrometer and to eliminate elements generating potential isobaric interferences on Fe masses. This procedure was repeated twice for each sample to assure that all matrix elements were eliminated (Dauphas et al., 2004a). Bio-Rad Poly-Prep columns were filled with 1 mL anion exchange resin (AG1-X8 200-400 mesh chloride form). The resin was cleaned three times with 10 ml H_2O and 5 ml 1 M HNO_3. It was then preconditioned in HCl medium by running 10 ml H_2O, 10 ml 0.4 M HCl, 5 ml H_2O and 2 ml 6 M HCl. Depending on the sample (IF or carbonates), half or one third (300 µl or 200 µl, respectively) of the sample solution was loaded on the column in 6 M HCl. Matrix elements were eluted with 8 ml 6 M HCl, whereas Fe(III) was strongly adsorbed on the resin and quantitatively retained. Fe was subsequently eluted in 10 ml 0.4 M HCl. The Fe blank level of the present procedure has been evaluated by systematic analyses of one blank in each sample series,

prepared as described above but without any sample powder. The blank was always below 30 ng Fe (average ~20 ng), thus representing less than 0.3 % of the bulk Fe.

Iron isotope compositions were measured using a Neptune Plus™ ThermoFischer MC-ICP-MS (Multiple Collector Inductively Coupled Plasma Mass Spectrometer) at the Institut de Physique du Globe de Paris (IPGP). The samples were analyzed in 0.3 M HNO_3 at a concentration of ~2 ppm Fe. Iron isotopes were fully resolved from argide interferences using the high-resolution mode of the Neptune (Weyer and Schwieters, 2003; Schoenberg and Von Blanckenburg, 2005). Instrumental mass discrimination was corrected for using the conventional sample-standard bracketing (SSB) approach (Rouxel et al., 2003). The $^{56}Fe/^{54}Fe$ and $^{57}Fe/^{54}Fe$ ratios were expressed in the usual δ notation in per mil (‰) as,

$$\delta^{56}Fe = [(^{56}Fe/^{54}Fe)_{sample} / (^{56}Fe/^{54}Fe)_{standard} - 1] \times 1000$$

$$\delta^{57}Fe = [(^{57}Fe/^{54}Fe)_{sample} / (^{57}Fe/^{54}Fe)_{standard} - 1] \times 1000$$

where the standard is IRMM-014, a pure synthetic Fe metal from the Institute for Reference Materials and Measurements (Taylor et al., 1992). Based on replicate analyses of IRMM-014 and international rock geostandard IF-G (a banded iron formation from Isua, Greenland), the external precision was always better than 0.05‰ for $\delta^{56}Fe$ and 0.08‰ for $\delta^{57}Fe$ (2σ). IF-G isotope measurements provided $\delta^{56}Fe$ and $\delta^{57}Fe$ values of 0.616 ± 0.025‰ and 0.886 ± 0.079‰, respectively (2σ; 8 measurements of four digested powders), in good agreement with recommended values (Dauphas et al., 2009; Craddock and Dauphas, 2011b).

4.4.5 Organic carbon isotopes

Total organic carbon (TOC) content and isotope composition were determined on decarbonated samples. Carbonates from powdered samples were removed using 6N HCl and a chromium chloride reducing solution for 2 h at 80 °C, following the method from Muller et al. (Muller et al., 2017). The residue was rinsed with distilled water and centrifuged several times until neutral pH was reached, and then dried at 50 °C for 2 days. After drying, the decarbonated powders were weighed and mass balance was done for subsequent calculation of the total organic C content. The powders were ground again in an agate mortar to avoid any heterogeneity related to the decarbonation procedure. Aliquots of dried decarbonated samples (50 to 100 mg) were weighed and sealed in tin capsules. All capsules were analyzed on a Flash EA1112 elemental analyzer coupled to a Thermo Finnigan Deltaplus XP mass-spectrometer via a Conflo IV interface under a helium continuous flow. Three internal standards, calibrated against international standards, were used to calculate the $\delta^{13}C$ values of all samples. Standards were measured every 6 samples to monitor and correct for a potential drift. Blanks were evaluated with empty capsules, yielding negligible contribution to the total signal. Replicate analyses on standards gave an external precision better than ± 0.1‰ (1σ). Five different amounts of an internal standard were used to estimate total organic C content of the samples. The data were reported using the conventional δ unit (in permil) with respect to the V-PDB standard, such as,

$$\delta^{13}C_{org} = [(^{13}C/^{12}C)_{sample} / (^{13}C/^{12}C)_{standard} - 1] \times 1000$$

At least three replicate analyses of each sample were performed for $\delta^{13}C_{org}$ measurements, but only the average values are provided herein. The reproducibility on samples TOC

content and $\delta^{13}C_{org}$ values was always better than ± 0.3 wt.% (1σ) and ± 0.4‰ (1σ), respectively.

4.5 Results

The two cores studied (FD55 and FD365) consist of finely laminated jaspilites formed by mm-scale laminae of chert (*e.g.* microcrystalline quartz) intercalated with euhedral magnetite and red jasper. Spherulitic hematite and minor amounts of ankerite occur disseminated in the chert matrix (Fig. 4.2, A-C). A major difference between the two cores is the occurrence of two main carbonate intervals present only in core FD-55, that are so far the oldest carbonates reported in South America.

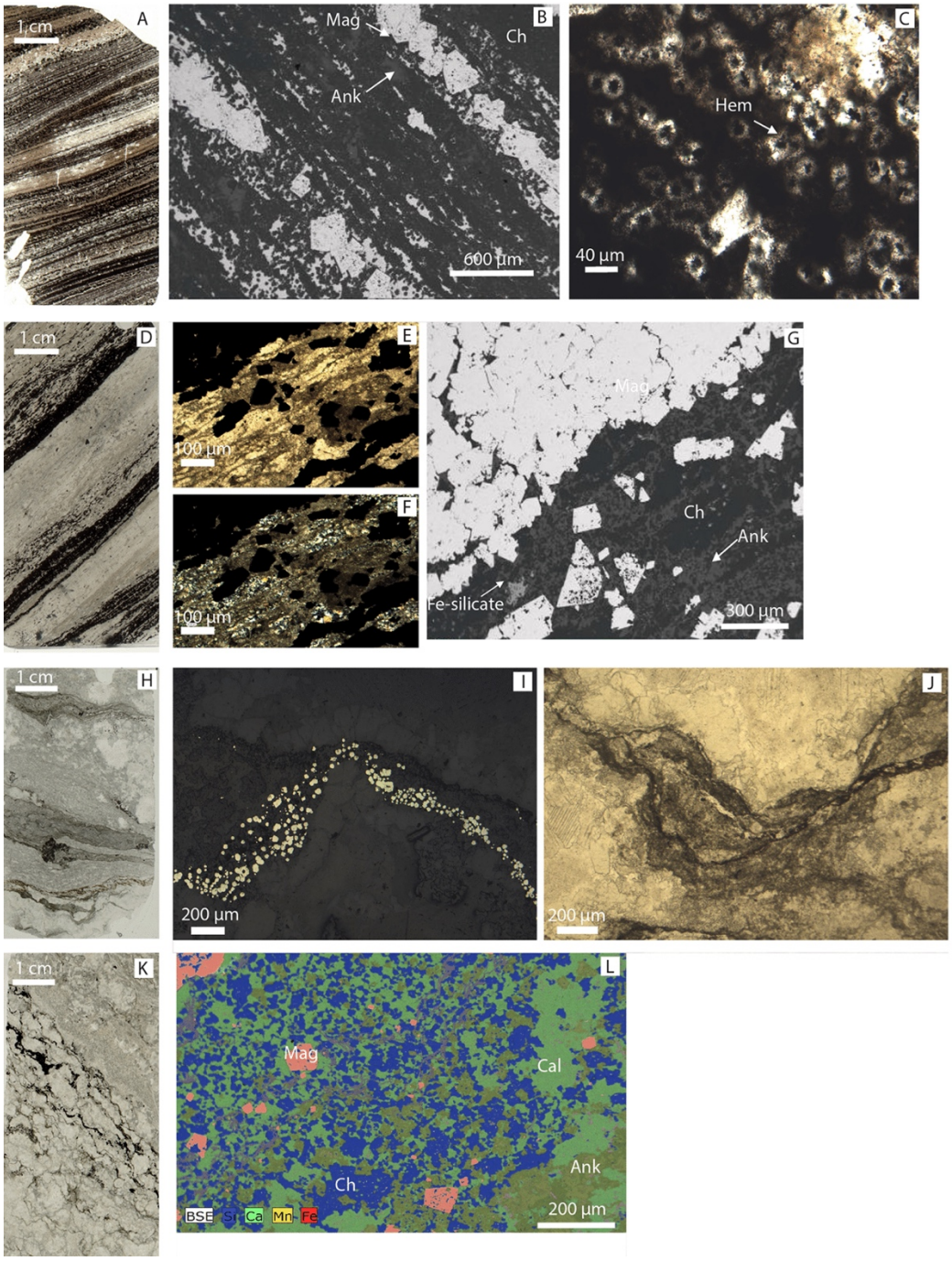

Figure 4. 2: Different facies among both studied cores (FD-55 and FD-365) showing IFs being represented by finely laminated jaspilites formed by mm-scale laminae of chert (e.g. microcrystalline quartz) intercalated with euhedral magnetite and red jasper with spherulitic hematite and minor amounts of ankerite disseminated in the chert matrix (A-C). Fe-rich carbonates composed dominantly of ankerite and microcrystalline quartz intercalated with magnetite layers (D-G) and Fe-poor carbonates composed of calcite, ankerite and rare finely-laminated magnetite layers locally displaying wrinkly laminated features (H-L). Framboidal

pyrites are commonly present in the Fe-poor carbonate interval, particularly in the wrinkly-laminated features, which are usually associated with organic matter (I,J).

Two main types of carbonate are present: i) Fe-rich carbonates composed dominantly of ankerite and microcrystalline quartz intercalated with magnetite layers (Fig. 4.2, D-G) and ii) Fe-poor carbonates composed of calcite, ankerite and rare finely-laminated magnetite layers locally displaying wrinkly laminated features (Fig. 4.2, H-L). Framboidal pyrites are common in Fe-poor carbonate intervals, particularly in the wrinkly-laminated samples, which are usually associated with the presence of organic matter (Fig. 4.2, I-J). Minor amounts of Fe-silicates (e.g. stilpnomelane and minnesotaite) are also present in the Fe-poor carbonate layers.

Iron formations from both cores have very low abundances of poorly mobile elements, including Al, Ti, Zr, Th and Hf. Al contents in IFs range from 0.02 to 0.2 wt.% (mean = 0.06 wt.%, n=15), while Ti, Zr and Th concentrations are below 70, 21 and 0.25 ppm, respectively. Iron-rich and iron-poor carbonates show an enrichment in Al compared to IFs, with concentrations slightly below 1 wt.% for the most enriched samples (mean Al content in carbonate is 0.17 wt.%, n=24; Fig. 4.3). Only IFs and carbonates with Al content below 0.2 wt.% will be considered in the following discussion to avoid potential detrital contribution and focus on the purely chemical and authigenic signatures of the sediment. In general, rare earth and yttrium (REY) data normalized to post Archean Australian shale (PAAS; McLennan, 1989) show positive La, Eu and Y anomalies in IFs and carbonates. Cerium anomalies (Ce/Ce*) were calculated according to Bau and Dulski (1996) using the projection between La and Pr, but evaluated against Pr/Pr* to distinguish false Ce anomalies arising from the presence of positive La anomalies, which occur in our sample set (Fig. 4.4). No significant true Ce anomalies, either positive or negative, were observed among the studied samples (Fig. 4.5). Positive

Eu anomalies (Eu/Eu*) are highly variable, with several extreme values up to 18. Relative abundances of Y are also very high, with an average Y/Ho ratio that is strongly super-chondritic at 83.3 (n=56). The light REY (LREY) are not depleted relative to the heavy REY (HREY) as demonstrated by the ratio Pr/Yb_{sn} with an average value of 1.06 (n=56).

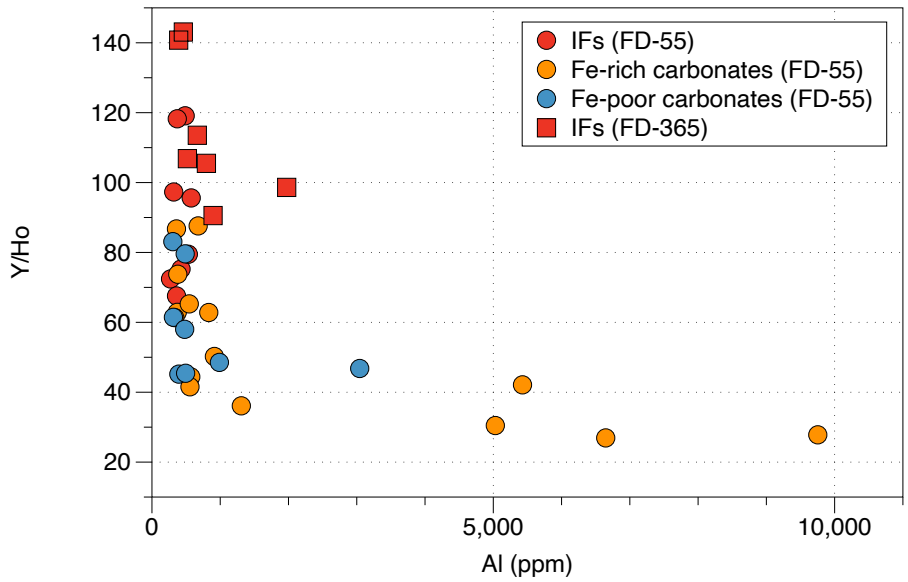

Figure 4. 3: Detrital-free IFs shown by low concentrations of Al and super-chondritic Y/Ho values.

The iron isotope compositions of the IFs are remarkably homogeneous throughout the two drill core depth intervals (~ 200 and 150 m depths) and show an enrichment in the heavier isotope with δ^{56}Fe values ranging from +1.03 to +1.95‰ with an average of +1.39 ± 0.22 (1SD, n=27). Iron-rich and Fe-poor carbonates show distinct δ^{56}Fe values of +0.2 to +0.8‰ and -0.4 to +0.07‰, respectively, and one anomalous Fe-rich carbonate sample with -0.8‰. The isotopic composition of organic carbon in IFs and carbonates shows significant variability, with $\delta^{13}C_{org}$ values from -23.50 to -28.17‰ and -21.17 to -31.80‰, respectively, and an average $\delta^{13}C_{org}$ value of -25.5 ± 2.7‰ (1SD, n=15).

4.6 Discussion

4.6.1 Anoxic conditions during IF deposition in the Carajás basin

Shale-normalized Rare Earth and Yttrium (REY) data are extensively used as a geochemical tool to characterize conditions in which IFs were formed (Planavsky et al., 2010a). In modern seawater and marine sediments, the REY system is controlled by terrestrial versus hydrothermal inputs and particle-solution interactions that are susceptible to change with salinity, water depth, and redox state (Robbins et al., 2019b). Similarities between REY patterns from modern environments and the geological record imply the preservation of a primary seawater signature from which these rocks were formed (Oonk et al., 2018). Detrital contamination, however, has been proven to mute or mask primary signals, but is easily identified by increasing concentration of poorly mobile elements such as Al, Ti, Sc, Zr, U, Th or Hf. Additionally, the influence of post-depositional processes (*e.g.* diagenesis and metamorphism) does not alter significantly the primary REY composition of IFs (Bau and Möller, 1993). The IFs from Carajás studied here are almost detritus-free, and with the exception of one sample with Al concentration at 0.2 wt.%, all other IFs show Al content < 0.1 wt.% (Fig. 4.3). The Fe and Si contents in IFs vary between 31.7 to 63.1 wt.% and 33.3 to 54.2 wt.%, respectively, indicating that no open system alteration and/or mass loss (*e.g.* silica leaching) took place after rock deposition. Additionally, these rocks experienced low metamorphic grade (Machado et al., 1991; Rosière et al., 2006; Krymsky et al., 2007b), which make them an ideal target to explore past redox conditions in the basin.

Rare earth elements are generally found under a single oxidation state (+3) and share similar geochemical behavior but two of them, Cerium (Ce) and Europium (Eu), can behave differently depending on local and/or global redox conditions. Under oxic

conditions, Ce can be oxidized from its trivalent to tetravalent state, and less soluble Ce(IV) is readily removed from seawater onto Mn(IV)-Fe(III)-oxyhydroxides, organic matter, and clay particles (Konhauser et al., 2017). This behavior imparts a negative cerium anomaly on modern oxygenated seawater.

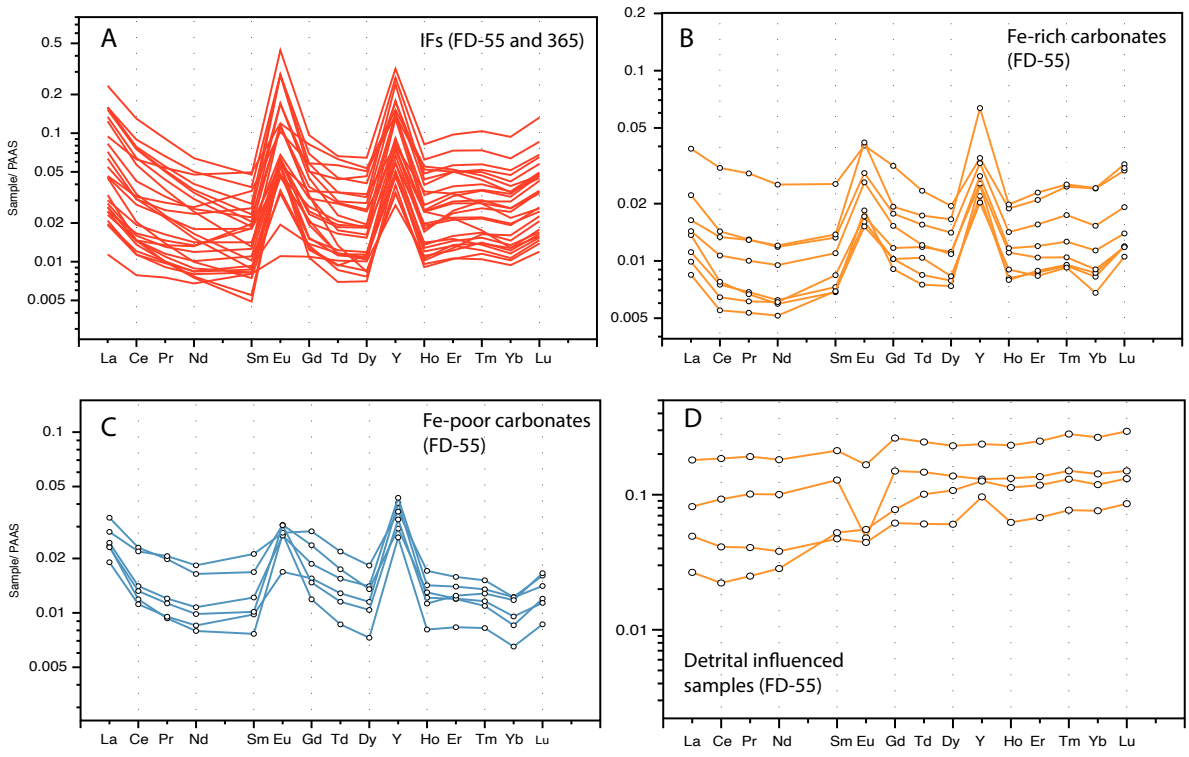

Figure 4. 4: Rare Earth Elements and Yttrium (REY) abundancies normalized to Post-Archean Australian Shales (PAAS) for IFs, Fe-rich and Fe-poor carbonates (A-C), including few samples influenced by detrital contamination (D).

Most pre-GOE IFs that were not altered by secondary processes (*e.g.* Bonnand *et al.*, 2020) lack a negative Ce anomaly (*e.g.* Lindenmayer *et al.*, 2001; Hofmann, 2005; Døssing *et al.*, 2009; Planavsky *et al.*, 2010; Mloszewska *et al.*, 2012; Haugaard *et al.*, 2013, 2016) indicating that the adsorption of REY occurred under anoxic water conditions. Similarly, IFs from Carajás show no significant true Ce anomalies, either positive or negative, as indicated by the general absence of data with Ce/Ce* <1 and Pr/Pr* >1, or Ce/Ce* >1 and Pr/Pr*

<1, respectively (Fig. 4.5). We attribute the few values falling in the Ce/Ce*<1 and Pr/Pr*>1 field, close to PAAS values of 1, as reflecting either small compositional differences between PAAS and local detrital inputs, or artifacts arising from the slightly curved REE spectra of our dataset. Calculations of Ce anomalies using alternatively proposed projections (e.g. calculation of Ce* by projection backward from Pr and Nd; Lawrence and Kamber, 2006) yielded non-negligible but clearly false Ce anomalies that are most likely explained by the same potential artifacts; the Bau and Dulski (1996) method proved more reliable in this regard as the Ce anomalies are clearly identified as artifacts. A comparison with Archean IFs from Isua, Greenland, demonstrates similar anoxic conditions, in contrast to modern microbialites and seawater that show the clear imprint of Ce redox cycling in an oxygenated environment (Fig. 4.5).

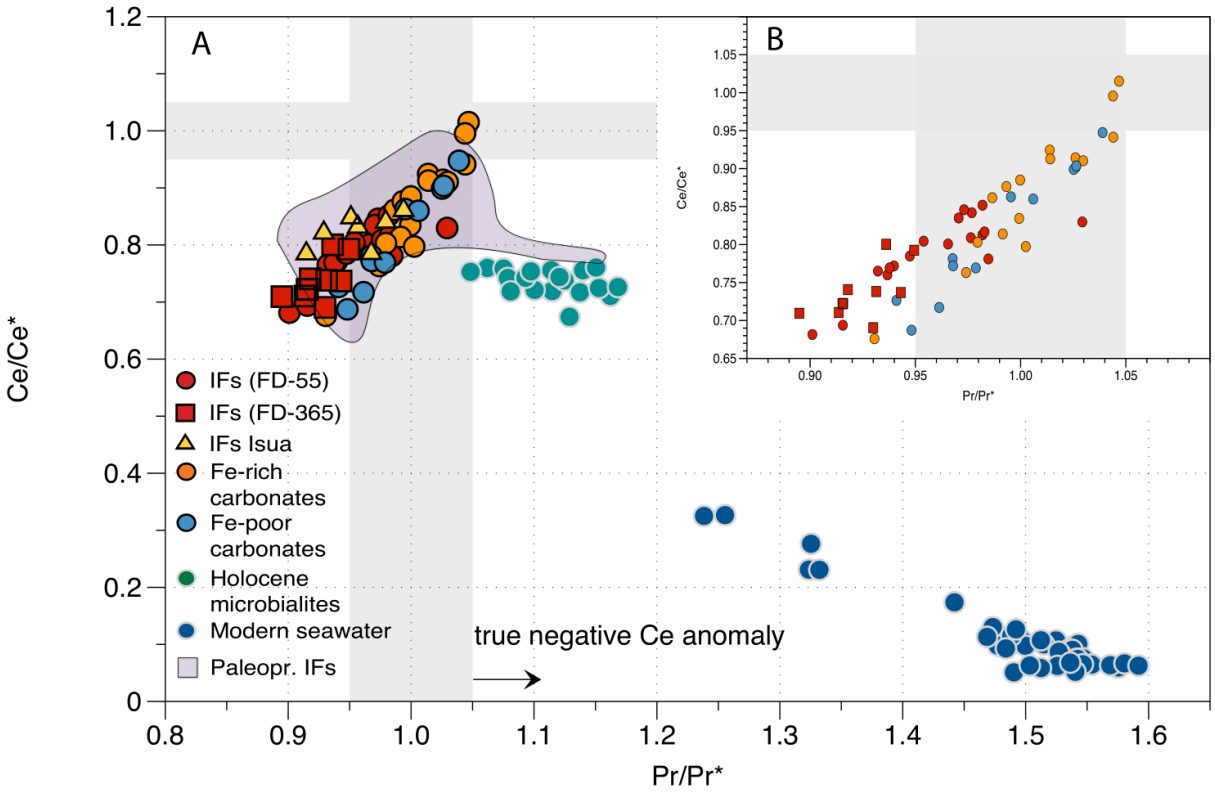

Figure 4. 5: Ce anomalies in IFs and carbonates from the CMP compared with IFs from Isua, Greenland (Bolhar et al., 2004), Paleoproterozoic IFs (Bau and Dulski, 1996; Frei et al., 2008; Haugaard et al., 2016b; Teixeira et al., 2017; Oonk et al., 2018) Holocene microbialites (Webb and

Kamber, 2000) and modern seawater (Zhang and Nozaki, 1996) (A), and detailed view of the studied sample set (B).

Additionally, Paleoproterozoic IFs from other cratons throughout the globe argue in favor of more oxidizing conditions with Ce/Ce* values <0.9 and Pr/Pr*>1.02, contrasting with Archean and Neoarchean values (Wang et al., 2016; Oonk et al., 2018; Sampaio et al., 2018; Warchola et al., 2018). This suggests that the Carajás IFs formed under anoxic conditions, possibly due to limited generation and accumulation of O_2 produced by oxygenic photosynthetic organisms (if present) that were not likely abundant during the Late Archean (Ossa et al., 2019).

Europium can be reduced to a divalent state under high-temperature and low-Eh conditions, rendering it more soluble under hydrothermal conditions than strictly trivalent REYs (Bau and Möller, 1993). Consequently, hydrothermal fluids from modern and past environments are characterized by a positive Eu anomaly, a feature usually interpreted as a hydrothermal Fe source in IFs. A compilation of Eu anomalies and their variation in time are shown for the major known IFs (Fig. 4.6). A significant increase in the magnitude of positive Eu anomalies was already noted for IFs deposited from ~2.7 to 2.6 Ga (Viehmann et al., 2015a). Here we report unprecedented positive anomalies for the ~2.74 Ga Carajás IFs, with Eu/Eu* values up to 18 (Fig. 4.6), as compared to maximum values of ~8 and ~5 from other Neoarchean IFs (Viehmann et al., 2015a; Garcia et al., 2016). Moreover, the fact that there is no depletion in LREY compared to HREY in our samples (average Pr/Yb_{sn} value of 1.06), which is normally found in modern seawater and reflected in a Pr/Yb_{sn} ratio < 1 (*e.g.* Bolhar *et al.*, 2004), reinforces the idea that the REY signatures in Carajás IFs reflect the mixing of seawater and hydrothermal fluids. This suggests that IF deposition in the Carajás Basin coincided with a period of intense

hydrothermal activity, possibly triggered by a major mantle plume event (Viehmann et al., 2015a). The Carajás Basin is so far the only location that has recorded such strong positive Eu anomaly, which can be related to a combination of factors, such as IFs deposition in a restricted environment where significant hydrothermal activity was taking place. This differs from previous studied Neoarchean and Paleoproterozoic IFs that likely had a more pronounced contribution from open ocean seawater (Viehmann et al., 2015a). This intense hydrothermal activity would have provided substantial ferrous iron and maintained general anoxic conditions in the Carajás Basin.

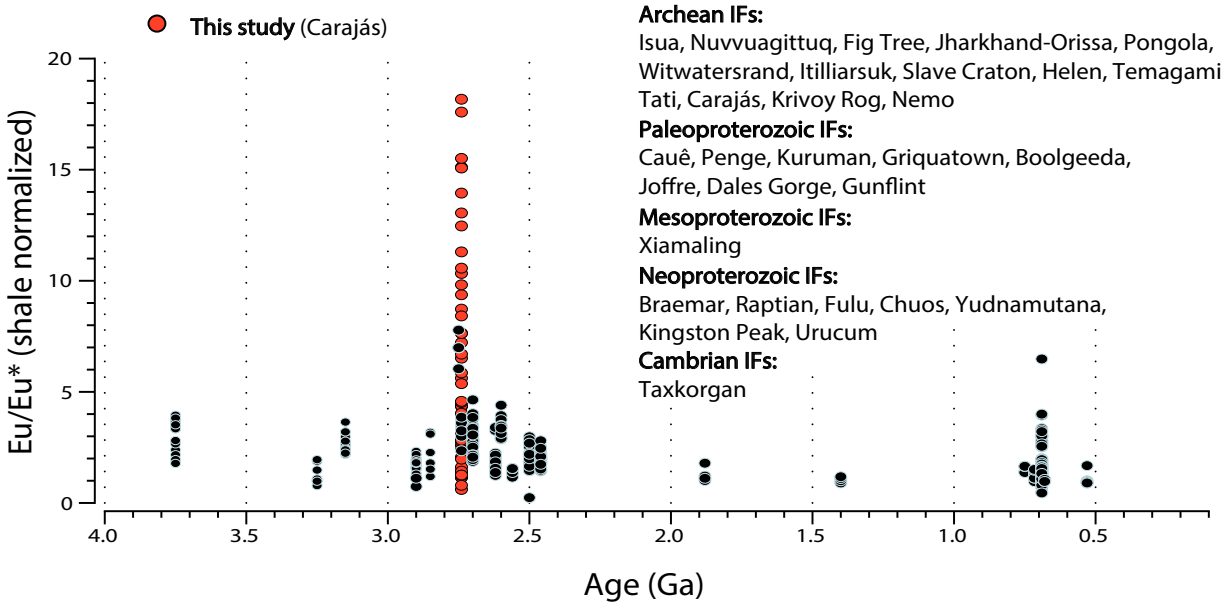

Figure 4. 6: Compilation of shale-normalized Eu anomalies for major IFs deposited mainly throughout the Precambrian, including Archean (Derry and Jacobsen, 1990; Hofmann, 2005; Bhattacharya et al., 2007; Frei and Polat, 2007; Alexander et al., 2008; Frei et al., 2008; Bau and Alexander, 2009; Døssing et al., 2009; Fabre et al., 2011; Mloszewska et al., 2012; Haugaard et al., 2016a, 2016b, 2017, 2013; Viehmann et al., 2015a, 2015b; Garcia et al., 2016), Paleoproterozoic (Danielson et al., 1992; Bau and Dulski, 1996; Teixeira et al., 2017; Lantink et al., 2018b; Warchola et al., 2018), Mesoproterozoic (Canfield et al., 2018), Neoproterozoic (Lottermoser and Ashley, 2000; Halverson et al., 2011; Viehmann et al., 2016; Busigny et al., 2018; Lechte et al., 2019b) and Cambrian IFs (Li et al., 2018).

4.6.2 Defining an oxidative mechanism from Fe and C isotopes

The presence of ferric minerals in IFs requires oxidation of $Fe(II)_{aq}$ to $Fe(III)_{aq}$ leading to subsequent precipitation of Fe oxyhydroxide particles (Tangalos et al., 2010). Under oxic conditions and at circum-neutral pH, $Fe(II)_{aq}$ can be rapidly and completely oxidized to thermodynamically stable $Fe(III)_{aq}$ without significant Fe isotope fractionation, thus, Fe(III) oxyhydroxides will inherit the Fe isotopic composition of the Fe(II) source (Rouxel et al., 2018). However, if oxidation rates are slow, such as under low Eh conditions, Fe(II) can be partially oxidized, producing large Fe isotope fractionation between Fe(II) and Fe(III) species and a ferric iron precipitate enriched in heavy isotopes, as observed in many Archean IFs (Dauphas et al., 2004b; Planavsky et al., 2012; Czaja et al., 2013, 2018). Additionally, sample alteration by metamorphism was shown as an unlikely process to explain heavy δ^{56}Fe values, thus, reflecting changes in the biogeochemical cycle of Fe (Dauphas et al., 2007; Frost et al., 2007; Hyslop et al., 2008). The Fe isotope composition of the 2.74 Ga IFs in the Carajás Basin is enriched in heavy isotopes but also remarkably homogeneous, with an average δ^{56}Fe value of $+1.39 \pm 0.22$‰ (1SD, n=27; Fig. 4.7). Assuming hydrothermally-sourced $Fe(II)_{aq}$ remained similar in isotopic composition throughout Earth's history, with δ^{56}Fe values close to modern hydrothermal vent systems (*e.g.*~ -0.5 to 0‰, Heard & Dauphas, 2020) our positive Fe isotope data support dissolved Fe content in excess of available oxidizing agents in the Carajás Basin since low degrees of partial Fe oxidation can be deduced in both cores from Serra Sul and Serra Norte, which are located 50 km from each other. Additionally, the δ^{56}Fe values between -0.4 to +0.07‰ of Fe-poor carbonates in core FD55 further corroborate a fluid source around 0‰ since Fe isotope fractionation between Fe-carbonate and $Fe(II)_{aq}$ ranges between -0.2 to -0.7‰ (Wiesli et al., 2004; Blanchard et al.,

2009). The homogeneity of δ^{56}Fe values of IFs within each core and between the two cores can only be explained by a constant and well-buffered Fe isotope composition of seawater at the basin scale. This implies a constant rejuvenation of Fe(II) from the source into the water column, as opposed to a limited source that would result in a depleted δ^{56}Fe eventually recorded in the sediment. In this case, an isotopically light residual iron was not expressed, but likely sequestered in carbonates and pyrites. This suggests that dissolved Fe(II) concentrations were high and little affected by Fe-oxyhydroxide precipitation, again supporting strong hydrothermal activity in the basin, in agreement with the prominent Eu anomaly. The homogeneity of δ^{56}Fe values in IFs indicates a constancy in both δ^{56}Fe values of the dissolved Fe(II) source and the magnitude of the isotope fractionation leading to the formation of Fe precipitate.

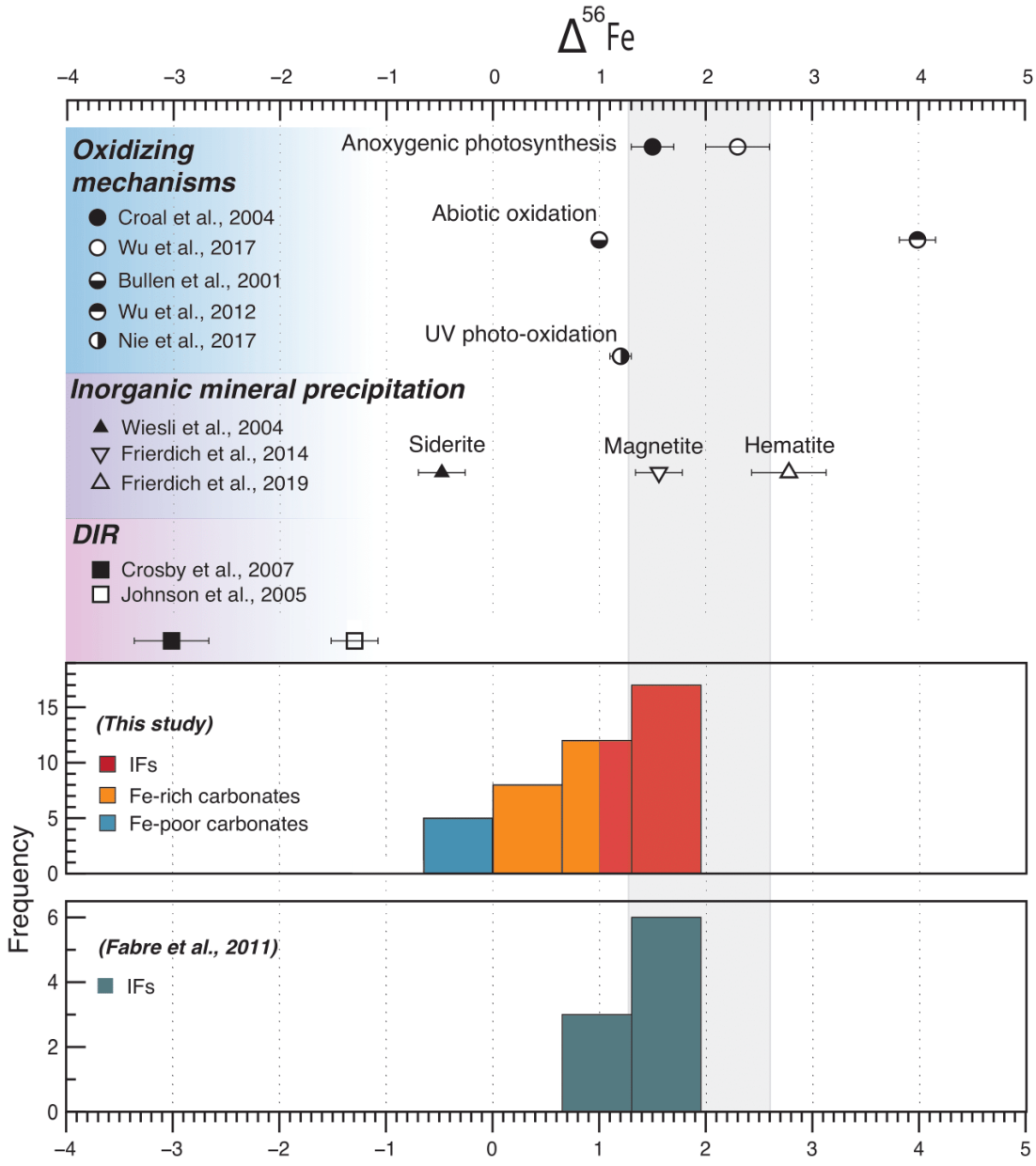

Figure 4. 7: Iron isotope fractionation factors of IFs and carbonates (this study) including previous results from the Carajás Basin (Fabre et al., 2011) compared with experimental studies showing fractionation factors for different oxidizing mechanisms (Bullen et al., 2001; Croal et al., 2004; Wu et al., 2012; Nie et al., 2017b), inorganic mineral precipitation (Wiesli et al., 2004; Frierdich et al., 2014b, 2019) and dissimilatory iron reduction (DIR; Johnson *et al.*, 2005; Crosby *et al.*, 2007)

The oxidizing mechanism involved in this partial oxidation can be difficult to define based solely on Fe isotopes. According to most models regarding IF genesis, either anoxygenic and/or oxygenic photosynthesis is the main responsible mechanism, discarding previous models that invoke the reduced Fe-silicate phase (e.g. greenalite) as a primary precipitate (Tosca et al., 2016; Robbins et al., 2019a). Photo-oxidation by UV photons is proven to be an effective abiotic mechanism to oxidize Fe(II) to Fe(III) with experimental results showing a product enriched in the heavy Fe isotope, consistent with measured values in IFs (Nie et al., 2017b). However, previous studies have demonstrated as an unlikely mechanism for extensive IF deposition during the Archean (Konhauser et al., 2007a; Pecoits et al., 2015). Based on REY systematics and Fe isotopes, anoxic conditions likely prevailed during IF deposition in the Carajás Basin, thus, anoxygenic photosynthesis would appear to be the most plausible oxidizing mechanism. Experimental studies estimated Fe isotope fractionation of +2.3 ± 0.3‰ for Fe(II) oxidation by photoferrotrophs in conditions similar to Precambrian oceans (Wu et al., 2017). A related experiment with the same bacterial strain, however in the absence of Si, provided a δ^{56}Fe fractionation between Fe(III) precipitates and aqueous Fe(II) ranging from +0.96‰ to +1.98‰ (Swanner et al., 2015b), while a freshwater bacterial strain showed Fe isotope fractionation of ~+1.5 ± 0.2‰ (Croal et al., 2004). The remarkable homogeneous δ^{56}Fe values (~ +1.39‰) of Carajás IFs imply that the isotope fractionation associated with Fe oxidation was constant both in time and space. Although the Fe isotope composition of seawater at that time is unknown, a value between -0.5 to 0‰ seems reasonable (Johnson et al., 2008b; Heard and Dauphas, 2020), which yields an overall Fe isotope fractionation between fluid and Fe-oxyhydroxide comprised between +1.35 and 1.85 ‰. These fractionation values determined from the Fe isotope compositions measured in the present study as well as previous data obtained on the

Carajás Basin (*e.g.* Fabre *et al.*, 2011) are consistent with the range inferred from experimental studies described above, further supporting photoferrotrophic bacteria as a potential oxidizing pathway (Fig. 4.7). Additionally, variations in the carbon isotope composition of sedimentary organic matter provide further insights into diverse mechanisms used by organisms to fix organic matter (Hayes, 2001). Carbon isotope ratios in the studied IFs and carbonates show variable $\delta^{13}C_{org}$ values, ranging from -23.50 to -28.17 ‰ and -21.17 to -31.80 ‰, respectively (Fig. 4.8). The average $\delta^{13}C_{org}$ value of -25.6 ± 1.7 ‰ (n=5) in IFs is consistent with a kinetic isotope fractionation produced by autotrophic organisms, which are depleted in ^{13}C compared to the CO_2 source (Schidlowski, 2001). Moreover, the organic carbon content in the IFs from Carajás, which varies from 0.01 to 0.06 wt.%, are consistent with previous published values (Thompson et al., 2019). Given the range of both $\delta^{13}C_{org}$ and $\delta^{56}Fe$ values, and considering that Fe(II) was likely dissolved in excess as opposed to available oxidizing agents, we cannot completely rule out an operating cryptic oxygen cycle. This suggests that chemolithoautotrophic and/or microaerophilic organisms could have been thriving under limited oxygen conditions (Konhauser et al., 2002; Smith et al., 2013). Overall our results argue for autotrophic photosynthesis as the main mechanism of primary production in the Carajás Basin, which, together with REY and Fe isotope data, more likely support the anoxygenic photosynthesis hypothesis.

The role of photoferrotrophs in the Archean is considered to be significant, as these organisms have been suggested to account for most, if not all, Fe(III) deposited in IFs (Konhauser et al., 2002, 2018; Schad et al., 2019b). Ferruginous conditions might have been toxic for cyanobacteria in early Precambrian oceans (*e.g.* Swanner *et al.*, 2015a), but we cannot completely rule out their presence in surface oxic layers where Fe(II) concentrations might be suppressed. In any case, photoferrotrophs could have oxidized

dissolved hydrothermal Fe(II) before reaching the surface (*e.g.* Kappler *et al.*, 2005; Ozaki *et al.*, 2019) as they are more adapted to low-light conditions (Jones et al., 2015). The ecophysiology of photoferrotrophs likely favored their abundance in Precambrian oceans (Hegler et al., 2008; Posth et al., 2008) as modern analogs have provided palpable evidence of their role in Fe cycling, particularly as agents of Fe oxidation (Walter et al., 2014; Llirós et al., 2015; Koeksoy et al., 2016).

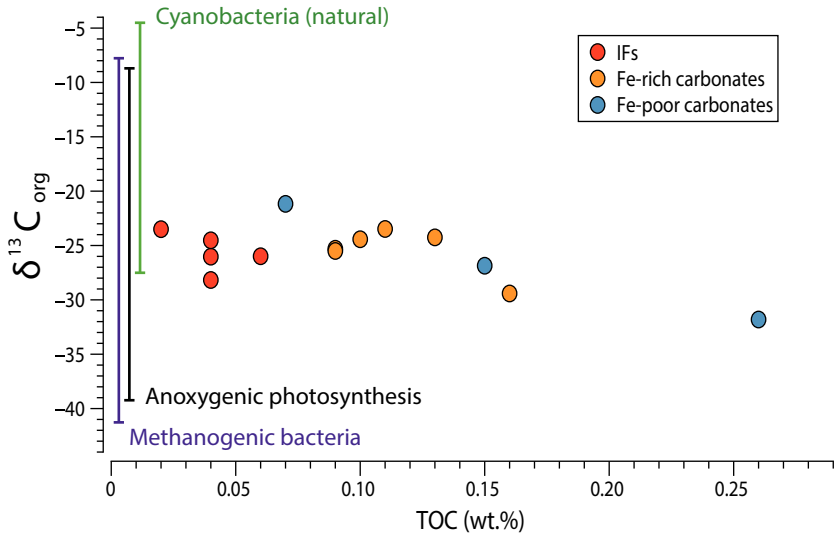

Figure 4. 8: Distribution of organic carbon isotope compositions from IFs and carbonates, including ranges characterizing cyanobacteria, methanogenic bacteria and anoxygenic photosynthetic bacteria (Schidlowski, 2001)

Previous studies usually refer to photosynthesis, directly or indirectly, as the main oxidizing mechanism forming Fe(III) minerals in IFs (*e.g.* Croal *et al.*, 2009; Johnston *et al.*, 2009; Czaja *et al.*, 2013, 2018; Gauger *et al.*, 2015, 2016; Thompson *et al.*, 2019). However, by combining trace element data with Fe and C isotopes, we propose anoxygenic photosynthesis as a predominant oxidizing mechanism favoring IFs deposition in the Carajás Basin.

4.7 Conclusions

The approach used here combines REY data with Fe and C isotopes to provide evidence that photoferrotrophs were active in the Carajás Basin and were oxidizing Fe coupled to the fixation of carbon using light energy, without the need of free oxygen (Kappler and Newman, 2004). Despite the indication of oxygenic photosynthesis during the Archean in oceanic and terrestrial settings (e.g. Planavsky *et al.*, 2014; Lalonde & Konhauser, 2015; Eickmann *et al.*, 2018), the Carajás IFs show consistent and narrow positive range in δ^{56}Fe values, which can be best explained by partial Fe oxidation in conditions with very low to no free O_2, while Fe-rich and Fe-poor carbonates precipitated restrictedly in potentially less reducing conditions. Moreover, a constant and significant hydrothermal Fe(II) source, shown by the highest Eu anomalies registered in IFs, avoided the depletion of an Fe(II) reservoir, as opposed to later Paleoproterozoic IFs in the Hamersley and Transvaal basins (Czaja et al., 2018). Thus, we infer that photoferrotrophic bacteria were responsible for the main iron oxidation mechanism via anoxygenic photosynthesis, as suggested by $\delta^{13}C_{org}$ values, that led to the precipitation of ferric minerals and subsequent deposition of IFs at a regional scale in the Carajás basin.

4.8 Supplementary figures:

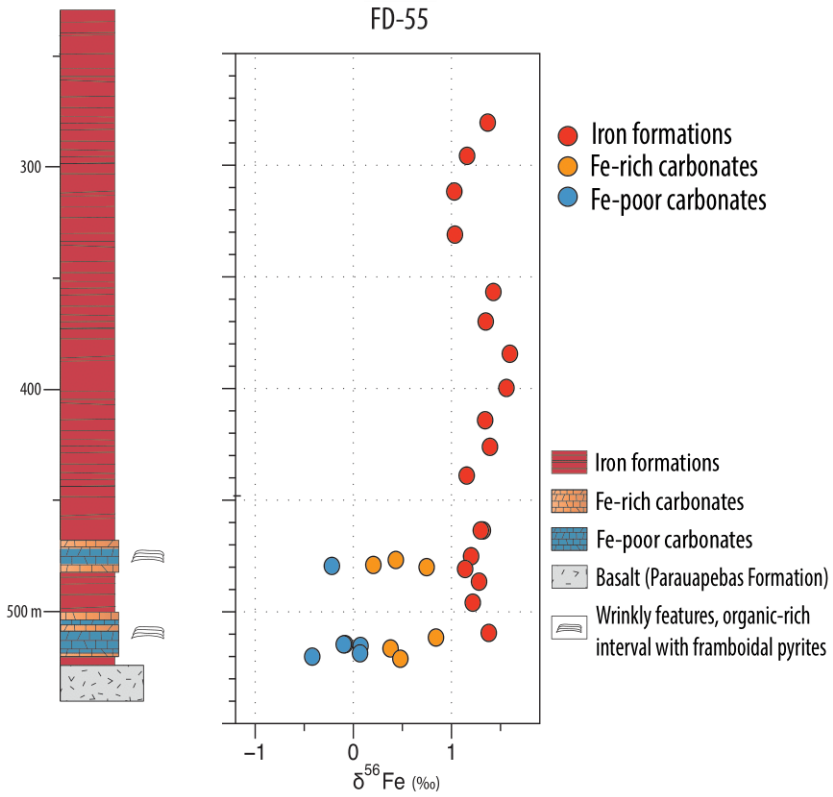

Figure 4. 9: Stratigraphic profile of core FD-55 showing the Fe isotope composition of iron formations, Fe-rich and Fe-poor carbonates

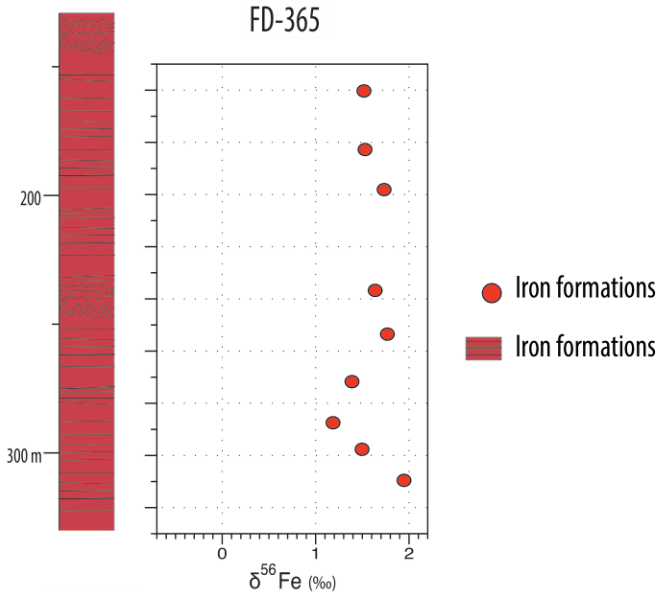

Figure 4. 10: Stratigraphic profile of core FD-365 showing the Fe isotope composition of iron formations.

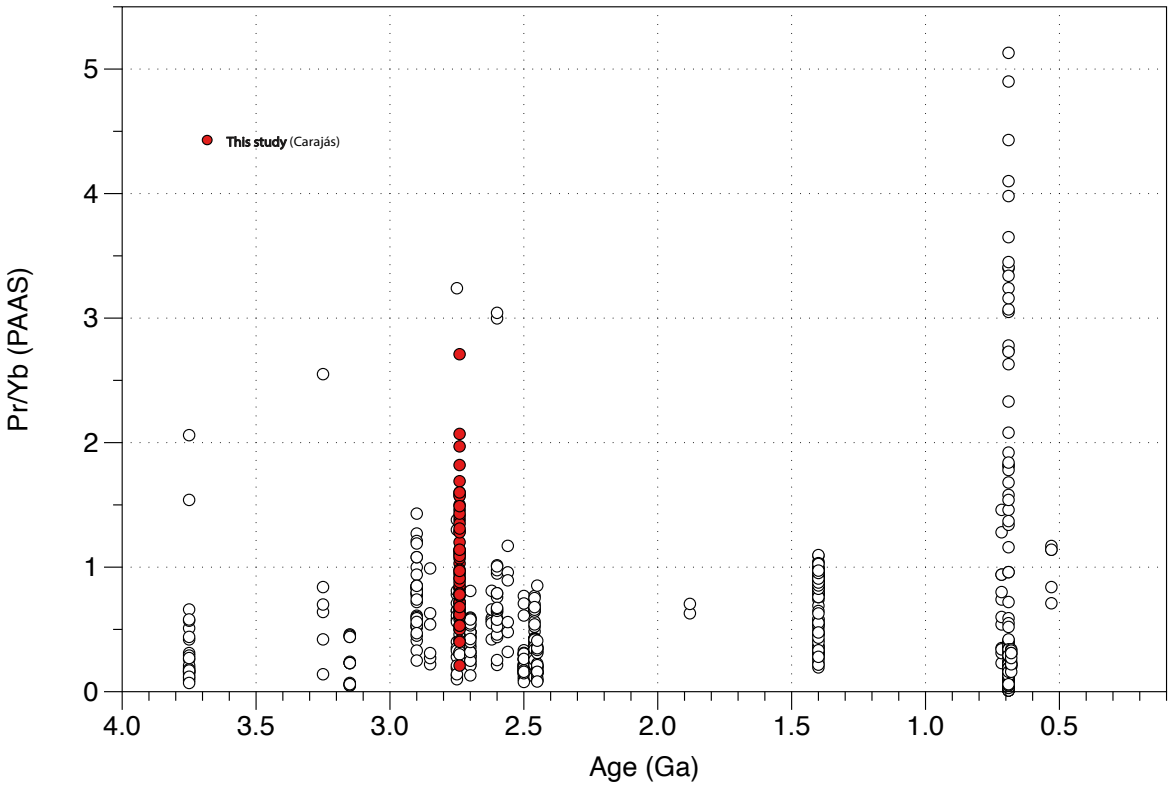

Figure 4. 11: Compilation of shale-normalized Pr/Yb ratios for major IFs deposited mainly throughout the Precambrian, including Archean (Derry and Jacobsen, 1990; Hofmann, 2005;

Bhattacharya et al., 2007; Frei and Polat, 2007; Alexander et al., 2008; Frei et al., 2008; Bau and Alexander, 2009; Døssing et al., 2009; Fabre et al., 2011; Mloszewska et al., 2012; Haugaard et al., 2016a, 2016b, 2017, 2013; Viehmann et al., 2015a, 2015b; Garcia et al., 2016), Paleoproterozoic (Danielson et al., 1992; Bau and Dulski, 1996; Teixeira et al., 2017; Lantink et al., 2018b; Warchola et al., 2018), Mesoproterozoic (Canfield et al., 2018), Neoproterozoic (Lottermoser and Ashley, 2000; Halverson et al., 2011; Viehmann et al., 2016; Busigny et al., 2018; Lechte et al., 2019b) and Cambrian IFs (Li et al., 2018)

Chapter 4 is now published in *Geobiology* along with all supplementary data (major and trace elements, Fe and C isotope data):

Rego, E.S., Busigny, V., Lalonde, S. V., Philippot, P., Bouyon, A., Rossignol, C., Babinski, M., and Cássia Zapparoli, A., 2021, Anoxygenic photosynthesis linked to Neoarchean iron formations in Carajás (Brazil): Geobiology, v. 19, p. 326–341, doi:10.1111/gbi.12438.

4.9 The iron isotope composition of siltstones and shales in the Carajás Basin: preliminary results

4.9.1 Introduction

Sedimentary rocks and minerals deposited between ~2.7 and 2.5 Ga are significantly depleted in ^{56}Fe compared to other periods in Earth's history (Rouxel et al., 2005; Johnson et al., 2008; Planavsky et al., 2010; Ostrander et al., 2021). Presently, these Fe isotope signatures are explained as either products of extensive precipitation of isotopically heavy Fe(III)-oxyhydroxides (*i.e.* under reducing conditions) leaving a residual isotopically light Fe(II) pool from which minerals (*e.g.* pyrites) could precipitate

from, an Fe(II) source depleted in ^{56}Fe as a product of dissimilatory iron reduction (DIR), and/or kinetic isotope effects associated to pyrite precipitation. Distinguishing between these processes has proven to be challenging (Heard et al., 2020; Ostrander et al., 2021), and additional samples from other locations apart from those already well-studied localities (*e.g*. from Western Australia, Mt. McRae Shale and Jeerinah Fm.; and South Africa, Klein Note Formation) could provide clues on how the Fe cycle was operating at this time interval. Interestingly, this period of large $\delta^{56}Fe$ variation occurs right before the onset of the Great Oxidation Event (GOE, ~2.45 Ga; Philippot et al., 2018). In this section, we provide new bulk-rock Fe isotope compositions of siltstones and shales from the Igarapé Bahia Group (maximum depositional age of 2684 $\pm$ 10 Ma; Rossignol et al., 2020) and the Azul Fm. (with a maximum depositional age of 2273 $\pm$ 35 Ma; Araujó et al., 2021), and give preliminary paleo-environmental implications.

Sample description

Two drill-cores intercepting the main sedimentary units above the Carajás Formation were selected to investigate local changes in the Fe cycle during the Neoarchean and possibly Paleoproterozoic. The studied drill-cores were GT 16, which intercepts the Igarapé Bahia Group/Serra Sul Formation, and the DH 02 intercepting the Azul/Águas Claras Formation. The GT-16 drill-core is composed of conglomerates interbedded with sandstones (facies S1, Fig. 4.12 A,B) and fine-grained sediments (facies F1, Fig. 4.12 B,C). The Facies S1 consists of medium-grained sand to gravel and commonly contains floating clasts and diagenetic pyrite. Petrographic observations indicate that these sandstones are mainly made up of lithic fragments (cherts and polycrystalline quartz grains) and monocrystalline quartz grains (Rossignol et al., 2020, see Annex).

Facies F1 consist of fine-grained sediments (fine sandstone to siltstone and clay) defining horizontal laminations underlined by thin sandstone layer (Rossignol et al., 2020, see Annex). The DH-02 drill-core consists of a monotonous succession of millimeter- to centimeter-scale intercalation between normally graded sandstone and laminated shales arranged in upward-fining intervals, also referred to as rythmite (Fig. 4.12 D,E; Araujo et al., 2021).

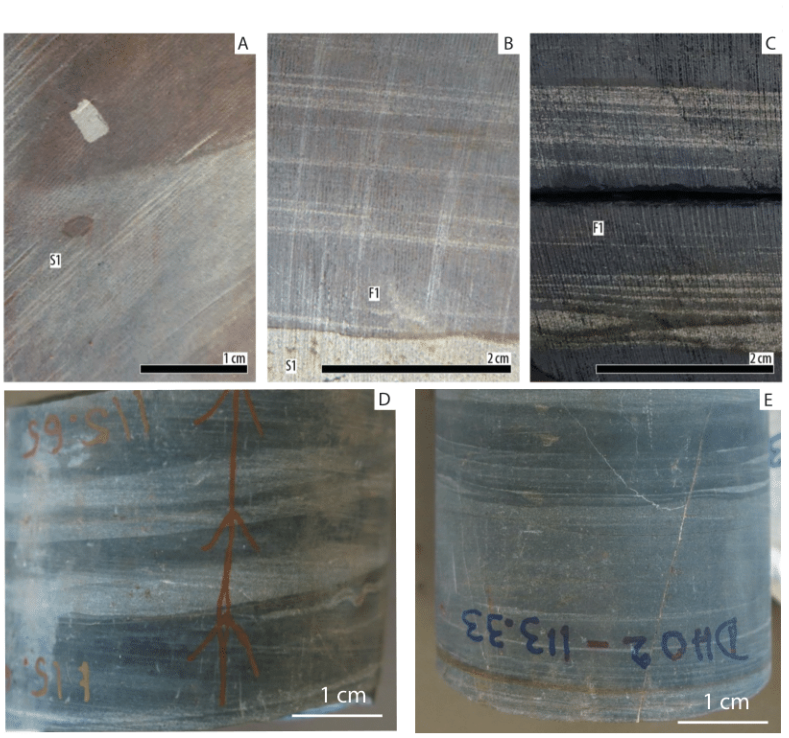

Figure 4. 12: Facies sampled for Fe-isotope measurements composed of medium-grained sand (facies S1; A,B) and fine sandstone to siltstone (facies F1; B,C) and fine siltstones and shales, also interpreted as rythmites (D,E).

Even though the Igarapé Bahia Group overlies the iron formations of the Carajás Formation, the contact between these two units has not been observed but is generally assumed to be concordant (Araújo et al., 2021). However, the Igarapé Bahia Group directly overlies the basalts of the Parauapebas Formation in some localities, suggesting

that the Igarapé Bahia Group could overlie discordantly the Carajás Formation (Dreher et al., 2005; Melo et al., 2019).

Results and Discussion

The iron isotope composition of whole-rock samples from GT 16 drill-core had δ^{56}Fe values ranging from +0.55 to +0.99 ‰ with an average of +0.66 ± 0.10 ‰ (n=15), while DH-02 had δ^{56}Fe values ranging from +0.27 to +0.70 ‰ with an average of +0.53 ± 0.12 ‰ (n=10) (Table 4.1). Both drill-cores had an overall positive and homogeneous δ^{56}Fe values reflecting an enrichment in ^{56}Fe in the shales and siltstone samples (Fig. 4.13).

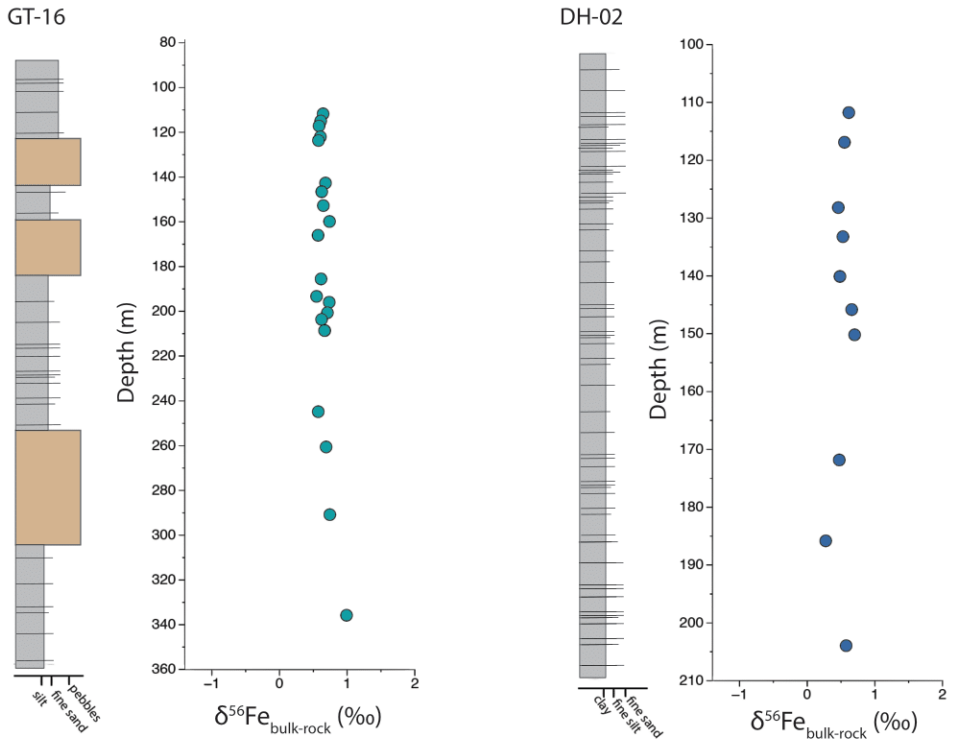

Figure 4. 13: Stratigraphic profile of drill-cores GT 16 and DH 02 showing the Fe isotope composition of siltstones and shales.

Normally, modern shales and other detrital-rich samples have δ^{56}Fe values close to 0 ‰, hence, reflecting weathering and erosion of crustal rocks (Dauphas et al., 2017)

Distinctively, Archean shales are often pyrite-rich and show negative δ^{56}Fe values. However, this is not the case for the siltstones and shales in the Carajás Basin, which are significantly enriched in ^{56}Fe. The identification of the main Fe source in these samples (*e.g.* oxides, carbonate, sulfides) will be key to interpret our results. Although it would have been useful to have a mineralogical composition of these samples, it has not been determined in the present work yet. However, major element relationships allow to speculate that Fe could be carried by carbonates (Fig. 4.14). For instance, if Fe is sourced mainly from carbonates, it is possible that dissimilatory iron reduction (DIR) had a role in reducing extensively Fe-oxides and generating a dissolved Fe(II) pool enriched in ^{56}Fe. This could explain the heavy δ^{56}Fe values measured in GT 16 and DH 02, but still contrast with very light δ^{56}Fe values measured in shales younger than 2.7 Ga elsewhere (Rouxel et al., 2005; Johnson et al., 2008; Planavsky et al., 2010; Ostrander et al., 2021).

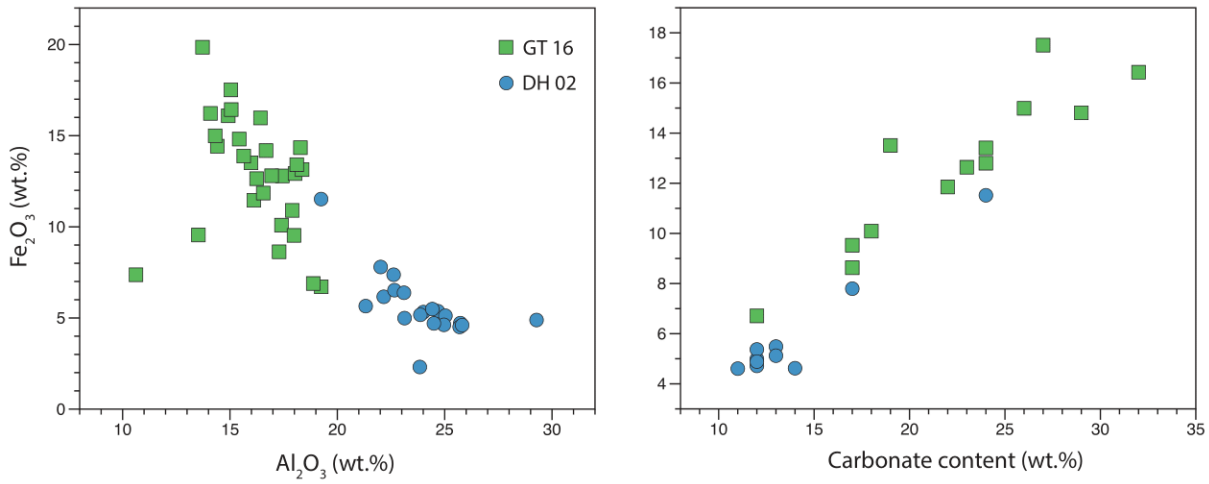

Figure 4.14: Correlation between Fe_2O_3 (wt.%) and Al_2O_3 (wt.%) and Fe_2O_3 (wt.%) and the amount of carbonate (wt.%) present in samples from drill-cores GT 16 and DH 02

Despite similar isotopic signature for both drill cores, GT 16 has slightly higher Fe content and slightly heavier δ^{56}Fe values, particularly in its base, compared to DH 02 (Fig. 4.13). Additionally, GT 16 has a higher Fe content compared to DH 02 likely reflecting its

stratigraphic proximity to the Fe-rich sediments of the Carajás Formation (Fig. 4.15). Some of these shales could also potentially be products of reworked and/or weathering products (*i.e.* dissolution and reprecipitation) of iron formations that were previously deposited in the Carajás Formation. This potentially suggests that Carajás records a local Fe isotopic signal, but further investigations are still required to understand the oxidation and reduction reactions involved in the generation of such heavy Fe isotope signatures in these siliciclastic rocks. There is an ongoing project aimed at identifying major mineral phases and applying C and N isotope systematics in samples from GT and DH drill-cores.

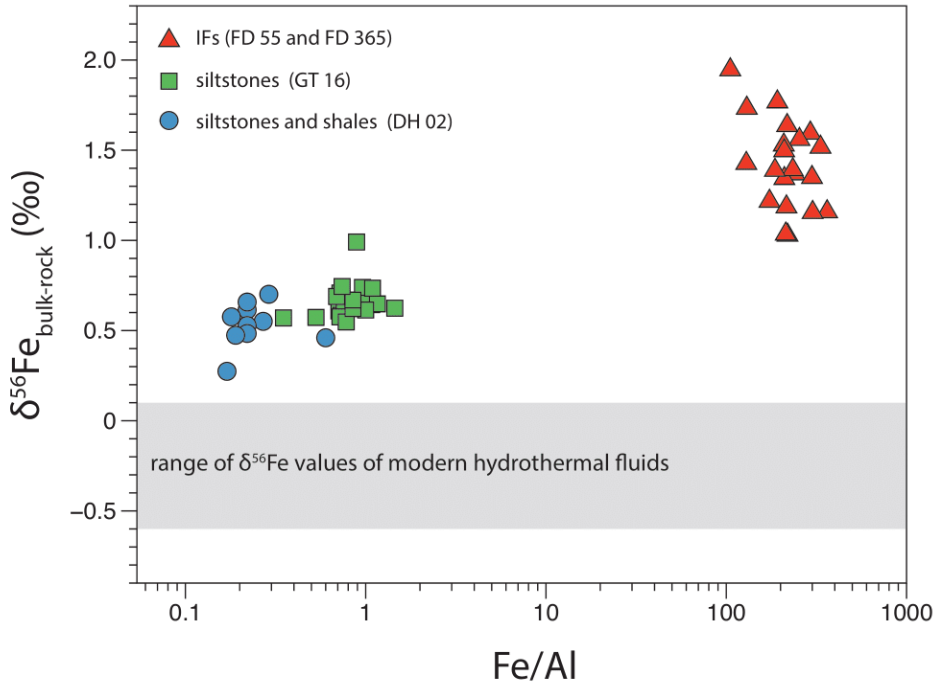

Figure 4.15: Iron isotope composition and Fe/Al ratios for siliciclastic rocks and iron formations from Carajás.

Table 4. 1: Iron isotope composition of siltstones and shales from drill-cores GT 16 and DH 02.

DH 02

Depth (m)	Lithology	δ^{56}Fe (‰)	±2SD	δ^{57}Fe (‰)	±2SD

111.765	org.-rich shale	0.62	0.04	0.93	0.03
116.9	org.-rich shale	0.55	0.06	0.83	0.06
128.19	org.-rich shale	0.46	0.01	0.70	0.04
133.225	org.-rich shale	0.53	0.03	0.78	0.04
140.1	org.-rich shale	0.48	0.03	0.70	0.05
145.83	org.-rich shale	0.66	0.03	0.99	0.04
150.19	org.-rich shale	0.70	0.05	1.07	0.06
171.835	org.-rich shale	0.47	0.01	0.68	0.11
185.82	org.-rich shale	0.27	0.02	0.46	0.05
203.95	org.-rich shale	0.58	0.03	0.86	0.09

GT 16

Depth (m)	**Lithology**	**δ^{56}Fe (‰)**	**±2SD**	**δ^{57}Fe (‰)**	**±2SD**
111.775	siltstone	0.64	0.05	0.34	0.06
114.98	siltstone	0.61	0.04	0.35	0.08
117.2	siltstone	0.58	0.03	0.28	0.16
122.04	shale	0.61	0.04	0.30	0.13
123.71	shale	0.58	0.05	0.28	0.11
142.695	siltstone	0.68	0.05	0.35	0.06
146.585	siltstone	0.62	0.01	0.36	0.18
152.775	siltstone	0.65	0.01	0.35	0.07
159.885	shale	0.74	0.07	0.36	0.08
166.05	shale	0.57	0.03	0.30	0.04
185.545	shale	0.61	0.03	0.25	0.11
193.335	shale	0.55	0.05	0.26	0.05
195.97	shale	0.74	0.02	0.30	0.11
200.64	shale	0.71	0.02	0.41	0.09
203.625	shale	0.62	0.01	0.30	0.13
208.61	shale	0.67	0.04	0.29	0.16
244.845	siltstone	0.57	0.03	0.30	0.03
260.61	siltstone	0.69	0.03	0.35	0.11
290.835	shale	0.74	0.04	0.39	0.04
335.795	shale	0.99	0.03	0.52	0.05

4.10 References

Alexander, B.W., Bau, M., Andersson, P., and Dulski, P., 2008, Continentally-derived solutes in shallow Archean seawater: Rare earth element and Nd isotope evidence in iron formation from the 2.9 Ga Pongola Supergroup, South Africa: Geochimica et Cosmochimica Acta, v. 72, p. 378–394, doi:10.1016/j.gca.2007.10.028.

Araújo, R., Araújo Filho, R.C., and Costa, L., 2021, Tectono-sedimentary evolution of the Paleoproterozoic succession of the Carajás Basin, southeastern Amazonian Craton, Brazil: Insights from sedimentology, stratigraphy, and U–Pb detrital zircon geochronology: Precambrian Research, v. 362, p. 106290, doi:10.1016/j.precamres.2021.106290.

Bau, M., and Alexander, B.W., 2009, Distribution of high field strength elements (Y, Zr, REE, Hf, Ta, Th, U) in adjacent magnetite and chert bands and in reference standards FeR-3 and FeR-4 from the Temagami iron-formation, Canada, and the redox level of the Neoarchean ocean: Precambrian Research, v. 174, p. 337–346, doi:10.1016/j.precamres.2009.08.007.

Bau, M., and Dulski, P., 1996, Distribution of yttrium and rare-earth elements in the Penge and Kuruman iron-formations, Transvaal Supergroup, South Africa: Precambrian Research, v. 79, p. 37–55.

Bau, M., and Möller, P., 1993, Rare earth element systematics of the chemically precipitated component in early precambrian iron formations and the evolution of the terrestrial atmosphere-hydrosphere-lithosphere system: Geochimica et Cosmochimica Acta, v. 57, p. 2239–2249, doi:10.1016/0016-7037(93)90566-F.

Beisiegel, V.D.R., Bernardelli, A.L., Drummond, N.F., Ruff, A.W., and Tremaine, J.W.R.,

1973, Geologia e Recursos Minerais da Serra dos Carajás: Revista Brasileira de Geociências, v. 3, p. 215–242, http://www.ppegeo.igc.usp.br/index.php/rbg/article/view/12491/12051.

Bhattacharya, H.N., Chakraborty, I., and Ghosh, K.K., 2007, Geochemistry of some banded iron-formations of the archean supracrustals, Jharkhand-Orissa region, India: Journal of Earth System Science, v. 116, p. 245–259, doi:10.1007/s12040-007-0024-4.

Blanchard, M., Poitrasson, F., Méheut, M., Lazzeri, M., Mauri, F., and Balan, E., 2009, Iron isotope fractionation between pyrite (FeS2), hematite (Fe2O3) and siderite (FeCO3): A first-principles density functional theory study: Geochimica et Cosmochimica Acta, v. 73, p. 6565–6578, doi:10.1016/j.gca.2009.07.034.

Blankenship, R.E., Sadekar, S., and Rymond, J., 2007, The Evolutionary Transition from Anoxygenic to Oxygenic Photosynthesis, *in* Evolution of Primary Producers in the Sea, Elsevier, p. 21–35, doi:10.1016/B978-012370518-1/50004-7.

Bolhar, R., Kamber, B.S., Moorbath, S., Fedo, C.M., and Whitehouse, M.J., 2004, Characterisation of early Archaean chemical sediments by trace element signatures: Earth and Planetary Science Letters, v. 222, p. 43–60, doi:10.1016/j.epsl.2004.02.016.

Bonnand, P., Lalonde, S.V., Boyet, M., Heubeck, C., Homann, M., Nonnotte, P., Foster, I., Konhauser, K.O., and Köhler, I., 2020, Post-depositional REE mobility in a Paleoarchean banded iron formation revealed by La-Ce geochronology: A cautionary tale for signals of ancient oxygenation: Earth and Planetary Science Letters, v. 547, p. 116452, doi:10.1016/j.epsl.2020.116452.

Bullen, T.D., White, A.F., Childs, C.W., Vivit, D. V., and Schultz, M.S., 2001, Demonstration of significant abiotic iron isotope fractionation in nature: Geology, v. 29, p. 699–702, doi:10.1130/0091-7613(2001)029<0699:DOSAII>2.0.CO;2.

Busigny, V., Planavsky, N.J., Goldbaum, E., Lechte, M.A., Feng, L., and Lyons, T.W., 2018, Origin of the Neoproterozoic Fulu iron formation, South China: Insights from iron isotopes and rare earth element patterns: Geochimica et Cosmochimica Acta, v. 242, p. 123–142, doi:10.1016/j.gca.2018.09.006.

Busigny, V., Planavsky, N.J., Jézéquel, D., Crowe, S., Louvat, P., Moureau, J., Viollier, E., and Lyons, T.W., 2014, Iron isotopes in an Archean ocean analogue: Geochimica et Cosmochimica Acta, v. 133, p. 443–462, doi:10.1016/j.gca.2014.03.004.

Cabral, A.R. et al., 2013, Trace-element and multi-isotope geochemistry of Late-Archean black shales in the Carajás iron-ore district, Brazil: Chemical Geology, v. 362, p. 91–104, doi:10.1016/j.chemgeo.2013.08.041.

Cabral, A.R., Bühn, B., Seabra Gomes, A.A., Galbiatti, H.F., Lehmann, B., and Halder, S., 2017, Multiple sulfur isotopes from the Neoarchaean Serra Sul black shale, Carajás mineral province, northern Brazil: Journal of South American Earth Sciences, v. 79, p. 377–383, doi:10.1016/j.jsames.2017.08.002.

Canfield, D.E., Habicht, K.S., and Thamdrup, B., 2000, The Archean sulfur cycle and the early history of atmospheric oxygen: Science, v. 288, p. 658–661, doi:10.1126/science.288.5466.658.

Canfield, D.E., Rosing, M.T., and Bjerrum, C., 2006, Early anaerobic metabolisms: Philosophical Transactions of the Royal Society B: Biological Sciences, v. 361, p. 1819–1834, doi:10.1098/rstb.2006.1906.

Canfield, D.E., Zhang, S., Wang, H., Wang, X., Zhao, W., Su, J., Bjerrum, C.J., Haxen, E.R., and Hammarlund, E.U., 2018, A Mesoproterozoic iron formation: Proceedings of the National Academy of Sciences of the United States of America, v. 115, p. E3895–E3904, doi:10.1073/pnas.1720529115.

Cotten, J., Le Dez, A., Bau, M., Caroff, M., Maury, R.C., Dulski, P., Fourcade, S., Bohn, M.,

and Brousse, R., 1995, Origin of anomalous rare-earth element and yttrium enrichments in subaerially exposed basalts: Evidence from French Polynesia: Chemical Geology, v. 119, p. 115–138, doi:10.1016/0009-2541(94)00102-E.

Craddock, P.R., and Dauphas, N., 2011, Iron Isotopic Compositions of Geological Reference Materials and Chondrites: Geostandards and Geoanalytical Research, v. 35, p. 101–123, doi:10.1111/j.1751-908X.2010.00085.x.

Croal, L.R., Jiao, Y., Kappler, A., and Newman, D.K., 2009, Phototrophic Fe(II) oxidation in an atmosphere of H2: Implications for Archean banded iron formations: Geobiology, v. 7, p. 21–24, doi:10.1111/j.1472-4669.2008.00185.x.

Croal, L.R., Johnson, C.M., Beard, B.L., and Newman, D.K., 2004, Iron isotope fractionation by Fe(II)-oxidizing photoautotrophic bacteria: Geochimica et Cosmochimica Acta, v. 68, p. 1227–1242, doi:10.1016/j.gca.2003.09.011.

Crosby, H.A., Roden, E.E., Johnson, C.M., and Beard, B.L., 2007, The mechanisms of iron isotope fractionation produced during dissimilatory Fe(III) reduction by Shewanella putrefaciens and Geobacter sulfurreducens: Geobiology, v. 5, p. 169–189, doi:10.1111/j.1472-4669.2007.00103.x.

Crowe, S.A. et al., 2008, Photoferrotrophs thrive in an Archean Ocean analogue: Proceedings of the National Academy of Sciences of the United States of America, v. 105, p. 15938–15943, doi:10.1073/pnas.0805313105.

Czaja, A.D., Johnson, C.M., Beard, B.L., Roden, E.E., Li, W., and Moorbath, S., 2013, Biological Fe oxidation controlled deposition of banded iron formation in the ca. 3770Ma Isua Supracrustal Belt (West Greenland): Earth and Planetary Science Letters, v. 363, p. 192–203, doi:10.1016/j.epsl.2012.12.025.

Czaja, A.D., Van Kranendonk, M.J., Beard, B.L., and Johnson, C.M., 2018, A multistage origin for Neoarchean layered hematite-magnetite iron formation from the Weld

Range, Yilgarn Craton, Western Australia: Chemical Geology, v. 488, p. 125–137, doi:10.1016/j.chemgeo.2018.04.019.

Dalstra, H., and Guedes, S., 2004, Giant hydrothermal hematite deposits with Mg-Fe metasomatism: A comparison of the Carajás, Hamersley, and other iron ores: Economic Geology, v. 99, p. 1793–1800, doi:10.2113/gsecongeo.99.8.1793.

Danielson, A., Möller, P., and Dulski, P., 1992, The europium anomalies in banded iron formations and the thermal history of the oceanic crust: Chemical Geology, v. 97, p. 89–100.

Dauphas, N., Janney, P.E., Mendybaev, R.A., Wadhwa, M., Richter, F.M., Davis, A.M., Van Zuilen, M., Hines, R., and Foley, C.N., 2004a, Hromatographic separation and multicollection-ICPMS analysis of iron. Investigating mass-dependent and -independent isotope effects: Analytical Chemistry, v. 76, p. 5855–5863, doi:10.1021/ac0497095.

Dauphas, N., Pourmand, A., and Teng, F.Z., 2009, Routine isotopic analysis of iron by HR-MC-ICPMS: How precise and how accurate? Chemical Geology, v. 267, p. 175–184, doi:10.1016/j.chemgeo.2008.12.011.

Dauphas, N., van Zuilen, M., Busigny, V., Lepland, A., Wadhwa, M., and Janney, P.E., 2007, Iron isotope, major and trace element characterization of early Archean supracrustal rocks from SW Greenland: Protolith identification and metamorphic overprint: Geochimica et Cosmochimica Acta, v. 71, p. 4745–4770, doi:10.1016/j.gca.2007.07.019.

Dauphas, N., Van Zuilen, M., Wadhwa, M., Davis, A.M., Marty, B., and Janney, P.E., 2004b, Clues from Fe isotope variations on the origin of early Archean BIFs from Greenland: Science, v. 306, p. 2077–2080, doi:10.1126/science.1104639.

Derry, L.A., and Jacobsen, S.B., 1990, The chemical evolution of Precambrian seawater:

Evidence from REEs in banded iron formations: Geochimica et Cosmochimica Acta, v. 54, p. 2965–2977, doi:10.1016/0016-7037(91)90174-4.

Døssing, L.N., Frei, R., Stendal, H., and Mapeo, R.B.M., 2009, Characterization of enriched lithospheric mantle components in ~2.7 Ga Banded Iron Formations: An example from the Tati Greenstone Belt, Northeastern Botswana: Precambrian Research, v. 172, p. 334–356, doi:10.1016/j.precamres.2009.06.004.

Dreher, A.M., Xavier, R.P., and Martini, S.L., 2005, Fragmental rocks if the Igarape Bahia Cu-Au deposits, Carajas minaral Province, Brazil: Revista Brasileira de Geociências, v. 35, p. 359–368.

Fabre, S., Nédélec, A., Poitrasson, F., Strauss, H., Thomazo, C., and Nogueira, A., 2011, Iron and sulphur isotopes from the Carajás mining province (Pará , Brazil): Implications for the oxidation of the ocean and the atmosphere across the Archaean – Proterozoic transition: Chemical Geology, v. 289, p. 124–139, doi:10.1016/j.chemgeo.2011.07.019.

Farquhar, J., Bao, H., and Thiemens, M., 2000, Atmospheric influence of Earth's earliest sulfur cycle: Science, v. 289, p. 756–758, doi:10.1126/science.289.5480.756.

Fischer, W.W., Hemp, J., and Johnson, J.E., 2016, Evolution of Oxygenic Photosynthesis: Annual Review of Earth and Planetary Sciences, v. 44, p. 647–683, doi:10.1146/annurev-earth-060313-054810.

Frei, R., Dahl, P.S., Duke, E.F., Frei, K.M., Hansen, T.R., Frandsson, M.M., and Jensen, L.A., 2008, Trace element and isotopic characterization of Neoarchean and Paleoproterozoic iron formations in the Black Hills (South Dakota, USA): Assessment of chemical change during 2.9-1.9 Ga deposition bracketing the 2.4-2.2 Ga first rise of atmospheric oxygen: Precambrian Research, v. 162, p. 441–474,

doi:10.1016/j.precamres.2007.10.005.

Frei, R., and Polat, A., 2007, Source heterogeneity for the major components of ~ 3.7 Ga Banded Iron Formations (Isua Greenstone Belt, Western Greenland): Tracing the nature of interacting water masses in BIF formation: Earth and Planetary Science Letters, v. 253, p. 266–281, doi:10.1016/j.epsl.2006.10.033.

Frierdich, A.J., Beard, B.L., Scherer, M.M., and Johnson, C.M., 2014, Determination of the Fe(II)aq-magnetite equilibrium iron isotope fractionation factor using the three-isotope method and a multi-direction approach to equilibrium: Earth and Planetary Science Letters, v. 391, p. 77–86, doi:10.1016/j.epsl.2014.01.032.

Frierdich, A.J., Nebel, O., Beard, B.L., and Johnson, C.M., 2019, Iron isotope exchange and fractionation between hematite (α-Fe2O3) and aqueous Fe(II): A combined three-isotope and reversal-approach to equilibrium study: Geochimica et Cosmochimica Acta, v. 245, p. 207–221, doi:10.1016/j.gca.2018.10.033.

Frost, C.D., von Blanckenburg, F., Schoenberg, R., Frost, B.R., and Swapp, S.M., 2007, Preservation of Fe isotope heterogeneities during diagenesis and metamorphism of banded iron formation: Contributions to Mineralogy and Petrology, v. 153, p. 211–235, doi:10.1007/s00410-006-0141-0.

Garcia, T.I., Gorton, M.P., Li, H., Wortmann, U.G., and Spooner, E.T.C., 2016, The geochemistry of the 2.75 Ga-old Helen Iron Formation, Wawa, Ontario - Insights into iron formation deposition from carbon isotopes and rare earth elements: Precambrian Research, v. 275, p. 357–368, doi:10.1016/j.precamres.2016.01.013.

Gauger, T., Byrne, J.M., Konhauser, K.O., Obst, M., Crowe, S., and Kappler, A., 2016, Influence of organics and silica on Fe(II) oxidation rates and cell-mineral aggregate formation by the green-sulfur Fe(II)-oxidizing bacterium Chlorobium ferrooxidans

KoFox - Implications for Fe(II) oxidation in ancient oceans: Earth and Planetary Science Letters, v. 443, p. 81–89, doi:10.1016/j.epsl.2016.03.022.

Gauger, T., Konhauser, K., and Kappler, A., 2015, Protection of phototrophic iron(II)-oxidizing bacteria from UV irradiation by biogenic iron(III) minerals: Implications for early archean banded iron formation: Geology, v. 43, p. 1067–1070, doi:10.1130/G37095.1.

Gibbs, A.K., Wirth, K.R., Hirata, W.K., and Olszewski, W.J., 1986, Age and composition of the Grão Pará Group volcanics, Serra dos Carajás: Revista Brasileira de Geociências, v. 16, p. 201–211.

Halverson, G.P., Poitrasson, F., Hoffman, P.F., Nédélec, A., Montel, J.M., and Kirby, J., 2011, Fe isotope and trace element geochemistry of the Neoproterozoic syn-glacial Rapitan iron formation: Earth and Planetary Science Letters, v. 309, p. 100–112, doi:10.1016/j.epsl.2011.06.021.

Hamilton, T.L., 2019, The trouble with oxygen: The ecophysiology of extant phototrophs and implications for the evolution of oxygenic photosynthesis: Free Radical Biology and Medicine, v. 140, p. 233–249, doi:10.1016/j.freeradbiomed.2019.05.003.

Haugaard, R., Frei, R., Stendald, H., and Konhauser, K., 2013, Petrology and geochemistry of the ~2.9 Ga Itilliarsuk banded iron formation and associated supracrustal rocks, West Greenland: Source characteristics and depositional environment: Precambrian Research, v. 229, p. 150–176, doi:10.1016/j.precamres.2012.04.013.

Haugaard, R., Ootes, L., Creaser, R.A., and Konhauser, K.O., 2016a, The nature of Mesoarchaean seawater and continental weathering in 2.85 Ga banded iron formation, Slave craton, NW Canada: Geochimica et Cosmochimica Acta, v. 194, p. 34–56, doi:10.1016/j.gca.2016.08.020.

Haugaard, R., Ootes, L., and Konhauser, K., 2017, Neoarchaean banded iron formation within a ~2620 Ma turbidite-dominated deep-water basin, Slave craton, NW Canada: Precambrian Research, v. 292, p. 130–151, doi:10.1016/j.precamres.2017.01.025.

Haugaard, R., Pecoits, E., Lalonde, S., Rouxel, O., and Konhauser, K., 2016b, The Joffre banded iron formation, Hamersley Group, Western Australia: Assessing the palaeoenvironment through detailed petrology and chemostratigraphy: Precambrian Research, v. 273, p. 12–37, doi:10.1016/j.precamres.2015.10.024.

Hayes, J.M., 2001, Fractionation of the Isotopes of Carbon and Hydrogen in Biosynthetic Processes, *in* Mineralogical Society of America, p. 1–31.

Heard, A.W., and Dauphas, N., 2020, Constraints on the coevolution of oxic and sulfidic ocean iron sinks from archean-paleoproterozoic iron isotope records: Geology, v. 48, p. 358–362, doi:10.1130/G46951.1.

Hegler, F., Posth, N.R., Jiang, J., and Kappler, A., 2008, Physiology of phototrophic iron(II)-oxidizing bacteria: Implications for modern and ancient environments: FEMS Microbiology Ecology, v. 66, p. 250–260, doi:10.1111/j.1574-6941.2008.00592.x.

Hofmann, A., 2005, The geochemistry of sedimentary rocks from the Fig Tree Group, Barberton greenstone belt: Implications for tectonic, hydrothermal and surface processes during mid-Archaean times: Precambrian Research, v. 143, p. 23–49, doi:10.1016/j.precamres.2005.09.005.

Holland, H.D., 2006, The oxygenation of the atmosphere and oceans: , p. 903–915, doi:10.1098/rstb.2006.1838.

Hyslop, E.V., Valley, J.W., Johnson, C.M., and Beard, B.L., 2008, The effects of metamorphism on O and Fe isotope compositions in the Biwabik Iron Formation, northern Minnesota: Contributions to Mineralogy and Petrology, v. 155, p. 313–328,

doi:10.1007/s00410-007-0244-2.

James, H.L., 1983, Distribution of banded iron-formation in space and time: Developments in Precambrian Geology, v. 6, p. 471–490, doi:10.1016/S0166-2635(08)70053-7.

Johnson, C.M., Beard, B.L., Klein, C., Beukes, N.J., and Roden, E.E., 2008a, Iron isotopes constrain biologic and abiologic processes in banded iron formation genesis: Geochimica et Cosmochimica Acta, v. 72, p. 151–169, doi:10.1016/j.gca.2007.10.013.

Johnson, C.M., Beard, B.L., and Roden, E.E., 2008b, The Iron Isotope Fingerprints of Redox and Biogeochemical Cycling in Modern and Ancient Earth: Annual Review of Earth and Planetary Sciences, v. 36, p. 457–493, doi:10.1146/annurev.earth.36.031207.124139.

Johnson, C.M., Roden, E.E., Welch, S.A., and Beard, B.L., 2005, Experimental constraints on Fe isotope fractionation during magnetite and Fe carbonate formation coupled to dissimilatory hydrous ferric oxide reduction: Geochimica et Cosmochimica Acta, v. 69, p. 963–993, doi:10.1016/j.gca.2004.06.043.

Johnston, D.T., Wolfe-Simon, F., Pearson, A., and Knoll, A.H., 2009, Anoxygenic photosynthesis modulated Proterozoic oxygen and sustained Earth's middle age: Proceedings of the National Academy of Sciences of the United States of America, v. 106, p. 16925–16929, doi:10.1073/pnas.0909248106.

Jones, C., Nomosatryo, S., Crowe, S.A., Bjerrum, C.J., and Canfield, D.E., 2015, Iron oxides, divalent cations, silica, and the early earth phosphorus crisis: Geology, v. 43, p. 135–138, doi:10.1130/G36044.1.

Kappler, A., and Newman, D.K., 2004, Formation of Fe(III)-minerals by Fe(II)-oxidizing photoautotrophic bacteria: Geochimica et Cosmochimica Acta, v. 68, p. 1217–1226, doi:10.1016/j.gca.2003.09.006.

Kappler, A., Pasquero, C., Konhauser, K.O., and Newman, D.K., 2005, Deposition of banded iron formations by anoxygenic phototrophic Fe(II)-oxidizing bacteria: Geology, v. 33, p. 865–868, doi:10.1130/G21658.1.

Klein, C., 2005, Some Precambrian banded iron-formations (BIFs) from around the world: Their age, geologic setting, mineralogy, metamorphism, geochemistry, and origin: American Mineralogist, v. 90, p. 1473–1499, doi:10.2138/am.2005.1871.

Klein, C., and Ladeira, E.A., 2002, Petrography and geochemistry of the least altered banded iron-formation of the Archean Carajás formation, northern Brazil: Economic Geology, v. 97, p. 643–651, doi:10.2113/gsecongeo.97.3.643.

Koeksoy, E., Halama, M., Konhauser, K.O., and Kappler, A., 2016, Using modern ferruginous habitats to interpret Precambrian banded iron formation deposition: International Journal of Astrobiology, v. 15, p. 205–217, doi:10.1017/S1473550415000373.

Konhauser, K.O. et al., 2017, Iron formations: A global record of Neoarchaean to Palaeoproterozoic environmental history: Earth-Science Reviews, v. 172, p. 140–177, doi:10.1016/j.earscirev.2017.06.012.

Konhauser, K.O. et al., 2018, Phytoplankton contributions to the trace-element composition of Precambrian banded iron formations: Bulletin of the Geological Society of America, v. 130, p. 941–951, doi:10.1130/B31648.1.

Konhauser, K.O., Amskold, L., Lalonde, S. V, Posth, N.R., Kappler, A., and Anbar, A., 2007, Decoupling photochemical Fe(II) oxidation from shallow-water BIF deposition: Earth and Planetary Science Letters, v. 258, p. 87–100, doi:10.1016/j.epsl.2007.03.026.

Konhauser, K.O., Hamade, T., Raiswell, R., Morris, R.C., Ferris, F.G., Southam, G., and Canfield, D.E., 2002, Could bacteria have formed the Precambrian banded iron formations? Geology, v. 30, p. 1079–1082, doi:10.1130/0091-

7613(2002)030<1079:CBHFTP>2.0.CO;2.

Krymsky, R.S., Macambira, M.J.B., Lafon, J.M., and Estumano, G.S., 2007, Uranium-lead dating method at the Pará-Iso isotope geology laboratory, UFPA, Belém - Brazil: Anais da Academia Brasileira de Ciencias, v. 79, p. 115–128, doi:10.1590/S0001-37652007000100014.

Lalonde, S. V, and Konhauser, K.O., 2015, Benthic perspective on Earth's oldest evidence for oxygenic photosynthesis: Proceedings of the National Academy of Sciences, v. 112, p. 995–1000, doi:10.1073/pnas.1415718112.

Lantink, M.L., Oonk, P.B.H., Floor, G.H., Tsikos, H., and Mason, P.R.D., 2018, Fe isotopes of a 2.4 Ga hematite-rich IF constrain marine redox conditions around the GOE: Precambrian Research, v. 305, p. 218–235, doi:10.1016/j.precamres.2017.12.025.

Lechte, M.A., Wallace, M.W., van Smeerdijk Hood, A., Li, W., Jiang, G., Halverson, G.P., Asael, D., McColl, S.L., and Planavsky, N.J., 2019, Subglacial meltwater supported aerobic marine habitats during Snowball Earth: Proceedings of the National Academy of Sciences of the United States of America, v. 116, p. 25478–25483, doi:10.1073/pnas.1909165116.

Li, Z.Q., Zhang, L.C., Xue, C.J., Zheng, M.T., Zhu, M.T., Robbins, L.J., Slack, J.F., Planavsky, N.J., and Konhauser, K.O., 2018, Earth's youngest banded iron formation implies ferruginous conditions in the Early Cambrian ocean: Scientific Reports, v. 8, p. 1–10, doi:10.1038/s41598-018-28187-2.

Lindenmayer, Z., Laux, J., and Teixeira, J., 2001, Consideração sobre a origem das formações ferríferas da Formação Carajás, Serra dos Carajás: Revista Brasileira de Geociências, v. 31, p. 21–28.

Llirós, M. et al., 2015, Pelagic photoferrotrophy and iron cycling in a modern ferruginous

basin: Scientific Reports, v. 5, p. 1–8, doi:10.1038/srep13803.

Lottermoser, B.G., and Ashley, P.M., 2000, Geochemistry, petrology and origin of Neoproterozoic ironstones in the eastern part of the Adelaide Geosyncline, South Australia: Precambrian Research, v. 101, p. 49–67, doi:10.1016/S0301-9268(99)00098-4.

Macambira, J.B., and Schrank, A., 2002, Químio-estratigrafia e evolução dos jaspilitos da Formação Carajás (PA): Revista Brasileira de Geociências, v. 32, p. 567–578.

Machado, N., Lindenmayer, Z., Krogh, T.E., and Lindenmayer, D., 1991, U-Pb geochronology of Archean magmatism and basement reactivation in the Carajás area, Amazon shield, Brazil: Precambrian Research, v. 49, p. 329–354, doi:10.1016/0301-9268(91)90040-H.

Martin, W.F., Bryant, D.A., and Beatty, J.T., 2018, A physiological perspective on the origin and evolution of photosynthesis: FEMS Microbiology Reviews, v. 42, p. 205–231, doi:10.1093/FEMSRE/FUX056.

Martins, P.L.G., Toledo, C.L.B., Silva, A.M., Chemale, F., Santos, J.O.S., and Assis, L.M., 2017, Neoarchean magmatism in the southeastern Amazonian Craton, Brazil: Petrography, geochemistry and tectonic significance of basalts from the Carajás Basin: Precambrian Research, v. 302, p. 340–357, doi:10.1016/j.precamres.2017.10.013.

Melo, G.H.C., Monteiro, L.V.S., Xavier, R.P., Moreto, C.P.N., Arquaz, R.M., and Silva, M.A.D., 2019, Evolution of the Igarapé Bahia Cu-Au deposit, Carajás Province (Brazil): Early syngenetic chalcopyrite overprinted by IOCG mineralization: Ore Geology Reviews, v. 111, p. 102993, doi:10.1016/j.oregeorev.2019.102993.

Mloszewska, A.M., Pecoits, E., Cates, N.L., Mojzsis, S.J., O'Neil, J., Robbins, L.J., and Konhauser, K.O., 2012, The composition of Earth's oldest iron formations: The

Nuvvuagittuq Supracrustal Belt (Québec, Canada): Earth and Planetary Science Letters, v. 317–318, p. 331–342, doi:10.1016/j.epsl.2011.11.020.

Moreto, C.P.N., Monteiro, L.V.S., Xavier, R.P., Creaser, R.A., DuFrane, S.A., Tassinari, C.C.G., Sato, K., Kemp, A.I.S., and Amaral, W.S., 2015, Neoarchean and paleoproterozoic iron oxide-copper-gold events at the sossego deposit, Carajás Province, Brazil: Re-Os and U-Pb geochronological evidence: Economic Geology, v. 110, p. 809–835, doi:10.2113/econgeo.110.3.809.

Muller, É., Ader, M., Chaduteau, C., Cartigny, P., Baton, F., and Philippot, P., 2017, The use of chromium reduction in the analysis of organic carbon and inorganic sulfur isotope compositions in Archean rocks: Chemical Geology, v. 457, p. 68–74, doi:10.1016/j.chemgeo.2017.03.014.

Nie, N.X., Dauphas, N., and Greenwood, R.C., 2017, Iron and oxygen isotope fractionation during iron UV photo-oxidation: Implications for early Earth and Mars: Earth and Planetary Science Letters, v. 458, p. 179–191, doi:10.1016/j.epsl.2016.10.035.

Oonk, P.B.H., Mason, P.R.D., Tsikos, H., and Bau, M., 2018, Fraction-specific rare earth elements enable the reconstruction of primary seawater signatures from iron formations: Geochimica et Cosmochimica Acta, v. 238, p. 102–122, doi:10.1016/j.gca.2018.07.005.

Ossa, F.O., Hofmann, A., Spangenberg, J.E., Poulton, S.W., Stüeken, E.E., Schoenberg, R., Eickmann, B., Wille, M., Butler, M., and Bekker, A., 2019, Limited oxygen production in the Mesoarchean ocean: Proceedings of the National Academy of Sciences of the United States of America, v. 116, p. 6647–6652, doi:10.1073/pnas.1818762116.

Ozaki, K., Thompson, K.J., Simister, R.L., Crowe, S.A., and Reinhard, C.T., 2019, Anoxygenic photosynthesis and the delayed oxygenation of Earth's atmosphere:

Nature Communications, v. 10, p. 3026, doi:10.1038/s41467-019-10872-z.

Pecoits, E., Smith, M.L., Catling, D.C., Philippot, P., Kappler, A., and Konhauser, K.O., 2015, Atmospheric hydrogen peroxide and Eoarchean iron formations: Geobiology, v. 13, p. 1–14, doi:10.1111/gbi.12116.

Planavsky, N.J. et al., 2014, Evidence for oxygenic photosynthesis half a billion years before the Great Oxidation Event: Nature Geoscience, v. 7, p. 283–286, doi:10.1038/ngeo2122.

Planavsky, N., Bekker, A., Rouxel, O.J., Kamber, B., Hofmann, A., Knudsen, A., and Lyons, T.W., 2010, Rare Earth Element and yttrium compositions of Archean and Paleoproterozoic Fe formations revisited: New perspectives on the significance and mechanisms of deposition: Geochimica et Cosmochimica Acta, v. 74, p. 6387–6405, doi:10.1016/j.gca.2010.07.021.

Planavsky, N., Rouxel, O.J., Bekker, A., Hofmann, A., Little, C.T.S., and Lyons, T.W., 2012, Iron isotope composition of some Archean and Proterozoic iron formations: Geochimica et Cosmochimica Acta, v. 80, p. 158–169, doi:10.1016/j.gca.2011.12.001.

Posth, N.R., Hegler, F., Konhauser, K.O., and Kappler, A., 2008, Alternating Si and Fe deposition caused by temperature fluctuations in Precambrian oceans: Nature Geoscience, v. 1, p. 703–708, doi:10.1038/ngeo306.

Ribeiro da Luz, B., and Crowley, J.K., 2012, Morphological and chemical evidence of stromatolitic deposits in the 2.75Ga Carajás banded iron formation, Brazil: Earth and Planetary Science Letters, v. 355–356, p. 60–72, doi:10.1016/j.epsl.2012.08.028.

Robbins, L.J. et al., 2019a, Hydrogeological constraints on the formation of Palaeoproterozoic banded iron formations: Nature Geoscience, v. 12, p. 558–563, doi:10.1038/s41561-019-0372-0.

Robbins, L.J., Konhauser, K.O., Warchola, T.J., Homann, M., Thoby, M., Foster, I.,

Mloszewska, A.M., Alessi, D.S., and Lalonde, S. V., 2019b, A comparison of bulk versus laser ablation trace element analyses in banded iron formations: Insights into the mechanisms leading to compositional variability: Chemical Geology, v. 506, p. 197–224, doi:10.1016/j.chemgeo.2018.12.036.

Rosière, C.A., Baars, F.J., Seoane, J.C.S., Lobato, L.M., da Silva, L.L., de Souza, S.R.C., and Mendes, G.E., 2006, Structure and iron mineralisation of the Carajás Province: Transactions of the Institutions of Mining and Metallurgy, Section B: Applied Earth Science, v. 115, p. 126–133, doi:10.1179/174327506X138986.

Rossignol, C., Siciliano Rego, E., Narduzzi, F., Teixeira, L., Ávila, J.N., Silva, M.A.L., Lana, C., and Philippot, P., 2020, Stratigraphy and geochronological constraints of the Serra Sul Formation (Carajás Basin, Amazonian Craton, Brazil): Precambrian Research, v. 351, p. 105981, doi:10.1016/j.precamres.2020.105981.

Rouxel, O.J., Bekker, A., and Edwards, K.J., 2005, Iron Isotope Constraints on the Archean and Paleoproterozoic Ocean Redox State: Science, v. 307, p. 1088–1091, doi:10.1126/science.1105692.

Rouxel, O., Dobbek, N., Ludden, J., and Fouquet, Y., 2003, Iron isotope fractionation during oceanic crust alteration: Chemical Geology, v. 202, p. 155–182, doi:10.1016/j.chemgeo.2003.08.011.

Rouxel, O., Toner, B., Germain, Y., and Glazer, B., 2018, Geochemical and iron isotopic insights into hydrothermal iron oxyhydroxide deposit formation at Loihi Seamount: Geochimica et Cosmochimica Acta, v. 220, p. 449–482, doi:10.1016/j.gca.2017.09.050.

Sampaio, G.M.S., Pufahl, P.K., Raye, U., Kyser, K.T., Abreu, A.T., Alkmim, A.R., and Nalini, H.A., 2018, Influence of weathering and hydrothermal alteration on the REE and δ56Fe composition of iron formation, Cauê Formation, Iron Quadrangle, Brazil: Chemical Geology, v. 497, p. 27–40, doi:10.1016/j.chemgeo.2018.08.014.

Satkoski, A.M., Beukes, N.J., Li, W., Beard, B.L., and Johnson, C.M., 2015, A redox-stratified ocean 3.2 billion years ago: Earth and Planetary Science Letters, v. 430, p. 43–53, doi:10.1016/j.epsl.2015.08.007.

Schad, M., Konhauser, K.O., Sánchez-Baracaldo, P., Kappler, A., and Bryce, C., 2019, How did the evolution of oxygenic photosynthesis influence the temporal and spatial development of the microbial iron cycle on ancient Earth? Free Radical Biology and Medicine, v. 140, p. 154–166, doi:10.1016/j.freeradbiomed.2019.07.014.

Schidlowski, M., 2001, Carbon isotopes as biogeochemical recorders of life over 3.8 Ga of earth history: Evolution of a concept: Precambrian Research, v. 106, p. 117–134, doi:10.1016/S0301-9268(00)00128-5.

Schoenberg, R., and Von Blanckenburg, F., 2005, An assessment of the accuracy of stable Fe isotope ratio measurements on samples with organic and inorganic matrices by high-resolution multicollector ICP-MS: International Journal of Mass Spectrometry, v. 242, p. 257–272, doi:10.1016/j.ijms.2004.11.025.

Smith, A.J.B., Beukes, N.J., and Gutzmer, J., 2013, The Composition and Depositional Environments of Mesoarchean Iron Formations of the West Rand Group of the Witwatersrand Supergroup, South Africa: Economic Geology, v. 108, p. 111–134, doi:10.2113/econgeo.108.1.111.

Strelow, F.W.E., 1980, Improved separation of iron from copper and other elements by anion-exchange chromatography on a 4% cross-linked resin with high concentrations of hydrochloric acid: Talanta, v. 27, p. 727–732, doi:10.1016/0039-9140(80)80166-4.

Swanner, E.D., Mloszewska, A.M., Cirpka, O.A., Schoenberg, R., Konhauser, K.O., and Kappler, A., 2015a, Modulation of oxygen production in Archaean oceans by episodes of Fe(II) toxicity: Nature Geoscience, v. 8, p. 126–130, doi:10.1038/ngeo2327.

Swanner, E.D., Wu, W., Schoenberg, R., Byrne, J., Michel, F.M., Pan, Y., and Kappler, A., 2015b, Fractionation of Fe isotopes during Fe(II) oxidation by a marine photoferrotroph is controlled by the formation of organic Fe-complexes and colloidal Fe fractions: Geochimica et Cosmochimica Acta, v. 165, p. 44–61, doi:10.1016/j.gca.2015.05.024.

Tangalos, G.E., Beard, B.L., Johnson, C.M., Alpers, C.N., Shelobolina, E.S., Xu, H., Konishi, H., and Roden, E.E., 2010, Microbial production of isotopically light iron(II) in a modern chemically precipitated sediment and implications for isotopic variations in ancient rocks: Geobiology, v. 8, p. 197–208, doi:10.1111/j.1472-4669.2010.00237.x.

Taylor, P.D.P., Maeck, R., and De Bièvre, P., 1992, Determination of the absolute isotopic composition and Atomic Weight of a reference sample of natural iron: International Journal of Mass Spectrometry and Ion Processes, v. 121, p. 111–125, doi:10.1016/0168-1176(92)80075-C.

Teixeira, N.L., Caxito, F.A., Rosière, C.A., Pecoits, E., Vieira, L., Frei, R., Sial, A.N., and Poitrasson, F., 2017, Trace elements and isotope geochemistry (C, O, Fe, Cr) of the Cauê iron formation, Quadrilátero Ferrífero, Brazil: Evidence for widespread microbial dissimilatory iron reduction at the Archean/Paleoproterozoic transition: Precambrian Research, v. 298, p. 39–55, doi:10.1016/j.precamres.2017.05.009.

Thompson, K.J. et al., 2019, Photoferrotrophy, deposition of banded iron formations, and methane production in Archean oceans: Science Advances, v. 5, p. 1–10, doi:10.1126/sciadv.aav2869.

Thompson, K.J., Simister, R.L., Hahn, A.S., Hallam, S.J., and Crowe, S.A., 2017, Nutrient acquisition and the metabolic potential of photoferrotrophic Chlorobi: Frontiers in Microbiology, v. 8, p. 1–16, doi:10.3389/fmicb.2017.01212.

Tolbert, G.E., Tremaine, J.W., Melcher, G.C., and Gomes, C.B., 1971, The Recently Discovered Serra dos Carajas Iron Deposits, Northern Brazil: Economic Geology, v. 66, p. 985–994, doi:10.2113/gsecongeo.66.7.985.

Tosca, N.J., Guggenheim, S., and Pufahl, P.K., 2016, An authigenic origin for Precambrian greenalite: Implications for iron formation and the chemistry of ancient seawater: Bulletin of the Geological Society of America, v. 128, p. 511–530, doi:10.1130/B31339.1.

Trendall, A.F., Basei, M.A.S., De Laeter, J.R., and Nelson, D.R., 1998, SHRIMP zircon U-Pb constraints on the age of the Carajas formation, Grao Para Group, Amazon Craton: Journal of South American Earth Sciences, v. 11, p. 265–277, doi:10.1016/S0895-9811(98)00015-7.

Viehmann, S., Bau, M., Bühn, B., Dantas, E.L., Andrade, F.R.D., and Walde, D.H.G., 2016, Geochemical characterisation of Neoproterozoic marine habitats: Evidence from trace elements and Nd isotopes in the Urucum iron and manganese formations, Brazil: Precambrian Research, v. 282, p. 74–96, doi:10.1016/j.precamres.2016.07.006.

Viehmann, S., Bau, M., Hoffmann, J.E., and Münker, C., 2015a, Geochemistry of the Krivoy Rog Banded Iron Formation, Ukraine, and the impact of peak episodes of increased global magmatic activity on the trace element composition of Precambrian seawater: Precambrian Research, v. 270, p. 165–180, doi:10.1016/j.precamres.2015.09.015.

Viehmann, S., Bau, M., Smith, A.J.B., Beukes, N.J., Dantas, E.L., and Bühn, B., 2015b, The reliability of ~2.9 Ga old Witwatersrand banded iron formations (South Africa) as archives for Mesoarchean seawater: Evidence from REE and Nd isotope systematics: Journal of African Earth Sciences, v. 111, p. 322–334,

doi:10.1016/j.jafrearsci.2015.08.013.

Walter, X.A., Picazo, A., Miracle, M.R., Vicente, E., Camacho, A., Aragno, M., and Zopfi, J., 2014, Phototrophic Fe(II)-oxidation in the chemocline of a ferruginous meromictic lake: Frontiers in Microbiology, v. 5, p. 1–9, doi:10.3389/fmicb.2014.00713.

Wang, C., Konhauser, K.O., Zhang, L., Zhai, M., and Li, W., 2016, Decoupled sources of the 2.3-2.2 Ga Yuanjiacun banded iron formation: Implications for the Nd cycle in Earth's early oceans: Precambrian Research, v. 280, p. 1–13, doi:10.1016/j.precamres.2016.04.016.

Warchola, T., Lalonde, S. V., Pecoits, E., von Gunten, K., Robbins, L.J., Alessi, D.S., Philippot, P., and Konhauser, K.O., 2018, Petrology and geochemistry of the Boolgeeda Iron Formation, Hamersley Basin, Western Australia: Precambrian Research, v. 316, p. 155–173, doi:10.1016/j.precamres.2018.07.015.

Webb, G.E., and Kamber, B.S., 2000, Rare earth elements in Holocene reefal microbialites: a new shallow seawater proxy: Geochimica et Cosmochimica Acta, v. 64, p. 1557–1565, doi:10.1016/S0016-7037(99)00400-7.

Weyer, S., and Schwieters, J.B., 2003, High precision Fe isotope measurements with high mass resolution MC-ICPMS: International Journal of Mass Spectrometry, v. 226, p. 355–368, doi:10.1016/S1387-3806(03)00078-2.

Widdel, F., Schnell, S., Heising, S., Ehrenreich, A., Assmus, B., and Schink, B., 1993, Ferrous iron oxidation by anoxygenic phototrophic bacteria: Nature, v. 362, p. 834–836, doi:10.1038/362834a0.

Wiesli, R.A., Beard, B.L., and Johnson, C.M., 2004, Experimental determination of Fe isotope fractionation between aqueous Fe(II), siderite and "green rust" in abiotic systems: Chemical Geology, v. 211, p. 343–362, doi:10.1016/j.chemgeo.2004.07.002.

Wu, L., Percak-Dennett, E.M., Beard, B.L., Roden, E.E., and Johnson, C.M., 2012, Stable

iron isotope fractionation between aqueous Fe(II) and model Archean ocean Fe-Si coprecipitates and implications for iron isotope variations in the ancient rock record: Geochimica et Cosmochimica Acta, v. 84, p. 14–28, doi:10.1016/j.gca.2012.01.007.

Wu, W., Swanner, E.D., Kleinhanns, I.C., Schoenberg, R., Pan, Y., and Kappler, A., 2017, Fe isotope fractionation during Fe(II) oxidation by the marine photoferrotroph Rhodovulum iodosum in the presence of Si – Implications for Precambrian iron formation deposition: Geochimica et Cosmochimica Acta, v. 211, p. 307–321, doi:10.1016/j.gca.2017.05.033.

Zhang, J., and Nozaki, Y., 1996, Rare earth elements and yttrium in seawater: ICP-MS determinations in the East Caroline, Coral Sea, and South Fiji basins of the western South Pacific Ocean: Geochimica et Cosmochimica Acta, v. 60, p. 4631–4644, doi:10.1016/S0016-7037(96)00276-1.

CHAPTER 5

5. Low phosphorus concentrations and important ferric hydroxide scavenging in Archean seawater

Abstract

The availability of nutrients in seawater, such as dissolved phosphorous (P), is thought to have regulated the evolution and activity of microbial life in Earth's early oceans. Marine concentrations of bioavailable phosphorous spanning the Archean Eon remain debated, with variable estimates indicating either low (0.04 to 0.13 μM P) or high (10 to 100 μM P) dissolved P in seawater. The large uncertainty on these estimates reflects in part a lack of clear proxy signals recorded in sedimentary rocks. Contrary to some recent views, we show here that iron formations (IFs) are reliable recorders of past phosphorous concentrations and preserved a primary seawater signature. Using measured P and iron (Fe) contents in Neoarchean IF from Carajás (Brazil), we demonstrate for the first time a clear partitioning coefficient relationship in the P-Fe systematics of this IF which, in combination with experimental and Archean literature data, permits us to constrain Archean seawater to a mean value of 0.063 ± 0.05 μM dissolved phosphorous. Our dataset suggests that low-phosphorus conditions prevailed throughout the first half of Earth's history, likely as the result of limited continental emergence, supporting prior suggestions that changes in ancient marine P availability and recycling at the end of the Archean ultimately modulated the redox state of Earth's early oceans and atmosphere.

5.1 Introduction

Phosphorus (P) is an essential nutrient for all living organisms on Earth and its availability has been crucial for the development and proliferation of life on geological time scales (Westheimer, 1987; Tyrrell T., 1999). In the oceans, P availability has a significant control on biological productivity, and its concentration throughout Earth's history likely modulated the redox state of the ocean and atmosphere (Bjerrum and Canfield, 2002; Hao et al., 2020; Alcott et al., 2022). Quantitatively assessing past oceanic P levels based on the geological record has been a major challenge in previous studies, but it is of paramount importance for understanding biological and geochemical evolution through time (Planavsky et al., 2010b; Reinhard et al., 2017b).

Reconstructions of dissolved P concentrations in Precambrian oceans are highly debated and rely to a large extent on iron (Fe) and P contents measured in iron-rich chemical sediments, which are interpreted to reflect seawater conditions at their time of formation (Bjerrum and Canfield, 2002; Planavsky et al., 2010b; Jones et al., 2015). Previous works support contrasting views of either low dissolved P concentrations in Archean seawater (< 1 μM) compared to average modern values (~2.3 μM) (Bjerrum and Canfield, 2002; Jones et al., 2015), or significantly higher P content in seawater, particularly prior to 2.45 Ga, with proposed concentrations from 5 to 50 times higher than modern values (~10 μM to 100 μM; (Rasmussen et al., 2021; Ingalls et al., 2022).

Phosphorus concentrations in ancient seawater can be estimated using the phosphorus to iron ratio (P/Fe) in well-preserved Fe-rich chemical sedimentary rocks (Bjerrum and Canfield, 2002; Konhauser et al., 2007; Planavsky et al., 2010; Jones et al., 2015). This relies on the premise that iron oxide P/Fe ratios scale linearly as a function of ambient dissolved phosphate (PO_4^{3-}) concentrations according to a predictable

distribution coefficient model, as observed to occur in modern hydrothermal plumes (Feely et al., 1998). Therefore, dissolved phosphate concentration (P_D) in a given solution is equal to the P/Fe ratios in ferric oxyhydroxide precipitates divided by a specific distribution coefficient (K_D) representative of the fluid's composition, such that: $[P_D] = (1/K_D) \times P/Fe$ (Bjerrum and Canfield, 2002). Given that K_D values will change in relation to the fluid's composition, as shown by the enrichment and/or depletion of Si and divalent cations (Ca^{2+}, Mg^{2+}) inhibiting and/or facilitating P adsorption, experimental studies have proposed distribution coefficients representative of Archean and Proterozoic seawater (Konhauser, 2007; Jones et al., 2015), thus allowing new estimates of dissolved P in ancient ocean to be determined.

However, despite clear correlation between P and Fe in modern sediments (Berner 1973, Feely et al., 1998), no such evidence has ever been reported in samples from the Precambrian rock record. On the contrary, a lack of correlation was observed in ~2.45 Ga old iron formations from Australia and South Africa, suggesting that these rocks did not capture past oceanic conditions (Rasmussen et al., 2021). It remains to be seen whether other IF deposits may record P-Fe systematics indicative of P uptake behavior conforming with the distribution coefficient model, and thus may be useful for constraining the paleomarine P reservoir. Here, we use P and Fe contents from Archean iron-rich chemical sediments to investigate the potential of iron formations as recorders of past P contents in seawater, and to estimate dissolved P concentrations in seawater prior to the Great Oxidation Event (GOE). Our work is based on Neoarchean (~2.74 Ga) sedimentary rocks from Carajás, Brazil, along with previously published P/Fe ratios from Archean Iron Formations (IFs), modern environmental data, and laboratory experiments. The sedimentary succession studied (*see* Supp. Mat.) include IFs

intercalated with several Fe-rich and Fe-poor carbonate intervals, therefore representing an opportunity for evaluating P levels in the ocean independently of these lithological variations. Collectively, the results provide key insights into past nutrient availability, which likely influenced the dynamics of oxygen production and accumulation in Earth's Precambrian oceans and atmosphere.

5.2 Identifying an Archean Fe-P trap

The weight percent (wt.%) variations of P_2O_5 and total Fe (Fe_2O_3) in the studied IF samples range from 0.076 to 0.1 wt.% and 37.7 to 63.1 wt.%, respectively, while Fe-carbonates (Fe-rich and Fe-poor) have P_2O_5 and Fe_2O_3 contents varying between 0.039 to 0.079 wt.% and 16.9 to 45.8 wt.%, respectively. A well-defined positive correlation is observed between the concentrations of P_2O_5 and Fe_2O_3 measured in the different chemical sedimentary lithologies from the Carajás Formation (Fig. 5.1a). Moreover, when compared to whole-rock IF literature data filtered for low detritus (<0.3 wt.% Al), our samples are within the range of values measured for other Archean samples (3.8 to 2.6 Ga, Fig. 5.1b), although less scattered. Our results show a similar trend to the one measured in modern hydrothermal systems (*e.g.* positive correlation between P_2O_5 and Fe_2O_3), but with a different slope. The modern correlation is interpreted as reflecting the adsorption of dissolved bioavailable phosphate (PO_4^{3-}) onto Fe-oxide precipitates (Berner, 1973; Wheat et al., 1996; Feely et al., 1998). Previous studies relied on this observational model to propose an active P-removal from seawater by Fe-oxide precipitation in the Archean ocean (Fe-P trap; Bjerrum and Canfield, 2002; Jones et al., 2015).

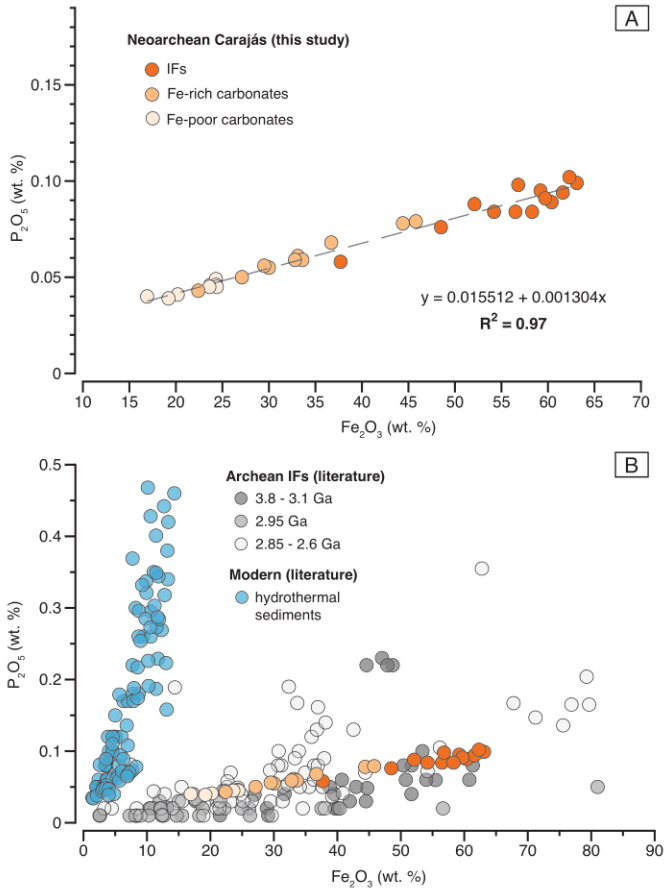

Figure 5. 1: Variations of bulk Fe_2O_3 and P_2O_5 measured in (A) Neoarchean (~2.74 Ga-old) iron formations, Fe-rich and Fe-poor carbonates from Carajás Brazil, and compared in (B) to Archean IF literature data (3.8 – 2.6 Ga; Bjerrum and Canfield, 2002; Bhattacharya et al., 2007; Cates and Mojzsis, 2007; Alexander et al., 2008; Nutman et al., 2010; Planavsky et al., 2010; Mloszewska et al., 2012; Haugaard et al., 2016; Araújo and Lobato, 2019) and modern hydrothermal sediments (Lyle, 1986)

The trend defined by the Carajás samples consisting of different rock types (carbonates and IFs) further supports the interpretation that Fe-oxides were likely responsible for P removal from seawater during the Archean, as observed in modern environments (Fig. 5.1). This in turn indicates that ferric oxyhydroxides, and not simply ferrous hydroxides, were primary mineral phases in IFs (*e.g.* Robbins et al., 2019). More importantly, our data demonstrates empirically for the first time that IFs may indeed

show P-Fe systematics consistent with aqueous adsorptive and co-precipitative partitioning according to the distribution coefficient model. This evidence confirms that a Fe-P trap mechanism was in fact operating, certainly for the Carajás IF (2.74 Ga), and probably for others deposited between 3.8 to 2.6 Ga. Whether this mechanism limited past ocean P availability (*e.g.* dissolved P concentrations) is still an ongoing question (Rasmussen et al., 2021) and requires further assessment. Nonetheless, given the correlation between P and Fe for the Carajás samples (R^2 = 0.97), we can estimate the concentration of dissolved P in seawater using the slope of the linear regression (~0.0013) combined with previous published distribution coefficient ([K_D]) values (Table 5.1, Table 5.1).

5.3 Archean P *vs*. Fe trend – preservation *vs*. alteration

The Archean literature dataset broadly overlaps with the newly analyzed Carajás samples. However, literature values display larger scattering in P-Fe space (R^2 = 0.34), which contrasts with well-correlated Carajás values (*e.g*. R^2=0.97) (Fig. 5.2). Such differences could be related to rock preservation effects. For instance, a loss of Fe and/or P during diagenetic and metamorphic reactions would be expected to produce some variability, hence scattering, in the primary composition of the sediments. These conditions are observed in the ancient rock record, where Fe can be leached by metasomatic fluids (Dauphas et al., 2007), and also in modern environments analogous of Archean settings, where the reduction and dissolution of ferric oxyhydroxides release previously adsorbed phosphate to the water column, allowing Fe(II) phosphate mineral

(*e.g*. vivianite) to precipitate (Busigny et al., 2016). Vivianite, once precipitated, can react with calcite with increasing temperature and pressure to form apatite (Hao et al., 2020). Considering that reduction of Fe(III) minerals was likely occurring in the Archean (*e.g*. dissimilatory iron reduction; Archer and Vance, 2006; Craddock and Dauphas, 2011; Marin-Carbonne et al., 2020), and that each location was exposed to different metamorphic regimes (*e.g*. low-greenschist to high-amphibolite facies), it is likely that varying proportions of Fe and P loss will be imprinted in Archean samples, thus supporting the scattering observed in Figure 5.2.

Table 5. 1: Estimations of dissolved P for Carajás samples based on K_D values taken from NaCl and seawater experiments.

Experimental Conditions	K_D values	P (μM)[1]
Seawater + 0 mM Si	0.338	0.004
Seawater + 0.67 mM Si	0.042	0.03
Seawater + 2.2 mM Si	0.008	0.18

[1]Estimated dissolved P based on P/Fe mol ratio (0.0015) for Carajás IFs (2.74 Ga).

On the contrary, the preserved correlation between Fe and P in Neoarchean Carajás samples can be explained by two scenarios. These are (i) minimal loss of Fe and P, suggesting remarkable sample preservation, resembling modern hydrothermal environments and/or (ii) loss of Fe and P in similar molar proportions, which would not have affected the primary correlation. The first scenario might have been favored for the Carajás IF considering that it shows abundant carbonate-facies IF, and that the same enhanced alkalinity favoring calcium carbonate precipitation may also act to trap P in sediments by promoting carbonate fluorapatite formation (Zhao et al., 2020). Although the second scenario seems unlikely, we cannot completely exclude it. In any case, this is

not critical to our interpretation as it would imply an unmodified P/Fe ratio. Moreover, measured P/Fe ratios from Neoarchean Carajás and Archean literature data both define a log normal distribution, while P and Fe concentrations show linear correlations with slopes of 0.0013 for Carajás and 0.0020 for Archean data (Fig. 5.2).

The P/Fe ratio of Carajás IF is thus relatively similar to other Archean IFs. Therefore, estimates of dissolved P based on P/Fe ratios in the Archean (*e.g.* Planavsky et al., 2010; Jones et al., 2015) should be well-represented by combining and comparing the two datasets.

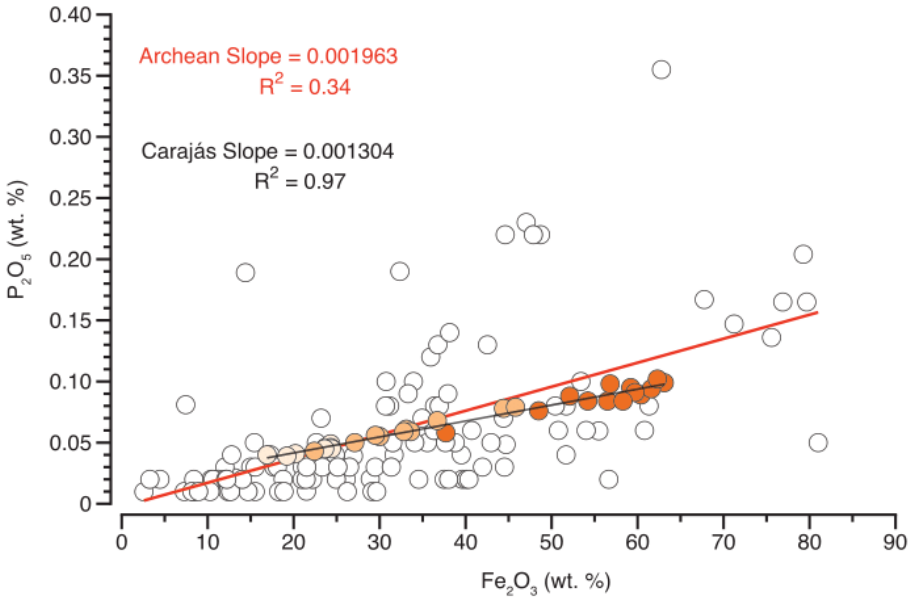

Figure 5. 2: Comparison of linear regressions based on Fe_2O_3 (wt. %) and P_2O_5 (wt. %) contents from Archean and Carajás datasets showing their respective slopes and R^2 coefficients.

5.4 Phosphorus-limited Archean ocean

Laboratory experiments have demonstrated that Si and other ferrihydrite-reactive ions may significantly influence P adsorption by competitive interactions, especially Si

(Konhauser et al., 2007). Given that Archean oceans had different chemistry compared to modern oceans, Jones et al. (2015) proposed a wide range of distribution coefficients (K_D) representative of Precambrian's seawater composition. When combining all K_D values for solutions with varying Si, Ca^{2+}, and Mg^{2+} contents with the P/Fe ratio (0.0015) from the Neoarchean Carajás succession, the estimated dissolved P concentration in paleoseawater ranges from 0.004 μM (for seawater with no dissolved silica) to 0.18 μM (for seawater with 2.2 mM Si) (Table 5.1). The estimated concentration of 0.004 μM [P] can be regarded as a minimum but unrealistic value given that Archean seawater was likely Si-rich (Konhauser et al., 2007). Concentrations reaching 0.18 μM [P] were calculated based on seawater saturated in Si with respect to amorphous silica (2.2 mM Si). However, Si content reaching 2.2 mM in seawater has been argued as a theoretical maximum for the Precambrian ocean (Jones et al., 2015). Therefore, dissolved P in Archean seawater during Carajás deposition was likely in the range of 0.004 μM < $P_{Carajás}$ μM <0.18 μM. The highest possible scenario for dissolved P in Carajás paleoseawater (0.18 μM), even though an overestimation, represents only 7.8% of the present-day value. This indicates a low-P content in Carajás paleoseawater compared to modern ocean. Our estimates are in good agreement with studies advocating low P conditions during the Archean (0.04 to 0.13 μM; Jones et al., 2015), but contrast with those arguing for P concentrations similar to (~2.0 μM; Planasvky et al., 2010) or significantly higher than (up to 100 μM; Rasmussen et al., 2021; Ingalls et al., 2022) modern values.

In order to discuss the evolution of the marine P reservoir throughout the Archean, it is necessary to establish an approximate value of dissolved Si in ancient seawater. Based on Jones et al. (2015), Si concentrations in the Archean ocean were likely between 0.5 to

1.5 mM as determined from Si:Fe ratios in IFs and Si sorption experiments to Fe-oxides. Therefore, we used here a K_D value reflecting seawater with 0.67 mM Si ($K_D = 0.042$), which is the proposed distribution coefficient for Archean seawater in equilibrium with respect to cristobalite, the intermediate scenario between low (0 mM) and high (2.2 mM) Si end-members (Jones et al., 2015). Based on this K_D value, we estimated dissolved P using previously measured P/Fe ratios from Archean IFs (3.8 to 2.6 Ga; Bhattacharya et al., 2007; Cates and Mojzsis, 2007; Alexander et al., 2008; Nutman et al., 2010; Mloszewska et al., 2012; Haugaard et al., 2016; Araújo and Lobato, 2019), including previously published P compilation datasets (3.2 to 2.6 Ga, Bjerrum and Canfield, 2002; 2.9 to 2.6 Ga, Planavsky et al., 2010).

Based on the varying P/Fe ratios and a K_D value representative of Archean seawater, it is possible to infer that from 3.8 to 2.6 Ga, dissolved P concentrations were on average 0.063 ± 0.05 μM (n = 145), with minimum and maximum values of 0.01 μM and 0.3 μM, respectively (Fig. 5.3). Planavsky et al. (2010) argued that Archean P levels were similar to modern-day values. However, when applying the same K_D value used in this study to their measured Archean P/Fe ratios (2.95 – 2.6 Ga), we estimate concentrations of dissolved P to be generally < 0.2 μM, thus still supporting low phosphorus contents in Archean seawater. We were not able, however, to reproduce higher P concentrations from 10 μM to 100 μM using available IF P/Fe ratio data.

Overestimations of marine P concentrations up to 100 μM during the Archean (Rasmussen et al., 2021) seems unreasonable in light of the present results. Rasmussen et al. (2021) argued that Fe-oxides did not control phosphorus removal from the water column due to the lack of correlation between P and Fe in their Paleoproterozoic dataset. The compilation presented in our study suggests that the apparent lack of correlation in

their data might be the result of a dataset of limited size (*e.g.* only three studies from early Paleoproterozoic in South Africa and Australia including Trendall and Blockley, 1970; Klein and Beukes, 1989; Beukes and Klein, 1990). Moreover, the authors do not consider that some of these correlations might not be preserved due to later diagenetic effects, such as Fe and/or P loss and/or apatite precipitation due to the reaction of vivianite and calcite associated with burial diagenesis (Hao et al., 2020). Furthermore, it may prove that special conditions (such as high alkalinity favoring P retention via apatite formation) might be required to limit post-depositional P loss and permit the preservation of adsorptive P-Fe scaling relationships in the rock record. Furthermore, the authors considered the results obtained on cherts, containing virtually no Fe oxides, to be readily extrapolated to IFs (with 10 to 50 wt.% Fe), which is clearly not the case. The present dataset, encompassing a large number of Archean IFs of different ages (Bjerrum and Canfield, 2002; Bhattacharya et al., 2007; Cates and Mojzsis, 2007; Alexander et al., 2008; Nutman et al., 2010; Planavsky et al., 2010; Mloszewska et al., 2012; Haugaard et al., 2016; Araújo and Lobato, 2019), suggests that scavenging of phosphorus by Fe-oxyhydroxide particles was the rule in Archean oceans. This further supports the convention that Fe-oxyhydroxides were indeed a primary mineral phase precipitating from Archean seawater (Konhauser et al., 2017; Robbins et al., 2019a). In contrast, the rare evidence available that suggests that Archean seawater P concentrations could have been relatively high (*e.g.* sustaining calcium phosphate mineral precipitation from seawater; Rasmussen et al., 2021) may possibly reflect diagenetic processes or local exceptions.

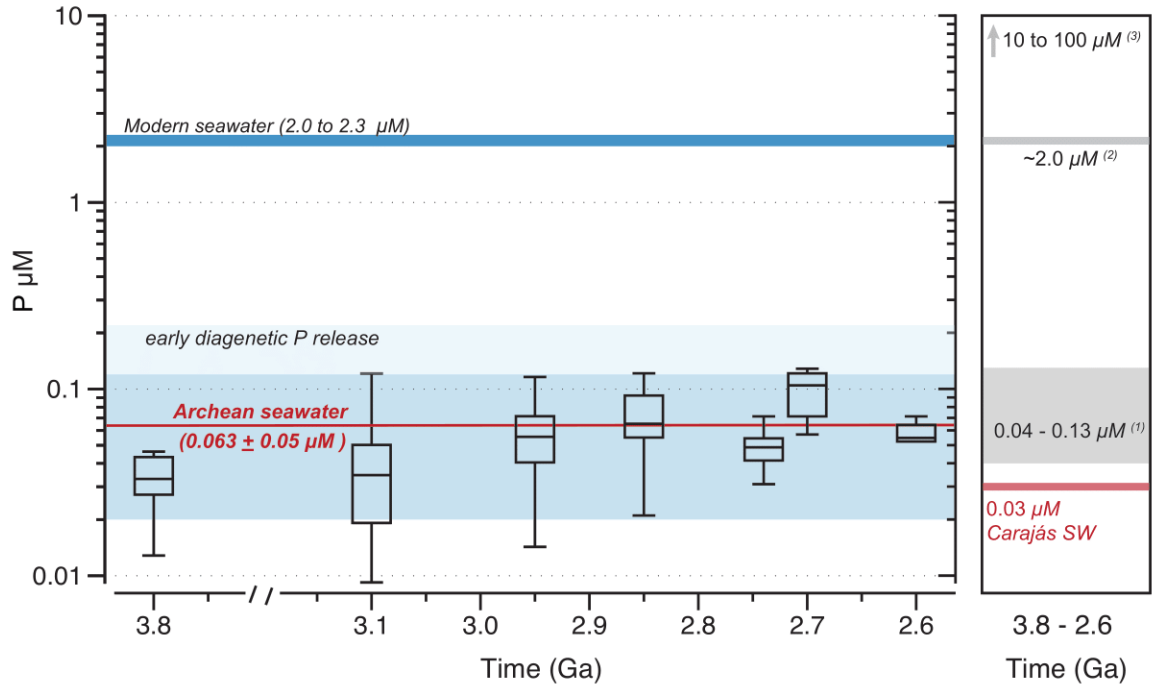

Figure 5. 3: Box-plot showing data distribution for estimates of dissolved phosphorus in Archean seawater with 0.67 mM of Si from 3.8 to 2.6 Ga from measured and literature P/Fe ratios (Bjerrum and Canfield, 2002; Bhattacharya et al., 2007; Cates and Mojzsis, 2007; Alexander et al., 2008; Nutman et al., 2010; Planavsky et al., 2010; Mloszewska et al., 2012; Haugaard et al., 2016; Araújo and Lobato, 2019). Average dissolved P concentration for Archean is shown with red line, while one standard deviation is illustrated by the blue-shaded area. Modern seawater (Feely et al., 1998) is shown for comparison. The right panel summarizes the previous estimates of P concentrations in Archean ocean (*e.g.* (1) Jones et al., 2015; (2) Planavsky et al., 2010; (3) Rasmussen et al., 2021). The light-blue area represents the range of P concentration of Archean seawater, assuming the sediments experienced 50% loss during early diagenesis.

Our observation of P-Fe scaling relationships in IF consistent with partitioning via a distribution coefficient model provides new support for their application as a proxy of Archean seawater P concentrations, and our new analyses clearly indicate that Earth's ocean surface was likely P-limited. Although the present data (Fig. 5.1b) suggest minor modifications related to diagenesis, assuming a typical release up to 50% of the adsorbed phosphorus to the overlying seawater (Jones et al., 2015) would imply that Archean P concentrations were at least 10 times lower than modern-day values (Fig. 5.3). This low

P availability likely reflects the balance of more important phosphorous sinks (*e.g*. iron formation scavenging) relative to limited sources, such as weathering of emerged continental landmasses, which increased significantly only towards the end of the Archean (Bindeman et al., 2018; Alcott et al., 2022).

5.5 Conclusions and implications

Our results provide evidence that scavenging of dissolved P by Fe-oxide precipitates was an active mechanism throughout the Archean Era. The concept of an Fe-P trap mechanism in the Precambrian was first suggested based on modern observational data (Berner, 1973; Wheat et al., 1996; Feely et al., 1998; Bjerrum and Canfield, 2002), which was later supported by numerical simulations (Derry, 2015; Reinhard et al., 2017). However, clear empirical constraints from the rock record on marine P concentrations in deep time were lacking. Iron formations from Carajás combined with a larger Archean literature dataset supports the notion of a low phosphorus ocean and highlights the capability of IFs to record past environmental conditions by the predictable nature of their trace element adsorption reactions. Using the analogous nature of P-Fe partitioning in Carajás IFs compared to modern marine environments as well as experimental studies, we estimated dissolved phosphorous contents in paleoseawater locally and globally, based on measured, experimental, and literature data. We confirm that from 3.8 to 2.6 Ga, phosphorous was most likely scarce in seawater, and estimate average concentrations of 0.063 ± 0.05 μM P for this period.

This finding has implications for the P cycle in the Archean and allows us to question whether IF deposition was limiting marine phosphorus concentration. If we take the Carajás basin as an example, we can calculate the flux of P (mol yr^{-1}) exiting seawater

based on the average P concentration in IFs, a range of well-constrained sedimentation rates determined for IF (Beukes and Gutzmer, 2008; Konhauser et al., 2018; Lantink et al., 2019), and the areal extend of the basin. Considering sedimentation rates of 300 m Myr^{-1}, 100 m Myr^{-1}, and 6 m Myr^{-1}, we determine a high (1.85 x 10^8 mol yr^{-1}), medium (6.18 x 10^7 mol yr^{-1}) and low (3.71 x 10^6 mol yr^{-1}) flux of P for the Carajás basin, respectively. Given the dissolved P concentration (*e.g.* 0.03 μM) for Carajás paleoseawater, we can thus calculate the P amount in 100 m and 1000 m depth, and finally estimate a residence time for P in seawater. A maximum residence time of 146 years was calculated for the Carajás basin (*i.e.* considering 1000 m depth and low flux of P), which is significantly lower compared to the residence time of P in the modern ocean (20000 to 80000 years; Benitez-Nelson, 2000). The difference with modern values is even more distinctive if a high flux is considered (*e.g.* 1.85 x 10^8 mol yr^{-1}), providing a residence time of 3 years. Therefore, these results imply that IF were an important P sink and likely limited P availability in Carajás paleoseawater.

Finally, the long-term availability of phosphorous in Earth's ocean controls the capacity of oxygen to accumulate in the atmosphere by increasing primary biomass production, which will either be buried in sediments, favoring a net O_2 accumulation, or recycled back to bioavailable forms (Reinhard and Planavsky, 2020). Recently, it has been argued that changes in P recycling over time as a result of increased electron acceptors would have modulated biological production (Kipp and Stücken, 2017), and would have been the cause for Earth's major redox tipping point, the Great Oxidation Event (Alcott et al., 2022). Therefore, prior to higher rates of continental weathering and corresponding P influx, and prior to the expansion of sulfidic conditions in continental margins (*e.g.* less effective P adsorption in sulfides; (Krom and Berner, 1981; Kraal et al., 2022),

phosphorous-limited seawater conditions prevailed during the first half of Earth's history and likely contributed strongly to the general anoxia of the atmosphere and ocean throughout much of the Archean Eon.

5.6 Methods

Approximately 250 mg of rock powder were dissolved in closed teflon vessel (Savillex) at about 90°C for one day using 3 ml of concentrated HF (40%), 3 mL of concentrated HCl (32%), and 1 mL of concentrated HNO_3 (65%). Afterwards, 93 mL of H_3BO_3 aqueous solution (20 g L^{-1} H_3BO_3) were added to neutralize the excess HF. All reagents used were graded analytically. Elements were measured by Inductively Coupled Plasma-Atomic Emission Spectrometry (ICP-AES) using a Horiba Jobin Yvon® Ultima 2 spectrometer at the PSO/IUEM (Pôle Spectrométrie Océan, Institut Universitaire Européen de la Mer, Brest, France), following the analytical procedure of (Cotten et al., 1995). The boron included in the solution was used as an internal standard. The precision and accuracy were evaluated using international standards IF-G, ACE, JB2 and WSE. The relative standard deviation is ≤ 1% for SiO_2 and ≤ 2% for the other major elements.

5.7 Supplementary Material

5.7.1 Geological context

The Carajás Mineral Province (CMP) is located in the southeastern part of the Amazonian Craton, Brazil (Fig. 5.4 A), and contains remarkable metallogenic diversity including world-class deposits of iron oxide-copper-gold (IOCG), large IFs, and Mn ore

(Klein and Ladeira, 2002; Moreto et al., 2015b). The Carajás Basin, within the CMP (Fig. 5.4 B,C), comprises Neoarchean and Paleoproterozoic sedimentary units that have been deposited on a basement made up of granulites, migmatites and metavolcanic rocks emplaced from ca. 3080 Ma to ca. 3000 Ma (Machado et al., 1991; Pidgeon et al., 2000; Moreto et al., 2015b). The crystalline basement is overlain unconformably by volcano-sedimentary sequences from the Grão Pará Group, which have undergone subgreenschist to low-greenschist facies metamorphism (Machado et al., 1991; Rosière et al., 2006; Krymsky et al., 2007b).

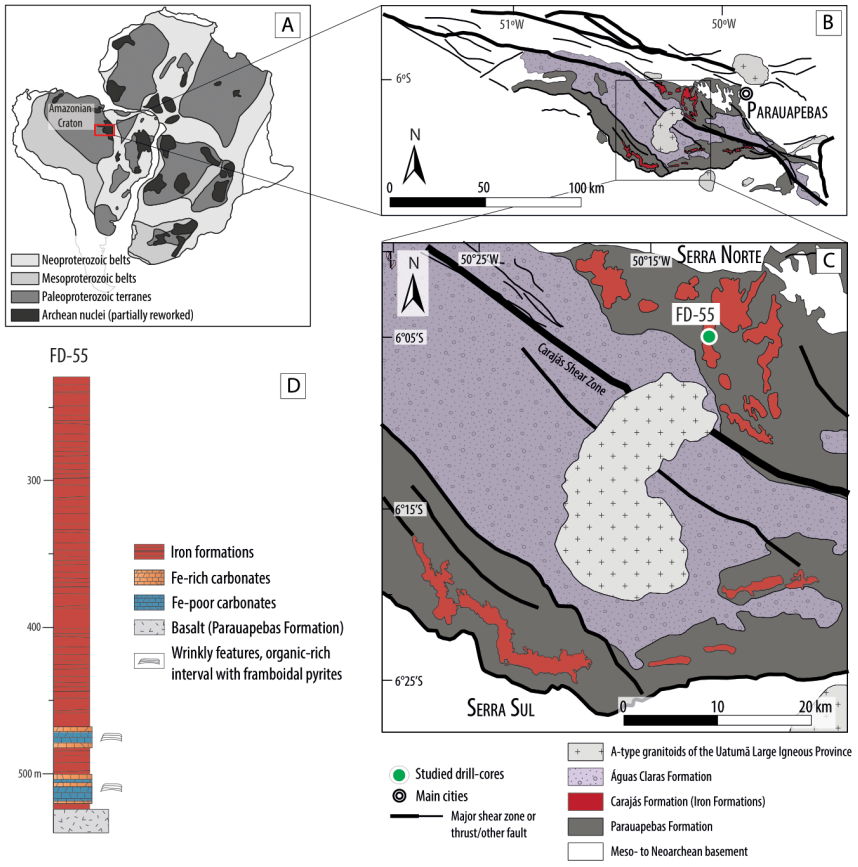

Figure 5. 4: Geological map of the Carajás basin, located in the southeastern portion of the Amazonian Craton (A), showing the location of the drill core FD-55 in Serra Norte (B,C) and the main lithological components varying as a function of depth (m) (D) (after Rego et al., 2021).

At the base of the Grão Pará Group lies the Parauapebas Formation, composed by basalts and basaltic andesites, while IFs from the Carajás Formation conformably overlie or are occasionally interlayered with the basalts, a typical characteristic of Algoma-type IFs (Klein and Ladeira, 2002; Dalstra and Guedes, 2004; Martins et al., 2017b).

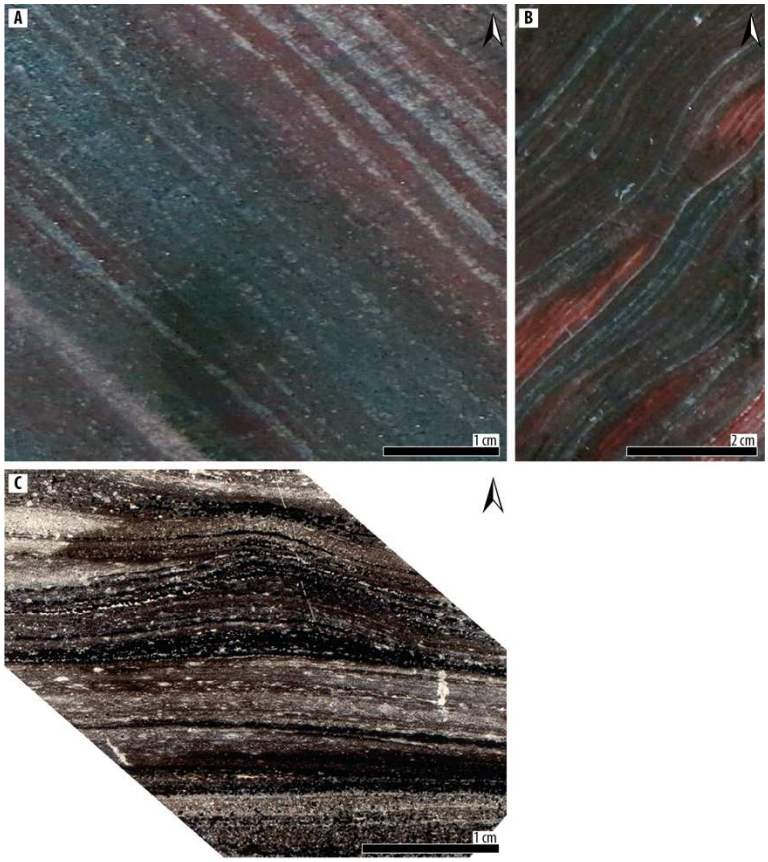

Figure 5. 5: Banded iron facies from the Carajás Formation. Arrows point to the stratigraphic top. A. Sample FD55 486.45. Fine horizontal laminations (sub-mm scale) of iron-bearing minerals (magnetite and hematite) and chert layers. B. Sample FD55 495.80. Finely laminated siliceous BIF displaying wavy laminations. C. Sample FD55 480.80. Thin section in reflected light showing a reactivation surface in a jaspilitic BIF

The main lithology comprising the Carajás Formation are oxide-facies banded iron formations alternating iron-rich and chert layers, but minor black shales and conglomeratic layers have also been reported (Cabral et al., 2013, 2017). These were

interpreted to have been deposited in a range of environments from shallow water, low energy environments, to deep and quiet water settings (Tolbert et al., 1971; Lindenmayer et al., 2001; Macambira and Schrank, 2002a; Ribeiro da Luz and Crowley, 2012; Justo et al., 2020b).

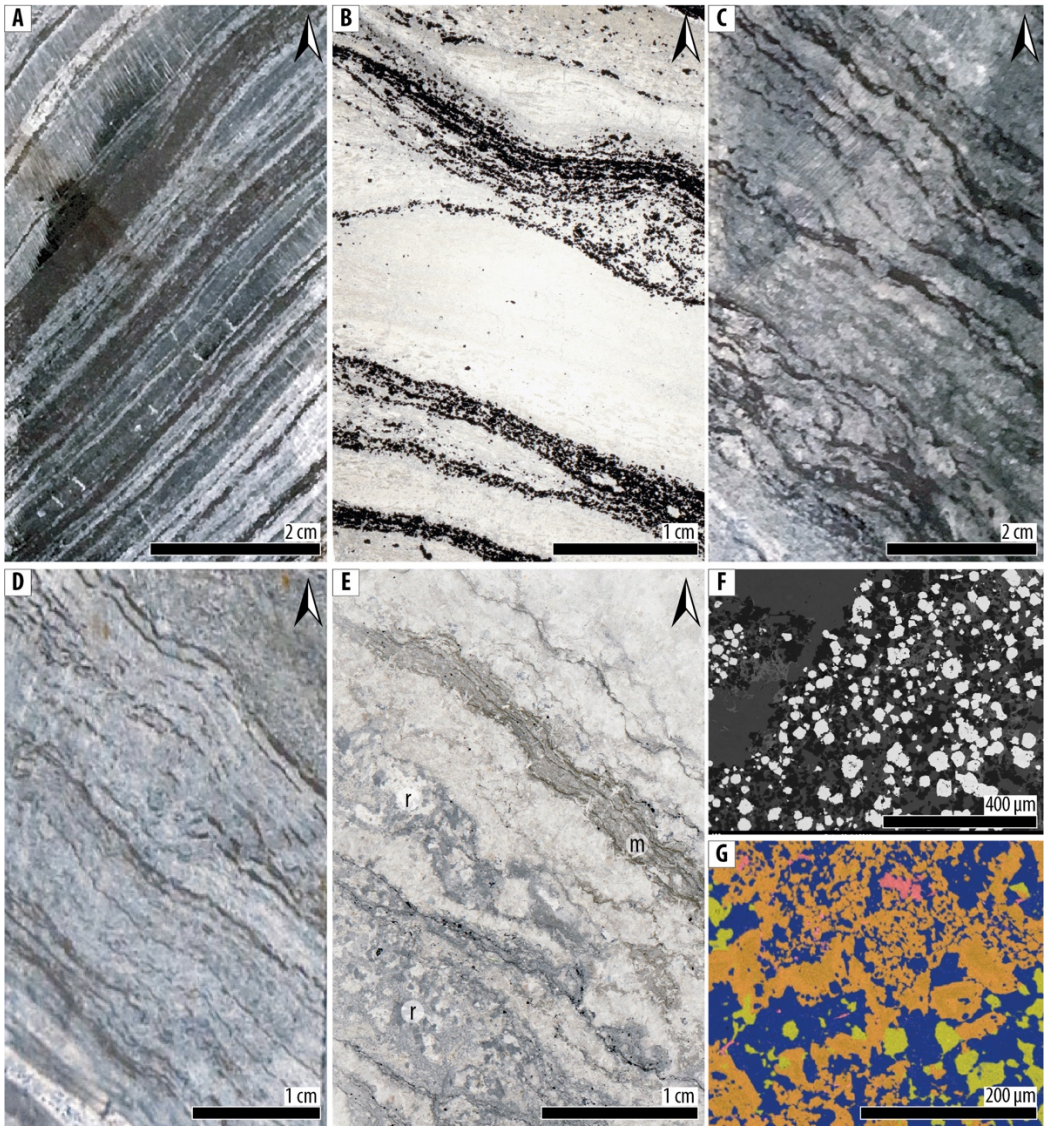

Figure 5. 6: Carbonate facies of the Carajás Formation. Arrows point to the stratigraphic top. A. Sample FD55 521.60. Fine laminations (mm to cm scale) of iron-bearing minerals (mainly magnetite) and carbonate layers. B. Sample FD55 521.12. Thin section in reflected light showing wavy laminations underlined by magnetite grains and carbonates. C. Sample FD55 518.50. Carbonate with irregular, crinkled magnetite laminations and pinching out geometries. D. Sample FD55 522.56. Carbonate with very fine, crinkled lamination underlined by very fine (mm thick) magnetite layers. E. Sample FD55 520.06. Thin section in reflected light showing a microbial

mat (m) within carbonate displaying a clotted micritic texture. Some areas show recrystallized (r) textures. F. Sample FD55 514.57. Electron backscattered image showing diagenetic framboidal pyrite (bright white) minerals within a carbonate matrix. G. Sample FD55 514.57. EDS electron image showing Si, Ca and Fe-rich mineral phases.

A Late Archean to Early Paleoproterozoic sedimentary cover overlies the IFs, however its age is still debated (Rossignol et al., 2020). The depositional age of the Carajás IFs is well-constrained by U-Pb zircon ages of ca. 2.76-2.75 Ga in the basalts underlying and intercalating the IFs (2759 ± 2 Ma, Machado et al., 1991; 2751 ± 4, Krymsky et al., 2007) and U-Pb zircon ages from a possible tuff (2743 ± 11 Ma) and a dolerite dyke (2740 ± 8 Ma) cross-cutting the Carajás Formation (Trendall et al., 1998). The iron deposits have an average thickness of 200-250 m in the Serra Norte and 300 m in the Serra Sul regions (Beisiegel et al., 1973). The drill core FD-55 intercepting the IF deposit in Serra Norte was selected for this study (Fig. 5.4 D), particularly because it has two carbonate-rich intervals intercalated with iron formations, thus reflecting changes in depositional environments (*e.g*. shallower and deeper settings).

The IF facies in core FD-55 is characterized by alternating layers of Fe-rich minerals (magnetite and hematite) and chert with microcrystalline quartz and a few Fe-carbonate (*e.g.* ankerite) disseminated in the matrix. Laminations are mm- to cm-thick and usually exhibit an homogeneous banding (Fig. 5.5 A). Some laminations however display wavy structures (Fig. 5.5 B), pinching geometries and erosion surfaces (Fig. 5.5 C). A gradual change is observed from IF facies to Fe-rich/IF carbonates and Fe-poor carbonates (Rego et al., 2021). The Fe-rich carbonates also comprise banded (Fig. 5.6 A), wavy (Fig. 5.6 B) and irregular Fe-oxides (mainly magnetite) layers (Fig. 5.6 C), while carbonate phases consist mainly of ankerite with minor calcite. Iron-poor carbonate facies show mm- to cm-thick wavy to crinkly carbonates laminae and minor iron oxides (Fig. 5.6 D,E). As

carbonate content increases (calcite and ankerite), distinct intervals containing framboidal pyrites and organic matter were also identified Fig. 5.6 F, G.

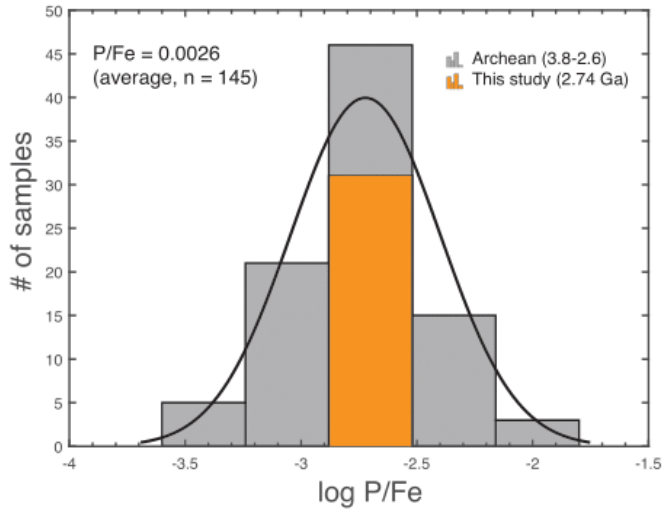

Figure 5. 7: Normal distribution shown by log P/Fe ratios from Archean and Neoarchean Carajás (this study) IFs fitted with a gaussian distribution curve.

Table 5. 2: Additional K_D values based of experimental condition reproducing ancient ocean conditions with varying Si, Ca^{2+}, and Mg^{2+} contents (Jones et al., 2015) and in NaCl amended solutions (Konhauser et al., 2007).

Experimental Conditions	K_D values	P (μM)[1]
Jones et al., 2015		
0.56 M NaCl + 0 mM Si	0.078	0.02
0.56 M NaCl + 0.67 mM Si	0.01	0.15
0.56 M NaCl + 0.67 mM Si + 50 mM Mg2+	0.054	0.03
0.56 M NaCl + 0.67 mM Si + 10 mM Ca2+	0.119	0.01
0.56 M NaCl + 0.67 mM Si + 50 mM Mg2+ + 10 mM Ca2+ (modern ocean [Ca and Mg])	0.066	0.02
0.56 M NaCl + 2.2 mM Si + 45 mM Mg2+ + 55 mM Ca2+ (ancient calcite sea)	0.021	0.07
0.56 M NaCl + 2.2 mM Si + 10 mM Mg2+ + 24 mM Ca2+ (ancient aragonite sea)	0.013	0.11
0.56 M NaCl + 0 mM Si + 50 mM Mg2+ + 10 mM Ca2+	0.23	0.006
Konhauser et al., 2007		
NaCl + 0 Si	0.075	0.02
NaCl + 0.67 mM Si	0.011	0.13
NaCl + 2.2 mM Si	0.002	0.73

[1]Estimated dissolved P based on P/Fe mol ratio (0.0015) for Carajás IFs (2.74 Ga)

Table 5. 3: Major element composition for iron formation, Fe-rich and Fe-poor carbonate samples.

Sample depth (m)	SiO2 %	TiO2 %	Al2O3 %	Fe2O3 %	MnO %	MgO %	CaO %	Na2O %	K2O %	P2O5 %	LOI	Total
FD55 280.90_96	34.7	0.01	0.3	63.1	0.153	0.41	0.16	<LD	<LD	0.099	0.76	99.69
FD55 295.75_85	36.6	0.01	0.2	60.4	0.153	0.48	NaN	<LD	0.00	0.089	0.51	98.39
FD55 311.75_80	50.3	0.01	0.2	48.5	0.186	0.91	0.06	<LD	<LD	0.076	0.68	100.89
FD55 331.04_09	35.4	0.01	0.3	61.6	0.153	1.10	1.25	<LD	0.00	0.094	0.98	100.97
FD55 356.76_78	54.2	0.01	0.3	37.7	0.308	1.29	2.74	<LD	<LD	0.058	3.33	99.97
FD55 369.96_370.02	38.4	0.01	0.2	56.5	0.236	1.07	1.61	<LD	0.00	0.084	0.97	99.10
FD55 384.40_46	43.6	0.01	0.2	52.1	0.173	1.05	1.43	<LD	0.00	0.088	0.98	99.59
FD55 399.70_77	33.3	0.01	0.2	62.3	0.060	1.74	0.50	<LD	<LD	0.102	-0.47	97.76
FD55 414.17_22	37.6	0.01	0.3	59.2	0.112	1.22	1.20	<LD	<LD	0.095	1.16	100.81
FD55 426.07_15	40.8	0.01	0.2	56.8	0.080	1.20	1.28	<LD	<LD	0.098	0.59	101.11
FD55 438.93_99	35.7	0.01	0.2	59.7	0.106	1.34	1.49	<LD	<LD	0.091	0.90	99.53
FD55 478.03_13	24.6	0.01	0.0	23.7	0.357	1.68	26.7	0.00	0.00	0.046	24.23	101.38
FD55 478.34_42	34.7	0.01	0.1	24.3	0.419	2.33	17.6	0.00	0.00	0.049	20.46	99.96
FD55 478.98_479.02	19.0	0.01	0.1	33.1	0.447	2.12	20.5	0.00	0.00	0.061	23.59	98.86
FD55 479.05_10	21.3	0.01	0.2	24.3	0.466	1.90	24.21	0.00	<LD	0.046	26.96	99.47
FD55 495.87_90	39.8	0.01	0.3	54.2	0.129	1.34	2.20	<LD	<LD	0.084	2.41	100.54
FD55 503.22_30	34.1	0.01	0.3	58.3	0.122	1.75	2.38	<LD	<LD	0.084	2.42	99.40
FD55 511.92_512.03	34.3	0.01	0.0	24.4	0.242	1.61	21.0	0.00	0.00	0.045	18.81	100.39
FD55 512.59_65	15.3	0.01	0.8	44.4	0.368	5.15	13.9	0.08	0.27	0.078	18.52	98.85
FD55 512.98_513.06	35.7	0.01	0.0	20.2	0.426	6.76	16.0	0.00	0.00	0.041	22.50	101.75
FD55 513.72_80	25.0	0.01	0.0	23.6	0.448	7.23	18.2	0.00	0.00	0.045	25.89	100.49
FD55 515.23_30	14.7	0.01	0.1	16.9	0.381	2.04	34.6	0.00	0.02	0.040	29.70	98.55
FD55 515.34_41	23.2	0.01	0.1	30.0	0.620	3.10	19.7	0.00	0.00	0.055	22.73	99.45
FD55 517.15_25	35.0	0.01	0.0	33.6	0.420	2.38	12.0	0.00	0.00	0.059	15.46	98.99
FD55 517.65_70	36.3	0.01	0.1	19.2	0.480	2.12	20.3	0.00	0.01	0.039	22.28	100.74
FD55 517.70_78	24.9	0.01	0.1	29.5	0.575	2.78	18.1	0.00	0.01	0.056	22.32	98.28
FD55 518.53_60	30.2	0.01	0.0	32.8	0.456	2.55	14.5	0.00	0.00	0.059	18.10	98.79
FD55 520.38_48	29.3	0.01	0.0	36.7	0.594	2.92	10.6	0.00	0.00	0.068	17.97	98.27
FD55 520.58_66	46.8	0.01	0.0	22.4	0.439	2.27	12.2	0.00	0.00	0.043	15.85	100.08
FD55 520.66_73	47.0	0.01	0.0	27.1	0.404	2.12	10.3	0.00	0.00	0.050	13.62	100.63
FD55 521.63_73	35.3	0.01	0.1	45.8	0.407	2.47	6.8	0.00	0.00	0.079	9.09	100.05

Chapter 5 is now submitted to *Geology* and await for further reviews.

5.8 References

Alcott, L.J., Mills, B.J.W., Bekker, A., and Poulton, S.W., 2022, Earth's Great Oxidation Event facilitated by the rise of sedimentary phosphorus recycling: Nature Geoscience, v. 15, p. 210–215, doi:10.1038/s41561-022-00906-5.

Alexander, B.W., Bau, M., Andersson, P., and Dulski, P., 2008, Continentally-derived solutes in shallow Archean seawater: Rare earth element and Nd isotope evidence in iron formation from the 2.9 Ga Pongola Supergroup, South Africa: Geochimica et Cosmochimica Acta, v. 72, p. 378–394, doi:10.1016/j.gca.2007.10.028.

Araújo, J.C.S., and Lobato, L.M., 2019, Depositional model for banded iron formation host to gold in the Archean Rio das Velhas greenstone belt, Brazil, based on geochemistry and LA-ICP-MS magnetite analyses: Journal of South American Earth Sciences, v. 94, p. 102205, doi:10.1016/j.jsames.2019.05.021.

Archer, C., and Vance, D., 2006, Coupled Fe and S isotope evidence for Archean microbial Fe(III) and sulfate reduction: Geology, v. 34, p. 153–156, doi:10.1130/G22067.1.

Benitez-Nelson, C.R., 2000, The biogeochemical cycling of phosphorus in marine systems: Earth Science Reviews, v. 51, p. 109–135, doi:10.1016/S0012-8252(00)00018-0.

Berner, R.A., 1973, Phosphate removal from sea water by adsorption on volcanogenic ferric oxides: Earth and Planetary Science Letters, v. 18, p. 77–86, doi:10.1016/0012-821X(73)90037-X.

Beukes, N.J., and Gutzmer, J., 2008, Origin and Paleoenvironmental Significance of Major Iron Formations at the Archean-Paleoproterozoic Boundary, *in* Banded Iron Formation-Related High-Grade Iron Ore, Society of Economic Geologists, v. 15, p. 5–47, doi:10.5382/Rev.15.01.

Beukes, N.J., and Klein, C., 1990, Geochemistry and sedimentology of a facies transition

- from microbanded to granular iron-formation - in the early Proterozoic Transvaal Supergroup, South Africa: Precambrian Research, v. 47, p. 99–139, doi:10.1016/0301-9268(90)90033-M.

Bindeman, I.N., Zakharov, D.O., Palandri, J., Greber, N.D., Dauphas, N., Retallack, G.J., Hofmann, A., Lackey, J.S., and Bekker, A., 2018, Rapid emergence of subaerial landmasses and onset of a modern hydrologic cycle 2.5 billion years ago: Nature, v. 557, p. 545–548, doi:10.1038/s41586-018-0131-1.

Bhattacharya, H.N., Chakraborty, I., and Ghosh, K.K., 2007, Geochemistry of some banded iron-formations of the archean supracrustals, Jharkhand-Orissa region, India: Journal of Earth System Science, v. 116, p. 245–259, doi:10.1007/s12040-007-0024-4.

Bjerrum, C.J., and Canfield, D.E., 2002, Ocean productivity before about 1.9 Gyr ago limited by phosphorus adsorption onto iron oxides: Nature, v. 417, p. 159–162, doi:10.1038/417159a.

Busigny, V., Jézéquel, D., Cosmidis, J., Viollier, E., Benzerara, K., Planavsky, N.J., Albéric, P., Lebeau, O., Sarazin, G., and Michard, G., 2016, The Iron Wheel in Lac Pavin: interaction with Phosphorus Cycle, *in* Sime-Ngando, T., Boivin, P., Chapron, E., Jezequel, D., and Meybeck, M. eds., Lake Pavin: History, Geology, Biogeochemistry, and Sedimentology of a Deep Meromictic Maar Lake, Cham, Springer International Publishing, p. 205–220, doi:10.1007/978-3-319-39961-4.

Cates, N.L., and Mojzsis, S.J., 2007, Pre-3750 Ma supracrustal rocks from the Nuvvuagittuq supracrustal belt, northern Québec: Earth and Planetary Science Letters, v. 255, p. 9–21, doi:10.1016/j.epsl.2006.11.034.

Cotten, J., Le Dez, A., Bau, M., Caroff, M., Maury, R.C., Dulski, P., Fourcade, S., Bohn, M.,

and Brousse, R., 1995, Origin of anomalous rare-earth element and yttrium enrichments in subaerially exposed basalts: Evidence from French Polynesia: Chemical Geology, v. 119, p. 115–138, doi:10.1016/0009-2541(94)00102-E.

Craddock, P.R., and Dauphas, N., 2011, Iron and carbon isotope evidence for microbial iron respiration throughout the Archean: Earth and Planetary Science Letters, v. 303, p. 121–132, doi:10.1016/j.epsl.2010.12.045.

Dauphas, N., van Zuilen, M., Busigny, V., Lepland, A., Wadhwa, M., and Janney, P.E., 2007, Iron isotope, major and trace element characterization of early Archean supracrustal rocks from SW Greenland: Protolith identification and metamorphic overprint: Geochimica et Cosmochimica Acta, v. 71, p. 4745–4770, doi:10.1016/j.gca.2007.07.019.

Derry, L.A., 2015, Causes and consequences of mid-Proterozoic anoxia: Geophysical Research Letters, v. 42, p. 8538–8546, doi:10.1002/2015GL065333.

Feely, R.A., Trefry, J.H., Lebon, G.T., and German, C.R., 1998, The relationship between P/Fe and V/Fe ratios in hydrothermal precipitates and dissolved phosphate in seawater: Geophysical Research Letters, v. 25, p. 2253–2256.

Hao, J., Knoll, A.H., Huang, F., Hazen, R.M., and Daniel, I., 2020, Cycling phosphorus on the Archean Earth: Part I. Continental weathering and riverine transport of phosphorus: Geochimica et Cosmochimica Acta, v. 273, p. 70–84, doi:10.1016/j.gca.2020.01.027.

Haugaard, R., Ootes, L., Creaser, R.A., and Konhauser, K.O., 2016, The nature of Mesoarchaean seawater and continental weathering in 2.85 Ga banded iron formation, Slave craton, NW Canada: Geochimica et Cosmochimica Acta, v. 194, p. 34–56, doi:10.1016/j.gca.2016.08.020.

Ingalls, M., Grotzinger, J.P., Present, T., Rasmussen, B., and Fischer, W.W., 2022,

Carbonate-Associated Phosphate (CAP) Indicates Elevated Phosphate Availability in Neoarchean Shallow Marine Environments: Geophysical Research Letters, v. 49, doi:10.1029/2022gl098100.

Jones, C., Nomosatryo, S., Crowe, S.A., Bjerrum, C.J., and Canfield, D.E., 2015, Iron oxides, divalent cations, silica, and the early earth phosphorus crisis: Geology, v. 43, p. 135–138, doi:10.1130/G36044.1.

Klein, C., and Beukes, N.J., 1989, Geochemistry and sedimentology of a facies transition — from limestone to iron-formation deposition in the early Proterozoic Transvaal Supergroup, South Africa: Economic Geology, v. 84, p. 1733–1774, doi:10.1016.

Konhauser, K.O. et al., 2017, Iron formations: A global record of Neoarchaean to Palaeoproterozoic environmental history: Earth-Science Reviews, v. 172, p. 140–177, doi:10.1016/j.earscirev.2017.06.012.

Konhauser, K.O. et al., 2018, Phytoplankton contributions to the trace-element composition of Precambrian banded iron formations: Bulletin of the Geological Society of America, v. 130, p. 941–951, doi:10.1130/B31648.1.

Konhauser, K.O., 2007, Was There Really an Archean: ScienceScience, v. 315, p. 2, www.sciencemag.org/cgi/content/full/315/5816/1234/dc1.

Konhauser, K.O., Lalonde, S. V., Amskold, L., and Holland, H.D., 2007, Was there really an archean phosphate crisis? Science, v. 315, p. 1234, doi:10.1126/science.1136328.

Kraal, P., van Genuchten, C.M., and Behrends, T., 2022, Phosphate coprecipitation affects reactivity of iron (oxyhydr)oxides towards dissolved iron and sulfide: Geochimica et Cosmochimica Acta, v. 321, p. 311–328, doi:10.1016/j.gca.2021.12.032.

Krom, M.D., and Berner, R.A., 1981, The diagenesis of phosphorus in a nearshore marine sediment: Geochimica et Cosmochimica Acta, v. 45, p. 207–216, doi:10.1016/0016-

7037(81)90164-2.

Lantink, M.L., Davies, J.H.F.L., Mason, P.R.D., Schaltegger, U., and Hilgen, F.J., 2019, Climate control on banded iron formations linked to orbital eccentricity: Nature Geoscience, v. 12, p. 369–374, doi:10.1038/s41561-019-0332-8.

Lyle, M., 1986, Major element composition of Leg 92 Sediments: Initial Reports of the Deep Sea Drilling Project, v. 92, p. 355–370.

Marin-Carbonne, J. et al., 2020, In Situ Fe and S isotope analyses in pyrite from the 3.2 Ga Mendon Formation (Barberton Greenstone Belt, South Africa): Evidence for early microbial iron reduction: Geobiology, p. 1–20, doi:10.1111/gbi.12385.

Mloszewska, A.M., Pecoits, E., Cates, N.L., Mojzsis, S.J., O'Neil, J., Robbins, L.J., and Konhauser, K.O., 2012, The composition of Earth's oldest iron formations: The Nuvvuagittuq Supracrustal Belt (Québec, Canada): Earth and Planetary Science Letters, v. 317–318, p. 331–342, doi:10.1016/j.epsl.2011.11.020.

Nutman, A.P., Friend, C.R.L., Bennett, V.C., Wright, D., and Norman, M.D., 2010, ≥3700Ma pre-metamorphic dolomite formed by microbial mediation in the Isua supracrustal belt (W. Greenland): Simple evidence for early life? Precambrian Research, v. 183, p. 725–737, doi:10.1016/j.precamres.2010.08.006.

Planavsky, N.J., Rouxel, O.J., Bekker, A., Lalonde, S. V, Konhauser, K.O., Reinhard, C.T., and Lyons, T.W., 2010, The evolution of the marine phosphate reservoir: Nature, v. 467, p. 1088–1090, doi:10.1038/nature09485.

Rasmussen, B., Muhling, J.R., Suvorova, A., and Fischer, W.W., 2021, Apatite nanoparticles in 3 . 46 – 2 . 46 Ga iron formations : Evidence for phosphorus-rich hydrothermal plumes on early Earth: v. XX, p. 1–5, doi:10.1130/G48374.1/5227469/g48374.pdf.

Reinhard, C.T., Planavsky, N.J., Gill, B.C., Ozaki, K., Robbins, L.J., Lyons, T.W., Fischer, W.W., Wang, C., Cole, D.B., and Konhauser, K.O., 2017a, Evolution of the global phosphorus cycle: Nature, v. 541, p. 386–389, doi:10.1038/nature20772.

Reinhard, C.T., Planavsky, N.J., Gill, B.C., Ozaki, K., Robbins, L.J., and Timothy, W., 2017b, Evolution of the global phosphorus cycle: Nature Publishing Group, v. 541, p. 386–389, doi:10.1038/nature20772.

Robbins, L.J. et al., 2019, Hydrogeological constraints on the formation of Palaeoproterozoic banded iron formations: Nature Geoscience, v. 12, p. 558–563, doi:10.1038/s41561-019-0372-0.

Smith, A.J.B., Beukes, N.J., and Gutzmer, J., 2013, The Composition and Depositional Environments of Mesoarchean Iron Formations of the West Rand Group of the Witwatersrand Supergroup, South Africa: Economic Geology, v. 108, p. 111–134, doi:10.2113/econgeo.108.1.111.

Trendall, A.F., and Blockley, J.G., 1970, The iron formations of the Precambrian Hamersley Group Western Australia: Geological Survey of Western Australia Bulletin, v. 119, p. 391.

Tyrrell T., 1999, The relative influences of nitrogen and phosphorus on oceanic primary production.: Nature, v. 400, p. 525–531.

Westheimer, F.H., 1987, Nature Chose Phosphates The Role of Phosphates The Importance of Being Ionized: Science, v. 235, p. 1173–1178.

Wheat, C.G., Feely, R.A., and Mottl, M.J., 1996, Phosphate removal by oceanic hydrothermal processes: an update of the phosphorus budget in the oceans: Geochimica et Cosmochimica Acta, v. 60, p. 3593–3608, doi:0016-7037/9.

Zhao, M., Zhang, S., Tarhan, L.G., Reinhard, C.T., and Planavsky, N., 2020, The role of calcium in regulating marine phosphorus burial and atmospheric oxygenation:

Nature Communications, v. 11, doi:10.1038/s41467-020-15673-3.

CHAPTER 6

6. The iron and carbon isotope composition of iron formations and carbonates: distinguishing between primary and secondary signatures imprinted in the rock record

This chapter explores the Fe isotope composition of carbonate and magnetite, and the C isotope of carbonates in Neoarchean IF and carbonates, to understand if they reflect either primary (*i.e.* seawater) and/or secondary features such as early diagenesis (*e.g.* microbial respiration) and/or late diagenesis (*e.g.* burial metamorphism). There is a large debate on the potential use of Fe-carbonates as archives of the ancient oceanic and atmospheric conditions (Rosing et al., 2010; Johnson et al., 2013). One line of evidence suggests that some carbonates have precipitated in equilibrium with seawater, therefore reflecting past environmental conditions (Ohmoto et al., 2004; Rosing et al., 2010). Other lines of evidence suggest that Fe-carbonates are a product of microbial iron reduction (*i.e.* through respiration; Johnson et al., 2013; Craddock and Dauphas, 2011), thus reflecting an early diagenetic signal and/or were formed completely abiotically (Jiang et al., 2022; Tsikos et al., 2022). These distinct lines of interpretations are largely based on specific Fe and C isotopic signatures.

By assuming a low variability of the carbon isotopic reservoir ($\delta^{13}C \cong 0‰$) of dissolved inorganic carbon (DIC) in seawater throughout the geological record (*e.g.* Fischer et al., 2009), Fe-poor Ca-Mg carbonates with $\delta^{13}C$ values of $0 \pm 2‰$ are generally

interpreted to have precipitated in near-equilibrium with seawater (Heimann et al., 2010; Craddock and Dauphas, 2011; Johnson et al., 2013). Contrary, carbonates with a light C isotope composition (< -8‰) are interpreted as product of microbial respiration, which generates a DIC in pore space depleted in ^{13}C due to organic matter oxidation (Jonhson et al., 2013), and/or reflect kinetic effects associated to mineral precipitation (Jiang et al., 2022). In the case of Fe-carbonate formation, such as commonly observed in the Archean and Paleoproterozoic, experiments have determined the Fe isotope equilibrium fractionation associated to siderite precipitation abiotically (-0.48 $\pm$ 0.22‰; Wiesli et al., 2014). Additionally, experiments involving microbial dissimilatory iron reduction (DIR) have shown that $Fe(II)_{aq}$ produced from anaerobic respiration is always depleted in ^{56}Fe compared to precursor ferric substrate by ~-1 to -2.6‰ (Beard et al., 1999, 2003; Icopini et al., 2004; Johnson et al., 2005 ; Crosby et al., 2005; 2007; Wu et al., 2009; Tangalos et al., 2010; Percak-Dennett et al., 2011; Fortney et al., 2016, 2020). Therefore, by combining measurements of C isotopes in carbonates, and Fe isotopes in carbonates and oxides, we expect to distinguish between a seawater component and/or diagenetic features.

Here the C isotope composition of Neoarchean IF, and Fe-rich and Fe-poor carbonates were measured, along with the Fe isotope composition of carbonate leachates (see Chapter 3, Rego et al., submitted) and magnetite from the same sample set. Carbon isotope composition of carbonate suggests the presence of microbial respiration in the Neoarchean in Carajás, as similarly observed elsewhere (Australia, South Africa, China), as opposed to Fe isotopes in mineral separates which seemed to be re-equilibrated by low-grade metamorphism at relatively low temperature, thus lacking (or obliterating) significant fractionation associated to DIR. We therefore suggest that the Fe isotope composition of carbonate can hardly be used as a proxy of primary seawater composition or DIR influence in Archean rocks but that bulk Fe isotope measurements together with

C isotope composition in carbonates are an ideal combination to identify the role of microbial dissimilatory iron reduction in the ancient rock record.

6.1 Analytical Methods

The same samples presented by Rego et al. (2021) consisting of iron formations (IFs), Fe-rich and Fe-poor carbonates were used in this study. Additionally, three iron formation samples from Isua, Greenland, were also analyzed (IS-04-01, -06, -11). Here, magnetite was separated from bulk samples magnetically with a hand magnet, while carbonates were leached with Acetic acid (HAc) following the procedure described in Chapter 3 (Rego et al., in review). Approximately 50 mg of bulk sample powder were leached with 5% HAc and left overnight at room temperature. Afterwards, samples were centrifuged and the supernatant was removed to be analyzed for trace element and Fe isotopic compositions. In order to test whether 5% HAc could release Fe from magnetite, which is the main Fe-oxide component in these samples, the same leaching procedure was applied to magnetite samples. In good agreement with previous studies (Blanckenburg et al., 2008), only trace amounts of Fe were detected (*i.e.* <0.1%). This supports that, if any, a contamination of the carbonate fraction by dissolution of magnetite using HAc was negligible.

6.1.1 Fe isotopes

Approximately 10-20 mg of magnetite was separated for each sample and dissolved with mixtures of HCl and HNO_3. Carbonate leachates in HAc were evaporated and acidified with HNO_3 to ensure that all iron was in its ferric state. All samples were dissolved in 6M HCl prior to iron column chemistry. The following ion chromatography

procedure, adapted from Dauphas et al. (2004), has been previously described in Busigny et al. (2014; 2017; 2018). Bio-Rad Poly-Prep columns were filled with 1 ml anion exchange resin (AG1-X8 200-400 mesh chloride form). The resin was cleaned three times with 10 ml H_2O and 5 ml 1 M HNO_3. It was then preconditioned in HCl medium by running 10 ml H_2O, 10 ml 0.4 M HCl, 5 ml H_2O and 2 ml 6 M HCl. Matrix elements were eluted in 8 ml 6 M HCl, whereas Fe(III) was strongly adsorbed on the resin and quantitatively retained. Iron was subsequently eluted in 10 ml 0.4 M HCl. This procedure was repeated twice for each sample to assure that all matrix elements were eliminated (Dauphas et al., 2004).

Iron isotope composition were measured using a ThermoFischer Neptune MC-ICP-MS (Multiple Collector Inductively Coupled Plasma Mass Spectrometer) at the Institut de Physique du Globe de Paris (IPGP). The samples were analyzed in 0.3 M HNO_3 at a concentration of ~2 ppm Fe and introduced into the mass spectrometer with a quartz cyclonic spray chamber. Iron isotopes were fully resolved from argide interferences using the high-resolution mode of the Neptune (Weyer & Schwieters, 2003; Schoenberg & Von Blanckenburg, 2005). Instrumental mass discrimination was corrected for using the conventional sample-standard bracketing (SSB) approach (Rouxel *et al.*, 2003). The $^{56}Fe/^{54}Fe$ and $^{57}Fe/^{54}Fe$ ratios were expressed in the usual δ notation in per mil (‰) as,

$$\delta^{56}Fe = [(^{56}Fe/^{54}Fe)_{sample} / (^{56}Fe/^{54}Fe)_{standard} - 1] \times 1000$$

$$\delta^{57}Fe = [(^{57}Fe/^{54}Fe)_{sample} / (^{57}Fe/^{54}Fe)_{standard} - 1] \times 1000$$

where the standard is IRMM-014, a pure synthetic Fe metal from the Institute for Reference Materials and Measurements (Taylor *et al.*, 1992). Based on replicate analysis of international rock geostandards (IF-G, AC-E, BCR-2, and BHVO-2) and an in-house/internal standard (ISVB), the external precision and accuracy were always better than 0.03‰ for $\delta^{56}Fe$ and 0.07‰ for $\delta^{57}Fe$ (2SD). The Fe isotopic compositions of

geostandards were in good agreement with recommended values (Craddock & Dauphas, 2011)

6.1.2 Carbon isotopes

The carbon isotope compositions of carbonates were carried out at the PSO/IUEM (Pôle Spectrométrie Océan, Institut Universitaire Européen de la Mer, Brest, France). They were measured using a MAT-235 (Thermo Scientific) mass spectrometer, coupled with a Carbo-Kiel Device for automated CO_2 preparation from IFs, Fe-rich and Fe-poor carbonate samples (n=52). The reaction was produced by adding phosphoric acid to individual samples at 70 °C for 400 seconds. Isotopic data are reported in conventional delta (δ) notation, relative to the Vienna Pee Dee Belemnite (VPDB). Two calcite standards (NSB-18 and -19) and an internal standard were used. Analytical uncertainties based on replicates and standard analyses are ±0.05‰ for carbon isotopes and ±0.09‰ for oxygen isotopes.

6.1.3 Raman spectroscopy

The Raman spectra were obtained utilizing a Horiba Jobin Yvon LabRam HR800UV Raman micro-spectrometer at the Laboratoire d'Océanologie et de Géosciences, Université de Lille. A 532 nm focused-laser was used to obtain the spectra through an Olympus BX41 microscope. Filters were used to avoid heating damage to the organic matter and targets were focused several micrometers below the polished surface. Five bands/shoulders are shown in Raman spectra (G, D1, D2, D3, and D4), which are referred to as medium-grade carbonaceous material (Kouketsu et al., 2014). The software PeakFit was used for fitting the spectral features. The fitting method F was used

(Kouketsu et al., 2014), which satisfied the observed spectral characteristics (*e.g.* 1600 cm^{-1}/1350 cm^{-1} intensity ratios lower than 1.32 and the presence of D4). Geo-temperatures were calculated using Equation 1 of Kouketsu et al. (2014): T(C°) = -2.15(FWHM-D1) + 478, where FWHM represents the full-width at half maximum. An error of $\pm$ 30ºC is accounted for this fitting method.

6.2 Results

6.2.1 Iron isotopes

The iron isotopic compositions from both studied cores (FD55 and FD365) are given in Table 6.1 and illustrated as a function of depth in Fig. 6.1. The iron isotopic compositions of magnetite and carbonates for the three Isua samples are reported in Table 6.2. The $\delta^{56}Fe$ values in magnetite samples from the Carajás Formation show a large range from +0.34 to +2.23‰ with an average of +1.01‰ (n=31). Heavier $\delta^{56}Fe$ values are recorded in magnetite from IFs (+1.03 to +2.23‰), while Fe-rich and Fe-poor carbonates have magnetite values varying from +0.34 to +0.88‰ and +0.52 to +0.93‰, respectively. Carbonate leachates have an iron isotopic composition between -0.54 to +1.60‰ with a mean value of +0.04‰ (n=31). Carbonate leachates from IFs show $\delta^{56}Fe$ values from -0.01 to +0.66‰, except an anomalous sample from drill core FD365 being significantly enriched in the heavier Fe isotope (+1.60‰). Both Fe-rich and Fe-poor carbonate leachates present similar $\delta^{56}Fe$ values, from -0.53 to -0.06‰ and -0.54 to +0.01‰, respectively. Interestingly, magnetite and carbonate separates in both drill cores have a nearly constant fractionation of ~1‰ between the two mineralogical phases ($\Delta^{56}Fe_{mag - Fe\text{-}carb.}$) = +0.98 $\pm$ 0.11‰, n=31 pairs of magnetite and siderite/ankerite).

Bulk rock $\delta^{56}Fe$ values have been published in a previous paper (Rego et al., 2021) and show a strong mineralogical control. For instance, IFs are dominated by magnetite and display positive $\delta^{56}Fe$ values between +1.03 and +1.95‰. In contrast, Fe-poor carbonates containing abundant pyrite grains within stromatolitic layers with minor Fe-oxides show the most negative values, down to -0.42‰ (Fig. 6.1). As iron concentration gradually increases, carbonate content decreases, and magnetite becomes more prominent in Fe-rich carbonates and IFs, while the $\delta^{56}Fe$ values of bulk rock also becomes more positive. The same variation is observed in magnetite and carbonate separates, in which $\delta^{56}Fe$ is isotopically lighter in carbonate facies and gradually heavier towards IFs facies.

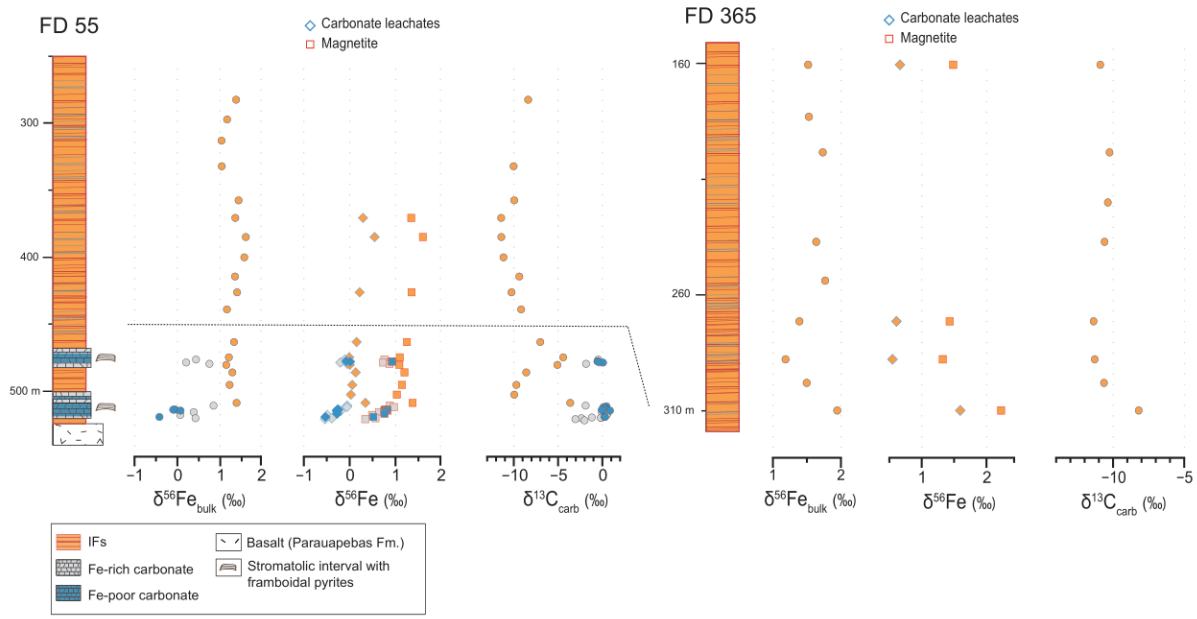

Figure 6. 1: Stratigraphic profile of core FD-55 and FD 365 showing the Fe isotope composition of iron formations, Fe-rich and Fe-poor carbonates in bulk samples and in mineral separates, and the C isotope composition of carbonate within the same samples.

Magnetite from Isua had varying $\delta^{56}Fe$ values from +0.17 to +0.64 ‰ (average of +0.40 $\pm$ 0.24 ‰), while leached carbonates were more homogenous with two samples IS-

04-1 and -11 having $\delta^{56}Fe$ values of -0.26 $\pm$ 0.21 ‰ and -0.25 $\pm$ 0.19 ‰, respectively, and IS-04-6 with a $\delta^{56}Fe$ value of -0.01 $\pm$ 0.28 ‰.

Table 6. 1: Iron isotope composition of magnetite and carbonate leachates, and C isotope data and carbonate content from carbonates in samples from drill-cores FD-55 and FD-365.

Drill core FD-55		$\delta^{56}Fe$ (‰)[a]				$\delta^{57}Fe$ (‰)[a]				$\delta^{13}C$ (‰)[b]	Carb. (wt.%)
Depth (m)	Lithology	Magnetite	SD	Fe-carb.	SD	Magnetite	SD	Fe-carb.	SD	Carb	
280.93	IFs									-8.38	0.4
295.8	IFs										
311.78	IFs										
331.07	IFs									-10.02	2.8
356.77	IFs									-9.95	5.6
369.99	IFs	1.344	0.020	0.290	0.018	2.033	0.049	0.442	0.027	-11.42	3.6
384.43	IFs	1.598	0.040	0.543	0.013	2.369	0.052	0.800	0.017	-11.40	1.9
399.735	IFs									-11.16	1.0
414.195	IFs									-9.38	2.5
426.11	IFs	1.352	0.027	0.217	0.014	2.006	0.018	0.346	0.022	-10.26	2.4
438.96	IFs									-9.17	2.6
463.55	IFs	1.248	0.033	0.151	0.029	1.798	0.079	0.230	0.031	-7.01	5.6
475.1	IFs	1.093	0.033	-0.01	0.008	1.628	0.070	0.00	0.009	-4.42	6.1
476.765	Fe-rich carbonate	0.758	0.017	-0.107	0.020	1.128	0.034	-0.142	0.024	-0.46	30.7
478.08	Fe-poor carbonate	0.914	0.062	-0.080	0.024	1.313	0.089	-0.130	0.034	-0.56	50.3
478.38	Fe-poor carbonate	0.931	0.046	0.010	0.044	1.390	0.064	0.030	0.086	-0.47	41.4
479	Fe-rich carbonate	0.727	0.023	-0.205	0.023	1.025	0.046	-0.339	0.046	-0.30	40.9
479.05	Fe-poor carbonate									0.07	56.0
479.43	Fe-poor carbonate										
479.98	Fe-rich carbonate	0.870	0.017	-0.055	0.062	1.306	0.041	-0.093	0.092	-1.84	7.2
480.8	IFs	1.083	0.043	0.002	0.031	1.637	0.062	0.018	0.033	-5.08	4.1
486.48	IFs	1.196	0.011	0.131	0.018	1.808	0.022	0.197	0.052	-8.59	4.2
495.885	IFs	1.140	0.018	0.056	0.016	1.689	0.059	0.068	0.030	-9.71	3.6
503.26	IFs	1.029	0.017	0.026	0.024	1.512	0.041	0.020	0.031	-9.95	6.2
509.435	IFs	1.373	0.025	0.343	0.014	2.056	0.028	0.554	0.055	-3.63	16.2
511.5	Fe-rich carbonate	0.875	0.019	-0.056	0.022	1.333	0.051	-0.099	0.037	-1.89	10.8
511.975	Fe-poor carbonate									0.46	41.0
512.62	Fe-rich carbonate	0.965	0.034	-0.062	0.037	1.423	0.047	-0.129	0.029	0.11	34.9
513.02	Fe-poor carbonate									0.22	40.4

513.76	Fe-poor carbonate									0.29	37.3
514.45	Fe-poor carbonate	0.768	0.014	-0.264	0.017	1.122	0.011	-0.425	0.032	0.45	47.6
514.57	Fe-poor carbonate	0.821	0.040	-0.247	0.028	1.156	0.065	-0.371	0.028	-0.05	39.4
515.265	Fe-poor carbonate	0.755	0.044	-0.285	0.022	1.153	0.093	-0.424	0.032	0.86	64.8
515.375	Fe-rich carbonate	0.823	0.055	-0.194	0.037	1.229	0.043	-0.311	0.064	0.06	45.2
516.38	Fe-rich carbonate	0.640	0.033	-0.272	0.037	0.966	0.081	-0.381	0.064	-0.05	30.2
517.2	Fe-rich carbonate									0.43	32.2
517.675	Fe-poor carbonate	0.758	0.036	-0.275	0.028	1.121	0.027	-0.408	0.053	0.53	48.3
517.74	Fe-rich carbonate									0.31	44.1
518.565	Fe-rich carbonate	0.489	0.014	-0.490	0.016	0.695	0.049	-0.733	0.018	0.49	36.7
520.05	Fe-poor carbonate	0.516	0.014	-0.529	0.014	0.738	0.054	-0.789	0.014	0.27	43.5
520.43	Fe-rich carbonate									-1.19	31.8
520.62	Fe-rich carbonate									-0.13	34.2
520.695	Fe-rich carbonate									-0.18	29.3
521	Fe-rich carbonate	0.562	0.040	-0.393	0.008	0.855	0.079	-0.524	0.021	-2.36	9.0
521.68	Fe-rich carbonate	0.342	0.023	-0.538	0.039	0.495	0.051	-0.768	0.047	-3.05	21.9
Drill core FD-365											
160.29	IFs	1.485	0.024	0.664	0.012	2.215	0.045	0.943	0.058	-10.90	8.4
198.11	IFs									-10.25	6
219.755	IFs									-10.37	6.4
236.75	IFs									-10.60	4
271.07	IFs	1.432	0.021	0.610	0.017	2.100	0.058	0.845	0.052	-11.37	2.9
287.475	IFs	1.326	0.029	0.548	0.022	2.000	0.049	0.762	0.048	-11.29	12.1
297.65	IFs									-10.64	12.5
309.55	IFs	2.225	0.032	1.595	0.030	3.298	0.059	2.360	0.038	-8.20	15

[a] Iron isotopic ratios are reported in per mil difference relative to iron metal standard IRMM-014.
[b] Carbon isotopic ratios are reported in per mil difference relative to PDB standard.

Table 6. 2: Iron isotope composition of iron formations from Isua, Greenland.

Isua									
		δ^{56}Fe (‰)[a]				δ^{57}Fe (‰)[a]			
Sample	Lithology	Magnetite	SD	Fe-carb.	SD	Magnetite	SD	Fe-carb.	SD
IS-04-01	IFs	0.168	0.019	-0.26	0.021	0.280	0.018	-0.391	0.024
IS-04-06	IFs	0.644	0.025	-0.01	0.028	0.969	0.017	-0.035	0.020
IS-04-11	IFs	0.393	0.043	-0.25	0.019	0.583	0.067	-0.371	0.024

[a] Iron isotopic ratios are reported in per mil difference relative to iron metal standard IRMM-014.

6.2.2 Carbon isotopes

The carbon isotopic composition of carbonates ($\delta^{13}C_{carb}$) correlates with the carbonate and iron contents (Fig. 6.2). Samples with lower carbonate and higher iron concentrations, such as IFs, have light $\delta^{13}C$ values (from -3.63 to -11.42‰) with an average of -9.30 $\pm$ 2.2‰ (n=24). As carbonate content increases, the $\delta^{13}C$ becomes heavier, with Fe-rich and Fe-poor carbonates varying between -3.05 to +0.49‰ and -0.56 to +0.86‰, respectively. These values overlap with previously measured IFs and carbonates from South Africa (Transvaal Craton: Beukes et al., 1990, Beukes and Klein, 1990; Kaufman, 1996; Fischer et al., 2009; Heimann et al., 2010; Eroglu et al., 2017) and Western Australia (Hamersley Basin: Johnson et al., 2008; Craddock and Dauphas, 2011).

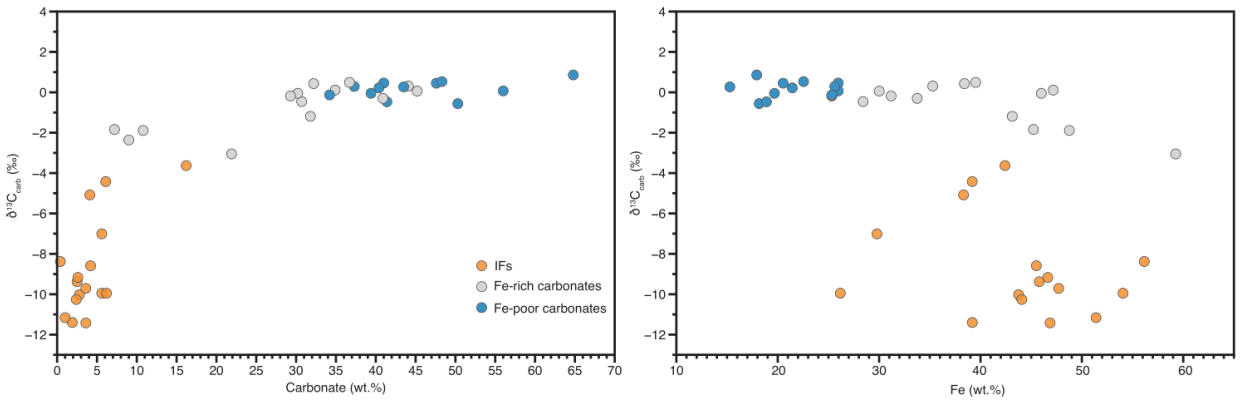

Figure 6. 2: Carbon isotope composition of carbonates in IFs, Fe-rich and Fe-poor samples showing a correlation with carbonate and iron content (wt.%).

6.3 Discussion

There is a wide range in Fe and C isotopic compositions among iron formations and carbonates from the Carajás Basin (Fig. 6.1). The identification whether such isotopic

variations record seawater, hence primary changes in the paleoenvironmental conditions in which these rocks formed, as opposed to an early and/or late diagenetic alteration or metamorphism, will be key to distinguish between biotic and abiotic processes and further gain insights into the coupled biogeochemical cycles of iron and carbon in the basin.

6.3.1 Evidence for microbial iron respiration in the Carajás Basin

A consensus lies upon a steady state carbon cycle over long timescales during the Precambrian (Schidlowski et al., 1979, 1988; Krissanten-totton et al., 2018). This implies a low variability of the carbon isotopic reservoir ($\delta^{13}C \cong 0‰$) of dissolved inorganic carbon (DIC) in seawater throughout the geological record (Kaufman et al., 1990; Fischer et al., 2009). Consequently, studies measuring $\delta^{13}C$ values of $0 \pm 2‰$ in shallow water carbonates (Fe-poor Ca-Mg carbonates) are generally interpreted to have precipitated in near-equilibrium with seawater (*e.g.* Heimann et al., 2010; Craddock and Dauphas, 2011; Johnson et al., 2013). This argument is also constrained by the experimentally-calculated fractionation factor between siderite and DIC of $-0.5 \pm 0.2‰$ (Jimenez-Lopes and Romanek, 2004) and supported by a vast literature showing $\delta^{13}C$ in modern and ancient carbonates with similar isotopic compositions (Becker and Clayton, 1972; Schidlowski et al., 1975; Veizer et al., 1989; Beukes et al., 1990; Shields and Veizer 2002; Eroglu et al., 2017). However, this is not always the case, particularly for Fe-rich carbonates and oxide-facies IFs containing abundant siderite ($FeCO_3$) and ankerite [$Ca(Fe,Mg,Mn)(CO_3)_2$], which are usually ^{13}C-depleted down to -16‰, with extreme values reaching -28‰ (Canfield et al., 2018).

The large range in $\delta^{13}C_{carb}$ (from -11.40 to +0.86‰) in the Carajás Basin covers previously measured values in the Hamersley and Transvaal basins, and IFs from North China (Fig. 6.3). This isotopic gradient with ^{13}C-depleted siderite/ankerite in deeper oxide-facies IFs changing towards more positive $\delta^{13}C$ values in shallower limestones and dolomites was argued to reflect stratification in the water column with respect to DIC and $\delta^{13}C$-DIC (Beukes et al., 1990; Beukes and Klein, 1990; Kaufman et al., 1990; Winter and Knauth, 1992). Similar systems are known for instance in modern redox-stratified lakes (Wittkop et al., 2020). However this hypothesis was discredited for the Archean due to the unlikelihood of a stronger biological pump compare to present level, a scenario necessary to generate such isotopic gradient on a global scale (Fischer et al., 2009). Mantle-derived carbon released to the ocean from hydrothermal vents usually have $\delta^{13}C$-DIC values around -6.5‰ and siderite precipitation from such fluids is feasible (Shanks III, 2001; Jiang and Tosca, 2019). Still, carbonates in Carajás have negative $\delta^{13}C$ values down to -11.40‰, which require an additional source of light carbon. A possible explanation may be related to microbial degradation of organic matter in sediment porewaters, as also suggested in previous studies (*e.g.* Becker and Clayton, 1972; Perry, 1973; Heimann et al., 2010; Craddock and Dauphas, 2011; Johnson et al., 2013; Canfield et al., 2018). Indeed organic matter of Archean sediments generally shows $\delta^{13}C$ values between -25 and -45‰ (e.g. Fischer et al., 2009), and its degradation would produce isotopically-light DIC, potentially transferred to Fe-carbonate. The $\delta^{13}C_{carb}$ in IFs from Carajás with light $\delta^{13}C$ values (average of -9.59 $\pm$ 2.0‰) suggests that these carbonates did not precipitate in equilibrium with seawater, but is rather consistent with a precipitation in sediment porewaters after mineralization of organic matter by microbial respiration. Given that conditions were mostly anoxic and the lack of sulfides in IFs, iron oxides were likely the

main electron acceptors for organic matter respiration via dissimilatory iron reduction (DIR) process (Lovley, 1993).

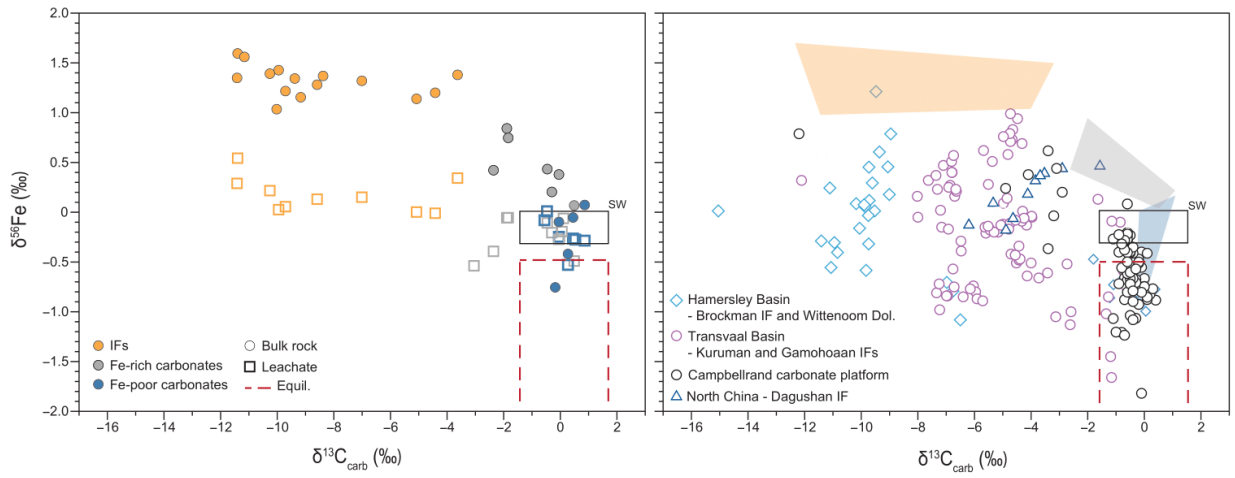

Figure 6. 3: Iron and carbon isotope compositions from Carajás compared with previously studied samples from Australia, South Africa and China (Johnson et al., 2008; Heimann et al., 2010; Craddock and Dauphas, 2011; Eroglu et al., 2018; Tong et al., 2021). Black rectangle delineates the range expected for Archean seawater (SW), while red rectangle delineates the predicted range expected for Fe-rich carbonates that precipitated in equilibrium with Archean seawater based on experimental and theoretical constrains.

Rego et al. (2021) recently showed that anoxygenic photosynthesis was a plausible mechanism responsible for Fe-oxidation in the Carajás Basin, producing organic matter in surface waters with $\delta^{13}C_{org}$ ~ -25‰. This light organic carbon was likely supplied to underlying sediments where remineralization occurred, providing a depleted ^{13}C DIC in porewaters to be mixed and exchanged with seawater DIC (~0‰). The ratios between these two DIC pools have been modeled and used to explain variations in $\delta^{13}C_{carb}$ in carbonates from the Transvaal craton (Heimann et al., 2010). Following the model of Heimann et al. (2010), if we consider that carbonates were formed from a completely organic-derived source, they would reflect $\delta^{13}C_{carb}$ values of ~-25‰. Carajás IFs with an average $\delta^{13}C_{carb}$ of -9.59 $\pm$ 2.0‰ are best explained by a contribution from both sources of

organic and inorganic DIC, as reported in Brockman Fe-rich carbonates (Craddock and Dauphas, 2011). In fact, the $\delta^{13}C_{carb}$ gradient from near-zero in carbonates to negative in IFs could reflect changes in the relative fluxes of these two sources, with for instance a variable efficiency of organic matter export from shallower to deeper settings. This assumption is supported by Fe-rich and Fe-poor carbonates with $\delta^{13}C_{carb}$ close to 0 (average -0.37 $\pm$ 1.01‰) favoring precipitation in near equilibrium with seawater, which argues for a lower imprint of microbial respiration associated with DIR in shallow waters.

Evidence from carbon isotopes suggests a locally active biological pump, with organic matter from photoferrotrophs feeding microbial iron reducers in deeper IFs facies grading towards a less pronounced DIR signal in shallow water Fe-carbonates. This may explain the low amount of organic material in IFs from Carajás (Rego et al., 2021), as also observed in major IFs deposits elsewhere (Konhauser et al., 2017; Thompson et al., 2019). Moreover, organic-rich Fe carbonates containing abundant framboidal pyrites within crinkly-laminated microbial layers could have been derived from sulfides reacting with Fe(III) hydroxides and removing their availability to microbial DIR (Johnson et al., 2008). This argues in favor of an absence of DIR in Fe-poor carbonates, but also possibly implies a local development of euxinic conditions in shallow waters concomitantly with ferruginous environment in the deeper portion of the Neoarchean Carajás Basin.

6.3.2 Fe isotopes in magnetite and carbonate: identifying DIR and isotopic re-equilibration

The Fe isotope composition of bulk rock IFs from Carajás has been shown to record Fe oxidation by anoxygenic photosynthesis in the water column (Rego et al., 2021). In

contrast, Fe isotope composition of carbonate leachates corroborates with previous study arguing against a primary precipitation with seawater, particularly for IFs (Heimann et al., 2010; Craddock and Dauphas, 2011; Johnson et al., 2013; Konhauser et al., 2017, Fig. 6.3). This is also supported by light $\delta^{13}C_{carb}$ values measured in IF facies (see discussion above) likely reflecting DIR. Given that Fe-carbonates from IF facies in Carajás have varying, but mainly positive, $\delta^{56}Fe$ values with an average of +0.25 $\pm$ 0.25‰ (except one anomalous sample with $\delta^{56}Fe$ value of +1.60‰), this further supports an efficient reductive dissolution of Fe-oxides by DIR leading to an authigenic dissolved Fe(II) pool enriched in ^{56}Fe in pore space. This allowed carbonates to inherit a heavy $\delta^{56}Fe$ composition (Craddock and Dauphas, 2011; Johnson et al., 2013), likely reflecting an efficient microbial activity (*i.e*. respiration) contributing to an early diagenetic isotopic signature.

Contrary, iron-carbonate facies with carbonate $\delta^{56}Fe$ average ratios of -0.24 $\pm$ 0.17‰ could fairly resemble siderite precipitation in equilibrium with Archean seawater if assuming a dissolved Fe(II) source with similar isotopic composition similar to modern hydrothermal fluids ($-0.5 < \delta^{56}Fe_{hydrothermal\ fluid} < +0.1$; Sharma et al., 2001; Beard et al., 2003; Johnson et al., 2008; Bennett et al., 2009; Rouxel et al., 2016). This was shown experimentally by mineral-fluid interactions yielding a net fractionation between siderite and aqueous Fe(II) of -0.48 $\pm$ 0.22‰ (Wiesli et al., 2004). Importantly, Fe-poor carbonate with abundant calcite in its composition (Rego et al., 2021) have likely a higher contribution from Fe incorporated into calcite grains, thus reflecting a hydrothermal fluid-like composition as shown with $\delta^{56}Fe$ values closer to 0‰ (Fig. 6.3). This notion of carbonates in Fe-rich carbonate-facies precipitating in equilibrium with Archean seawater is also reinforced by the $\delta^{13}C_{carb}$ values ~0‰ in the same samples (see discussion

above), as opposed to carbonates in IF-facies recording extensive DIR (carbonates with positive $\delta^{56}Fe$ values, and very negative $\delta^{13}C_{carb}$).

All experiments involving microbial DIR have shown that $Fe(II)_{aq}$ produced from anaerobic respiration is always depleted in ^{56}Fe compared to precursor ferric substrate by ~-1 to -2.6‰ (Beard et al., 1999, 2003; Icopini et al., 2004; Johnson et al., 2005; Crosby et al., 2005; 2007; Wu et al., 2009; Tangalos et al., 2010; Percak-Dennett et al., 2011; Fortney et al., 2016, 2020). This ^{56}Fe-depleted Fe(II) will either precipitate in reduced Fe phases (*e.g.* siderite, magnetite, pyrite) and/or diffuse and escape from sediment to water column. If microbial DIR was indeed present in IFs and not in coeval Fe-carbonates, we would expect to see a change in fractionation between carbonate and magnetite pairs among the two main lithologies. However, this does not occur (Fig. 6.1 and Fig. 6.4A), and a constant fractionation is observed ($\Delta^{56}Fe_{mag-Fe\text{-}carb} = +0.98 \pm 0.11$‰). This suggests that an alternative process was responsible for the unexpectedly homogeneous isotopic signal within both drill-cores situated about 50 km apart from one another in the basin. Based on the available theoretical and experimental studies that defined fractionation factors associated to mineral precipitation, it is difficult to explain the constant fractionation observed between oxides and carbonates in IF facies and Fe-carbonate facies (Schauble et al., 2001; Wiesli et al., 2004; Anbar et al., 2005; Blanchard et al., 2009; Frierdich et al., 2014). Therefore, an alternative scenario needs to be invoked.

It has been proposed that magnetite in IFs could have an exclusively metamorphic origin by thermal decomposition of siderite at temperatures >200ºC (Rasmussen and Muhling, 2018). However, metamorphism on itself could not explain the gradual change from magnetite-rich IFs to Fe-rich, and magnetite-poor Fe-carbonates observed in Carajás on a meter scale in a single drill-core. Other processes such as early diagenetic DIR,

perhaps with some contribution from thermochemical Fe(III) reduction coupled to biomass oxidation (Halama et al., 2016) is more likely to have occurred based on petrographic and geochemical evidence of the IFs from Carajás (Rego et al., 2021; Justo et al., 2020). Despite the unlikelihood of magnetite having a metamorphic origin, we cannot rule out an effect of temperature on fractionation. The experimentally determined fractionation factors for microbial DIR ($1‰ < \Delta^{56}Fe_{mag - Fe\text{-}carb.} < 3‰$) could be altered by temperature-dependent processes towards lower values (*e.g.* ~1‰) for abiotic reduction from temperatures >170 ºC as predicted from Mössbauer spectroscopy data (Polyakov and Mineev, 2000; Polyakov et al., 2007). Given that IFs from Carajás were exposed to at least sub-greenschist to low greenschist facies metamorphism (Rosière et al., 2006; Justo et al., 2020), it is plausible to suggest a closed-system re-equilibration of the isotopic system reflecting the constant fractionation, thus, lacking the larger fractionation factors expected during DIR (Chanda et al., 2021 and references therein).

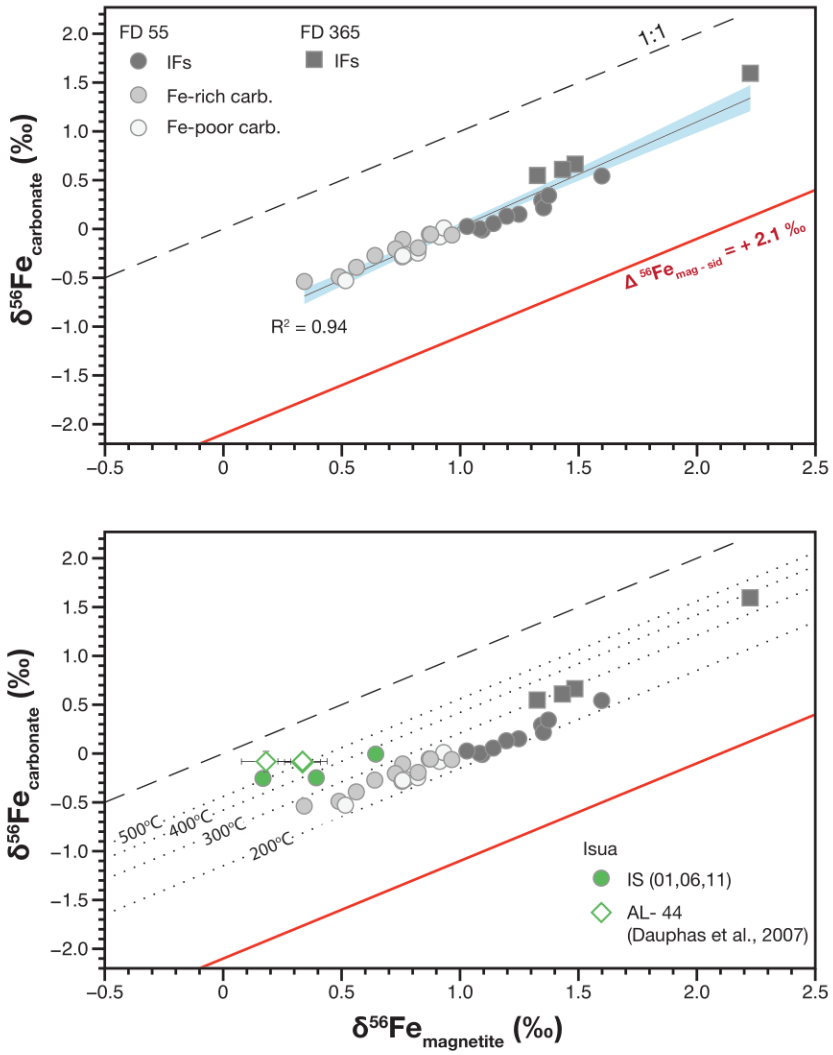

Figure 6. 4: Iron isotope composition of magnetite and carbonates from Carajás and Isua. The constant fractionation between magnetite and carbonate is shown (a) with a significant linear correlation. Red line shows the predicted fractionation of minerals precipitating in equilibrium with Archean seawater based on experimental results (Wiesli et al., 2004; Frierdich et al., 2014). Temperature estimates (b) were calculated based on the siderite and magnetite geothermometer considering theoretical data (Polyakov et al., 2007; Dauphas et al., 2007).

Only few studies have looked at the effects of metamorphism on the Fe isotopic system. Frost et al. (2007) argued that bulk samples from the ~1.8 Ga Biwabik IF were not affected by contact metamorphism given a lack of correlation between δ^{56}Fe values and their relative distance from the igneous contact. Hyslop et al. (2008), also working in Biwabik IFs, concluded that the δ^{56}Fe values of magnetite decreased in samples subjected

to higher metamorphic grade and that Fe isotopic re-equilibration among minerals might occur in a closed-system. In Fig. 6.4, we apply the same geothermometer used by Dauphas et al. (2007) constrained by the ß-factors of siderite and magnetite using Inelastic Nuclear Resonance X-ray Scattering (INRXS) (Polyakov and Mineev, 2000; Polyakov et al., 2007):

$$\Delta^{56}Fe_{mag-Fe\text{-}carb} = 0.13399x - 1.2668 * 10^{-3}x^2 + 0.54997 * 10^{-6}x^3 \, (‰/amu)$$

where $x = 10^6/T^2$ with the absolute temperature in degrees Kelvin (K). Based on 31 magnetite-carbonate mineral pairs in the two distinctly located drill cores in the Carajás Basin, a $\Delta^{56}Fe_{mag-Fe\text{-}carb.} = +0.98 \pm 0.11‰$ suggests that these rocks were exposed to temperatures likely between 200 to 300ºC (Fig. 6.4). Moreover, this temperature range is in agreement with an independent estimate based on Raman spectroscopy from two organic-rich carbonate samples, which yielded a temperature of 310 $\pm$ 7 (1SD) $\pm$ 30ºC (*i.e.* geothermometer error) (Fig. 6.5). Moreover, we applied the same leaching method and magnetite separation technique utilized in Carajás to IF samples from Isua (~3.8 Ga), to compare temperature estimations previously determined. Based on our measurements, Isua samples were exposed to temperatures likely between ~400ºC to > 500ºC as similarly determined by Dauphas et al. (2007). This further reinforces how carbonates can be targeted with weak acid leachates, and validate our measurements on pairs of magnetite and carbonate. Interestingly, the occurrence of an inter-mineral equilibration at relatively low temperature in Carajás samples masks clear evidence from any fractionation associated with DIR and corroborates with previous studies arguing towards a decrease in fractionation factors related to increasing temperatures (Dauphas et al., 2007; Polyakov et al., 2007; Hyslop et al., 2008).

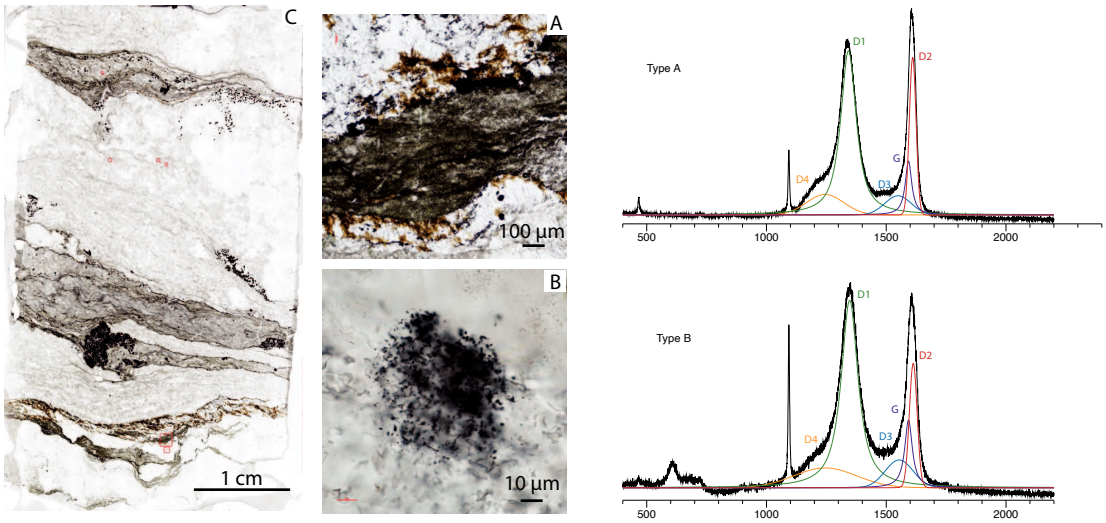

Figure 6. 5: Raman spectra showing the two types of organic matter (a,b) found in an Fe-poor carbonate sample (c).

Accordingly, a constant fractionation between magnetite and Fe-carbonates in a basin scale is best explained by a temperature induced re-equilibration of the Fe isotopic system. Surprisingly, calculated metamorphic temperature for the IF and carbonates in Carajás is likely between ~200 to 300ºC, which is lower than expected for re-equilibration of the Fe isotopic system (Hyslop et al., 2008). This implies that studies dealing with Fe isotope systematics, particularly in rocks that were subjected to relatively low metamorphic temperatures, should be cautious when interpreting their Fe isotopic composition on different mineralogical phases. Therefore, we concur with previous studies arguing that bulk-rock analysis (if in a closed-system) is best suited for samples that underwent post-alteration processes (*e.g.* burial metamorphism), which could still provide clues on the mechanisms responsible for Fe isotope fractionation (Frost et al., 2007).

6.4 Conclusions and Perspective

Here we coupled Fe and C isotopes in IFs and carbonates to distinguish primary and secondary processes in Neoarchean samples from Carajás, Brazil. Despite the lack of significant Fe isotopic fractionation associated to DIR, the negative $\delta^{13}C$ in IFs from Carajás supports compiling evidence in favor of microbial iron respiration. This reinforces the role of DIR in Fe cycling prior to the GOE. Moreover, we suggest that temperatures of ~200 to 300ºC holds the potential to re-equilibrate the Fe isotopic composition between carbonates (siderite/ankerite) and magnetite. Therefore, caution should be taken when interpreting the Fe isotopic composition of different mineralogical phases, including rocks that were only exposed to low metamorphic temperatures. In this case, the coupling between C and Fe isotopes in bulk-samples could be an alternative to identify the presence of DIR in the ancient rock record. Another alternative way to explore the Fe isotope variability could be done by *in situ* Fe isotope analyses in minerals, which might show some degrees of variability between cores and rims of carbonate and magnetite grains (*e.g*. core of large grains would eventually preserve a diagenetic signal related to DIR, while the rims would be re-equilibrated with magnetite).

6.5 References

Anbar, A.D., Jarzecki, A.A., and Spiro, T.G., 2005, Theoretical investigation of iron isotope fractionation between Fe(H2O)63+ and Fe(H2O) 62+: Implications for iron stable isotope geochemistry: Geochimica et Cosmochimica Acta, v. 69, p. 825–837, doi:10.1016/j.gca.2004.06.012.

Beard, B.L., and Johnson, C.M., 1999, High precision iron isotope measurements of

terrestrial and lunar materials: Geochimica et Cosmochimica Acta, v. 63, p. 1653–1660, doi:10.1016/S0016-7037(99)00089-7.

Beard, B.L., Johnson, C.M., Skulan, J.L., Nealson, K.H., Cox, L., and Sun, H., 2003, Application of Fe isotopes to tracing the geochemical and biological cycling of Fe: Chemical Geology, v. 195, p. 87–117, doi:10.1016/S0009-2541(02)00390-X.

Becker, R.H., and N. Clayton, R., 1972, Carbon isotopic evidence for the origin of a banded iron-formation in Western Australia: Geochimica et Cosmochimica Acta, v. 36, p. 577–595, doi:10.1016/0016-7037(72)90077-4.

Bennett, S.A., Rouxel, O., Schmidt, K., Garbe-Schönberg, D., Statham, P.J., and German, C.R., 2009, Iron isotope fractionation in a buoyant hydrothermal plume, 5°S Mid-Atlantic Ridge: Geochimica et Cosmochimica Acta, v. 73, p. 5619–5634, doi:10.1016/j.gca.2009.06.027.

Beukes, N.J., and Klein, C., 1990, Geochemistry and sedimentology of a facies transition - from microbanded to granular iron-formation - in the early Proterozoic Transvaal Supergroup, South Africa: Precambrian Research, v. 47, p. 99–139, doi:10.1016/0301-9268(90)90033-M.

Beukes, N.J., Klein, C., Kaufman, A.J., and Hayes, J.M., 1990, Carbonate petrography, kerogen distribution, and carbon and oxygen isotope variations in an early Proterozoic transition from limestone to iron-formation deposition, Transvaal Supergroup, South Africa: Economic Geology, v. 85, p. 663–690.

Blanchard, M., Poitrasson, F., Méheut, M., Lazzeri, M., Mauri, F., and Balan, E., 2009, Iron isotope fractionation between pyrite (FeS_2), hematite (Fe_2O_3) and siderite ($FeCO_3$): A first-principles density functional theory study: Geochimica et Cosmochimica Acta, v. 73, p. 6565–6578, doi:10.1016/j.gca.2009.07.034.

von Blanckenburg, F., Mamberti, M., Schoenberg, R., Kamber, B.S., and Webb, G.E., 2008,

The iron isotope composition of microbial carbonate: Chemical Geology, v. 249, p. 113–128, doi:10.1016/j.chemgeo.2007.12.001.

Busigny, V., Marin-Carbonne, J., Muller, E., Cartigny, P., Rollion-Bard, C., Assayag, N., and Philippot, P., 2017, Iron and sulfur isotope constraints on redox conditions associated with the 3.2 Ga barite deposits of the Mapepe Formation (Barberton Greenstone Belt, South Africa): Geochimica et Cosmochimica Acta, v. 210, p. 247–266, doi:10.1016/j.gca.2017.05.002.

Busigny, V., Planavsky, N.J., Goldbaum, E., Lechte, M.A., Feng, L., and Lyons, T.W., 2018, Origin of the Neoproterozoic Fulu iron formation, South China: Insights from iron isotopes and rare earth element patterns: Geochimica et Cosmochimica Acta, v. 242, p. 123–142, doi:10.1016/j.gca.2018.09.006.

Busigny, V., Planavsky, N.J., Jézéquel, D., Crowe, S., Louvat, P., Moureau, J., Viollier, E., and Lyons, T.W., 2014, Iron isotopes in an Archean ocean analogue: Geochimica et Cosmochimica Acta, v. 133, p. 443–462, doi:10.1016/j.gca.2014.03.004.

Canfield, D.E., Zhang, S., Wang, H., Wang, X., Zhao, W., Su, J., Bjerrum, C.J., Haxen, E.R., and Hammarlund, E.U., 2018, A Mesoproterozoic iron formation: Proceedings of the National Academy of Sciences of the United States of America, v. 115, p. E3895–E3904, doi:10.1073/pnas.1720529115.

Chanda, P., Amenabar, M.J., Boyd, E.S., Beard, B.L., and Johnson, C.M., 2021, Stable Fe isotope fractionation during dissimilatory Fe(III) reduction by a thermoacidophile in acidic hydrothermal environments: Geochimica et Cosmochimica Acta, v. 292, p. 427–451, doi:10.1016/j.gca.2020.09.025.

Craddock, P.R., and Dauphas, N., 2011a, Iron and carbon isotope evidence for microbial iron respiration throughout the Archean: Earth and Planetary Science Letters, v. 303, p. 121–132, doi:10.1016/j.epsl.2010.12.045.

Craddock, P.R., and Dauphas, N., 2011b, Iron Isotopic Compositions of Geological Reference Materials and Chondrites: Geostandards and Geoanalytical Research, v. 35, p. 101–123, doi:10.1111/j.1751-908X.2010.00085.x.

Crosby, H.A., Johnson, C.M., Roden, E.E., and Beard, B.L., 2005, Coupled Fe(II)-Fe(III) electron and atom exchange as a mechanism for Fe isotope fractionation during dissimilatory iron oxide reduction: Environmental Science and Technology, v. 39, p. 6698–6704, doi:10.1021/es0505346.

Crosby, H.A., Roden, E.E., Johnson, C.M., and Beard, B.L., 2007, The mechanisms of iron isotope fractionation produced during dissimilatory Fe(III) reduction by Shewanella putrefaciens and Geobacter sulfurreducens: Geobiology, v. 5, p. 169–189, doi:10.1111/j.1472-4669.2007.00103.x.

Dauphas, N., Janney, P.E., Mendybaev, R.A., Wadhwa, M., Richter, F.M., Davis, A.M., Van Zuilen, M., Hines, R., and Foley, C.N., 2004, Chromatographic separation and multicollection-ICPMS analysis of iron. Investigating mass-dependent and -independent isotope effects: Analytical Chemistry, v. 76, p. 5855–5863, doi:10.1021/ac0497095.

Dauphas, N., Pourmand, A., and Teng, F.Z., 2009, Routine isotopic analysis of iron by HR-MC-ICPMS: How precise and how accurate? Chemical Geology, v. 267, p. 175–184, doi:10.1016/j.chemgeo.2008.12.011.

Dauphas, N., van Zuilen, M., Busigny, V., Lepland, A., Wadhwa, M., and Janney, P.E., 2007, Iron isotope, major and trace element characterization of early Archean supracrustal rocks from SW Greenland: Protolith identification and metamorphic overprint: Geochimica et Cosmochimica Acta, v. 71, p. 4745–4770, doi:10.1016/j.gca.2007.07.019.

Eroglu, S., van Zuilen, M.A., Taubald, H., Drost, K., Wille, M., Swanner, E.D., Beukes,

N.J., and Schoenberg, R., 2017, Depth-dependent $\delta^{13}C$ trends in platform and slope settings of the Campbellrand-Malmani carbonate platform and possible implications for Early Earth oxygenation: Precambrian Research, v. 302, p. 122–139, doi:10.1016/j.precamres.2017.09.018.

Fischer, W.W., Schroeder, S., Lacassie, J.P., Beukes, N.J., Goldberg, T., Strauss, H., Horstmann, U.E., Schrag, D.P., and Knoll, A.H., 2009, Isotopic constraints on the Late Archean carbon cycle from the Transvaal Supergroup along the western margin of the Kaapvaal Craton, South Africa: Precambrian Research, v. 169, p. 15–27, doi:10.1016/j.precamres.2008.10.010.

Fortney, N.W., Beard, B.L., Hutchings, J.A., Shields, M.R., Bianchi, T.S., Boyd, E.S., Johnson, C.M., and Roden, E.E., 2021, Geochemical and stable Fe isotopic analysis of dissimilatory microbial iron reduction in Chocolate Pots Hot Spring, Yellowstone National Park: Astrobiology, v. 21, p. 83–102, doi:10.1089/ast.2019.2058.

Frierdich, A.J., Beard, B.L., Scherer, M.M., and Johnson, C.M., 2014, Determination of the Fe(II)aq-magnetite equilibrium iron isotope fractionation factor using the three-isotope method and a multi-direction approach to equilibrium: Earth and Planetary Science Letters, v. 391, p. 77–86, doi:10.1016/j.epsl.2014.01.032.

Frost, C.D., Blanckenburg, F., Schoenberg, R., Frost, B.R., and Swapp, S.M., 2007, Preservation of Fe isotope heterogeneities during diagenesis and metamorphism of banded iron formation: Contributions to Mineralogy and Petrology, v. 153, p. 211–235, doi:10.1007/s00410-006-0141-0.

Halama, M., Swanner, E.D., Konhauser, K.O., and Kappler, A., 2016, Evaluation of siderite and magnetite formation in BIFs by pressure–temperature experiments of Fe(III) minerals and microbial biomass: Earth and Planetary Science Letters, v. 450, p. 243–253, doi:10.1016/j.epsl.2016.06.032.

Heimann, A., Johnson, C.M., Beard, B.L., Valley, J.W., Roden, E.E., Spicuzza, M.J., and Beukes, N.J., 2010, Fe, C, and O isotope compositions of banded iron formation carbonates demonstrate a major role for dissimilatory iron reduction in ~2.5Ga marine environments: Earth and Planetary Science Letters, v. 294, p. 8–18, doi:10.1016/j.epsl.2010.02.015.

Hyslop, E.V., Valley, J.W., Johnson, C.M., and Beard, B.L., 2008, The effects of metamorphism on O and Fe isotope compositions in the Biwabik Iron Formation, northern Minnesota: Contributions to Mineralogy and Petrology, v. 155, p. 313–328, doi:10.1007/s00410-007-0244-2.

Icopini, G.A., Anbar, A.D., Ruebush, S.S., Tien, M., and Brantley, S.L., 2004, Iron isotope fractionation during microbial reduction of iron: The importance of adsorption: Geology, v. 32, p. 205–208, doi:10.1130/G20184.1.

Jiang, C.Z., Halevy, I., and Tosca, N.J., 2022, Kinetic isotope effect in siderite growth: Implications for the origin of banded iron formation siderite: Geochimica et Cosmochimica Acta, v. 322, p. 260–273, doi:10.1016/j.gca.2022.01.029.

Jiang, C.Z., and Tosca, N.J., 2019, Fe(II)-carbonate precipitation kinetics and the chemistry of anoxic ferruginous seawater: Earth and Planetary Science Letters, v. 506, p. 231–242, doi:10.1016/j.epsl.2018.11.010.

Jimenez-Lopez, C., and Romanek, C.S., 2004, Precipitation kinetics and carbon isotope partitioning of inorganic siderite at 25°C and 1 atm: Geochimica et Cosmochimica Acta, v. 68, p. 557–571, doi:10.1016/S0016-7037(03)00460-5.

Johnson, C.M., Beard, B.L., Klein, C., Beukes, N.J., and Roden, E.E., 2008a, Iron isotopes constrain biologic and abiologic processes in banded iron formation genesis: Geochimica et Cosmochimica Acta, v. 72, p. 151–169, doi:10.1016/j.gca.2007.10.013.

Johnson, C.M., Beard, B.L., and Roden, E.E., 2008b, The iron isotope fingerprints of redox

and biogeochemical cycling in modern and ancient Earth: Annual Review of Earth and Planetary Sciences, v. 36, p. 457–493, doi:10.1146/annurev.earth.36.031207.124139.

Johnson, C.M., Ludois, J.M., Beard, B.L., Beukes, N.J., and Heimann, A., 2013, Iron formation carbonates: Paleoceanographic proxy or recorder of microbial diagenesis? Geology, v. 41, p. 1147–1150, doi:10.1130/G34698.1.

Johnson, C.M., Roden, E.E., Welch, S.A., and Beard, B.L., 2005, Experimental constraints on Fe isotope fractionation during magnetite and Fe carbonate formation coupled to dissimilatory hydrous ferric oxide reduction: Geochimica et Cosmochimica Acta, v. 69, p. 963–993, doi:10.1016/j.gca.2004.06.043.

Justo, A.P., Dantas, E.L., Bau, M., Freitas-Silva, F.H., Santos, R.V., and Schorscher, J.H.D., 2020, Paleobasinal to band-scale REE+Y distribution in Iron Formations from Carajás Amazon Craton, Brazil: Ore Geology Reviews, p. 103750, doi:10.1016/j.oregeorev.2020.103750.

Kaufman, A.J., 1996, Geochemical and mineralogic effects of contact metamorphism on banded iron-formation: An example from the Transvaal Basin, South Africa: Precambrian Research, v. 79, p. 171–194, doi:10.1016/0301-9268(95)00093-3.

Konhauser, K.O. et al., 2017, Iron formations: A global record of Neoarchaean to Palaeoproterozoic environmental history: Earth-Science Reviews, v. 172, p. 140–177, doi:10.1016/j.earscirev.2017.06.012.

Kouketsu, Y., Mizukami, T., Mori, H., Endo, S., Aoya, M., Hara, H., Nakamura, D., and Wallis, S., 2014, A new approach to develop the Raman carbonaceous material geothermometer for low-grade metamorphism using peak width: Island Arc, v. 23, p. 33–50, doi:10.1111/iar.12057.

Krissansen-Totton, J., Buick, R., and Catling, D.C., 2015, A statistical analysis of the carbon isotope record from the Archean to Phanerozoic and implications for the rise of oxygen: American Journal of Science, v. 315, p. 275–316, doi:10.2475/04.2015.01.

Lovley, D., 1993, Dissimilatory Metal Reduction: Annual Review of Microbiology, v. 47, p. 263–290, doi:10.1146/annurev.micro.47.1.263.

Ohmoto, H., Watanabe, Y., and Kumazawa, K., 2004, Evidence from massive siderite beds for a CO2-rich atmosphere before ~1.8 billion years ago: Nature, v. 429, p. 395–399, doi:10.1038/nature02573

Percak-Dennett, E.M., Beard, B.L., Xu, H., Konishi, H., Johnson, C.M., and Roden, E.E., 2011, Iron isotope fractionation during microbial dissimilatory iron oxide reduction in simulated Archaean seawater: Geobiology, v. 9, p. 205–220, doi:10.1111/j.1472-4669.2011.00277.x.

Polyakov, V.B., Clayton, R.N., Horita, J., and Mineev, S.D., 2007, Equilibrium iron isotope fractionation factors of minerals: Reevaluation from the data of nuclear inelastic resonant X-ray scattering and Mössbauer spectroscopy: Geochimica et Cosmochimica Acta, v. 71, p. 3833–3846, doi:10.1016/j.gca.2007.05.019.

Polyakov, V.B., and Mineev, S.D., 2000, The use of Mossbauer spectroscopy in stable isotope geochemistry: Geochimica et Cosmochimica Acta, v. 64, p. 849–865, doi:10.1016/S0016-7037(99)00329-4.

Rasmussen, B., and Muhling, J.R., 2018, Making magnetite late again: Evidence for widespread magnetite growth by thermal decomposition of siderite in Hamersley banded iron formations: Precambrian Research, v. 306, p. 64–93, doi:10.1016/j.precamres.2017.12.017.

Rego, E.S., Busigny, V., Lalonde, S. V., Philippot, P., Bouyon, A., Rossignol, C., Babinski,

M., and Cássia Zapparoli, A., 2021, Anoxygenic photosynthesis linked to Neoarchean iron formations in Carajás (Brazil): Geobiology, v. 19, p. 326–341, doi:10.1111/gbi.12438.

Rosière, C.A., Baars, F.J., Seoane, J.C.S., Lobato, L.M., da Silva, L.L., de Souza, S.R.C., and Mendes, G.E., 2006, Structure and iron mineralisation of the Carajás Province: Transactions of the Institutions of Mining and Metallurgy, Section B: Applied Earth Science, v. 115, p. 126–133, doi:10.1179/174327506X138986.

Rosing, M.T., Bird, D.K., Sleep, N.H., and Bjerrum, C.J., 2010, No climate paradox under the faint early Sun: Nature, v. 464, p. 744–747, doi:10.1038/nature08955

Rouxel, O., Dobbek, N., Ludden, J., and Fouquet, Y., 2003, Iron isotope fractionation during oceanic crust alteration: Chemical Geology, v. 202, p. 155–182, doi:10.1016/j.chemgeo.2003.08.011.

Rouxel, O., Toner, B.M., Manganini, S.J., and German, C.R., 2016, Geochemistry and iron isotope systematics of hydrothermal plume fall-out at East Pacific Rise 9°50′N: Chemical Geology, v. 441, p. 212–234, doi:10.1016/j.chemgeo.2016.08.027.

Schauble, E.A., Rossman, G.R., and Taylor, H.P., 2001, Theoretical estimates of equilibrium Fe-isotope fractionations from vibrational spectroscopy: Geochimica et Cosmochimica Acta, v. 65, p. 2487–2497, doi:10.1016/S0016-7037(01)00600-7.

Schidlowski, M., 1988, A 3,800-million-year isotopic record of life from carbon in sedimentary rocks: Nature, v. 333, p. 313–318, doi:10.1038/333313a0.

Schidlowski, M., Appel, P.W.U., Eichmann, R., and Junge, C.E., 1979, Carbon isotope geochemistry of the 3.7 × 109-yr-old Isua sediments, West Greenland: implications for the Archaean carbon and oxygen cycles: Geochimica et Cosmochimica Acta, v. 43, p. 189–199, doi:10.1016/0016-7037(79)90238-2.

Schoenberg, R., and Von Blanckenburg, F., 2005, An assessment of the accuracy of stable

Fe isotope ratio measurements on samples with organic and inorganic matrices by high-resolution multicollector ICP-MS: International Journal of Mass Spectrometry, v. 242, p. 257–272, doi:10.1016/j.ijms.2004.11.025.

Sharma, M., Polizzotto, M., and Anbar, A.D., 2001, Iron isotopes in hot springs along the Juan de Fuca Ridge: Earth and Planetary Science Letters, v. 194, p. 39–51, doi:10.1016/S0012-821X(01)00538-6.

Shields, G., and Veizer, J., 2002, Precambrian marine carbonate isotope database: Version 1.1: Geochemistry, Geophysics, Geosystems, v. 3, doi:10.1029/2001GC000266.

Swanner, E.D., Lambrecht, N., Wittkop, C., Harding, C., Katsev, S., Torgeson, J., and Poulton, S.W., 2020, The biogeochemistry of ferruginous lakes and past ferruginous oceans: Earth-Science Reviews, v. 211, p. 103430, doi:10.1016/j.earscirev.2020.103430.

Tangalos, G.E., Beard, B.L., Johnson, C.M., Alpers, C.N., Shelobolina, E.S., Xu, H., Konishi, H., and Roden, E.E., 2010, Microbial production of isotopically light iron(II) in a modern chemically precipitated sediment and implications for isotopic variations in ancient rocks: Geobiology, v. 8, p. 197–208, doi:10.1111/j.1472-4669.2010.00237.x.

Taylor, P.D.P., Maeck, R., and De Bièvre, P., 1992, Determination of the absolute isotopic composition and Atomic Weight of a reference sample of natural iron: International Journal of Mass Spectrometry and Ion Processes, v. 121, p. 111–125, doi:10.1016/0168-1176(92)80075-C.

Thompson, K.J. et al., 2019, Photoferrotrophy, deposition of banded iron formations, and methane production in Archean oceans: Science Advances, v. 5, doi:10.1126/sciadv.aav2869.

Veizer, J., Hoefs, J., Lowe, D.R., and Thurston, P.C., 1989, Geochemistry of Precambrian carbonates: II. Archean greenstone belts and Archean sea water: Geochimica et

Cosmochimica Acta, v. 53, p. 859–871, doi:10.1016/0016-7037(89)90031-8.

Weyer, S., and Schwieters, J.B., 2003, High precision Fe isotope measurements with high mass resolution MC-ICPMS: International Journal of Mass Spectrometry, v. 226, p. 355–368, doi:10.1016/S1387-3806(03)00078-2.

Wiesli, R.A., Beard, B.L., and Johnson, C.M., 2004, Experimental determination of Fe isotope fractionation between aqueous Fe(II), siderite and "green rust" in abiotic systems: Chemical Geology, v. 211, p. 343–362, doi:10.1016/j.chemgeo.2004.07.002.

Winter, B.L., and Knauth, L.P., 1992, Stable isotope geochemistry of cherts and carbonates from the 2.0 Ga Gunflint iron formation: implications for the depositional setting, and the effects of diagenesis and metamorphism: Precambrian Research, v. 59, p. 283–313, doi:10.1016/0301-9268(92)90061-R.

Wittkop, C., Swanner, E.D., Grengs, A., Lambrecht, N., Fakhraee, M., Myrbo, A., Bray, A.W., Poulton, S.W., and Katsev, S., 2020, Evaluating a primary carbonate pathway for manganese enrichments in reducing environments: Earth and Planetary Science Letters, v. 538, p. 116201, doi:10.1016/j.epsl.2020.116201.

Wu, L., Beard, B.L., Roden, E.E., and Johnson, C.M., 2009, Influence of pH and dissolved Si on Fe isotope fractionation during dissimilatory microbial reduction of hematite: Geochimica et Cosmochimica Acta, v. 73, p. 5584–5599, doi:10.1016/j.gca.2009.06.026.

Conclusions and final remarks

This thesis allowed us to gain further insights into how the Fe cycle was operating during a key period of Earth's history, such as prior to the GOE, where oxygen concentrations in the atmosphere and oceans were still low, but most likely starting to increase at specific locations. Many of the well-studied stratigraphic successions spanning the Archean and Paleoproterozoic are located in Australia, South Africa, and/or North America. Therefore, it was relevant to find appropriate samples from other places, such as the Amazonia Craton in South America, to characterize them and finally place them in a global context. Samples were initially studied and placed in a geochronological framework (see Chapter 2, and Annex). Afterwards, samples were prepared for geochemical analysis and measured for their Fe and C isotope compositions, as well as major and trace element contents.

In chapter 3, the main methods used in this thesis are described, including some experimental results and discussion on the Fe isotope composition of Fe-carbonate phases extracted by weak acetic acid leaching protocols. A series of test with distinct acids (*e.g.* HAc and HCl) at different concentrations performed on Fe-carbonate standard (*i.e.* siderite) and natural samples common in the Precambrian (*i.e.* iron formations and Fe-rich and –poor carbonates) have shown that partial and/or total dissolution may occur depending on the Fe-carbonate mineral being dissolved. Importantly, the Fe isotope composition of the partially dissolved leachate fraction was undistinguishable from the values measured for a total siderite dissolution (*i.e*. utilizing HCl for longer reaction times, or concentrated HCl-HNO_3 solution). Therefore, this procedure could be utilized

when targeting Fe-carbonates from the ancient rock record, which provide clues on the chemical evolution of Earth's oceans through time.

Chapter 4 focuses on the bulk-rock Fe-isotope and trace element measurements of iron formation (IF), carbonates, and shales. The first part of the chapter shows that paleoenvironmental conditions in Neoarchean Carajás seawater were anoxic and that microorganisms likely played a central role in oxidizing dissolved Fe(II) (*i.e.* through anoxygenic photosynthesis). This was supported by an absence of negative Ce anomaly, together with positive and homogeneous Fe isotope composition of IFs and the presence of organic matter with a C isotope signature similarly produced by autotrophic organisms. Even though we cannot completely rule-out a cryptic oxygen cycle, we did not identify any "whiffs" of oxygen prior to the GOE in Carajás. The development of other proxies, perhaps more redox-sensitive systems (e.g. Ce isotopes), could represent an alternative to identify the presence of lower oxygen contents in ancient environments. The second part of Chapter 4 shows that siltstones and shales stratigraphically above the IF are enriched in ^{56}Fe. This could reflect extensive dissimilatory iron reduction, and therefore represent a local effect in the basin. Moreover, the age of these sedimentary successions is still not defined. Additional effort is being place to date these rocks by utilizing techniques such as Re-Os systematic and to finally reconstruct the paleoenvironment conditions in which these rocks were formed (*e.g.* N and C isotopes).

Chapter 5 shows that scavenging of dissolved P by Fe-oxide precipitates was an active mechanism throughout the Archean Era. By measuring P and Fe content in IFs, and using the analogous nature of P-Fe partitioning in Carajás IFs compared to modern marine environments as well as experimental studies, we estimated dissolved phosphorous contents in paleoseawater locally and globally, based on measured, experimental, and literature data. We confirm that from 3.8 to 2.6 Ga, phosphorous was

most likely scarce in seawater, and estimate average concentration of 0.063 $\pm$ 0.05 μM P for this period. Iron formations were likely a significant P sink and the residence time of P in Archean seawater was potentially significantly lower (*e.g.* 146 years), by two orders of magnitude, compared to modern ocean (e.g. ~ 20000 to 80000 years). Finally, this finding has also implication for oxygen accumulation in the atmosphere, as the long-term availability of phosphorous in Earth's oceans can increase and/or decrease primary biomass production.

The last chapter of the thesis (Chapter 6) shows the distinction between primary and secondary features (i.e. early diagenetic and/or later alteration and metamorphic processes) imprinted in the rock record. Carbon isotope compositions in carbonates from IF are depleted in ^{13}C, likely reflecting microbial respiration which produced a light DIR source, as similarly observed in other IFs throughout the globe. The Fe isotope compositions of carbonates and magnetite, however, do not show the expected large fractionation associated to DIR. Contrary, a constant fractionation between carbonates and magnetite is observed on a basin scale, suggesting a re-equilibration of the Fe-isotopic system in a closed system. By using a magnetite-siderite geothermometer and Raman spectroscopy, it was possible to infer that these rocks were exposed to temperature between 200 to 300ºC. These temperatures are significantly low to cause Fe isotopes to re-equilibrate. Therefore, caution should be taken when measuring Fe isotopes in mineral separates and referring to fractionation factors determined at room-temperature. Ideally, bulk-rock measurements would be most representative of the sample if a closed-system was maintained. Other alternatives could rely on *in situ* measurements, showing varying degrees of variability between cores and rims of carbonate and magnetite grains (*e.g.* core of large grains would eventually preserve a

diagenetic signal related to DIR, while the rims would be re-equilibrated with magnetite). A combination of *in situ* work with high-precision bulk-measurements (including possible in the near future the 4 stable isotopes) seems like a promising tool to continue investigations of the redox changes in Earth's past ocean and atmosphere, and co-evolution of biosphere.

Annex

(Manuscript submitted to Precambrian Research)

Neoarchean environments associated to a Large Igneous Province: insights from the Carajás Basin, Amazonia Craton

Camille Rossignol[a, b]*, **Eric Siciliano Rego**[c, d, e], Francesco Narduzzi[a, d], Lívia Teixeira[a], Marco A. L. Silva[f], Janaína N. Ávila[g, h], Cristiano Lana[f], Ricardo F. Trindade[a], Pascal Philippot[a, d]

[a]*Departamento de Geofísica, Instituto de Astronomia, Geofísica e Ciências Atmosféricas, Universidade de São Paulo, 05508-090 São Paulo – SP, Brazil*

[b]*Università degli Studi di Cagliari, Dipartimento di Scienze Chimiche e Geologiche, Cittadella Universitaria, 09042 Monserrato, Italy*

[c]*Institut de Physique du Globe de Paris, Université de Paris, CNRS, Paris, France*

[d]*Géosciences Montpellier, Université de Montpellier, CNRS, Université des Antilles, Montpellier, France*

[e]*Instituto de Geociências, Universidade de São Paulo, 05508-080 São Paulo – SP, Brazil*

[f]*Applied Isotope Research Group, Departamento de Geologia, Escola de Minas, Universidade Federal de Ouro Preto, 35400-000 Ouro Preto – MG, Brazil*

[g]*Griffith Centre for Social and Cultural Research, Griffith University, Nathan Queensland 4111, Australia*

[h]*Research School of Earth Sciences, The Australian National University, 142 Mills Road, Canberra ACT 2601, Australia*

**Corresponding author (e-mail: camille.rossignol@unica.it)*

Abstract

The Carajás Basin, Amazonia Carton, preserves sedimentary series deposited just after the emplacement of the ca. 2.75 Ga Parauapebas LIP, allowing to document the impact of this LIP on sedimentary systems and depositional environments. Immediately after the main volcanic event, the Carajás Formation was emplaced and is comprised mainly of extensive Fe-rich sediments (*i.e.* iron formations) deposited in various environments ranging from shallow to deep-water settings. The Carajás Formation also contains a few volcaniclastic layers, for which sedimentological and U-Pb geochronological evidence that the Parauapebas volcanism was still active, though limited, between 2732 ± 5 Ma and 2720 ± 6 Ma. These ages expand the previously inferred stratigraphic range of the Carajás Formation and show, together with literature data, that the deposition of iron formations in the Carajás Basin continued for a prolonged period that lasted 30 to 40 Myrs. Above the Carajás Formation, the Igarapé Bahia Group does not preserve evidence of a volcanic activity contemporaneous to the sedimentation but contains a few iron formations at its base, interbedded in terrigenous beds. These few iron formations could reflect either a long-lasting effect of the Parauapebas LIP on hydrothermal circulation, or the input of seawater enriched in iron by other Neoarchean magmatic provinces.

Keywords

Large Igneous Province; Banded Iron Formation; Paleoenvironment reconstruction; U-Pb geochronology; Chemical abrasion-LA-ICP-MS analyses.

1. Introduction

Emplacement of Large Igneous Provinces (LIPs) can cause large magnitude modifications to the surface environments of the Earth (*e.g.*, Wignall, 2005). In this respect, Neoarchean LIPs are of particular significance because they were associated to profound and irreversible changes of surface conditions of the Earth. For instance, Neoarchean LIPs fueled the deposition of large banded iron formations (BIFs) around the world by enhancing submarine hydrothermal fluxes of ferrous iron (Barley et al., 1997; Isley, 1995; Isley and Abbott, 1999; Viehmann et al., 2015). Neorchean LIPs may also have modulated atmospheric oxygenation, by the emission of reducing gases and solutes, thus delaying

O_2 accumulation (Catling and Claire, 2005). On the contrary, weathering of subaerial LIPs could have promoted atmospheric O_2 accumulation by releasing essential nutrients to the oceans, favoring oxygenic photosynthesis (Kump and Barley, 2007; Meixnerová et al., 2021; Narduzzi et al., 2021).

The pleiotropic effects of Neoarchean LIPs on the Earth's surface environments remains incompletely understood , because the chain of events associated with Neoarchean LIPs emplacements remains incompletely characterized. This is due to the fact that only a limited number of sedimentary series associated with Neoarchean LIPs are preserved and can record the aftermaths of LIPs emplacement (Kump and Barley, 2007). Documenting detailed paleoenvironmental evolution following LIP emplacement thus represents an important task to better constrain their impact on the Earth's surface.

In the Amazonia Craton (Fig. 1A), a Neoarchean LIP referred to as the Parauapebas LIP has recently been recognized (Rossignol et al., 2021), but associated paleoenvironments remain undocumented. For this purpose, this study aims at reconstructing the depositional environments that existed in the Carajás Basin (Fig. 1B, C), where the Parauapebas LIP has been emplaced, by focusing on sedimentary units that have been deposited immediately after the emplacement of the LIP. This study provides a description of the depositional environments of these sedimentary units and new zircon U-Pb ages to constrain their age and contemporaneity with the Parauapebas LIP volcanic activity. These results allow discussing the Neoarchean paleoenvironmental evolution in the eastern part of the Amazonian Craton with emphasis on the links with LIP volcanism.

2. Geological setting

2.1. Regional context

The Carajás Basin is located on the Carajás Domain (Fig. 1B), which is made up of polymetamorphic tonalitic to granodioritic gneisses and migmatites with protolith ages of ca. 3080 Ma to ca. 3000 Ma (Machado et al., 1991; Moreto et al., 2015; Pidgeon et al., 2000). The basement has been later intruded by tonalites, trondhjemites and granodiorites (TTG) between ca. 2960 Ma and ca. 2930 Ma (Feio et al., 2013), between ca. 2870 Ma to 2830 Ma (Feio et al., 2013; Machado et al., 1991; Moreto et al., 2015; Pidgeon et al., 2000), and at 2820 ± 22 Ma (Feio et al., 2013). A long-lasting but poorly characterized tectono-

thermal event occurred between ca. 2600 and 2450 Ma (Machado et al., 1991; Melo et al., 2017; Requia et al., 2003; Tallarico et al., 2005; Toledo et al., 2019).

To the north, the Bacajá Domain is mainly made up of Rhyacian granitoids intruded in a tonalitic basement with a protolith age of ca. 2670 Ma (Macambira et al., 2009). To the south the Rio Maria Domain comprises Mesoarchean greenstone belts with komatiites (Siepierski and Ferreira Filho, 2016) and TTG emplaced between ca. 2980 and ca. 2920 Ma (Almeida et al., 2013) and between ca. 2870 Ma and ca. 2860 Ma (Almeida et al., 2013; Althoff et al., 2014; Feio et al., 2013; Macambira and Lancelot, 1996). The Rio Maria and the Carajás Domain are accreted since the end of the Mesoarchean, between ca. 2.87 Ga and ca. 2.83 Ga (Tavares et al., 2018). To the west, the Carajás Basin is overlain by volcanic and volcaniclastic rocks of the Uatumã Supergroup of the ca. 1.88 Ga Uatumã Silicic LIP (Antonio et al., 2021, 2017) while the eastern boundary of the basin is obliterated by the Neoproterozoic Araguaia Belt (Fig. 1B).

During the end of the Neoarchean and the Paleoproterozoic, different tectonic events affected the basement and overlying sediments, forming a WNW trending strike-slip system (Pinheiro and Holdsworth, 1997; Tavares et al., 2018; Toledo et al., 2019). Major shear zones are sealed by the ca. 1.88 Ga granitoids (Fig. 1C), and the Carajás Basin was subjected to minor tectonic and magmatic events afterward (Pinheiro and Holdsworth, 1997; Teixeira et al., 2019).

2.2. Parauapebas LIP

Between ca. 2770 Ma and ca. 2740 Ma, important mafic magmatism produced a 4 to 6 km thick basaltic series forming the Parauapebas Formation, with a peak in magmatic activity at ca. 2745 Ma (Fig. 2; Table 1; Lacasse et al., 2020; Machado et al., 1991; Martins et al., 2017; Olszewski et al., 1989; Toledo et al., 2019; Trendall et al., 1998; Wirth et al., 1986). Because the Parauapebas Formation has been largely eroded, it remains difficult to assess the exact areal extent of this formation, but present-day outcrops and inliers suggest that it covered most of the southeast Amazonia Craton (Souza et al., 2020; Vasquez et al., 2008). Associated with the basalts of the Parauapebas Formation, magmatic rocks including layered ultramafic and mafic plutons, as well as A-type granitoids, were emplaced between ca. 2760 Ma to ca. 2730 Ma (Barros et al., 2009; Feio et al., 2013, 2012; Machado et al., 1991; Mansur and Ferreira Filho, 2016; Sardinha et al., 2006;

Siepierski and Ferreira Filho, 2020). These magmatic rocks were emplaced in an intraplate tectonic setting (Olszewski et al., 1989; Feio et al., 2012; Martins et al., 2017; Toledo et al., 2019; Lacasse et al., 2020) and are characteristic of a LIP (Bryan and Ernst, 2008; Rossignol et al., 2021).

Recent paleomagnetic investigations suggest that the Amazonia Craton was located at a low latitude, close to the paleoequator, during the emplacement of the Parauapebas LIP (P. L. G. Martins et al., 2021a). Although ambiguous, paleogeographic reconstructions further suggest that the Parauapebas LIP could have been emplaced on a large continental domain comprising both Superior and Amazonia cratons (P. L. G. Martins et al., 2021a).

2.3. Stratigraphic framework

The sedimentary units overlying the Parauapebas LIP consist of the Carajás Formation and the Igarapé Bahia Group (Fig. 3). The Carajás Formation is mainly made up of BIFs (Dalstra and Guedes, 2004; Klein and Ladeira, 2002; Tolbert et al., 1971) deposited in an anoxic setting under the control of anoxygenic photosynthetic organisms (Rego et al., 2021). The Carajás Formation also comprises minor black shales and conglomeratic layers (Cabral et al., 2017) and microstructures of probable biogenic origin (Ribeiro da Luz and Crowley, 2012). Geochemical analyses of BIFs show very low content in lithophile elements, indicating that sediments from the Carajás Formation were devoid of terrigenous input, thus suggesting that this formation has been deposited far away from emerged lands (Justo et al., 2020; Macambira and Schrank, 2002; P. L. G. Martins et al., 2021b). The interlayering of volcanic rocks and BIFs shows that the Carajás Formation was deposited, at least in part, coevally with the Parauapebas LIP (Gibbs et al., 1986; Martins et al., 2017). These stratigraphic relationships indicate that the Carajás Formation is younger than 2759 ± 2 Ma, corresponding to the emplacement age of underlying volcanic rocks (Table 2; Machado et al., 1991). Dolerite sills intruded some BIFs at 2751 ± 4 Ma (Krymsky et al., 2007) and 2740 ± 8 Ma (Table 2; Trendall et al., 1998).

The Carajás Formation is overlain by the Igarapé Bahia Group (Fig. 3). The contact between these two units has not been observed but is generally assumed to be concordant (Araújo et al., 2021). However, the Igarapé Bahia Group directly overlies the basalts of the Parauapebas Formation in some localities, suggesting that the Igarapé Bahia Group

could overlie discordantly the Carajás Formation (Dreher et al., 2005; Melo et al., 2019). At its base, the Igarapé Bahia Group comprises BIF layers up to 10 m thick, grading upward to sandstone and siltstone interbedded with polymictic conglomerate containing angular clasts of BIF, chert, and volcanic rocks (Dreher et al., 2008, 2005; Galarza et al., 2008; Melo et al., 2019; Ronze et al., 2000). Volcanism coeval to the sedimentation has been suggested based on the occurrence of volcanic pebbles in the conglomerate. A maximum depositional age (MDA) of 2784 ± 27 Ma, relying on only one detrital zircon grain, has been proposed for this unit (Melo et al., 2019). Hydrothermal monazite gave a U-Pb date of 2575 ± 12 Ma interpreted as the age of fluid circulation (Tallarico et al., 2005), which suggests that the Igarapé Bahia Group would be older than ca. 2.6 Ga (Table 2). At a regional scale, the age of hydrothermal circulations is further corroborated by Re-Os dates on sulfides at 2576 ± 8 Ma and 2568 ± 8 Ma (Requia et al., 2003), and by the emplacement of small granitic bodies and pegmatites at 2557 ± 26 Ma and 2562 ± 39 Ma, respectively (U-Pb zircon age; Toledo et al., 2019).

The Igarapé Bahia Group bears striking similarities with the recently defined Serra Sul Formation regarding their sedimentary facies and depositional environments (Dreher et al., 2008, 2005; Galarza et al., 2008; Melo et al., 2019; Ronze et al., 2000; Rossignol et al., 2020b). Both sedimentary units also experienced a similar low grade regional metamorphism (Araújo and Nogueira, 2019; Galarza et al., 2008; Tallarico et al., 2005; Villas and Santos, 2001). The Serra Sul Formation is younger than 2684 ± 10 Ma (U-Pb zircon MDA; Fig. 3; Table 2;Rossignol et al., 2020b) and probably older than the age of fluid circulation imparting it at ca. 2575 ± 12 Ma (U-Pb date on hydrothermal monazite; Fig. 3; Table 2; Tallarico et al., 2005), suggesting a similar age to the Igarapé Bahia Group. Despite their similarities, the exact relationship between the Igarapé Bahia Group and the Serra Sul Formation remains unclear (Araújo and Nogueira, 2019; Rossignol et al., 2021).

3. Methodology

3.1. Sedimentological analyses and sampling

Seven fully cored wells were studied (Fig. 1C, Appendix 1), among which six intercept the Carajás Formation (FD55, FD110, FD353, FD354, FD365 and S11D214) and one (FD52) intersects the Igarapé Bahia Group. The drill cores were surveyed and logged at the 1/500

to 1/100 scales to identify their sedimentary facies. The lithology, sedimentary structures, petrography, clast lithology and shape, grading, syn-sedimentary deformational structures, and nature of the bedding contacts between successive facies are described.

The mineralogy was determined petrographically by reflected and transmitted light microscopy, complemented by scanning electron microscopy (SEM) and energy dispersive X-ray spectroscopy (EDS) for semi-quantitative SEM-EDS analysis. Three volcaniclastic samples from the Carajás Formation and four sandstone and conglomerate samples from the Igarapé Bahia Group have been collected for zircon U-Pb dating. Different sedimentary facies were sampled in order to minimize potential bias associated with sediment transport (Lawrence et al., 2011).

3.2. U-Pb zircon geochronology

3.2.1. Analytical methods

The zircon grains were extracted following a classical mineral separation procedure and handpicked under a binocular microscope. Zircon crystals from the Carajás Formation were subjected to a thermal annealing and chemical abrasion (TACA) treatment before Laser Ablation – Inductively Coupled Plasma – Mass Spectrometry (LA-ICP-MS) analysis to dissolve the parts of the grains where radiation damages and most likely Pb loss occurred while keeping undissolved the crystalline part of the grains (Crowley et al., 2014). The procedure follows the one implemented by L. Martins et al. (2021) and is summarized here. Thermal annealing was performed in ceramic crucibles at 850°C for 60 hours. After cooling, the grains were transferred into Teflon vials for partial dissolution into a 0.8 mL concentrated hydrofluoric acid (48% HF) and 3.6 mL 1:1 8M HNO_3 + H_20 solution. Dissolution was performed using an Ultra-wave single reaction chamber microwave digestion system. Internal chamber conditions were set at 175°C for 10 minutes, followed by a second 10 minutes step at 60°C. The grains were then cleaned through rinsing with 4M HCl solution, repeated rinsing with distilled water, and evaporated to dryness. After embedding the grains in an epoxy resin, the pucks were hand grounded to reveal equatorial cross-sections and imaged by cathodoluminescence to choose laser microsampling sites. No TACA treatment has been applied to zircon grains from the Igarapé Bahia Group. Detailed analytical set-up is given in Appendix 2. Potential biases related to TACA treatment have been controlled by comparing untreated

and TACA grains from the same samples and appears limited in this study. Further discussion about pre-analytical treatment is presented in Appendix 2.

3.2.2. Age calculations, data filtering and statistical analyses

A two-step procedure has been applied to derive maximum depositional ages (MDAs). The first step consisted in filtering the data based on their probability of concordance (Ludwig, 1998), calculated using the relevant function in Isoplot 3.00 (Ludwig, 2012) with a cut-off level of 10% including decay constant errors (Rossignol et al., 2016). Hereafter, concordant analyses refer to those having a probability of concordance ≥ 10%. Concordant analyses were kept for the second step that consists in calculating MDAs using the youngest cluster of at least three grains overlapping in age at 2σ (standard deviation) to ensure a robust estimate of the MDAs (Dickinson and Gehrels, 2009). MDAs were calculated as the concordia age of these youngest clusters using Isoplot 3.00 (Ludwig, 2012, 1998) and are provided with 95% confidence limits.

To complement the qualitative comparison between the Igarapé Bahia Group and the Serra Sul Formation, we performed quantitative comparisons of the bulk detrital zircon age distributions via Multi-Dimensional Scaling (MDS), which produces a "map" where each point, corresponding to a given age distribution, plots together (or not) according to their (dis)similarity (Vermeesch, 2013). The dissimilarity between age distributions can be assessed using various metrics, each having its own limitations (Pritchard et al., 2009; Rossignol et al., 2020a; Sircombe and Hazelton, 2004; Vermeesch, 2018). For this study, we used the L^2, Kolmogorov-Smirnov (KS) and Kuiper metrics. The L^2 metric is commonly used to compare the distance between densities (Pritchard et al., 2009; Sircombe and Hazelton, 2004), but has a tendency to blow up when distributions become concentrated which could produce counter intuitive results (Pritchard et al., 2009). The KS and Kuiper metrics are equally sensitive to the lateral offset between distributions, but the Kuiper metric is more sensitive than the KS to tails in age distributions (Vermeesch, 2018). These three metrics are implemented in the *provenance* package (Vermeesch et al., 2016) run with the R software (https://www.r-project.org).

4. Sedimentary facies analyses

4.1. Carajás Formation

Ten facies were recognized (Fig. 4; Table 3), defining three facies associations (Table 4). Representative BIF facies are presented in Fig. 5. Diagenetic and syn-depositional deformations are shown in Fig. 6, granular iron formations in Fig. 7, conglomerates in Fig. 8 and carbonate facies in Fig. 9.

4.1.1. Facies association 1

Description. The most common facies consists of BIFs (I1; Table 3) made up of alternating layers of Fe-rich minerals (magnetite and hematite) and chert with microcrystalline quartz and a few ankerite minerals disseminated in the matrix. Laminations are mm- to cm-thick and usually exhibit an even banding (Fig. 5A). Some laminations, however, display wavy structures (Fig. 5B), pinching geometries and erosion surfaces (Fig. 5C). The bedding is horizontal, but some layers show abrupt changes in bed orientation, suggesting slumped structures. Diagenetic features in the I1 facies comprise inflated beds that form cm-thick magnetite layers parallel to the bedding (Fig. 6A) and a few layers comprise secondary minerals (Fig. 6B).

Association 1 comprises two other less common IF facies (I2 and I3; Table 3). I2 facies has a similar lithology to I1 facies but exhibits chaotic structures (Fig. 6C). Granular Iron Formation (GIF; I3 facies) consists of cm to tens of cm-thick beds comprising very elongated clasts (1:5 width to length ratio, with largest clasts of cm scale), generally with rounded to sub-rounded ends (Fig. 7A). GIF beds are ungraded to normally graded and are interbedded within I1 facies (Fig. 7B). The clasts sometimes display buckled shapes attesting plastic deformation during transport and are generally flattened parallel to bedding (Fig. 7A, C).

In addition to microconglomerate GIF beds (I3 facies), association 1 also comprises matrix-supported ironstone flat-pebble conglomerate (G1; Table 3). The pebbles correspond to elongate (up to 10 cm long) intraformational rip-up clasts with sub-angular and cuspate shapes (Fig. 8A). Some clasts have sub-rounded to rounded ends (Fig. 8B, C), showing that they experienced various degrees of reworking. The clasts are generally flattened parallel to bedding (Fig. 8A, B, C). As being intraformational, most of the clasts are made up of chert or silicate-rich BIF, while a few are made up of GIF (Fig. 8D, E) or

greenish sandstones. The conglomerate beds are up to tens of meters thick, ungraded to normally graded, and have non-erosive bases.

Minor facies in association 1 are occasionally represented by a few black shale beds (F2; Table 3) that are commonly deformed and intruded by clastic dykes (Fig. 6F), 1-5 cm-thick greyish claystone layers, and a few m-thick beds made up of greenish, chlorite-rich, strongly weathered basaltic sandstone (V2; Table 3). These layers, without apparent sedimentary structure, are interbedded in sharp contact with BIFs and contain zircon grains.

Interpretation. The prevalence of finely laminated BIF suggests a deposition by settling of Fe-rich chemical mud in a deep-water environment, below storm wave-base (Table 4; Klein, 2005; Morris, 1993; Trendall, 2002). The sedimentary structures in BIFs, such as erosion surfaces, also attest for current reworking of fine-grained sedimentary particles and suggest deposition by turbidity currents (Dimroth, 1975; Rasmussen et al., 2013). Inflated beds formed during late diagenesis by seepage of reducing fluids that remobilized Fe along fractures oriented parallel to the bedding (Czaja et al., 2018). The few GIF layers interbedded within BIFs are also indicative of turbidity currents reworking chert clasts coarser than the silt-sized elements forming the main BIF deposits (Rasmussen et al., 2013; Simonson and Goode, 1989). The occurrence of chaotic beds is interpreted as slumped beds (Martinsen, 1994) and compares with previous observations of slumps in similar facies of the same formation (P. L. G. Martins et al., 2021b). G1 facies is interpreted to be deposited by the failure, induced either by storm or seismic activity, of loosely consolidated deposits (Myrow et al., 2004). Clastic dykes indicate rapid deposition from short-lived flows (i.e., subaqueous mass flow during the deposition of conglomerates) or liquefaction related to seismicity. The occurrence of black shale suggests that biological activity was high and took place at least locally. Volcanic and volcaniclastic beds indicate episodic volcanic inputs. Several cm-thick greyish clay beds are interpreted as diagenetic ashes formed as fallout deposits emitted by distal volcanic centers (Sohn et al., 2008). Thicker beds of basaltic sandstone can correspond either to hyaloclastic deposits with limited transport of the volcaniclasts, or to subaqueous debris flow reworking basaltic volcaniclasts (Sohn et al., 2008).

4.1.2. Facies association 2

Description. This association comprises mainly carbonate-rich BIFs (I4, Table 3) exhibiting sedimentary structures that are essentially like those of I1 facies, with horizontal to wavy laminations and reactivation surfaces (Fig. 5D). Carbonate-rich BIFs are made up of magnetite interlayered with ankerite and chert layers and containing a few Fe-silicate and pyrites.

Minor facies of association 2 consist of GIF (I3) and black shales (F2). Carbonate-rich BIFs exhibit numerous syn-sedimentary ductile deformation features marked by contorted laminations (Fig. 6D) and syn-sedimentary faults occurring together with angular intraformational clasts (Fig. 6E).

Interpretation. The overall characteristics of association 2 are similar to those of association 1, suggesting a rather similar deep-water environment, below wave base (Table 4). The precipitation of carbonate can be explained by deposition above the carbonate compensation depth, climate change to warmer temperatures (Beukes, 1983), change to more alkaline pH sea-water (Spier et al., 2007), or change in organic carbon input, allowing organic carbon to be exported from highly productive surface water and mineralized in deeper parts of the basin (Craddock and Dauphas, 2011; Heimann et al., 2010; Johnson et al., 2013). Because the studied drill cores do not show the relationship between facies association 2 and other facies associations, it is difficult to infer which of the above-mentioned processes favored the precipitation of carbonate. Based on other basins comprising similar facies, the likely depositional environment for association 2 is similar to association 1, but in a more proximal (shoreward) and shallower setting (Beukes and Gutzmer, 2008; Smith et al., 2013). The occurrence of numerous syn-sedimentary ductile and brittle deformation features indicates slope instability leading to the formation of slumps or slides (Martinsen, 1994).

4.1.3. Facies association 3

Description. This facies association comprises carbonate-rich BIF (I4) with even banded (Fig. 9A), wavy (Fig. 9B) and irregular layers (Fig. 9C), grading to facies C1 (Table 3), which is mainly made up of mm- to cm-thick wavy to crinkly carbonates laminae and minor iron oxides (Fig. 9D, E). Carbonates in facies C consist of ankerite and calcite, but

also contain framboidal pyrite, magnetite, chert, Fe-silicate and organic matter (Fig. 9F, G). The I4 and C1 beds alternate with silica-rich BIF (I1).

Association 3 also comprises numerous GIF beds up to ten cm-thick, occurring a few meters below and above I4 and C1 beds. Another minor facies consists of a few cm-thick beds made up of dark and fine-grained sediments (F1; Table 3).

Interpretation. The occurrence of crinkly laminae, framboidal pyrites and organic matter in facies C1 are indicative of microbially induced sedimentary structures (MISS), suggesting a shallow-water setting typical of the photic zone, above storm-wave base (Table 4; Hagadorn and Bottjer, 1997; Noffke et al., 2001; Riding, 2000; Vennin et al., 2015). This is consistent with the contribution of microbial anoxygenic photosynthesis to the precipitation of iron formations and carbonates in the Carajás Formation (Rego et al., 2021) and potentially an evidence for sulfate reducers in a sulfate-poor environment. The numerous GIF beds below and above MISS indicate an energetic environment allowing for reworking clasts ripped up from loosely lithified cherts (Beukes and Klein, 1990; Simonson and Goode, 1989).

4.2. Igarapé Bahia Group

The Igarapé Bahia Group is intersected by the drill core FD52 (Fig. 10). Six sedimentary facies were identified (Table 3) and grouped in two facies associations (Table 4).

4.2.1. Facies association 4

Description. The main facies consists of clast- to matrix-supported flat-pebble conglomerate made up of tens of cm to m-thick beds (facies G2; Table 3). The matrix comprises fine sand, silt or clay. The clasts are intraformational (Fig. 11A, B, C) and some preserves laminated structures (Fig. 11D). Most of the clasts are elongate (a few cm to tens of cm long), flattened parallel to the bedding (Fig. 11E) and with rounded ends, although a few clasts are sub-angular. Conglomeratic beds have a non-erosive base (Fig. 11E) and are generally ungraded, although some of them display a normal, inverse or inverse to normal grading.

Facies G2 is interbedded with finer lithologies composed of sand (S1 and S2; Table 3) and silt to clay (F1 and F2; Table 3). Sand facies are coarse- to fine-grained (Fig. 12A, B, C), commonly comprise intraformational muddy rip up clasts (Fig. 12B), contorted sandy

to muddy rafts (Fig. 12D), and consists of tens of cm to m-thick beds. Beds of S1 facies are either ungraded or normally graded and sometimes exhibit horizontal laminations. Horizons of S2 facies are characterized by chaotic stratification. Some horizons display anastomosed elutriation bands resulting from escaping water and elutriation of fine particles along vertical conduits (Fig. 12E), while others are made up of strongly folded horizons (Fig. 12F). Sand facies grades or alternate with greyish to dark fine sand and silt to clay that are generally finely laminated (Fig. 12A, C), except a few massive beds. F1 and F2 facies exhibit syn-sedimentary deformation shown by small syn-sedimentary faults and contorted beds.

Interpretation. Flat-pebble conglomerate results from the failure and subsequent ductile and brittle deformation of compacted to early cemented deposits (Myrow et al., 2004). Flat pebbles preserving angular shapes and laminated structure support limited transport, suggesting relatively proximal environments (Table 4). Failure of early cemented deposits can have been induced either by storm or seismic activity. The occurrence of disordered and chaotic horizons, rafted packages of sandstone and rip up mud clasts support the interpretation of flat-pebble conglomerate originating from the failure of loosely consolidated sediments along slide scars (Martinsen, 1994; Myrow et al., 2004). Such depositional process is also consistent with elutriation bands that are indicative of water escape from rapidly deposited sand (Lowe and LoPiccolo, 1974; Ravier et al., 2015). The interbedding of flat-pebble conglomerates and sandstone with fine-grained sediments indicates a deposition below the fair-weather wave base.

4.2.2. Facies association 5

Description. This association consists of tens of cm- to m-thick thinly laminated beds (Fig. 13A, B). These layers are made up of alternations of mm-thick magnetite layers with greyish to greenish layers made up of carbonates with minor clay and silt (C2, Table 3). From place to place, beds of facies C2 are faulted (Fig. 13B) or folded and crosscut by calcite veins (Fig. 13C).

Carbonate layers grade or alternate with siliciclastic layers corresponding either to S1 or F1 facies. S1 facies is made up of fine sand, is generally massive and sometimes comprise rip-up mud clasts. F1 facies is made up of silt to clay and exhibits horizontal laminations.

Interpretation. Facies association 5 is mainly made up of iron and carbonate-rich facies and occurs only toward the base of the drill core FD52. This association indicates periods of limited terrigenous input that allowed for the precipitation of iron oxides (Table 4).

5. Geochronological constraints

Analytical results and cathodoluminescence images of representative grains are available in the Appendix 3.

5.1. Carajás Formation

Although being collected in different lithologies (volcaniclastic basaltic sandstone, GIF), detrital zircon grains extracted from the different samples exhibit similar characteristics. Most of the grains have euhedral shape and are pinkish, slightly to very elongated (length to width ratio of 2:1 to 10:1), and sometimes contains small inclusions. Very few grains are sub-rounded. After TACA treatment, most of the grains were translucent and spotless, while a few remained pinkish with an etched surface. Most of the zircon crystals display a well-defined oscillatory zoning typical of magmatic zircon (Corfu et al., 2003), but some grains are not zoned or display a core-rim structure. The Th/U ratios of all concordant grains range between 0.32 and 3.44., also supporting a magmatic origin (Rubatto, 2002).

Most of the grains from the volcaniclastic sample *FD110 359.00-359.35* form a cluster giving a concordia date of 2719.6 ± 5.6 Ma (MSWD = 0.47; n = 35), interpreted as the MDA for this sample (Fig. 14A; Table 5). Another concordant grain has a date of 2889.5 ± 29.8 Ma and is interpreted as a xenocryst or an epicryst mixed with volcanic material during volcanic or sedimentary processes.

In the sample *FD353 188.10-188.30*, the youngest cluster gives a concordia date of 2732.4 ± 5.2 Ma (MSWD = 0.53; n = 37), interpreted as the MDA for this sample (Fig. 14A; Table 5). Four other grains, exhibiting similar morphology and color to those of the youngest cluster, give dates ranging between 2826.6 ± 36.2 Ma and 2998.9 ± 25.2 Ma and are interpreted as xenocrysts or epicrysts.

In the GIF sample *FD353 191.70-191.90*, concordant analyses give a date of 2728.5 ± 5.2 Ma (MSWD = 0.57; n = 38). This date is interpreted as the MDA for this sample (Fig. 14A; Table 5).

5.2. Igarapé Bahia Group

The detrital zircon grains collected in the Igarapé Bahia Group exhibit a much greater diversity in size, shapes, and colors, compared to those from the Carajás Formation. All samples from the Igarapé Bahia Group yielded euhedral to rounded zircon grains. Euhedral grains are translucent to pinkish and elongated. Rounded to sub-angular grains are reddish, yellowish, pinkish, or brownish, without apparent relationship between color and shape. Internal structures as well as Th/U ratios support a magmatic origin for all grains.

In the conglomerate *FD52 651.30-651.80*, the youngest cluster gives a concordia date of 2788 ± 12 Ma (n = 6, MSWD = 1.10), interpreted as a MDA (Fig. 14A; Table 5). Most of the other concordant dates spread from the MDA up to the mid Mesoarchean, at 3023 ± 31 Ma. One grain yielded a date of 2666 ± 29 Ma suggesting that the deposition of the sediment could have been significantly younger than the preferred MDA. However, because only one grain gives a date of ca. 2666 Ma, the statistical requirements are not met to confidently consider it as a MDA (Dickinson and Gehrels, 2009).

The youngest cluster of the sandstone *FD52 637.26-637.*65 gives a concordia date of 2829 ± 17 Ma (n = 3, MSWD = 0.48), interpreted as the MDA of this sample (Fig. 14A; Table 5). Other grains spread along the concordia curve up to 3007 ± 33 Ma. Three other zircon grains have dates of 2663 ± 27 Ma, 2740 ± 27 Ma and 2747 ± 27 Ma, that are younger than the preferred MDA. However, these dates do not allow to calculate a statistically robust MDA and the conservative interpretation of 2829 ± 17 Ma as the MDA is preferred here.

In the sample *FD52 602.40-603.00*, the youngest cluster gives a concordia date of 2753 ± 18 Ma (n = 3, MSWD = 0.44), interpreted as the MDA (Fig. 14A; Table 5). Eight other grains spread along the concordia curve up to 2985± 29 Ma.

The youngest cluster of the conglomerate *FD52 393.35-393.90* is defined by three analyses and gives a concordia date of 2785 ± 16 Ma (MSWD = 1.8). This date is interpreted as the MDA of this sample (Fig. 14A; Table 5). Other grains have dates ranging from the MDA up to 2997 ± 28 Ma. There is no obvious relationship between the size, color or shape and the age of zircon grains.

6. Discussion

6.1. Age, provenance, and contemporaneity of the Carajás Formation and Igarapé Bahia Group with the Parauapebas LIP

Volcaniclastic rocks of the Carajás Formation show limited evidence of reworking and gave MDAs ranging from ca. 2732 Ma to ca. 2720 Ma (Fig. 14A). These ages are similar to those of doleritic sills and magmatic rocks intruding the Carajás Formation (Feio et al., 2012; Krymsky et al., 2007; Sardinha et al., 2006; Trendall et al., 1998). The record of nearly identical minimal (intrusion) and maximum (detrital zircon) depositional ages supports the contemporaneity of volcanism and sedimentation. MDAs obtained in this study thus provide a direct estimate of the age of the Carajás Formation and slightly expand the previously inferred stratigraphic range of the Carajás Formation (Fig. 3; Table 2). Considering an average thickness of 250 m (Beisiegel et al., 1973; Lindenmayer et al., 2001) and a deposition between ca. 2750 Ma and ca. 2710 Ma (*i.e.*, the time span of deposition of the Carajás Formation, including uncertainties), an accumulation rate of ca. 6 $m.Ma^{-1}$ can be estimated. This value is in agreement with those already documented for IFs elsewhere (Barton et al., 1994; Beukes and Gutzmer, 2008; Lantink et al., 2019; Simonson and Hassler, 1996).

The volcaniclastic rocks preserved in the Carajás Formation are slightly younger than the magmatic peak of the Parauapebas LIP (Fig. 2) and show that a limited volcanic activity persisted until ca. 2720 Ma (Fig. 15A). This is consistent with the occurrence of plutonic rocks related to the Parauapebas LIP as young as ca. 2710 Ma (Fig. 2; Feio et al., 2013). Age distribution shows that all but a few zircon grains in the Carajás Formation derived from the waning volcanic activity of the Paraupebas LIP (Fig. 15A).

The youngest MDA from the Igarapé Bahia Group shows that its deposition is younger than 2753 ± 18 Ma (Fig. 14A). Assuming that the youngest grains from different samples derive from a cogenetic source, as suggested by their homogeneous Th/U ratios (0.76 ± 0.30), the youngest cluster gives a date of 2761 ± 10 Ma (n = 10; MSWD = 1.2; Fig. 14B). This date is interpreted as the MDA for the Igarapé Bahia Group and is in agreement with previously proposed MDA for this unit (2784 ± 27 Ma; Melo et al., 2019). Additional constraints on the age of the Igarapé Bahia Group comes from the occurrence of angular clasts of BIF derived from the underlying Carajás Formation (Dreher et al., 2008, 2005;

Galarza et al., 2008; Melo et al., 2019; Ronze et al., 2000), which has a MDA of 2720 ± 6 Ma (Fig. 14A). Hydrothermal circulation throughout the Igarapé Bahia Group occurred around 2.6 Ga (Requia et al., 2003; Tallarico et al., 2005), suggesting that this unit might be younger than ca. 2720 Ma and older than ca. 2.6 Ga.

No volcaniclast have been identified during the study of the drill-core FD52 (cf. section 4.2), but such clasts can be difficult to identify, especially in fine-grained sedimentary rocks (Cassidy et al., 2014). To identify a potential volcanic activity coeval to the sedimentation, we looked for zircon autocrysts (i.e., minerals that crystalized just before a given eruption), which could indicate a volcanic activity contemporaneous to the sedimentation (Rossignol et al., 2019). In the drill-core FD 52, MDAs are not getting younger upward (Fig. 14A). This indicates that the dated samples of the Igarapé Bahia Group do not contain zircon autocrysts, because of sampling bias, or because volcanic rocks did not contain such minerals, or because the volcanic activity was not contemporaneous with the sedimentation (Rossignol et al., 2019). Even if detection limits for the dated samples are rather high (Table 5), a sampling bias is unlikely given the fairly common occurrence of felsic and mafic alkaline volcanic rocks, arguably zircon-rich, in the Parauapebas LIP (Lacasse et al., 2020; Machado et al., 1991). For the same reason, it is unlikely that volcanic rocks did not contain any zircon autocrysts. Thus, the relationship between MDAs and stratigraphy suggests that there was no active volcanism during the deposition of the Igarapé Bahia Group. Detrital zircon age distribution of the Igarapé Bahia Group further show that the Igarapé Bahia Group comprises a ca. 2750 Ma zircon population, which likely indicate that the Parauapebas LIP was being eroded at that time (Fig. 15B). The other peaks in age distribution of the Igarapé Bahia Group match the age of the main magmatic events documented in the SE Amazonia Craton. The main peak in detrital zircon age distribution at ca. 2960 Ma, corresponds to the age of the oldest TTGs from the SE Amazonia Craton (Feio et al., 2013). Another peak at ca. 2800 Ma suggests that the 2820 ± 22 Ma TTGs (Feio et al., 2013) represented a source for the Igarapé Bahia Group. Smaller peaks in age distribution at 2890 Ma and 2840 Ma suggest a provenance from the TTGs south of the Carajás Basin (Feio et al., 2013; Machado et al., 1991; Moreto et al., 2015; Pidgeon et al., 2000). The youngest peak around 2660 Ma could indicate a provenance from the Bacajá Domain (Macambira et al., 2009).

6.2. Evolution of depositional environments following the emplacement of the Parauapebas LIP

Depositional environments indicated by facies associations of the Carajás Formation correspond to various settings, ranging from deep to shallow water (Fig. 16A). Facies associations 1 and 2 correspond to deep environments, probably below wave level. Facies association 3 is indicative of shallower settings, in the photic zone (Fig. 16A). MISS and carbonate-rich BIFs could be an indirect evidence of highly productive surface water (Craddock and Dauphas, 2011; Heimann et al., 2010; Johnson et al., 2013), echoing previous observations of bacterial activity (Rego et al., 2021; Ribeiro da Luz and Crowley, 2012). Together, these observations highlight environmental conditions favorable for microbial development in the Carajás Basin. The extremely low content in lithophile elements in IFs of the Carajás Formation indicates that the Carajás Basin did not have any continental influence at that time (Justo et al., 2020; Klein and Ladeira, 2002; Lindenmayer et al., 2001; Macambira and Schrank, 2002; P. L. G. Martins et al., 2021b; Rego et al., 2021).

Facies associations of the Igarapé Bahia Group are indicative of offshore settings, mostly below fair-weather wave base (Fig. 16B). Contrasting with the sedimentary facies of the Carajás Formation, Fe-rich chemical deposits (in the form of carbonates) represent a minor facies of the Igarapé Bahia Group, and all other facies of this unit are made up of terrigenous material. The nature of the sedimentation thus transitioned from a chemical- to a terrigenous-dominated system during the Neoarchean (Fig. 17A). This shift from iron to terrigenous sediments was probably controlled by relative inputs of terrigenous influxes and Fe-rich fluids, as already documented in other basins comprising mixed IFs and terrigenous sedimentary series (Fralick and Barrett, 1995; Schröder et al., 2011; Warchola et al., 2018).

The common occurrence of strong positive Eu anomalies in IFs of the Carajás Basin suggests that Fe mainly originates from Fe-rich hydrothermal fluids (Danielson et al., 1992; Justo et al., 2020; Klein and Ladeira, 2002; Lindenmayer et al., 2001; Macambira and Schrank, 2002; P. L. G. Martins et al., 2021b; Rego et al., 2021). The involvement of the Parauapebas LIP in the hydrothermal activity that supplied iron is likely given the contemporaneity between volcanism and the deposition of IFs from the Carajás Formation (Fig. 17B), and the predominantly mafic composition of this LIP (Lacasse et al., 2020). Besides this local source, an external iron source should also be considered

given the contemporaneity between Carajás IFs and a period of enhanced mafic magmatic activity worldwide (Fig. 17C; Abbott and Isley, 2002; Isley and Abbott, 1999). This is especially the case for the few IFs occurring at the base of the Igarapé Bahia Group. As this sedimentary unit has been deposited after the end of the Parauapebas volcanic activity, iron could have been supplied by long-lasting hydrothermal circulation driven by thermal effects of the Parauapebas LIP, or by external hydrothermal iron sources, or by a combination of local and external sources. The transition from IFs- to terrigenous-dominated system indicates that a drastic environmental change occurred during the course of the Neoarchean. This transition could have been related to a relative sea-level drop that promoted inland erosion and generated an influx of terrigenous materials into the basin (Schröder et al., 2011; Simonson and Hassler, 1996) that formed the bulk of the Igarapé Bahia Group. Moreover, the emergence of the Amazonia Craton could also be accounted for such significant environmental change, as the timing coincides with the worldwide emergence of extensive terrestrial areas (Fig. 17E; Albarede et al., 2020; Flament et al., 2008; Johnson and Wing, 2020; Kump and Barley, 2007; Reimink et al., 2021; Spencer et al., 2019; Wang et al., 2021)

Quantitative comparisons of detrital zircon age distributions from the Igarapé Bahia Group and the Serra Sul Formation using the KS (Fig. 18A), Kuiper (Fig. 18B), and L^2 (Fig. 18C) metrics, show that samples from these two units plot into a single cluster. Even if high stress values of MDS plots indicate relatively important distortions between the initial metric on densities and their resulting distance in the MDS plot, the three MDS maps give consistent results, suggesting that the two sedimentary units have rather similar zircon sources. Together marked similarities regarding their sedimentary facies and deformation patterns, quantitative comparisons of detrital zircon age distributions further point to a single sedimentary unit including both the Igarapé Bahia Group and the Serra Sul Formation (Rossignol et al., 2021). The Igarapé Bahia Group, including the Serra Sul Formation, corresponded to a range of depositional environments, from shallow to deep-water settings, characterized by diverse sedimentary facies with pronounced lateral variations. Deposits from the Igarapé Bahia Group are closely associated with faults (Fig. 1C), and comprise numerous soft sediment deformations potentially indicative of an active tectonic setting (Rossignol et al., 2020b). This suggests that the rift tectonic activity associated with the Parauapebas LIP continued during the deposition of the Igarapé Bahia Group and could have triggered and enhanced the influx

of terrigenous material in the basin (Fig. 17D; Feio et al., 2012; Martins et al., 2017; Olszewski et al., 1989; Tavares et al., 2018; Toledo et al., 2019). .

6.3. Relationships with Neoarchean paleoenvironmental changes

Although located in distinct paleogeographic locations, many cratons also comprise IFs that are contemporaneous to those from the Carajás Basin (Fig. 17F; P. L. G. Martins et al., 2021a; Salminen et al., 2019). In the Yilgarn Craton, IFs from the Wilgie Mia Formation are coeval with the Carajás Formation (Czaja et al., 2018; Van Kranendonk et al., 2013). In the Tanzanian Craton, the Upper Nyanzian Group contains ca. 2770 Ma to ca. 2720 Ma IFs that are also contemporaneous with those of the Amazonia Craton (Kwelwa et al., 2018). The Mulaingiri Formation, Dharwar Craton, contains ca. 2720 Ma IFs Ma that are coeval with those from the Carajás Basin (Sunder Raju and Mazumder, 2020). In the Rae Craton, the Mary River Group also comprises IFs that have been deposited around 2718 Ma (Bros and Johnston, 2017; Jackson et al., 1990). In the Superior Craton, which could have been part of the same paleocontinent with the Amazonia Craton at that time (P. L. G. Martins et al., 2021a), the Temagami Greenstone Belt comprises ca. 2736 Ma to ca. 2687 Ma IFs (Bowins and Heaman, 1991) and the Michipicoten Group comprises the 2.75 Ga Helen Iron Formation that also contains carbonate-rich BIFs similar to those of the Carajás Formation (Garcia et al., 2016). In the Zimbabwe Craton, IFs from the Tati Greenstone Belt are slightly older than 2.7 Ga and might have been deposited coevally to those of the Carajás Formation (Døssing et al., 2009). Although more speculative because of poorer temporal resolution, the ca. 2.7 Ga to ca. 2.5 Ga Xincai IFs from the North China Craton could correlate with the Amazonia Craton (Lan et al., 2019). In the São Francisco Craton, the 2780 Ma to 2600 Ma Rio das Velhas Greenstone Belt comprise IFs that could have been deposited coevally to those of the Amazonia Craton (Araújo and Lobato, 2019; Rossignol et al., 2020a). In the Baltica Craton, the age of the Krivoy Rog Basin IFs is not well constrained but could have been contemporaneous with those from the Carajás Basin (Kulik and Korzhnev, 1997; Viehmann et al., 2018, 2015).

Overall, numerous IFs have been deposited around the world around 2.75 Ga to 2.70 Ga (Fig. 17F). This period was characterized by important magmatic activity worldwide that might have favored the deposition of major BIFs, among which the Parauapebas LIPs probably represented an important contributor for hydrothermal

fluxes of ferrous iron (Barley et al., 1997; Isley, 1995; Isley and Abbott, 1999; Viehmann et al., 2015).

7. Conclusions

The main control exerted by the Parauapebas LIP on nearby environments consisted in the delivery of a large amount of reduced iron in seawater through hydrothermal activity. This favored the deposition of IFs in a variety of depositional settings, ranging from shallow to deep-water environments. Most of the IFs from the Carajás Basin have been deposited during the waning volcanic activity of the Parauapebas LIP, as attested by the occurrence of volcaniclastic rocks interbedded with IFs that indicate a Neoarchean depositional age, from 2732 ± 5 Ma to 2720 ± 6 Ma. Together with literature data, these ages expand the previously inferred stratigraphic range of the Carajás Formation and show, that the deposition of iron formations in the Carajás Basin occurred during a prolonged period of time that lasted 30 to 40 Myrs. Later during the Neoarchean, a few IFs have also been deposited in the overlying Igarapé Bahia Group, after the end of the Parauapebas LIP volcanic activity. IFs occurring at the base of this unit thus reflect either a long-lasting effect of the Parauapebas LIP on hydrothermal circulation, or the input of seawater enriched in iron by other Neoarchean magmatic provinces. Contrarily to the chemical nature of the Carajás Formation, the mainly detrital siliciclastic nature of the Igarapé Bahia Group suggests that the Amazonia Craton became available for erosion during the course of the Neoarchean, either through local tectonic activity or through continental scale emergence of the craton.

Acknowledgements

This research was funded by grants of the Fundação Amparo à Pesquisa do Estado de São Paulo (FAPESP; 2015/16235-2, 2018/02645-2, 2018/14617-3, 2018/05892-0, 2019/17732-0, 2019/16066-7, 2019/16271-0 and 2019/12132-5), the Conselho Nacional de Desenvolvimento Científico e Tecnológico (CNPq; 308045/2013-0 and 307353/2019-2), and the Fundação Amparo à Pesquisa do Minas Gerais (FAPEMIG; project APQ-03793-16). We acknowledge Adriana de Cássia Zapparoli, formerly at Vale company, for her help to access the Vale's drill core library in Carajás. J. Pereira, D. Vasconcelos, A. Mazoz

and A. R. Alkmim (Universidade Federal de Ouro Preto) are acknowledged for assistance during sample preparation, CL imaging (Microscopy and Microanalysis Network of Minas Gerais), and data acquisition. R. Rainbird and C. Spencer are acknowledged for constructive comments on an earlier version of this manuscript.

Data availability

Supplementary information is archived at the Pangea data repository at https://doi.org/10.1594/PANGAEA.931156

References

Abbott, D.H., Isley, A.E., 2002. The intensity, occurrence, and duration of superplume events and eras over geological time. J. Geodyn. 34, 265–307. https://doi.org/10.1016/S0264-3707(02)00024-8

Albarede, F., Thibon, F., Blichert-Toft, J., Tsikos, H., 2020. Chemical archeoceanography. Chem. Geol. 548. https://doi.org/10.1016/j.chemgeo.2020.119625

Almeida, J.A.C., Dall'Agnol, R., Leite, A.A.S., 2013. Geochemistry and zircon geochronology of the Archean granite suites of the Rio Maria granite-greenstone terrane, Carajás Province, Brazil. J. South Am. Earth Sci. 42, 103–126. https://doi.org/10.1016/j.jsames.2012.10.008

Althoff, F.J., Barbey, P., Boullier, A.M., 2014. 2.8-3.0 Ga plutonism and deformation in the SE Amazonian craton: The Archaean granitoids of Marajoara (Carajas Mineral Province, Brazil). Precambrian Res. 104, 187–206. https://doi.org/10.1016/S0301-9268(00)00103-0

Antonio, P.Y.J., D'Agrella-Filho, M.S., Nédélec, A., Poujol, M., Sanchez, C., Dantas, E.L., Dall'Agnol, R., Teixeira, M.F.B., Proietti, A., Martínez Dopico, C.I., Oliveira, D.C., Silva, F.F., Marangoanha, B., Trindade, R.I.F., 2021. New constraints for paleogeographic reconstructions at ca. 1.88 Ga from geochronology and paleomagnetism of the Carajás dyke swarm (eastern Amazonia). Precambrian Res. 353. https://doi.org/10.1016/j.precamres.2020.106039

Antonio, P.Y.J., D'Agrella-Filho, M.S., Trindade, R.I.F., Nédélec, A., de Oliveira, D.C., da Silva, F.F., Roverato, M., Lana, C., 2017. Turmoil before the boring billion:

Paleomagnetism of the 1880–1860 Ma Uatumã event in the Amazonian craton. Gondwana Res. 49, 106–129. https://doi.org/10.1016/j.gr.2017.05.006

Araújo, J.C.S., Lobato, L.M., 2019. Depositional model for banded iron formation host to gold in the Archean Rio das Velhas greenstone belt, Brazil, based on geochemistry and LA-ICP-MS magnetite analyses. J. South Am. Earth Sci. 94, 102205. https://doi.org/10.1016/j.jsames.2019.05.021

Araújo, R., Araújo Filho, R.C., Costa, L., 2021. Tectono-sedimentary evolution of the Paleoproterozoic succession of the Carajás Basin, southeastern Amazonian Craton, Brazil: Insights from sedimentology, stratigraphy, and U–Pb detrital zircon geochronology. Precambrian Res. 362, 106290. https://doi.org/10.1016/j.precamres.2021.106290

Araújo, R., Nogueira, A., 2019. Serra sul diamictite of the carajas basin (Brazil): A paleoproterozoic glaciation on the amazonian craton. Geology 47, 1166–1170. https://doi.org/10.1130/G46923.1

Barley, M.E., Pickard, A.L., Sylvester, P.J., 1997. Emplacement of a large igneous province as a possible cause of banded iron formation 2.45 billion years ago. Nature 385, 55–58.

Barros, C.E.M., Sardinha, A.S., Barbosa, J.P.O., MacAmbira, M.J.B., Barbey, P., Boullier, A.M., 2009. Structure, petrology, geochemistry and zircon U/Pb and Pb/Pb geochronology of the synkinematic Archean (2.7 Ga) A-type granites from the Carajas metallogenic province, northern Brazil. Can. Mineral. 47, 1423–1440. https://doi.org/10.3749/canmin.47.6.1423

Barton, E.S., Altermann, W., Williams, I.S., Smith, C.B., 1994. U-Pb zircon age for a tuff in the Campbell Group, Griqualand West sequence, South Africa: implications for early Proterozoic rock accumulation rates. Geology 22, 343–346. https://doi.org/10.1130/0091-7613(1994)022<0343:UPZAFA>2.3.CO;2

Beisiegel, V.D.R., Bernardelli, A.L., Drummond, N.F., Ruff, A.W., Tremaine, J.W.R., 1973. Geologia e Recursos Minerais da Serra dos Carajás. Rev. Bras. Geociências 3, 215–242.

Beukes, N.J., 1983. Palaeoenvironmental setting of iron-formations in the depositional basin of the Transvaal Supergroup, South Africa. Dev. Precambrian Geol. 6, 131–142. https://doi.org/10.1016/S0166-2635(08)70043-4

Beukes, N.J., Gutzmer, J., 2008. Origin and Paleoenvironmental Significance of Major Iron

Formations at the Archean-Paleoproterozoic Boundary, in: Hagemann, S., Rosière, C.A., Gutzmer, J., Beukes, N.J. (Eds.), Banded Iron Formation-Related High-Grade Iron Ore. Society of Economic Geologists, pp. 5–47. https://doi.org/10.5382/Rev.15.01

Beukes, N.J., Klein, C., 1990. Geochemistry and sedimentology of a facies transition - from microbanded to granular iron-formation - in the early Proterozoic Transvaal Supergroup, South Africa. Precambrian Res. 47, 99–139. https://doi.org/10.1016/0301-9268(90)90033-M

Bowins, R.J., Heaman, L.M., 1991. Age and timing of igneous activity in the Temagami Greenstone Belt, Ontario: a preliminary report. Can. J. Earth Sci. 28, 1873–1876. https://doi.org/10.1139/e91-167

Bros, E.R., Johnston, S.T., 2017. Field observations of the Mary River Group south of Tay Sound, northern Baffin Island, Nunavut: stratigraphy and structure of supracrustal sequences and surrounding plutonic units. Summ. Act. 2017 Canada-Nuvanut Geosci. Off. 69–80.

Bryan, S.E., Ernst, R.E., 2008. Revised definition of Large Igneous Provinces (LIPs). Earth-Science Rev. 86, 175–202. https://doi.org/10.1016/j.earscirev.2007.08.008

Cabral, A.R., Bühn, B., Seabra Gomes, A.A., Galbiatti, H.F., Lehmann, B., Halder, S., 2017. Multiple sulfur isotopes from the Neoarchaean Serra Sul black shale, Carajás mineral province, northern Brazil. J. South Am. Earth Sci. 79, 377–383. https://doi.org/10.1016/j.jsames.2017.08.002

Cassidy, M., Watt, S.F.L., Palmer, M.R., Trofimovs, J., Symons, W., Maclachlan, S.E., Stinton, A.J., 2014. Construction of volcanic records from marine sediment cores: A review and case study (Montserrat, West Indies). Earth-Science Rev. 138, 137–155. https://doi.org/10.1016/j.earscirev.2014.08.008

Catling, D.C., Claire, M.W., 2005. How earth's atmosphere evolved to an oxic state: A status report. Earth Planet. Sci. Lett. 237, 1–20. https://doi.org/10.1016/j.epsl.2005.06.013

Cordani, U.G., Ramos, V.A., Fraga, L.M., Cegarra, M., Delgado, I., de Souza, K.G., Gomes, F.E.M., Schobbenhaus, C., 2016. Tectonic map of South America at 1:5.9M. Scale 1 5 900 000 CGMW-CPRM-.

Corfu, F., Hanchar, J.M., Hoskin, P.W.O., Kinny, P., 2003. Atlas of Zircon Textures, in: Hanchar, J.M., Hoskin, P.W.O. (Eds.), Zircon. Mineralogical Society of America and

Geochemical Society, Washington, DC, United States, pp. 469–500.

Craddock, P.R., Dauphas, N., 2011. Iron and carbon isotope evidence for microbial iron respiration throughout the Archean. Earth Planet. Sci. Lett. 303, 121–132. https://doi.org/10.1016/j.epsl.2010.12.045

Crowley, Q., Heron, K., Riggs, N., Kamber, B., Chew, D., McConnell, B., Benn, K., 2014. Chemical Abrasion Applied to LA-ICP-MS U–Pb Zircon Geochronology. Minerals 4, 503–518. https://doi.org/10.3390/min4020503

Czaja, A.D., Van Kranendonk, M.J., Beard, B.L., Johnson, C.M., 2018. A multistage origin for Neoarchean layered hematite-magnetite iron formation from the Weld Range, Yilgarn Craton, Western Australia. Chem. Geol. 488, 125–137. https://doi.org/10.1016/j.chemgeo.2018.04.019

Dalstra, H., Guedes, S., 2004. Giant hydrothermal hematite deposits with Mg-Fe metasomatism: A comparison of the Carajás, Hamersley, and other iron ores. Econ. Geol. 99, 1793–1800. https://doi.org/10.2113/gsecongeo.99.8.1793

Danielson, A., Möller, P., Dulski, P., 1992. The europium anomalies in banded iron formations and the thermal history of the oceanic crust. Chem. Geol. 97, 89–100. https://doi.org/10.1016/0009-2541(92)90137-T

Dickinson, W.R., Gehrels, G.E., 2009. Use of U–Pb ages of detrital zircons to infer maximum depositional ages of strata: A test against a Colorado Plateau Mesozoic database. Earth Planet. Sci. Lett. 288, 115–125. https://doi.org/10.1016/j.epsl.2009.09.013

Dimroth, E., 1975. Paleo-environment of iron-rich sedimentary rocks. Geol. Rundschau 64, 751–767. https://doi.org/10.1007/BF01820694

Døssing, L.N., Frei, R., Stendal, H., Mapeo, R.B.M., 2009. Characterization of enriched lithospheric mantle components in ~2.7 Ga Banded Iron Formations: An example from the Tati Greenstone Belt, Northeastern Botswana. Precambrian Res. 172, 334–356. https://doi.org/10.1016/j.precamres.2009.06.004

Dreher, A.M., Xavier, R.P., Martini, S.L., 2005. Fragmental rocks if the Igarape Bahia Cu-Au deposits, Carajas minaral Province, Brazil. Rev. Bras. Geociências 35, 359–368.

Dreher, A.M., Xavier, R.P., Taylor, B.E., Martini, S.L., 2008. New geologic, fluid inclusion and stable isotope studies on the controversial Igarapé Bahia Cu-Au deposit, Carajás Province, Brazil. Miner. Depos. 43, 161–184. https://doi.org/10.1007/s00126-007-

0150-6

Feio, G.R.L., Dall'Agnol, R., Dantas, E.L., Macambira, M.J.B., Gomes, A.C.B., Sardinha, A.S., Oliveira, D.C., Santos, R.D., Santos, P.A., 2012. Geochemistry, geochronology, and origin of the Neoarchean Planalto Granite suite, Carajás, Amazonian craton: A-type or hydrated charnockitic granites? Lithos 151, 57–73. https://doi.org/10.1016/j.lithos.2012.02.020

Feio, G.R.L., Dall'Agnol, R., Dantas, E.L., Macambira, M.J.B., Santos, J.O.S., Althoff, F.J., Soares, J.E.B., 2013. Archean granitoid magmatism in the Canaã dos Carajás area: Implications for crustal evolution of the Carajás province, Amazonian craton, Brazil. Precambrian Res. 227, 157–185. https://doi.org/10.1016/j.precamres.2012.04.007

Flament, N., Coltice, N., Rey, P.F., 2008. A case for late-Archaean continental emergence from thermal evolution models and hypsometry. Earth Planet. Sci. Lett. 275, 326–336. https://doi.org/10.1016/j.epsl.2008.08.029

Fralick, P.W., Barrett, T.J., 1995. Depositional controls on iron formation associations in Canada. Spec. Publ. Int. Assoc. Sedimentol. 22, 137–156.

Galarza, M.A., Macambira, M.J.B., Villas, R.N., 2008. Dating and isotopic characteristics (Pb and S) of the Fe oxide-Cu-Au-U-REE Igarapé Bahia ore deposit, Carajás mineral province, Pará state, Brazil. J. South Am. Earth Sci. 25, 377–397. https://doi.org/10.1016/j.jsames.2007.07.006

Garcia, T.I., Gorton, M.P., Li, H., Wortmann, U.G., Spooner, E.T.C., 2016. The geochemistry of the 2.75 Ga-old Helen Iron Formation, Wawa, Ontario - Insights into iron formation deposition from carbon isotopes and rare earth elements. Precambrian Res. 275, 357–368. https://doi.org/10.1016/j.precamres.2016.01.013

Gibbs, A.K., Wirth, K.R., Hirata, W.K., Olszewski Jr, W.J., 1986. Age and composition of the Grão Pará groups volcanics, Serra dos Carajás. Rev. Bras. Geociências 16, 201–211.

Hagadorn, J.W., Bottjer, D.J., 1997. Wrinkle structures: Microbially mediated sedimentary structures common in subtidal siliciclastic settings at the Proterozoic-Phanerozoic transition. Geology 25, 1047–1050. https://doi.org/10.1130/0091-7613(1997)025<1047:WSMMSS>2.3.CO;2

Heimann, A., Johnson, C.M., Beard, B.L., Valley, J.W., Roden, E.E., Spicuzza, M.J., Beukes, N.J., 2010. Fe, C, and O isotope compositions of banded iron formation carbonates demonstrate a major role for dissimilatory iron reduction in ~2.5Ga marine

environments. Earth Planet. Sci. Lett. 294, 8–18. https://doi.org/10.1016/j.epsl.2010.02.015

Isley, A.E., 1995. Hydrothermal plumes and the delivery of iron to banded iron formation. J. Geol. 103, 169–185. https://doi.org/10.1086/629734

Isley, A.E., Abbott, D.H., 1999. Plume-related mafic volcanism and the deposition of banded iron formation. J. Geophys. Res. Solid Earth 104, 15461–15477. https://doi.org/10.1029/1999jb900066

Jackson, G.D., Hunt, P.A., Loveridge, W.D., Parrish, R.R., 1990. Reconnaissance geochronology of Baffin Island, N.W.T. Radiogenic Age Isot. Stud. Rep. 3 Geol. Surv. Canada Pap. 89-2 123–148.

Johnson, B.W., Wing, B.A., 2020. Limited Archaean continental emergence reflected in an early Archaean 18O-enriched ocean. Nat. Geosci. 13, 243–248. https://doi.org/10.1038/s41561-020-0538-9

Johnson, C.M., Ludois, J.M., Beard, B.L., Beukes, N.J., Heimann, A., 2013. Iron formation carbonates: Paleoceanographic proxy or recorder of microbial diagenesis? Geology 41, 1147–1150. https://doi.org/10.1130/G34698.1

Justo, A.P., Dantas, E.L., Bau, M., Freitas-Silva, F.H., Santos, R.V., Schorscher, J.H.D., 2020. Paleobasinal to band-scale REE+Y distribution in Iron Formations from Carajás Amazon Craton, Brazil. Ore Geol. Rev. 103750. https://doi.org/10.1016/j.oregeorev.2020.103750

Klein, C., 2005. Some Precambrian banded iron-formations (BIFs) from around the world: Their age, geologic setting, mineralogy, metamorphism, geochemistry, and origin. Am. Mineral. 90, 1473–1499. https://doi.org/10.2138/am.2005.1871

Klein, C., Ladeira, E.A., 2002. Petrography and Geochemistry of the Least Altered Banded Iron-Formation of the Archean Carajas Formation, Northern Brazil. Econ. Geol. 97, 643–651. https://doi.org/10.2113/97.3.643

Krymsky, R.S., Macambira, M.J.B., Lafon, J.-M., Estumano, G.S., 2007. Uranium-lead dating method at the Pará-Iso isotope geology laboratory, UFPA, Belém - Brazil. An. Acad. Bras. Cienc. 79, 115–128. https://doi.org/10.1590/S0001-37652007000100014

Kulik, D.A., Korzhnev, M.N., 1997. Lithological and geochemical evidence of Fe and Mn pathways during deposition of Lower Proterozoic banded iron formation in the Krivoy Rog Basin (Ukraine). Geol. Soc. Spec. Publ. 119, 43–80. https://doi.org/10.1144/GSL.SP.1997.119.01.04

Kump, L.R., Barley, M.E., 2007. Increased subaerial volcanism and the rise of atmospheric oxygen 2.5 billion years ago. Nature 448, 1033–1036. https://doi.org/10.1038/nature06058

Kwelwa, S.D., Sanislav, I.V., Dirks, P.H.G.M., Blenkinsop, T., Kolling, S.L., 2018. Zircon U-Pb ages and Hf isotope data from the Kukuluma Terrain of the Geita Greenstone Belt, Tanzania Craton: Implications for stratigraphy, crustal growth and timing of gold mineralization. J. African Earth Sci. 139, 38–54. https://doi.org/10.1016/j.jafrearsci.2017.11.027

Lacasse, C.M., Ganade, C.E., Mathieu, L., Teixeira, N.A., Lopes, L.B.L., Monteiro, C.F., 2020. Restoring original composition of hydrothermally altered Archean metavolcanic rocks of the Carajás Mineral Province (Brazil): Geodynamic implications for the transition from lid to mobile tectonics. Lithos 372–373, 105647. https://doi.org/10.1016/j.lithos.2020.105647

Lan, C., Yang, A.Y., Wang, C., Zhao, T., 2019. Geochemistry, U-Pb zircon geochronology and Sm-Nd isotopes of the Xincai banded iron formation in the southern margin of the North China Craton: Implications on Neoarchean seawater compositions and solute sources. Precambrian Res. 326, 240–257. https://doi.org/10.1016/j.precamres.2017.10.024

Lantink, M.L., Davies, J.H.F.L., Mason, P.R.D., Schaltegger, U., Hilgen, F.J., 2019. Climate control on banded iron formations linked to orbital eccentricity. Nat. Geosci. 12, 369–374. https://doi.org/10.1038/s41561-019-0332-8

Lawrence, R.L., Cox, R., Mapes, R.W., Coleman, D.S., 2011. Hydrodynamic fractionation of zircon age populations. Geol. Soc. Am. Bull. 123, 295–305. https://doi.org/10.1130/B30151.1

Lindenmayer, Z.G., Laux, J.H., Teixeira, J.B.G., 2001. Considerações sobre a origem das formações ferríferas da Formação Carajás, Serra dos Carajás. Rev. Bras. Geociências 31, 21–28. https://doi.org/10.25249/0375-7536.20013112128

Lowe, D.R., LoPiccolo, R.D., 1974. The Characteristics and Origins of Dish and Pillar Structures. J. Sediment. Res. 44, 484–501. https://doi.org/10.1306/74d72a68-2b21-11d7-8648000102c1865d

Ludwig, K.R., 2012. User's Manual for a geochronological toolkit for Microsoft Excel. Berkeley Geochronological Cent. 75.

Ludwig, K.R., 1998. On the Treatment of Concordant Uranium-Lead Ages. Geochim.

Cosmochim. Acta 62, 665–676. https://doi.org/10.1016/S0016-7037(98)00059-3

Macambira, M.J.B., Lancelot, J.R., 1996. Time constraints for the formation of the Archean Rio Maria crust, southeastern Amazonian Craton, Brazil. Int. Geol. Rev. 38, 1134–1142. https://doi.org/10.1080/00206819709465386

Macambira, M.J.B., Schrank, A., 2002. Químio-estratigrafia e evolução dos jaspilitos da Formação Carajás (PA). Rev. Bras. Geociências 32, 567–578. https://doi.org/10.25249/0375-7536.2002324567578

Macambira, M.J.B., Vasquez, M.L., Silva, D.C.C., Galarza, M.A., Barros, C.E.M., Camelo, J.F., 2009. Crustal growth of the central-eastern Paleoproterozoic domain, SW Amazonian craton: Juvenile accretion vs. reworking. J. South Am. Earth Sci. 27, 235–246. https://doi.org/10.1016/j.jsames.2009.02.001

Machado, N., Lindenmayer, Z., Krogh, T.E., Lindenmayer, D., 1991. U-Pb geochronology of Archean magmatism and basement reactivation in the Carajás area, Amazon shield, Brazil. Precambrian Res. 49, 329–354. https://doi.org/10.1016/0301-9268(91)90040-H

Mansur, E.T., Ferreira Filho, C.F., 2016. Magmatic structure and geochemistry of the Luanga Mafic–Ultramafic Complex: Further constraints for the PGE-mineralized magmatism in Carajás, Brazil. Lithos 266–267, 28–43. https://doi.org/10.1016/j.lithos.2016.09.036

Martins, L., Lana, C., Mazoz, A., Novo, T., 2021. Chemical-Abrasion U-Pb zircon geochronology reveals 150 Myr of partial melting events in the Archean crust of the São Francisco Craton. Geosci. Front. 13, 101289. https://doi.org/10.1016/j.gsf.2021.101289

Martins, P.L.G., Toledo, C.L.B., Silva, A.M., Antonio, P.Y.J., Chemale, F., Assis, L.M., Trindade, R.I.F., 2021a. Low paleolatitude of the Carajás Basin at ~2.75 Ga: Paleomagnetic evidence from basaltic flows in Amazonia. Precambrian Res. 365. https://doi.org/10.1016/j.precamres.2021.106411

Martins, P.L.G., Toledo, C.L.B., Silva, A.M., Chemale, F., Archer, C., de Assis, L.M., 2021b. Chemostratigraphy of the Carajás banded iron formation, Brazil: A record of Neoarchean Ocean chemistry. Gondwana Res. https://doi.org/10.1016/j.gr.2021.09.008

Martins, P.L.G., Toledo, C.L.B., Silva, A.M., Chemale, F., Santos, J.O.S., Assis, L.M., 2017.

Neoarchean magmatism in the southeastern Amazonian Craton, Brazil: Petrography, geochemistry and tectonic significance of basalts from the Carajás Basin. Precambrian Res. 302, 340–357. https://doi.org/10.1016/j.precamres.2017.10.013

Martinsen, O., 1994. Mass movements, in: Maltman, A. (Ed.), The Geological Deformation of Sediments. Springer Science, pp. 129–165. https://doi.org/10.1007/978-94-011-0731-0

Meixnerová, J., Blum, J.D., Johnson, M.W., Stüeken, E.E., Kipp, M.A., Anbar, A.D., Buick, R., 2021. Mercury abundance and isotopic composition indicate subaerial volcanism prior to the end-Archean "whiff" of oxygen. Proc. Natl. Acad. Sci. U. S. A. 118. https://doi.org/10.1073/pnas.2107511118

Melo, G.H.C., Monteiro, L.V.S., Xavier, R.P., Moreto, C.P.N., Arquaz, R.M., Silva, M.A.D., 2019. Evolution of the Igarapé Bahia Cu-Au deposit, Carajás Province (Brazil): Early syngenetic chalcopyrite overprinted by IOCG mineralization. Ore Geol. Rev. 111, 102993. https://doi.org/10.1016/j.oregeorev.2019.102993

Melo, G.H.C., Monteiro, L.V.S., Xavier, R.P., Moreto, C.P.N., Santiago, E.S.B., Dufrane, S.A., Aires, B., Santos, A.F.F., 2017. Temporal evolution of the giant Salobo IOCG deposit, Carajás Province (Brazil): constraints from paragenesis of hydrothermal alteration and U-Pb geochronology. Miner. Depos. 52, 709–732. https://doi.org/10.1007/s00126-016-0693-5

Moreto, C.P.N., Monteiro, L.V.S., Xavier, R.P., Creaser, R.A., DuFrane, S.A., Tassinari, C.C.G., Sato, K., Kemp, A.I.S., Amaral, W.S., 2015. Neoarchean and paleoproterozoic iron oxide-copper-gold events at the sossego deposit, Carajás Province, Brazil: Re-Os and U-Pb geochronological evidence. Econ. Geol. 110, 809–835. https://doi.org/10.2113/econgeo.110.3.809

Morris, R.C., 1993. Genetic modelling for banded iron-formation of the Hamersley Group, Pilbara Craton, Western Australia. Precambrian Res. 60, 243–286. https://doi.org/10.1016/0301-9268(93)90051-3

Myrow, P.M., Tice, L., Archuleta, B., Clark, B., Taylor, J.F., Ripperdan, R.L., 2004. Flat-pebble conglomerate: Its multiple origins and relationship to metre-scale depositional cycles. Sedimentology 51, 973–996. https://doi.org/10.1111/j.1365-3091.2004.00657.x

Narduzzi, F., Bosch, D., Philippot, P., 2021. Evolution of seawater continentally-sourced

Nd isotopic composition prior to and during the Great Oxidation Event. Precambrian Res. 362, 106292. https://doi.org/10.1016/j.precamres.2021.106292

Noffke, N., Gerdes, G., Klenke, T., Krumbein, W.E., 2001. Microbially induced sedimentary structures - A new category within the classification of primary sedimentary structures. J. Sediment. Res. 71, 649–656. https://doi.org/10.1306/d4268d60-2b26-11d7-8648000102c1865d

Olszewski, W.J., Wirth, K.R., Gibbs, A.K., Gaudette, H.E., 1989. The age, origin, and tectonics of the Grão Pará Group and associated rocks, Serra dos Carajás, Brazil: Archean continental volcanism and rifting. Precambrian Res. 42, 229–254. https://doi.org/10.1016/0301-9268(89)90013-2

Pidgeon, R.T., MacAmbira, M.J.B., Lafon, J.M., 2000. Th-U-Pb isotopic systems and internal structures of complex zircons from an enderbite from the Pium Complex, Carajas Province, Brazil: Evidence for the ages of granulite facies metamorphism and the protolith of the enderbite. Chem. Geol. 166, 159–171. https://doi.org/10.1016/S0009-2541(99)00190-4

Pinheiro, R.V.L., Holdsworth, R.E., 1997. Reactivation of Archaean strike-slip fault systems, Amazon region, Brazil. J. Geol. Soc. London. 154, 99–103. https://doi.org/10.1144/gsjgs.154.1.0099

Pritchard, G., Moloney, P., Russell, K., Whiten, B., 2009. Provenance of sedimentary rocks. MIIS Eprints Arch. 11–24.

R Development Core Team, 2008. R: A language and environment for statistical computing. R Foundation for Statistical Computing, Vienna, Austria.

Rasmussen, B., Meier, D.B., Krapež, B., Muhling, J.R., 2013. Iron silicate microgranules as precursor sediments to 2.5-billion-year-old banded iron formations. Geology 41, 435–438. https://doi.org/10.1130/G33828.1

Ravier, E., Guiraud, M., Guillien, A., Vennin, E., Buoncristiani, J.-F., Portier, E., 2015. Micro- to macro-scale internal structures, diagenesis and petrophysical evolution of injectite networks in the Vocontian Basin (France): Implications for fluid flow. Mar. Pet. Geol. 64, 125–151. https://doi.org/10.1016/j.marpetgeo.2015.02.040

Rego, E.S., Busigny, V., Lalonde, S.V., Philippot, P., Bouyon, A., Rossignol, C., Babinski, M., Zapparoli, A., 2021. Anoxygenic photosynthesis linked to Neoarchean iron formations in Carajás (Brazil). Geobiology 19, 326–341. https://doi.org/10.1111/gbi.12438

Reimink, J.R., Davies, J.H.F.L., Ielpi, A., 2021. Global zircon analysis records a gradual rise of continental crust throughout the Neoarchean. Earth Planet. Sci. Lett. 554, 116654. https://doi.org/10.1016/j.epsl.2020.116654

Requia, K., Stein, H., Fontboté, L., Chiaradia, M., 2003. Re-Os and Pb-Pb geochronology of the Archean Salobo iron oxide copper-gold deposit, Carajás mineral province, northern Brazil. Miner. Depos. 38, 727–738. https://doi.org/10.1007/s00126-003-0364-1

Ribeiro da Luz, B., Crowley, J.K., 2012. Morphological and chemical evidence of stromatolitic deposits in the 2.75Ga Carajás banded iron formation, Brazil. Earth Planet. Sci. Lett. 355–356, 60–72. https://doi.org/10.1016/j.epsl.2012.08.028

Riding, R., 2000. Microbial carbonates the geological record of calcified bacterial–algal mats and biofilms. Sedimentology 47, 179–214. https://doi.org/10.1046/j.1365-3091.2000.00003.x

Ronze, P.C., Soares, A.D.V., Santos, M.G.S., Barreira, C.F., 2000. Alemao copper-gold (U-REE) deposits, Carajas, Brazil, in: Porter, T.M. (Ed.), Hydrothermal Iron Oxide Copper-Gold and Related Deposits: A Global Perspective. PCG Publishing, pp. 191–202.

Rossignol, C., Antonio, P.Y.J., Narduzzi, F., Rego, E.S., Teixeira, L., de Souza, R.A., Ávila, J.N., Silva, M.A.L., Lana, C., Trindade, R.I.F., Philippot, P., 2021. Unraveling one billion years of geological evolution of the southeastern Amazonia Craton from detrital zircon analyses. Geosci. Front. 101202. https://doi.org/10.1016/j.gsf.2021.101202

Rossignol, C., Bourquin, S., Poujol, M., Hallot, E., Dabard, M.-P., Nalpas, T., 2016. The volcaniclastic series from the Luang Prabang Basin, Laos: A witness of a triassic magmatic arc? J. Asian Earth Sci. 120. https://doi.org/10.1016/j.jseaes.2016.02.001

Rossignol, C., Hallot, E., Bourquin, S., Poujol, M., Jolivet, M., Pellenard, P., Ducassou, C., Nalpas, T., Heilbronn, G., Yu, J., Dabard, M.-P., 2019. Using volcaniclastic rocks to constrain sedimentation ages: To what extent are volcanism and sedimentation synchronous? Sediment. Geol. 381. https://doi.org/10.1016/j.sedgeo.2018.12.010

Rossignol, C., Lana, C., Alkmim, F., 2020a. Geodynamic evolution of the Minas Basin, southern São Francisco Craton (Brazil), during the early Paleoproterozoic: Climate or tectonic? J. South Am. Earth Sci. 101, 102628. https://doi.org/10.1016/j.jsames.2020.102628

Rossignol, C., Rego, E.S., Narduzzi, F., Teixeira, L., Ávila, J.N., Silva, M.A.L., Lana, C., Philippot, P., 2020b. Stratigraphy and geochronological constraints of the Serra Sul Formation (Carajás Basin, Amazonian Craton, Brazil). Precambrian Res. 351, 105981. https://doi.org/10.1016/j.precamres.2020.105981

Rubatto, D., 2002. Zircon trace element geochemistry: partitioning with garnet and the link between U–Pb ages and metamorphism. Chem. Geol. 184, 123–138. https://doi.org/10.1016/S0009-2541(01)00355-2

Salminen, J., Oliveira, E.P., Piispa, E.J., Smirnov, A.V., Trindade, R.I.F., 2019. Revisiting the paleomagnetism of the Neoarchean Uauá mafic dyke swarm, Brazil: Implications for Archean supercratons. Precambrian Res. 329, 108–123. https://doi.org/10.1016/j.precamres.2018.12.001

Sardinha, A.S., Barros, C.E.M., Krymsky, R., 2006. Geology, geochemistry, and U-Pb geochronology of the Archean (2.74 Ga) Serra do Rabo granite stocks, Carajás Metallogenetic Province, northern Brazil. J. South Am. Earth Sci. 20, 327–339. https://doi.org/10.1016/j.jsames.2005.11.001

Schröder, S., Bedorf, D., Beukes, N.J., Gutzmer, J., 2011. From BIF to red beds: Sedimentology and sequence stratigraphy of the Paleoproterozoic Koegas Subgroup (South Africa). Sediment. Geol. 236, 25–44. https://doi.org/10.1016/j.sedgeo.2010.11.007

Siepierski, L., Ferreira Filho, C.F., 2020. Magmatic structure and petrology of the Vermelho Complex, Carajás Mineral Province, Brazil: Evidence for magmatic processes at the lower portion of a mafic-ultramafic intrusion. J. South Am. Earth Sci. 102, 102700. https://doi.org/10.1016/j.jsames.2020.102700

Siepierski, L., Ferreira Filho, C.F., 2016. Spinifex-textured komatiites in the south border of the Carajas ridge, Selva Greenstone belt, Carajás Province, Brazil. J. South Am. Earth Sci. 66, 41–55. https://doi.org/10.1016/j.jsames.2015.12.011

Simonson, B.M., Goode, A.D.T., 1989. First discovery of ferruginous chertarenites in the early Precambrian Hamersley Group of western Australia. Geology 17, 269–272.

Simonson, B.M., Hassler, S.W., 1996. Was the deposition of large precambrian iron formations linked to major marine transgressions? J. Geol. 104, 665–676. https://doi.org/10.1086/629861

Sircombe, K.N., Hazelton, M.L., 2004. Comparison of detrital zircon age distributions by kernel functional estimation. Sediment. Geol. 171, 91–111.

https://doi.org/10.1016/j.sedgeo.2004.05.012

Smith, A.J.B., Beukes, N.J., Gutzmer, J., 2013. The composition and depositional environments of Mesoarchean iron formations of the West Rand Group of the Witwatersrand Supergroup, South Africa. Econ. Geol. 108, 111–134. https://doi.org/10.2113/econgeo.108.1.111

Sohn, Y.K., Park, K.H., Yoon, S.-H., 2008. Primary versus secondary and subaerial versus submarine hydrovolcanic deposits in the subsurface of Jeju Island, Korea. Sedimentology 55, 899–924. https://doi.org/10.1111/j.1365-3091.2007.00927.x

Souza, S.R.C., Botelho, N.F., Dantas, E.L., Jiménez, F.A.C., Reis, M.A., Viana, C.S., 2020. Geochemistry and isotopic geology of the Lagoa Seca gold deposit in the Andorinhas greenstone-belt, Carajás Province, Brazil. J. South Am. Earth Sci. 99, 102523. https://doi.org/10.1016/j.jsames.2020.102523

Spencer, C.J., Partin, C.A., Kirkland, C.L., Raub, T.D., Liebmann, J., Stern, R.A., 2019. Paleoproterozoic increase in zircon δ18O driven by rapid emergence of continental crust. Geochim. Cosmochim. Acta 257, 16–25. https://doi.org/10.1016/j.gca.2019.04.016

Spier, C.A., de Oliveira, S.M.B., Sial, A.N., Rios, F.J., 2007. Geochemistry and genesis of the banded iron formations of the Cauê Formation, Quadrilátero Ferrífero, Minas Gerais, Brazil. Precambrian Res. 152, 170–206. https://doi.org/10.1016/j.precamres.2006.10.003

Sunder Raju, P.V., Mazumder, R., 2020. Archean sedimentation on Dharwar Craton, India and its implications. Earth-Science Rev. https://doi.org/10.1016/j.earscirev.2019.102999

Tallarico, F.H.B., Figueiredo, B.R., Groves, D.I., Kositcin, N., McNaughton, N.J., Fletcher, I.R., Rego, J.L., 2005. Geology and SHRIMP U-Pb geochronology of the Igarapé Bahia deposit, Carajás copper-gold belt, Brazil: An Archean (2.57 Ga) example of Iron-Oxide Cu-Au-(U-REE) mineralization. Econ. Geol. 100, 7–28. https://doi.org/10.2113/100.1.0007

Tavares, F.M., Trouw, R.A.J., da Silva, C.M.G., Justo, A.P., Oliveira, J.K.M., 2018. The multistage tectonic evolution of the northeastern Carajás Province, Amazonian Craton, Brazil: Revealing complex structural patterns. J. South Am. Earth Sci. 88, 238–252. https://doi.org/10.1016/j.jsames.2018.08.024

Teixeira, W., Hamilton, M.A., Girardi, V.A.V., Faleiros, F.M., Ernst, R.E., 2019. U-Pb

baddeleyite ages of key dyke swarms in the Amazonian Craton (Carajás/Rio Maria and Rio Apa areas): Tectonic implications for events at 1880, 1110 Ma, 535 Ma and 200 Ma. Precambrian Res. 329, 138–155. https://doi.org/10.1016/j.precamres.2018.02.008

Tolbert, G.E., Tremaine, J.W., Melcher, G.C., Gomes, C.B., 1971. The Recently Discovered Serra dos Carajás Iron Deposits, northern Brazil. Econ. Geol. 66, 985–994. https://doi.org/https://doi.org/10.2113/gsecongeo.66.7.985

Toledo, P.I.F., Moreto, C.P.N., Xavier, R.P., Gao, J.F., de Matos, J.H.S.N., de Melo, G.H.C., 2019. Multistage evolution of the Neoarchean (ca. 2.7 Ga) Igarapé cinzento (GT-46) iron oxide copper-gold deposit, Cinzento shear zone, Carajás Province, Brazil. Econ. Geol. 114, 1–34. https://doi.org/10.5382/econgeo.2019.4617

Trendall, A.F., 2002. The significance of iron-formation in the Precambrian stratigraphic record, in: Altermann, W., Corcoran, P.L. (Eds.), Special Publication of the International Association of Sedimentologists. International Association of Sedimentologists Special Publication, pp. 33–66.

Trendall, A.F., Basei, M.A.S., De Laeter, J.R., Nelson, D.R., 1998. SHRIMP zircon U-Pb constraints on the age of the Carajas formation, Grao Para Group, Amazon Craton. J. South Am. Earth Sci. 11, 265–277. https://doi.org/10.1016/S0895-9811(98)00015-7

Van Kranendonk, M.J., Ivanic, T.J., Wingate, M.T.D., Kirkland, C.L., Wyche, S., 2013. Long-lived, autochthonous development of the archean murchison domain, and implications for yilgarn craton tectonics. Precambrian Res. 229, 49–92. https://doi.org/10.1016/j.precamres.2012.08.009

Vasquez, M.L., Sousa, C.S., Carvalho, J.M.A., 2008. Mapa Geológico do Estado do Pará. Scale 11 000 000.

Vennin, E., Olivier, N., Brayard, A., Bour, I., Thomazo, C., Escarguel, G., Fara, E., Bylund, K.G., Jenks, J.F., Stephen, D.A., Hofmann, R., 2015. Microbial deposits in the aftermath of the end-Permian mass extinction: A diverging case from the Mineral Mountains (Utah, USA). Sedimentology 62, 753–792. https://doi.org/10.1111/sed.12166

Vermeesch, P., 2018. Dissimilarity measures in detrital geochronology. Earth-Science Rev. 178, 310–321. https://doi.org/10.1016/j.earscirev.2017.11.027

Vermeesch, P., 2013. Multi-sample comparison of detrital age distributions. Chem. Geol. 341, 140–146. https://doi.org/10.1016/j.chemgeo.2013.01.010

Vermeesch, P., 2012. On the visualisation of detrital age distributions. Chem. Geol. 312–313, 190–194. https://doi.org/10.1016/j.chemgeo.2012.04.021

Vermeesch, P., Resentini, A., Garzanti, E., 2016. An R package for statistical provenance analysis. Sediment. Geol. 336, 14–25. https://doi.org/10.1016/j.sedgeo.2016.01.009

Viehmann, S., Bau, M., Hoffmann, J.E., Münker, C., 2018. Decoupled Hf and Nd isotopes in suspended particles and in the dissolved load of Late Archean seawater. Chem. Geol. 483, 111–118. https://doi.org/10.1016/j.chemgeo.2018.01.017

Viehmann, S., Bau, M., Hoffmann, J.E., Münker, C., 2015. Geochemistry of the Krivoy Rog Banded Iron Formation, Ukraine, and the impact of peak episodes of increased global magmatic activity on the trace element composition of Precambrian seawater. Precambrian Res. 270, 165–180. https://doi.org/10.1016/j.precamres.2015.09.015

Villas, R.N., Santos, M.D., 2001. Gold deposits of the Carajás mineral province: Deposit types and metallogenesis. Miner. Depos. 36, 300–331. https://doi.org/10.1007/s001260100178

Wang, W., Cawood, P.A., Spencer, C.J., Pandit, M.K., Zhao, J.-H., Xia, X.-P., Zheng, J.-P., Lu, G.-M., 2021. Global-scale emergence of continental crust during the Mesoarchean – early Neoarchean. Geology in press, 1–5. https://doi.org/10.1130/G49418.1/5461425/g49418.pdf

Warchola, T.., Lalonde, S.V., Pecoits, E., von Gunten, K., Robbins, L.J., Alessi, D.S., Philippot, P., Konhauser, K.O., 2018. Petrology and geochemistry of the Boolgeeda Iron Formation, Hamersley Basin, Western Australia. Precambrian Res. 316, 155–173. https://doi.org/10.1016/j.precamres.2018.07.015

Wignall, P., 2005. The Link between Large Igneous Province Eruptions and Mass Extinctions. Elements 1, 293–297. https://doi.org/10.2113/gselements.1.5.293

Wirth, K.R., Gibbs, A.K., Olszewski, W.J., 1986. U-Pb ages of zircons from the Grão-Pará Group and Serra dos Carajás Granites, Pará, Brazil. Rev. Bras. Geociências 16, 195–200.

Figures and tables (including captions)

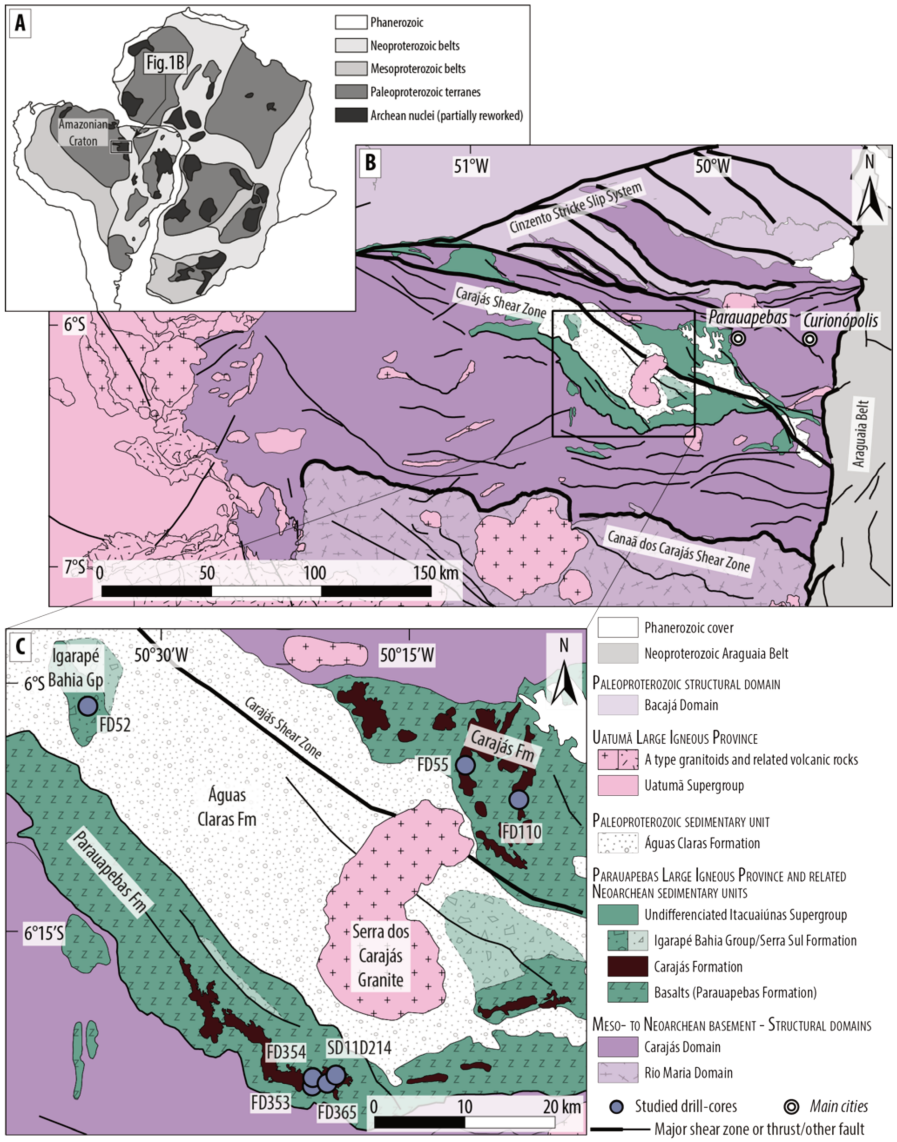

Fig. 1. Location of the Amazonia Craton and the Carajás Basin. **A**. Schematic West Gondwana reconstruction of the main tectonic elements of South America and Africa (Cordani et al., 2016). **B**. Geological map of the Carajás Basin (Vasquez et al., 2008). **C**. Location of the drill cores.

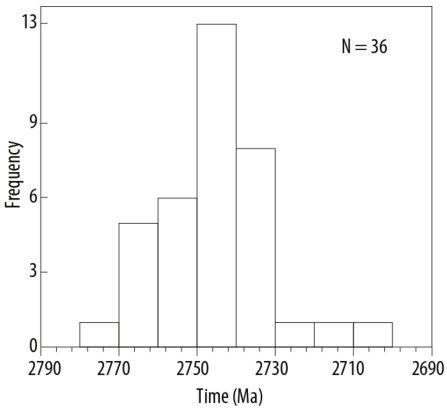

Fig. 2. Frequency distribution of zircon U-Pb and Pb-Pb dates of rocks from the Parauapebas Large Igneous Province. Data source: Table 1. Bin width: 10 Ma.

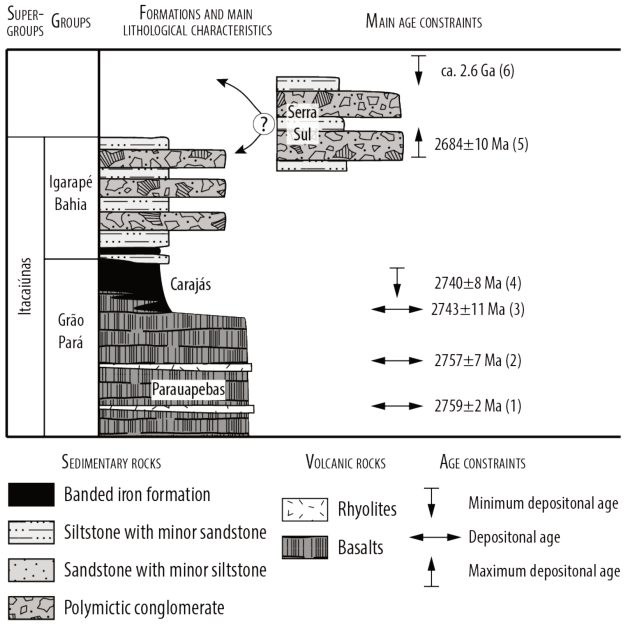

Fig. 3. Main sedimentary units of the Carajás Basin. Age constraints: Table 2.

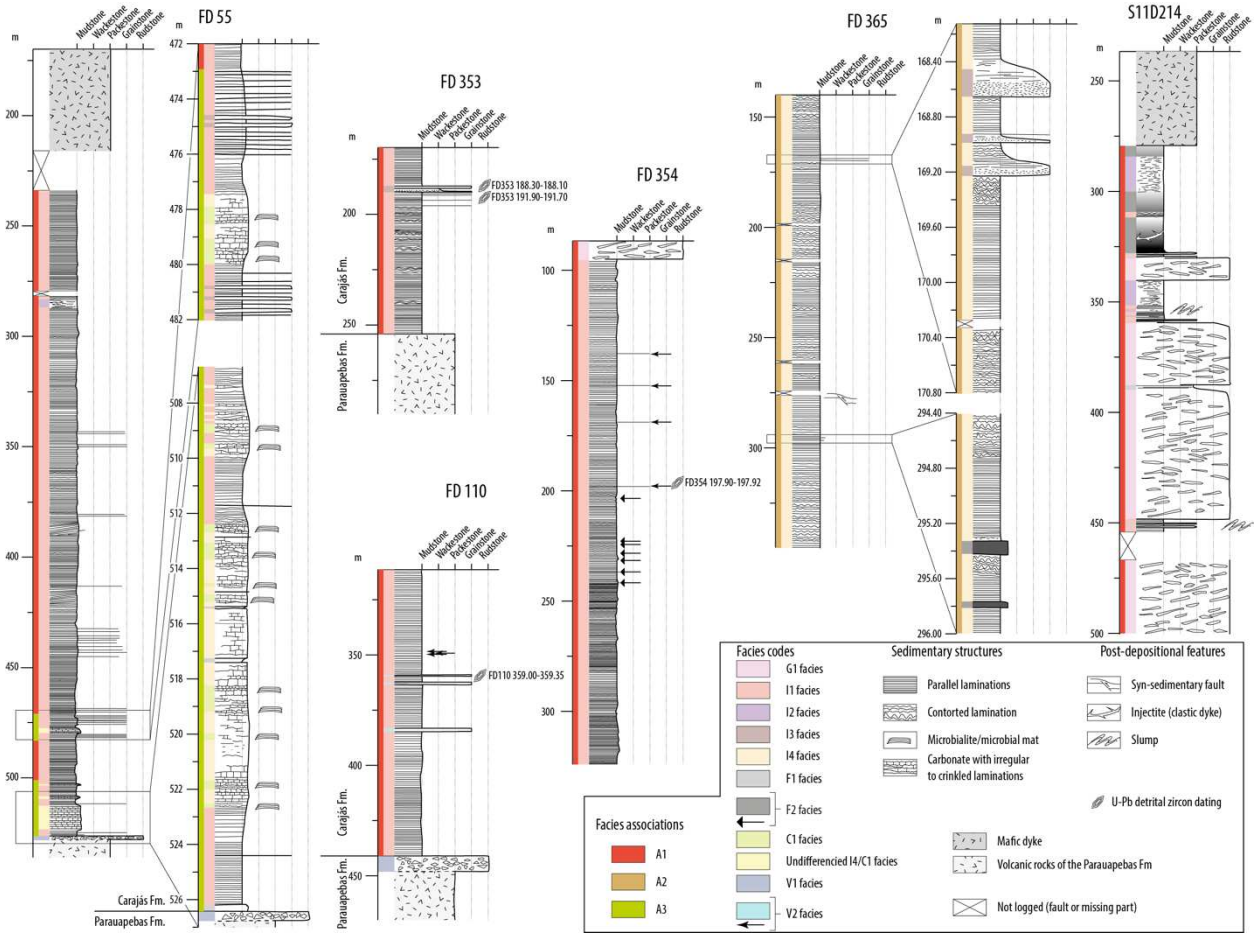

Fig. 4. Sedimentological logs of the drill cores intersecting the Carajás Formation. Facies codes: Table 3. Facies associations: Table 4.

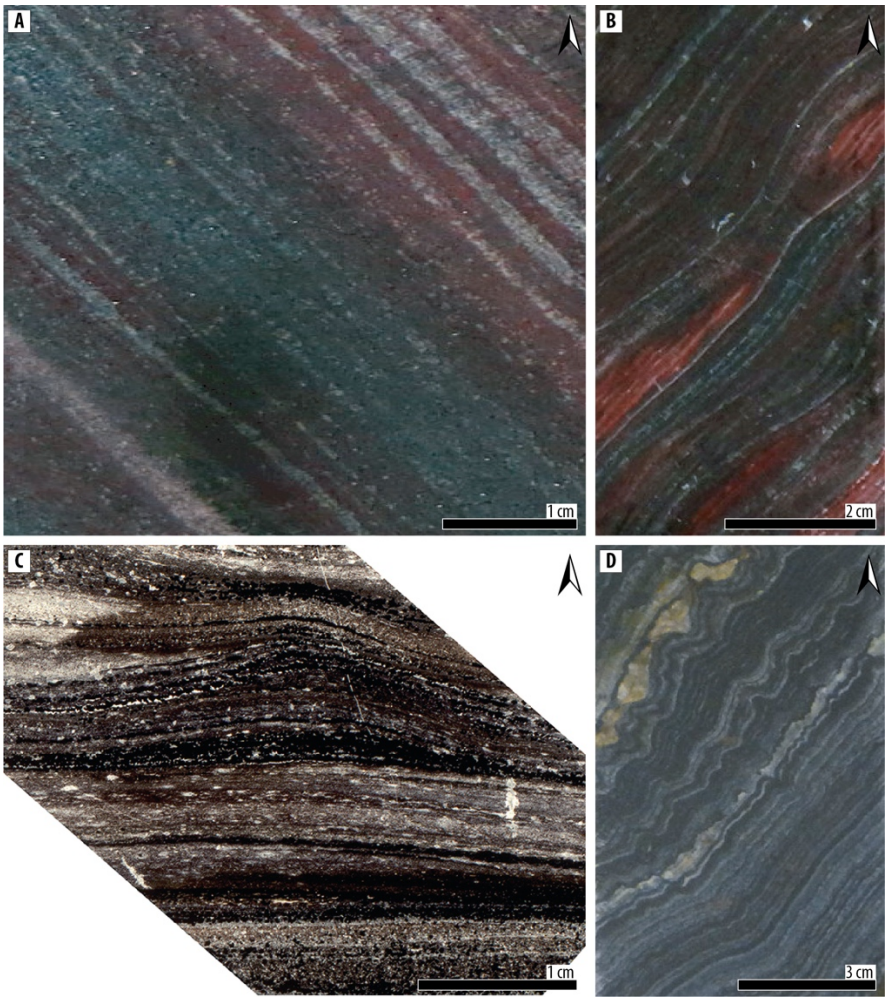

Fig. 5. Banded iron facies from the Carajás Formation. Arrows point to the stratigraphic top. **A**. Sample FD55 486.45. Fine horizontal laminations (sub-mm scale) of iron-bearing minerals (magnetite and hematite) and chert layers. **B**. Sample FD55 495.80. Finely laminated siliceous BIF displaying wavy laminations. **C.** Sample FD55 480.80. Thin section in reflected light showing a reactivation surface in a jaspilitic BIF. **D.** Sample FD365 182.70. Alternating layers of Fe-rich minerals and carbonates, forming a carbonate-rich BIF (facies I4) comprising wavy irregular laminations.

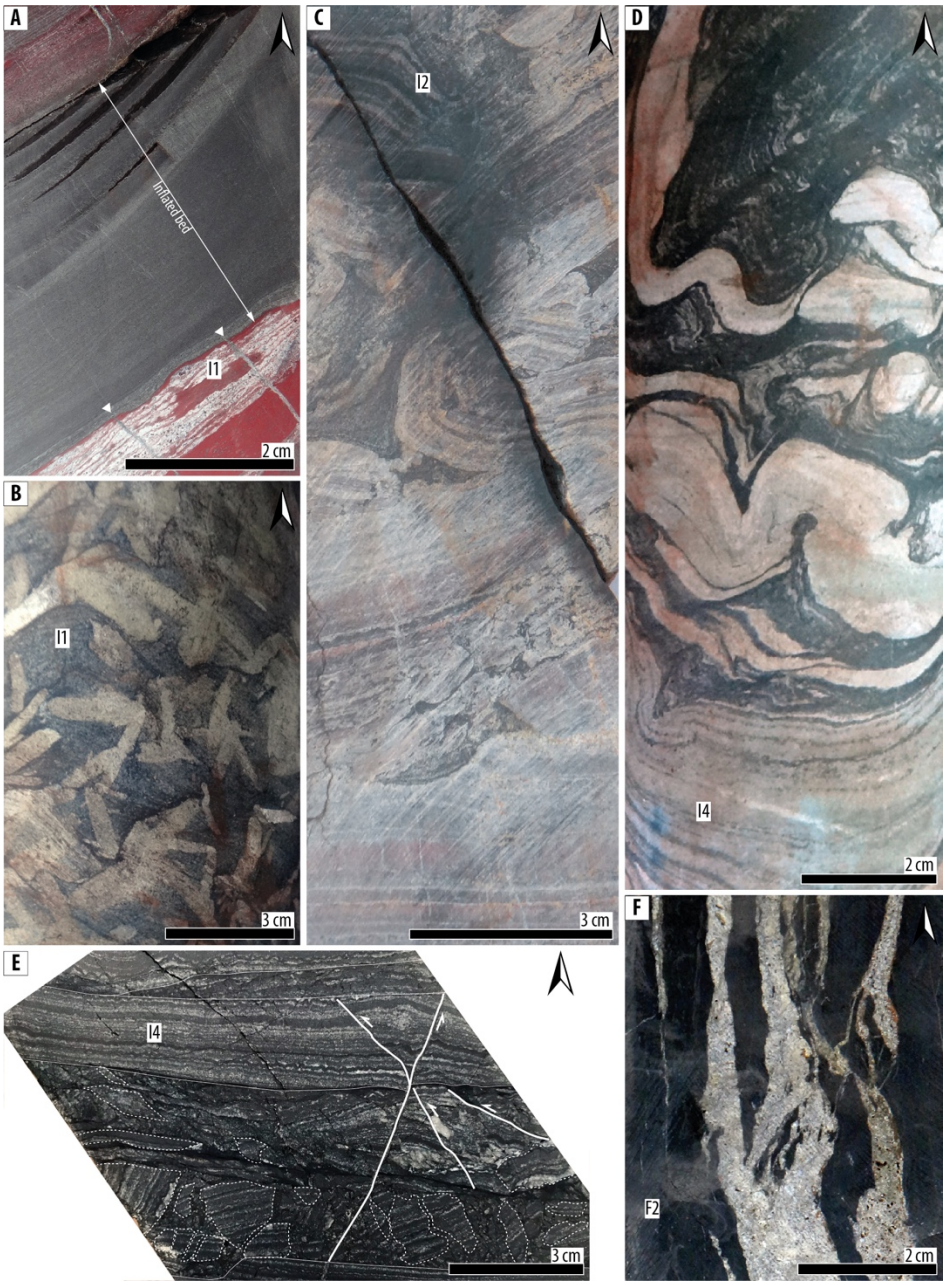

Fig. 6. Syn- to post-depositional deformations, diagenetic and metamorphic features affecting the deposits of the Carajás Formation. Arrows point to the stratigraphic top. Facies codes: Table 3. **A.** Sample FD55 351.90. Jaspilitic BIF comprising a late diagenetic inflated bed composed of magnetite with small veins rooted in the inflated bed (white triangles) crosscutting the underlying BIF. **B.** Sample FD354 242.20. Large secondary mineral in a jaspilitic BIF. **C.** Sample S11D214 449.00. Chert displaying folded layers and a few clasts, attesting for a ductile to brittle deformation attributed to slumping processes. **D.** Sample FD365 340.80. Highly contorted lamination in carbonate BIF resulting from the

loading of dense Fe-rich layers onto carbonate beds. **E.** Sample FD365 262.20. Carbonate BIF showing intraformational angular clasts along a slip surface. Syn-sedimentary faults crosscut both intraformational clasts and carbonate BIF. Two erosion surfaces are present above the intraformational angular clasts. **F.** Sample S11D214 323.10. Injectite in black shales.

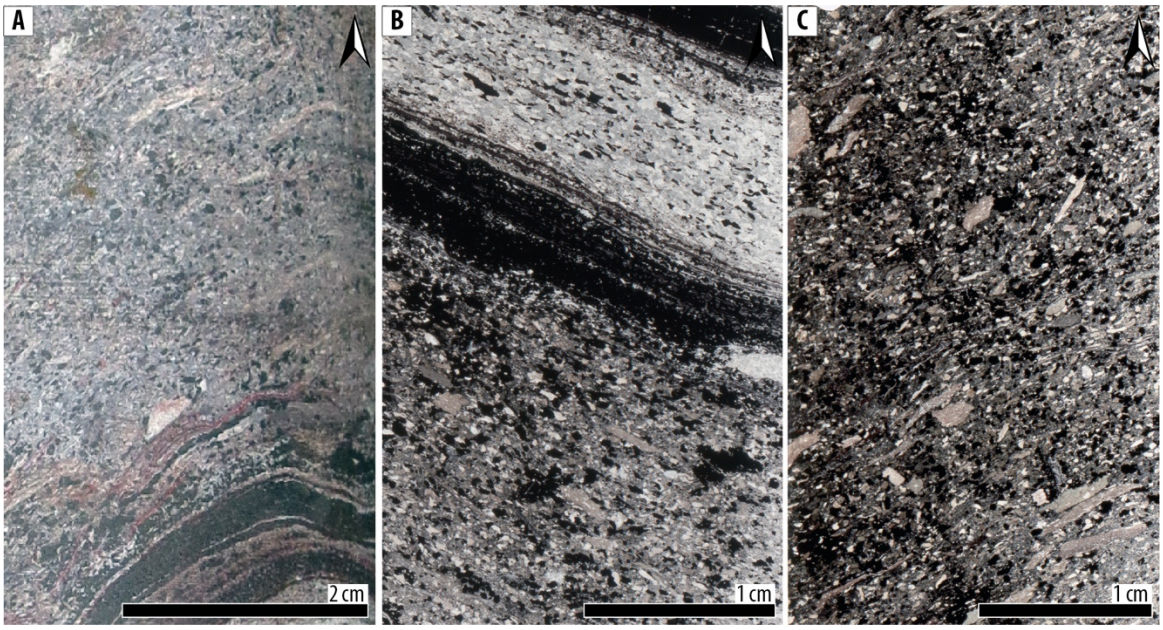

Fig. 7. Granular iron facies of the Carajás Formation. Arrows point to the stratigraphic top. **A.** Sample FD55 475.10. Granular Iron Formation (GIF) comprising very elongated, sub-angular to rounded chips with rounded ends and slight bending. The chips are made up of chert and are flattened parallel to the bedding. **B.** Sample FD55 475.05. Thin section in reflected light showing interlayered GIFs and BIFs. **C.** Sample FD55 475.15. Thin section in reflected light showing chert clasts with rounded to very elongated shapes. The chert clasts are embedded within a cherty matrix comprising oxide minerals. Elongated clasts are flattened parallel to the bedding.

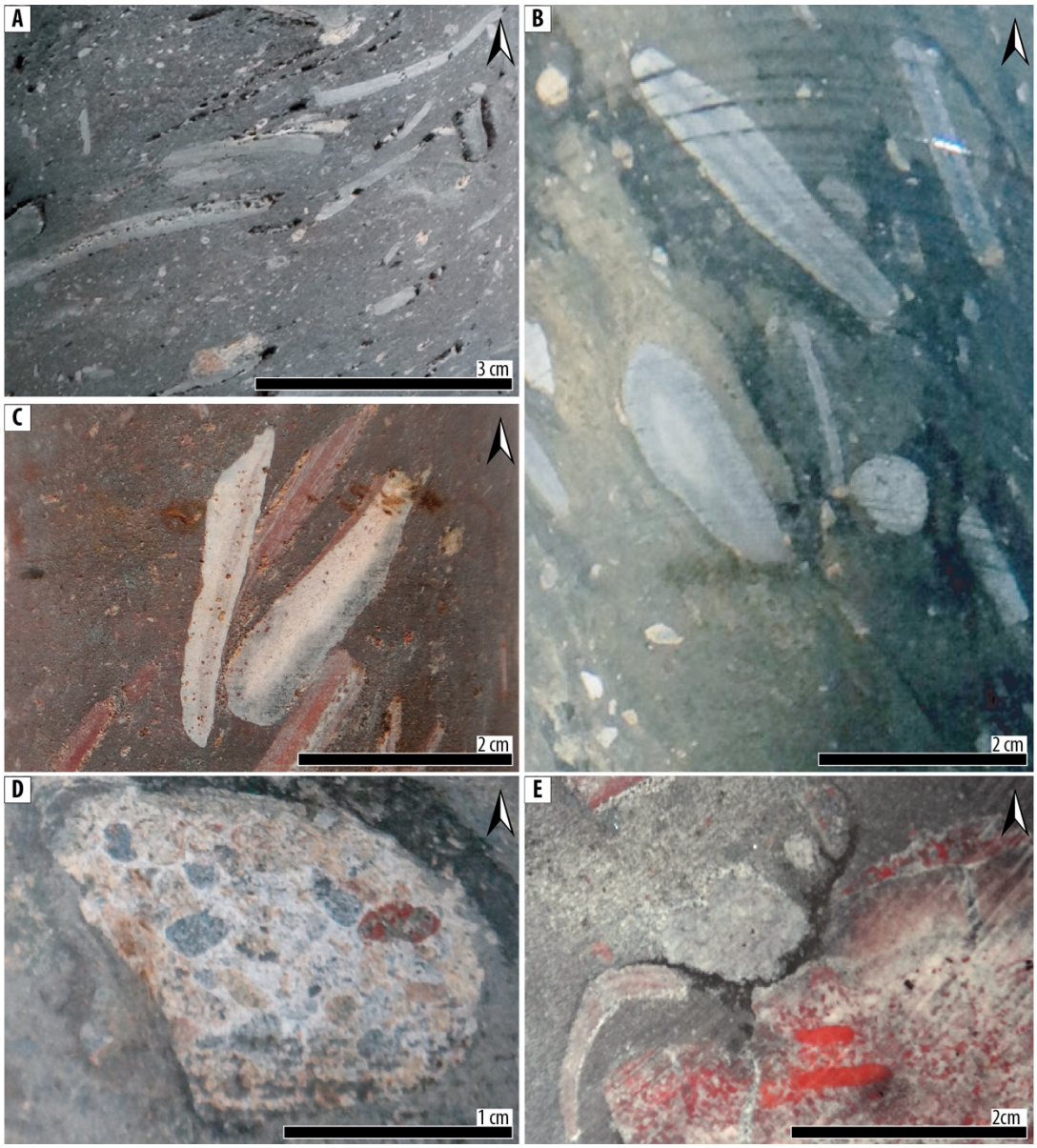

Fig. 8. Conglomerate facies of the Carajás Formation. Arrows point to the stratigraphic top. **A.** Sample FD354 91.60. Monomictic matrix-supported conglomerate with elongated clasts. Most of the clasts are slightly bended. Fine-grained ferruginous matrix. Long axes of clasts show a preferred orientation. **B.** Sample S11D214 339.50. Large clasts in a matrix-supported conglomerate. The clasts are elongated with exhibit rounded ends and display a preferred orientation. **C.** Sample S11D214 494.00. Matrix-supported conglomerate with elongated chert clasts in a very fine ferruginous matrix. The clasts exhibit a preferred orientation and rounded to sub-rounded ends. **D.** Sample S11D214 339.50. Clast made up of coarse sandstone. **E.** Sample S11D214 487.30. Conglomerate displaying rounded to sub-rounded clasts as well as bended and elongated chert clast.

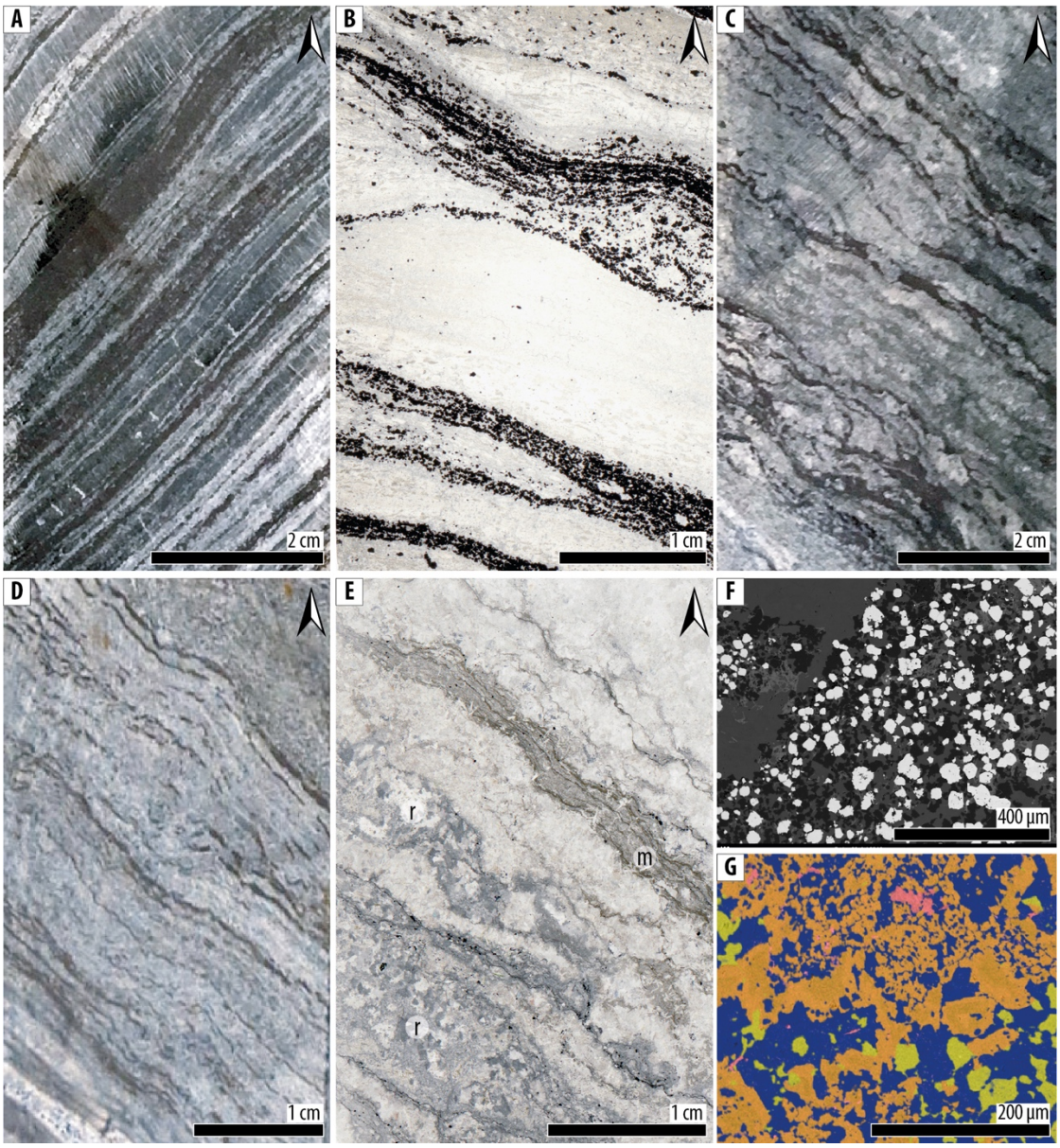

Fig. 9. Carbonate facies of the Carajás Formation. Arrows point to the stratigraphic top. **A.** Sample FD55 521.60. Fine laminations (mm to cm scale) of iron-bearing minerals (mainly magnetite) and carbonate layers. **B.** Sample FD55 521.12. Thin section in reflected light showing wavy laminations underlined by magnetite grains and carbonates. **C.** Sample FD55 518.50. Carbonate with irregular, crinkled magnetite laminations and pinching out geometries. **D.** Sample FD55 522.56. Carbonate with very fine, crinkled lamination underlined by very fine (mm thick) magnetite layers. **E.** Sample FD55 520.06.

Thin section in reflected light showing a microbial mat (m) within carbonate displaying a clotted micritic texture. Some areas show recrystallized (r) textures. **F.** Sample FD55 514.57. Electron backscattered image showing diagenetic framboidal pyrite (bright white) minerals within a carbonate matrix. **G.** Sample FD55 514.57. EDS electron image showing Si, Ca and Fe-rich mineral phases. Calcite appears in green, ankerite in orange, chert in dark blue, and magnetite in pink.

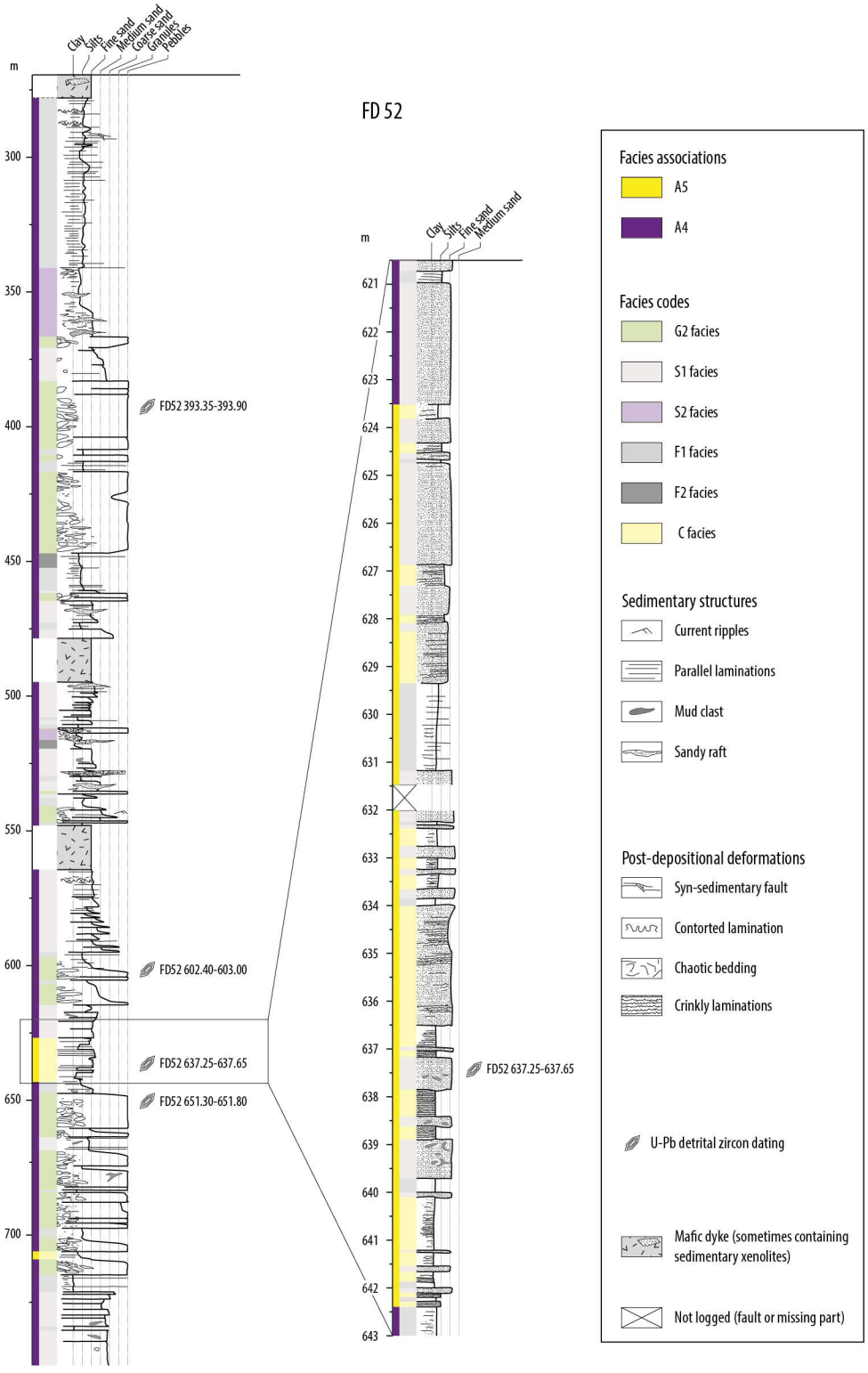

Fig. 10. Sedimentological log of the drill core intersecting the Igarapé Bahia Group. Facies codes: Table 3. Facies association: Table 4. The upper part of the drill core intercepts another younger formation and is presented in the Appendix 1.

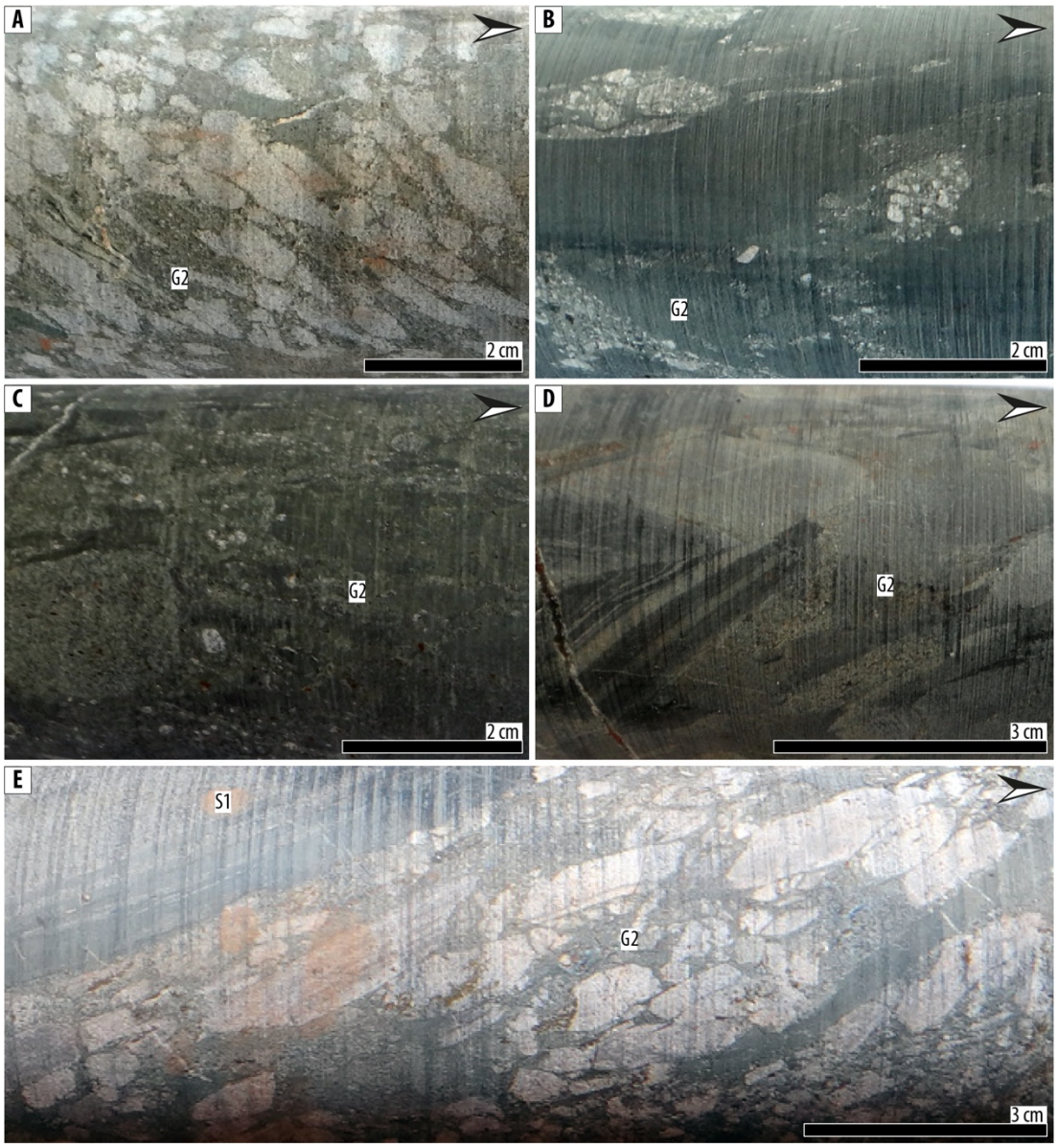

Fig. 11. Flat-pebbles conglomerate facies from the Igarapé Bahia Group. Arrows point to the stratigraphic top. Facies codes: Table 3. **A.** Sample FD52 546.50. Flat-pebble conglomerate made up of elongated, sub-angular to sub-rounded clasts embedded within a greenish matrix. Most of the clasts are sandy, a few clasts are muddy. **B.** Sample FD52 530.60. Flat-pebble conglomerate comprising sandy clasts embedded into a muddy to silty matrix. **C.** Sample FD52 392.65. Flat-pebble conglomerate, comprising mainly muddy clasts, sandy clasts and mixed clasts preserving original sedimentary structure. **D.** Sample FD52 441.85. Flat-pebble conglomerate, clasts supported. Some clasts preserve a sedimentary bedding. Occurrence of muddy clasts, sandy clasts and mixed clasts

preserving original sedimentary structure. **E.** Sample FD52 536.49. Flat-pebble conglomerate comprising sandy clasts flattened parallel to the bedding. The contact with the underlying fine sandstone to siltstone is sharp and non-erosive.

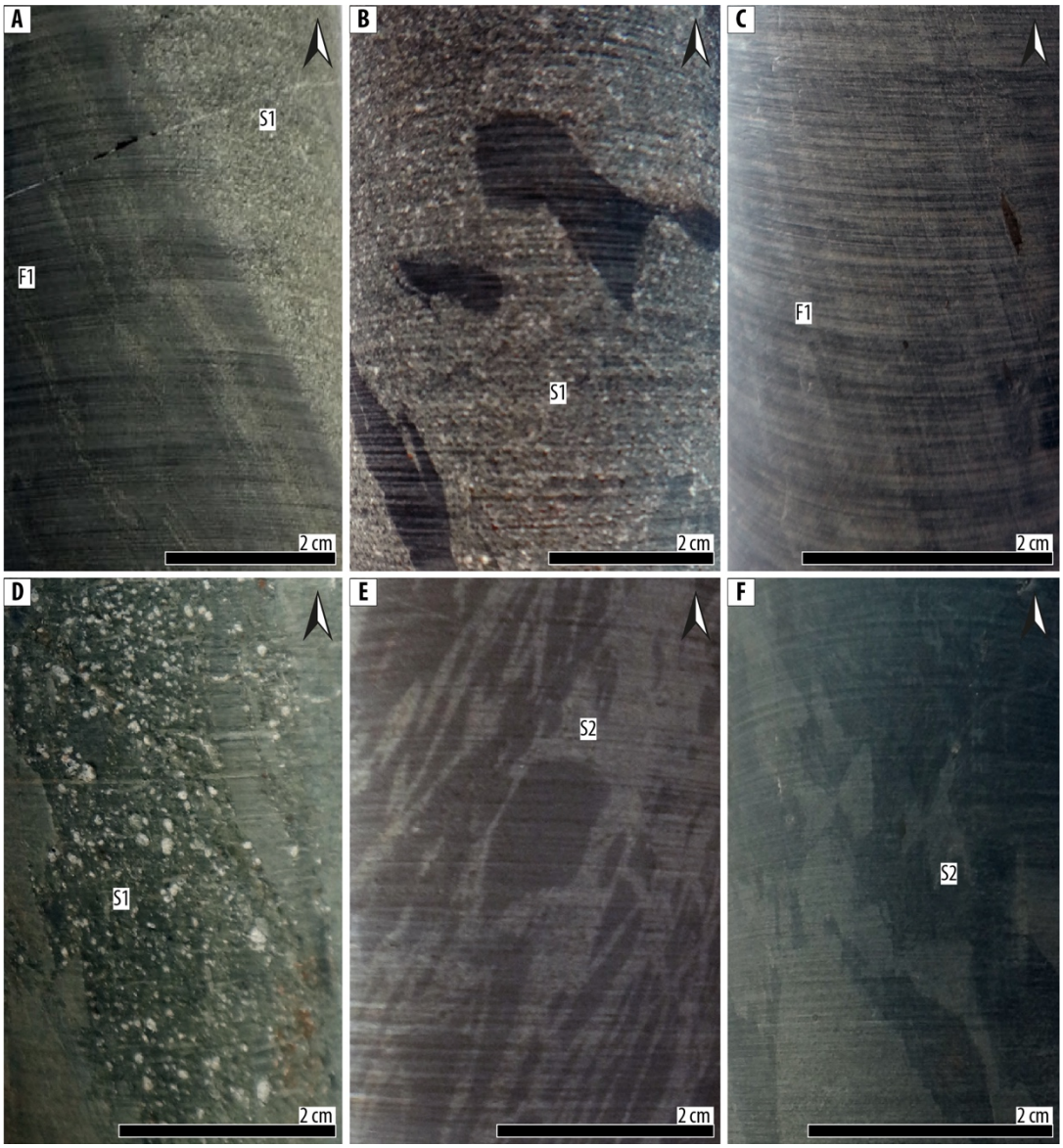

Fig. 12. Sandstone and siltstone facies from the Igarapé Bahia Group. Arrows point to the stratigraphic top. Facies codes: Table 3. **A.** Sample FD52 471.20. F1 facies with planar lamination underlined by fine sandstone layers grading to S1 facies. **B.** Sample FD52 618.80. S1 facies containing mud clasts. **C.** Sample FD52 320.30. F1 facies with fine horizontal laminations. **D.** Sample FD52 423.00. Fine sandstone to siltstone containing a

"raft" made up of coarse sand embedded within a muddy matrix. **E.** Sample FD52 515.80. Anastomosed elutriation bands. **F.** Sample FD52 355.40. Strongly folded sandstone to siltstone horizon, where initial bedding planes are not recognizable.

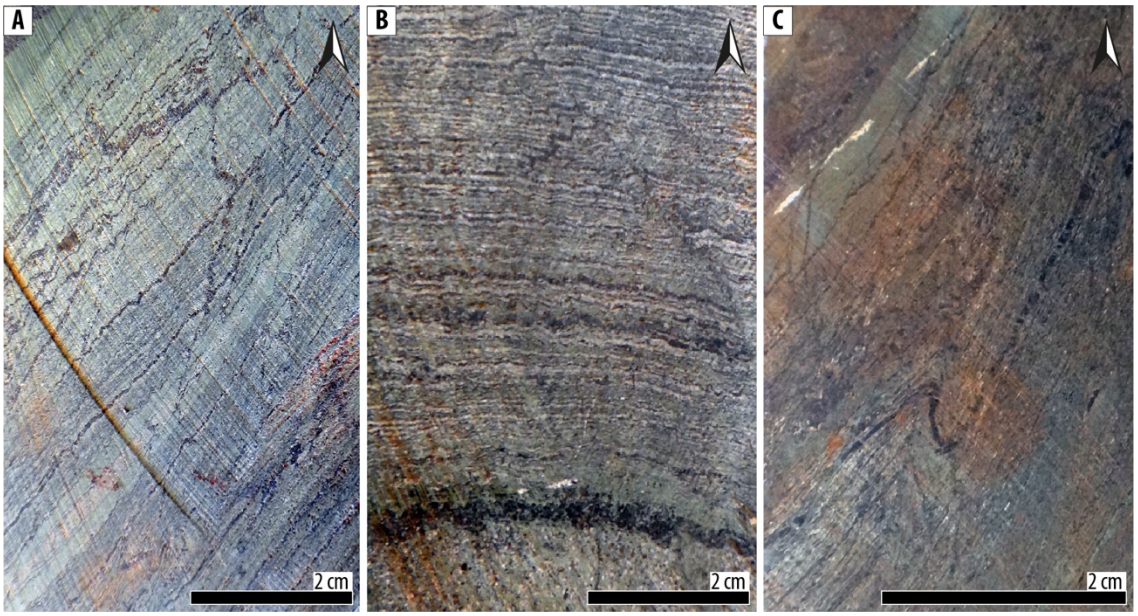

Fig. 13. Carbonate facies from the Igarapé Bahia Group. Arrows point to the stratigraphic top. **A.** Sample FD52 636.60. Thinly laminated greenish carbonate alternating with millimetric magnetite layers. Post-depositional micro-folding. **B.** Sample FD52 637.10. Thinly laminated greenish carbonate and magnetite layers displaying variable thicknesses. Post-depositional faults. **C.** Sample FD52 623.60. Greenish carbonate beds alternating with millimetric magnetite layers. Post-depositional folds and calcite veins.

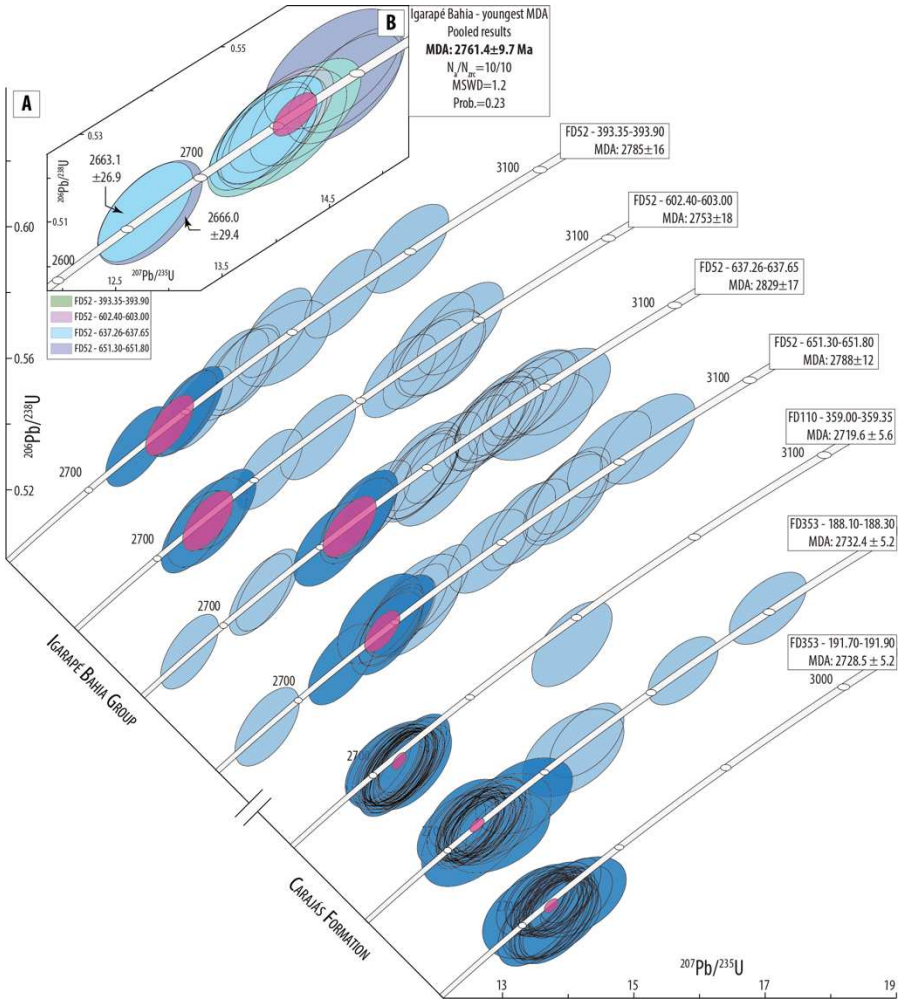

Fig. 14. Wetherill concordia diagrams. Error ellipses are depicted at the 2σ level. **A.** Analyses used to calculate the Maximum Depositional Age (MDA) are depicted in dark blue. Other concordant analyses are depicted by pale blue. The weighted mean error ellipse (concordia date) of the youngest cluster of concordant grains is depicted in pink. The number of analyses, the mean square weighted deviate for concordance and equivalence and the probability for concordance and equivalence for each MDA are provided in Table 4. **B.** MDA calculated from the youngest grains of four samples from the Igarapé Bahia Group, assuming the grains are cogenetic in origin. N_a: number of analyses; N_{zrc}: number of zircon grains; MSWD: Mean Square Weighted Deviate for concordance and equivalence; Prob.: probability for concordance and equivalence.

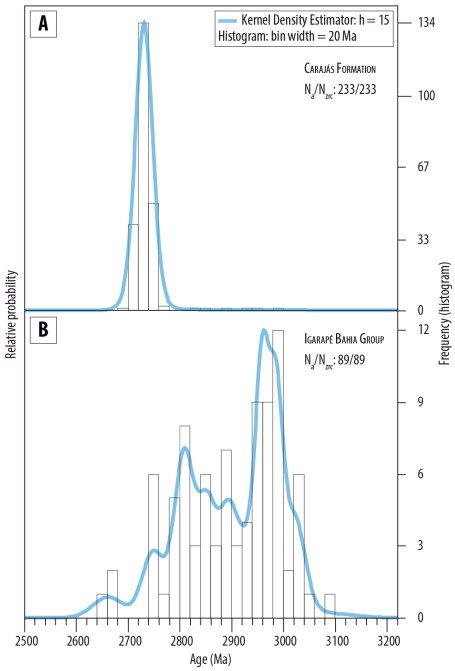

Fig. 15. Histograms and age probability distribution diagrams. Kernel density generated with Density Plotter 8.5 (Vermeesch, 2012). **A.** Carajás Formation, based on TACA and untreated grains (Appendix 3). **B.** Igarapé Bahia Group, based on this work and Melo et al. (2019). N_{zrc}: number of zircon grains.

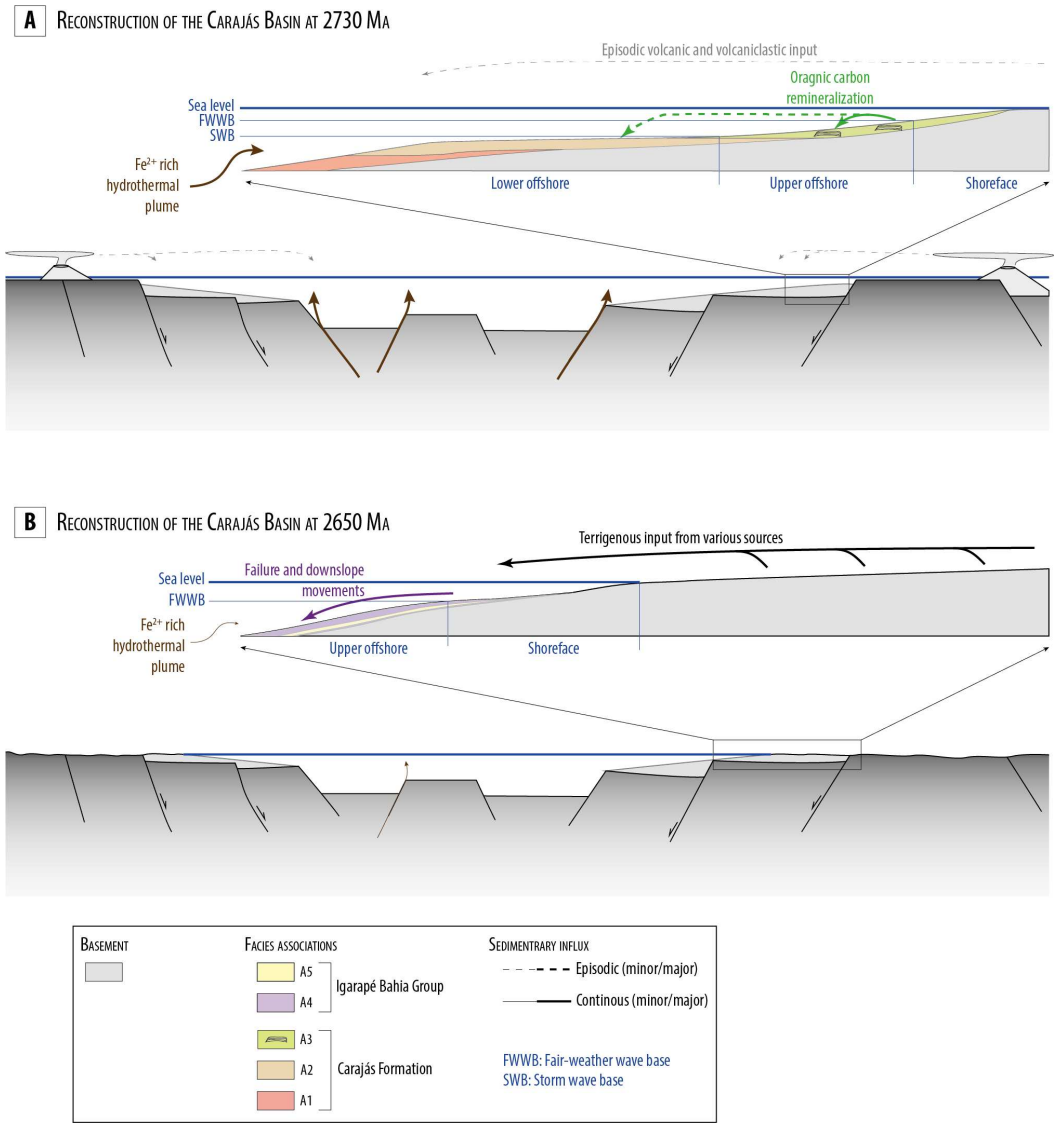

Fig. 16. Schematic cross-sections of the Carajás Basin during the Neoarchean. **A.** Paleoenvironmental and tectonic settings of the Carajás Basin during the deposition of the Carajás Formation, at ca. 2730 Ma. **B.** Paleoenvironmental and tectonic settings of the Carajás Basin during the deposition of the Igarapé Bahia Group at ca. 2650 Ma.

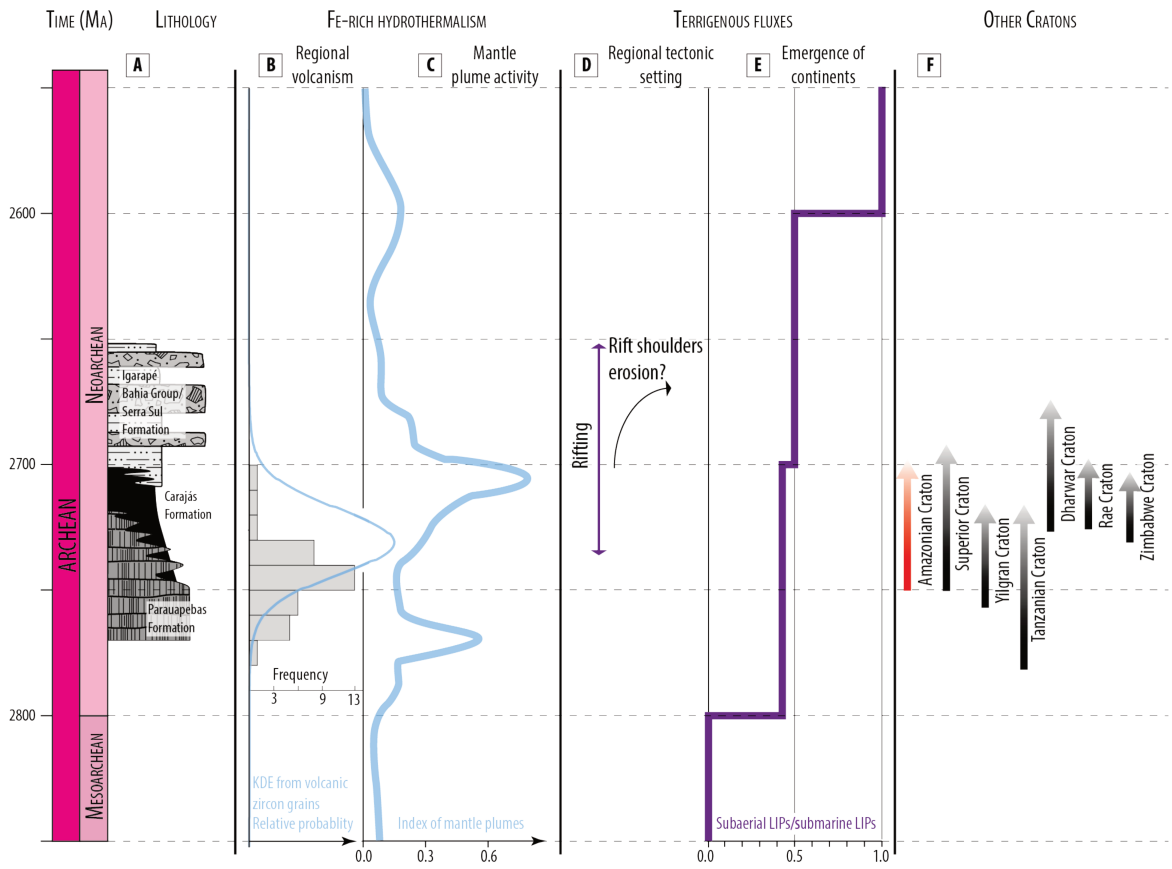

Fig. 17. Chart summarizing the main characteristics of the Carajás Formation and Igarapé Bahia Group and their relationships with regional and global Neoarchean geodynamic events. **A.** Synthetic lithostratigraphy. **B.** Index of volcanic activity from the age distribution of concordant zircon grains of the Carajás Formation. Histogram: frequency distribution of zircon U-Pb and Pb-Pb dates of rocks from the Parauapebas Large Igneous Province (Fig. 2). **C.** Index of mantle plume activity (after Abbott and Isley 2002). **D**. Regional tectonic setting (Feio et al., 2012; Martins et al., 2017; Olszewski et al., 1989; Tavares et al., 2018; Toledo et al., 2019). **E.** Histogram showing the number of LIPs for 100 million years age range, after Kump and Barley (2007). **F.** Comparison of the age of IFs deposits in the Amazonia Craton and in the Yilgarn (Czaja et al., 2018; Van Kranendonk et al., 2013), Tanzanian (Kwelwa et al., 2018), Dharwar (Sunder Raju and Mazumder, 2020), Rae Craton (Bros and Johnston, 2017; Jackson et al., 1990), Zimbabwe Craton (Døssing et al., 2009), and Superior cratons (Bowins and Heaman, 1991; Garcia et al., 2016).

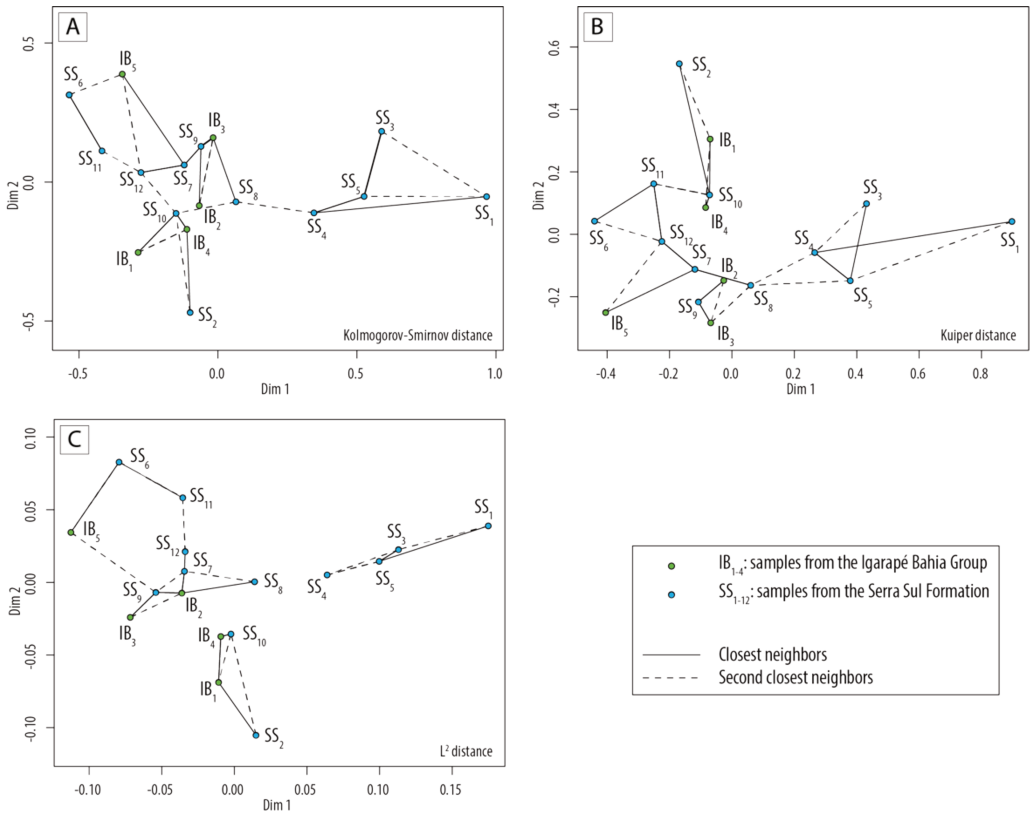

Fig. 18. Multidimensional scaling maps for the Igarapé Bahia Group and the Serra Sul Formation. Axes are dimensionless. Samples from the Serra Sul Formation (SS; Rossignol et al., 2020a): SS_1: GT13 211.95-212.15; SS_2: GT13 213.85-214.00; SS_3: GT16 134.15-134.45; SS_4: GT16 279.96-280.09; SS_5: GT16 295.85-296.07; SS_6: GT16 296.14-296.32; SS_7: GT12 353.40-353.70; SS_8: GT13 185.95-186.15; SS_9: GT16 140.51-140.65; SS_{10}: GT16 174.29-174.45; SS_{11}: GT16 250.40-250.55; SS_{12}: FD02 119.15-118.80. Samples from the Igarapé Bahia (IB_{1-4}; this study; IB_5: Melo et al., 2019): IB_1: FD52 393.35-393.90; IB_2: FD52 602.40-603.00; IB_3: FD52 637.26-637.65; IB_4: FD52 651.30-651.80; IB_5: DH02 407.70. **A.** MDS map using the Kolmogorov-Smirnov metric. Stress = 10.70. **B.** MDS map using the Kuiper metric. Stress = 12.10. **C.** MDS map using the L^2 metric. Stress = 9.05.

Tables

Table 1. Summary of reported ages from ultramafic, mafic and alkaline intraplate felsic rocks from the Parauapebas Large Igneous Province.

Rock type	Rock unit	Material	Method	Age (Ma)	Uncertainties (2σ level)	Reference
Plutonic rocks						
Anorthositic gabbro	Luanga	Zircon	U-Pb	2763	6	(Machado et al., 1991)

Syenogranite	Planalto suite	Zircon	U-Pb	2729	17	(Feio et al., 2012)
Syenogranite	Planalto suite	Zircon	U-Pb	2710	10	(Feio et al., 2012)
Syenogranite	Planalto suite	Zircon	U-Pb	2706	5	(Feio et al., 2012)
Gabbro	Planalto suite	Zircon	U-Pb	2735	5	(Feio et al., 2012)
Gabbronorite		Zircon	U-Pb	2739	6	(Moreto et al., 2015b)
Granite	Sossego	Zircon	U-Pb	2740	26	(Moreto et al., 2015b)
Granite	Cural	Zircon	U-Pb	2739	4	(Moreto et al., 2015b)
Syenogranite	Planalto suite	Zircon	U-Pb	2738	3	(Feio et al., 2013)
Syenogranite	Planalto suite	Zircon	U-Pb	2730	5	(Feio et al., 2013)
Trondjhemite	Pedra Branca	Zircon	U-Pb	2750	5	(Feio et al., 2013)
Granodiorite to syenogranite	Igarapé Gelado	Zircon	U-Pb	2763	4	(Melo et al., 2017)
Granitoid		Zircon	U-Pb	2741	5	(Moreto et al., 2015a)
Granitoid		Zircon	U-Pb	2745	4	Moreto et al., 2015a)
Granite	Bom Jesus	Zircon	U-Pb	2739	9	(Borba et al., 2021)
A-type granite	Planalto suite	Zircon	U-Pb	2739	19	(Borba et al., 2021)
A-type granite	Estrela Complex	Zircon	Pb-Pb	2763	7	(Barros et al., 2009)
A-type granite	Igarapé Gelado	Zircon	Pb-Pb	2731	26	(Barros et al., 2009)
A-type granite	Serra do Rabo	Zircon	Pb-Pb	2743	2	(Barros et al., 2009)
Norite		Zircon	Pb-Pb	2745.2	1.2	(Santos et al., 2013)
Gabbronorite		Zircon	Pb-Pb	2744.5	0.8	(Santos et al., 2013)
Gabbro		Zircon	Pb-Pb	2744.2	1.2	(Santos et al., 2013)
A-type granite	Serra do Rabo	Zircon	U-Pb	2743	2	(Sardinha et al., 2006)
Volcanic rocks						
Rhyodacite	Parauapebas Formation	Zircon	U-Pb	2759	2	(Machado et al., 1991)
Rhyolite	Parauapebas Formation	Zircon	U-Pb	2759	2	(Machado et al., 1991)
Rhyolite	Parauapebas Formation	Zircon	U-Pb	2760	11	(Trendall et al., 1998)
Rhyolite	Parauapebas Formation	Zircon	U-Pb	2757	7	(Trendall et al., 1998)
Basalt	Parauapebas Formation	Zircon	U-Pb	2751.4	3.7	(Krymsky et al., 2007)
Basalt	Parauapebas Formation	Zircon	U-Pb	2749.6	6.5	(Martins et al., 2017)
Basalt	Parauapebas Formation	Zircon	U-Pb	2745	5	(Martins et al., 2017)
Rhyolite	Parauapebas Formation	Zircon	U-Pb	2758	39	(Wirth et al., 1986)
Volcanic rocks	Parauapebas Formation	Zircon	U-Pb	2748	34	(Tallarico et al., 2005)
Mafic metavolcanic rock		Zircon	Pb-Pb	2745	1	(Galarza and Macambira, 2002)
Felsic metavolcanic rock		Zircon	Pb-Pb	2747	1	(Galarza and Macambira, 2002)
Metamorphosed mafic rocks (protolith age)						
Amphibolite	Salobo Group	Zircon	U-Pb	2761	3	(Machado et al., 1991)
Amphibolite		Zircon	U-Pb	2774	19	(Toledo et al., 2019)

Table 2. Summary of age constraints for the main sedimentary units of the Carajás Basin.

Number in Fig. 3	Dating method and interpretation	Reference
Parauapebas Formation		
1	U-Pb dating on zircon grains extracted from a metarhyolite: 2759 ± 2 Ma. Depositional age.	Machado et al., 1991
2	U-Pb dating on zircon grains extracted from a metarhyolite: 2757 ± 7 Ma. Depositional age.	Trendall et al., 1998

Carajás Formation		
3	U-Pb dating on zircon grains extracted from a probable tuff: 2743 ± 11 Ma. Depositional age.	Trendall et al., 1998
4	U-Pb dating on zircon grains extracted from an intrusive dolerite sill: 2740 ± 8 Ma. Minimum depositional age.	Trendall et al., 1998
Serra Sul Formation		
5	U-Pb dating on detrital zircon grains: 2684 ± 10 Ma. Maximum depositional age.	Rossignol et al., 2020
Igarapé Bahia Group		
6	U-Pb dating on hydrothermal monazite collected in the Igarapé Bahia Group: 2575 ± 12 Ma. Hydrothermal circulations at a regional scale are also indicated by Re-Os dates on sulfides at 2576 ± 8 Ma and 2568 ± 8 Ma, and by the emplacement of small bodies of granitic rocks and pegmatites at 2557 ± 26 Ma and 2562 ± 39 Ma, respectively (U-Pb dating on zircon). Minimum depositional age for the Igarapé Bahia Group: ca. 2.6 Ga	Tallarico et al., 2005 (U-Pb/Monazite); Requia et al., 2003 (Re-Os/sulfide); Toledo et al., 2019 (U-Pb/zircon)
All uncertainties are given at the 2σ level.		

Table 3. Sedimentary facies of the Carajás Formation and Igarapé Bahia Group.

Code	Lithology	Sedimentary structures	Depositional processes
Iron-rich facies			
I1	Alternating layers of Fe-rich minerals and chert (microcrystalline quartz) or jasper (i.e., chert with minor, disseminated microcrystalline hematite) (Fig. 5A, B, C). Thickness of chert BIF intervals: m to hundreds of m.	Banding over a range of scale, from meters (macrobands) to centimeters (mesobands) to millimeters and sub-millimeters layers (microbands). The laminations are generally evenly layered (Fig. 5A), but sometimes display a wavy (Fig. 5B), irregular banding, or exhibit reactivation surfaces (Fig. 5C). The layers sometimes display diagenetic inflated beds (Fig. 6A) and secondary mineralization (Fig. 6B).	Deposition from suspension of a Fe-rich chemical mud (Dimroth, 1975; Morris, 1993; Trendall, 2002; Klein, 2005) or by turbidity current (Dimroth, 1975; Krapež *et al.*, 2003; Rasmussen *et al.*, 2013).
I2	Chert, siliceous BIF or carbonate BIF. Bed thickness: m to tens of m.	Chaotic horizons, disordered or strongly folded (Fig. 6C). Intraformational angular clasts occurs at slip surfaces. Syn-sedimentary faults (Fig. 6E).	Slump and/or slide (Martinsen, 1994).
I3	Granular Iron Formation comprising very elongated (Fig. 7A) to rather spherical grains (Fig. 7B, C), mainly sub-angular to sub-rounded, made up of cherty material very similar to the one of the I1 facies.	Ungraded or normally graded. When elongated micro-clasts are present, they show an orientation and are flattened parallel to the bedding (Fig. 7C). Some clasts are bended or ductilely deformed.	Rip-up clasts redeposited by turbidity current and/or bottom return flow induced by storms (Simonson & Goode, 1989; Beukes & Klein, 1990). Preservation when seafloor silicification outpaced

	Bed thickness: cm to dm.		deposition of Fe-rich mud precursor of BIF, equivalent of Phanerozoic hardgrounds (Rasmussen *et al.*, 2015).
I4	Alternating layers of Fe-rich minerals (mainly magnetite) and carbonate (Fig. 5D) with minor amount of chert. Thickness of carbonate BIF intervals: cm to hundreds of m.	Banding over a range of scale, (macrobands, mesobands and microbands). The laminations range from a finely and regularly laminated structure to weak and irregular magnetite layers. The layers commonly display syn-sedimentary micro-folding (Fig. 5D), reactivation surfaces (Fig. 6E).	Similar to I1 facies above the carbonate compensation depth, or under warmer climate, which favor carbonate over chert precipitation (Beukes, 1983), or in more alkaline water (Spier *et al.*, 2007), or under a high organic carbon input which contributed as the source of carbon for carbonate precipitation (Craddock & Dauphas, 2011).
Conglomerate			
G1	Matrix-supported ironstone flat pebbles conglomerate. Clasts are mainly elongated and angular (Fig. 8A) but some have sub-rounded to rounded ends (Fig. 8B, C). Clasts are mainly made up of BIF or chert. A few clasts are made up of GIF (Fig. 8D, E) or greenish sandstone. Ferruginous, greenish to reddish matrix. Bed thickness: m to tens of m.	Ungraded to normally graded. The clasts exhibit an orientation (Fig. 8A, B, C). Some clasts are slightly curved to strongly bended (Fig. 8A, E). Non-erosive base.	Failure and mass movement of loosely consolidated sediments (Myrow *et al.*, 2004).
G2	Flat-pebbles conglomerate, matrix- to clast-supported. Clasts are elongated and generally exhibit sub-rounded to rounded shapes, with a few sub-angular clasts (Fig. 11A, B, C). Clasts are intraformational and made up of sand, silt to clay, or a mixture of sand	Generally ungraded but sometimes with inverse, normal or inverse to normal grading. The clasts generally exhibit an orientation and are flattened parallel to the bedding (Fig. 11A, E). Generally non-erosive base (Fig. 11E). A few beds have a slightly erosive base.	Failure and mass movement of loosely consolidated sediments and/or wave or storm reworking of shoreline deposits (Myrow *et al.*, 2004).

	and silts (Fig. 11D). The matrix is made up of similar material. Bed thickness: tens of cm to m.		
Sandstone and Fine			
S1	Fine to very coarse sand (Fig. 12A) with floating clasts (granules to pebbles, sometimes intraformational muddy ripped up clasts; Fig. 12B). Occurrence of contorted sandy to muddy rafts (Fig. 12D). Bed thickness: dm to m.	Massive or normal grading, sometimes with horizontal planar bedding. Few occurrences of contorted beds.	Hyper-concentrated density flow to turbidity flow (Mulder & Alexander, 2001) or rapid suspension fallout (Postma, 1990).
S2	Various lithologies, mainly sand and silt. Thickness: tens of cm to m.	Chaotic horizons, sometimes forming anastomosed elutriation bands (Fig. 12E), or strongly folded beds (Fig. 12F).	Slump and/or slide (Martinsen, 1994), deformation induced by water escape (Ravier *et al.*, 2015).
F1	Greyish to greenish siltstone, fine to medium sandstone Bed thickness: cm to tens of cm.	Generally horizontal laminations, sometimes massive.	Deposition from suspension.
F2	Darkish siltstone to claystone. fine to medium sandstone Bed thickness: cm to tens of cm.	Apparently massive. Sometimes crosscut by injectites (clastic dyke; Fig. 6F)	Deposition from suspension.
Volcaniclastic			
V1	Angular clasts made up of similar material than the under- and overlying basaltic rocks. Indistinct boundaries with under- and overlying basaltic rocks. Bed thickness: tens of cm.	Massive, ungraded.	Autoclastic or hyaloclastic deposits formed by fragmentation of the lava flow by contact with air or water (White & Houghton, 2006).
V2	Greyish clay layers, sometimes containing a few zircon grains, and greenish sandstone layers. Bed	No apparent sedimentary structure. Sharp contacts with under- and overlying BIF.	Diagenetic volcanic ashes, potentially reworked, and hyaloclastic deposits (White &

	thickness: cm (clays) to m (greenish sandstone).		Houghton, 2006) or subaqueous debris flow reworking volcaniclasts (Sohn *et al.*, 2008).
Carbonates			
C1	Carbonate (ankerite, calcite; Fig. 9G) comprising a few pyrite (Fig. 9F), iron oxides (mainly magnetite; Fig. 9G), and micritic texture (Fig. 9E). Continuous transition between C and I4. Thickness: dm to m.	mm to cm-thick parallel (Fig. 9A), crinkled, wavy (Fig. 9D), or irregular layering (Fig. 9C). Laminations are underlined by oxide layers ranging from cm-thick to very tiny (mm-thick) and discontinuous magnetite layers. Magnetite beds sometimes exhibit pinching geometries or underline wavy laminations (Fig. 9B).	In the Carajás Formation, C facies correspond to microbial mats or stromatolites (Hagadorn & Bottjer, 1997; Riding, 2000; Noffke *et al.*, 2001; Posth *et al.*, 2013) alternating with background carbonate sedimentation.
C2	Alternation of carbonate rich layers with fine terrigenous sand beds or fine magnetite layers and comprises a few clasts (Fig. 13A, B, C). Thickness: dm to m.	Thinly laminated, with evidence of post-depositional deformations.	Sediments deposited during periods of low detrital input, allowing for the deposition of carbonate and iron-rich layers.

Table 4. Facies associations of the Carajás Formation and Igarapé Bahia Group.

Code	Facies association	Depositional environment
Carajás Formation		
A1	I1 with minor occurrences of G1, I1 and I2, I3, F2 and rare occurrences of I4, and V2.	Deep-water, below storm wave-base (Klein, 2005; Krapež et al., 2003; Morris, 1993; Rasmussen et al., 2013; Trendall, 2002). Episodic volcanic inputs and reworking of volcanic loosely lithified volcanic deposits by subaqueous debris flow suggest a coeval volcanic activity (Ducassou et al., 2019; Sohn et al., 2008).
A2	I4 with rare occurrences of I3 and F2.	Similar to A1, but in a more proximal (shoreward) and shallower setting (Beukes and Gutzmer, 2008; Smith et al., 2013).
A3	I4 and C1 with occurrences of I1, I3 and rare occurrence of F1.	Shallow-water environment (photic zone), above storm wave-base, as attested by the occurrence of photosynthetic organisms in C1 facies (Rego et al., 2021) and of microbially-induced sedimentary structures (Hagadorn and Bottjer, 1997; Noffke et al., 2001; Riding,

2000; Vennin et al., 2015). Intermitant reworking of poorly lithified material suggesting a rather high-eneregy environment (Beukes and Klein, 1990; Simonson and Goode, 1989).

Igarapé Bahia Group		
A4	G2, S1, S2, F1 and F2.	Offshore environment (Myrow et al., 2004) under important terrigenous influx.
A5	C2, S1 and F1.	Similar to A4, but under low terrigenous influx, allowing for the development of iron-rich facies.

Table 5. Summary of maximum depositional ages.

Sample	N_{zr}	Probability of concordance ≥ 10%, decay constants errors included								
		Detection limits (%)				Maximum depositional age				
		$DL_{1(pL=0.5)}$	$DL_{1(pL=0.95)}$	$DL_{3(pL=0.5)}$	$DL_{1(pL=0.95)}$	Concordia age	± (2σ)	n	MSWD	Probability
Carajás Formation										
FD110 - 359.00-359.35	36	1.9	8.0	7.4	16.5	2719.6	5.6	35	0.47	1.00
FD353 - 188.10-188.30	41	1.7	7.0	6.5	14.6	2732.4	5.2	37	0.53	1.00
FD353 - 191.70-191.90	38	1.8	7.6	7.0	15.7	2728.5	5.2	38	0.57	1.00
Igarapé Bahia Group										
FD52 - 393.35-393.90	11	6.3	23.8	23.6	47.1	2785	16	3	1.8	0.11
FD52 - 602.40-603.00	11	6.3	23.8	23.6	47.1	2753	18	3	0.44	0.82
FD52 - 637.26-637.65	25	2.7	11.3	10.6	23.2	2829	17	3	0.48	0.79
FD52 - 651.30-651.80	19	3.6	14.6	13.9	29.6	2788	12	6	1.10	0.36
Igarapé Bahia Group – pooled results										
Igarapé Bahia	66	1.0	4.4	4.1	9.3	2761.4	9.7	10	1.2	0.23

N_{zr}: number of concordant zircon grain analyzed per sample; n: number of analyses used to calculate the maximum deposition age; DL: detection limit, calculated after Rossignol *et al.* (2019); DL_1: detection limit for at least one grain; DL_3: detection limit for at least three grains; $_{pL}$: probability level assigned to the detection limits; MSWD: mean square of weighted deviates. The MSWD and the probability given for the concordia ages are for both concordance and equivalence. Note that the MSWD of the samples from the Carajás Formation is below the range of acceptable values at 95% confidence level, which could indicate an overestimation of the uncertainties (Wendt & Carl, 1991; Spencer *et al.*, 2016). na: non applicable.

Appendices

Appendix 1. Coordinates of the studied drill cores and complementary sedimentological results.

Supplementary Table 1: Location of the studied drill cores

Complete name	Abbreviated name	Decimal Latitude[1]	Decimal Longitude[1]	Drill-core repository
SN4FD00055	FD 55	-6,082286622	-50,19299351	Vale S.A. Núcleo de Carajás
SN5FD00110	FD 110	-6,116937337	-50,13905439	Vale S.A. Núcleo de Carajás
SSDFD00353	FD 353	-6,405362884	-50,34734517	Vale S.A. Núcleo de Carajás
SSDFD00354	FD 354	-6,396814131	-50,34684967	Vale S.A. Núcleo de Carajás
SSDFD00365	FD 365	-6,402548496	-50,33233868	Vale S.A. Núcleo de Carajás
S11D214	S11D214	-6,394350618	-50,32346099	Vale S.A. Núcleo de Carajás
ALM-ALMO-FD052	FD 52	-6,02285	-50,57351	Vale S.A. Núcleo de Carajás

1: WGS 84 reference framework